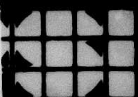


12

PSI TR-184

AD A 122 038



FINAL TECHNICAL REPORT
PULSED LASER PROPULSION STUDIES
Vol. I: Thruster Physics and Performance

ARPA ORDER NO: 3176
CONTRACTOR: PHYSICAL SCIENCES INC.
EFFECTIVE DATE OF CONTRACT: 1 March 1978
CONTRACT EXPIRATION DATE: 1 September 1981
REPORTING PERIOD: 1 March 1978 - 1 Sept. 1981
CONTRACT NO: N00014-78-C-0328
PRINCIPAL INVESTIGATOR: Dr. David I. Rosen
(617) 475-9030

DTIC
EXCERPT
DEC 2 1982

Sponsored by

A

Defense Advanced Research Projects Agency (DOD)
ARPA Order No. 3176

Monitored by

Office of Naval Research under Contract No. N00014-78-C-0328

This document has been approved
for public release and sale; its
distribution is unlimited.

DTIC FILE COPY

PHYSICAL SCIENCES INC.

Research Park, Andover, MA 01810

82 12 02 005

"The views and conclusions contained in this document are those of the authors and should not be interpreted as necessarily representing the official policies, either expressed or implied, of the Defense Advanced Research Projects Agency of the U.S. Government."

UNCLASSIFIED

SECURITY CLASSIFICATION OF THIS PAGE (When Data Entered)

REPORT DOCUMENTATION PAGE		READ INSTRUCTIONS BEFORE COMPLETING FORM
1. REPORT NUMBER	2. GOVT ACCESSION NO.	3. RECIPIENT'S CATALOG NUMBER
	AD-A222 038	
4. TITLE (and Subtitle)	5. TYPE OF REPORT & PERIOD COVERED	
PULSED LASER PROPULSION STUDIES Vol. I: Thruster Physics and Performance	Final Technical Report - Vol. I 1 March 1978 - 1 Sept. 1981	
7. AUTHOR(s)	6. PERFORMING ORG. REPORT NUMBER	
D. I. Rosen; N. H. Kemp; G. Weyl; P. E. Nebolsine and G. Kothandaraman	PR-184	
9. PERFORMING ORGANIZATION NAME AND ADDRESS	8. CONTRACT OR GRANT NUMBER(s)	
PHYSICAL SCIENCES INC. Research Park Andover, MA 01810	N00014-78-C-0328	
11. CONTROLLING OFFICE NAME AND ADDRESS	10. PROGRAM ELEMENT, PROJECT, TASK AREA & WORK UNIT NUMBERS	
Defense Advanced Research Projects Agency Strategic Technology Office 1400 Wilson Boulevard, Arlington, VA 22209	ARPA Order No. 3176	
14. MONITORING AGENCY NAME & ADDRESS (if different from Controlling Office)	12. REPORT DATE	
Office of Naval Research Arlington, VA 22217	October 1982	
	13. NUMBER OF PAGES	
	274	
	15. SECURITY CLASS. (of this report)	
	Unclassified	
	15a. DECLASSIFICATION/DOWNGRADING SCHEDULE	
16. DISTRIBUTION STATEMENT (of this Report)		
Unlimited distribution		
17. DISTRIBUTION STATEMENT (of the abstract entered in Block 20, if different from Report)		
18. SUPPLEMENTARY NOTES		
19. KEY WORDS (Continue on reverse side if necessary and identify by block number)		
Pulsed Laser Propulsion Laser-Induced Breakdown Laser-Supported Detonation Waves Pulse-Jets Non-steady Nozzle Flow MICROWES MICROWES		
20. ABSTRACT (Continue on reverse side if necessary and identify by block number)		
This report describes experimental and analytical studies on pulsed laser propulsion (carried out between May 1978 and December 1980). Volume I describes thruster performance and phenomenology studies. They include theoretical investigations of laser-induced gas breakdown at 10.6 μm and 0.35 μm , the development of a detailed computer model of the quasi-one dimensional nonsteady flow of real gases in the nozzle, and small-scale thruster performance and absorption physics experiments using pulsed CO_2 (10.6 μm) and XeF (0.35 μm) lasers. Volume II contains the results of mission analysis studies to evaluate		

UNCLASSIFIED

SECURITY CLASSIFICATION OF THIS PAGE(When Data Entered)

the system requirements of some candidate defense-related missions for pulsed laser propulsion. These studies address the problem of orbit-to-orbit transfer of satellites, as well as the launch of a vehicle from the earth.

The detailed and well-diagnosed experiments, coupled with the fluid dynamics model which includes laser absorption and real gas equilibrium, have led to a more reliable assessment and better understanding of the performance of a pulsed laser-powered thruster. Wavelength scaling was explored, with breakdown theory and the fluid dynamics model. It was found that more than 50% of the 0.35 μm radiation could be converted to blast wave energy in the propellant gas, when external focusing optics were used.

The results of the mission analyses, in Volume II, indicate that earth launch of practical payloads will require laser systems powers which probably will not be available for several decades. However, orbit-to-orbit transfer of satellites may be an attractive nearer term mission for laser propulsion.

A

UNCLASSIFIED

SECURITY CLASSIFICATION OF THIS PAGE(When Data Entered)

ABSTRACT

This report describes experimental and analytical studies on pulsed laser propulsion carried out between May 1978 and December 1980. Volume I describes thruster performance and phenomenology studies. They include theoretical investigations of laser-induced gas breakdown at 10.6 μm and 0.35 μm , the development of a detailed computer model of the quasi-one-dimensional nonsteady flow of real gases in the nozzle, and small-scale thruster performance and absorption physics experiments using pulsed CO_2 (10.6 μm) and XeF (0.35 μm) lasers. Volume II contains the results of mission analysis studies to evaluate the system requirements of some candidate defense-related missions for pulsed laser propulsion. These studies address the problem of orbit-to-orbit transfer of satellites, as well as the launch of a vehicle from the earth.

The detailed and well-diagnosed experiments, coupled with the fluid dynamics model which includes laser absorption and real gas equilibrium, have led to a more reliable assessment and better understanding of the performance of a pulsed laser-powered thruster. Wavelength scaling was explored, with breakdown and single-pulse experiments at 0.35 μm , coupled with the laser-induced gas breakdown theory and the fluid dynamics model. It was found that more than 50% of the 0.35 μm radiation could be converted to blast wave energy in the propellant gas, when external focusing optics were used.

The results of the mission analyses, in Volume II, indicate that earth launch of practical payloads will require laser systems powers which probably will not be available for several decades. However, orbit-to-orbit transfer of satellites may be an attractive nearer term mission for laser propulsion.



A

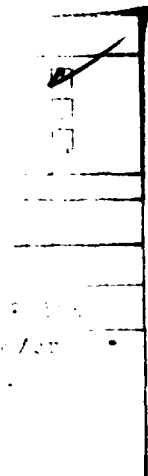


TABLE OF CONTENTS

<u>Section</u>	<u>Page</u>
1.	Introduction and Executive Summary 1
1.1	References 6
2.	Theoretical Studies of Laser-Induced Breakdown 7
2.1	Introduction 7
2.2	General Considerations 8
2.3	Breakdown at 10.6 μm 14
2.4	Breakdown at 0.35 μm 26
2.5	References 56
3.	Detailed Model of Quasi-One-Dimensional Flow of a Real Gas with Laser Energy Absorption 59
3.1	Introduction 59
3.2	Equations of Motion 62
3.3	Simplified Equilibrium Properties of Single- Ionized Argon 63
3.4	Absorption Coefficient for Singly-Ionized Argon 69
3.5	Steady Flow in Nozzle 71
3.6	One-Dimensional LSD Wave 75
3.7	Similarity Variables 80
3.8	Numerical Method 85
3.9	Results for Perfect Gases and Singly-Ionized Argon 91
3.10	Equilibrium Properties of Hydrogen 127
3.11	Improved Absorption Coefficients for Singly- Ionized Argon and Hydrogen 144
3.12	Equilibrium Properties of Multiply-Ionized Argon 149
3.13	Absorption Coefficients for Multiply-Ionized Argon 160
3.14	Results for Multiply-Ionized Argon 166
3.15	References 183
4.	Small-Scale Thruster Performance and Absorption Physics Phenomenology Experiments 185
4.1	Introduction 185
4.2	Thruster Performance Experiments at 10.6 μm 186
4.3	Absorption Physics Experiments 228
4.4	Preliminary Single-Pulse Thruster Performance Results at 0.35 μm 251
4.5	References 255
5.	Conclusions 257

LIST OF FIGURES

<u>Figure</u>		<u>Page</u>
1.1	Repetitively pulsed laser powered thruster.	2
2.1	Electron density for transition from free diffusion to ambipolar diffusion.	11
2.2	Comparison of Boltzmann code with DC breakdown measurements in argon.	16
2.3	Comparison of Boltzmann code with DC breakdown results in hydrogen.	17
2.4	Avalanche rate in H ₂ O, H ₂ , Ar and air as a function of 10.6 μm laser intensity.	18
2.5	Electron-neutral collision frequency in H ₂ , H ₂ O, air and Ar as a function of 10.6 μm laser intensity.	19
2.6	Gaunt factor for electron-ion bremsstrahlung absorption following Karzas and Latter.	22
2.7	10.6 μm breakdown thresholds in argon.	24
2.8	10.6 μm breakdown threshold in hydrogen.	25
2.9	Energy levels in argon.	27
2.10	Multiphoton ionization threshold in argon and nitrogen.	29
2.11	Electron-neutral inverse bremsstrahlung cross section \bar{K} in argon, $h\nu = 3.4$ eV.	33
2.12	Electron inelastic cross sections in argon.	35
2.13	Growth of electron population with time, argon at standard density.	41
2.14	Cascade rate coefficient α_4 as a function of laser intensity for early time cascade growth in argon, $h\nu = 3.5$ eV.	42
2.15	Electron distribution function in argon at two laser fluxes.	44
2.16	Effect of electron-electron collisions on the distribution function of electrons.	46

LIST OF FIGURES (Cont.)

<u>Figure</u>		<u>Page</u>
2.17	Potential energy curves for the system Ar + Ar.	48
2.18	Electron energy and gas temperature during breakdown, $n = 1$ amagat, $I = 10^{10}$ W/cm ² .	52
2.19	Growth of electron concentration and first excited state concentration in the late time breakdown of argon.	53
2.20	Various absorption mechanisms in argon.	54
3.1	Dependence on initial laser intensity I_1 of LSD wave velocity and temperature behind LSD wave. Perfect and real argon.	81
3.2	Structure of LSD wave as a function of percent of laser energy absorbed. Real argon.	82
3.3a	Calculated temperature profiles for an ordinary shock wave in real argon, initially at 1 atm, 300 K.	93
3.3b	Calculated pressure profiles for an ordinary shock wave in real argon, initially at 1 atm, 300 K.	94
3.4a	Calculated temperature profiles for an LSD wave in real argon initially at 1 atm, 300 K. $I_1 = 14.12$ MW/cm ² , $\Delta x = 1.E-3$ cm.	96
3.4b	Calculated pressure profiles for an LSD wave in real argon, initially at 1 atm, 300 K.	97
3.5a	Calculated temperature profiles for an LSD wave in real argon, initially at 1 atm, 300 K.	98
3.5b	Calculated pressure profiles for an LSD wave in real argon, initially at 1 atm, 300 K.	99
3.6a	Calculated temperature profiles for an LSD wave in real argon, initially at 1 atm, 300 K.	101
3.6b	Calculated pressure profiles for an LSD wave in real argon, initially at 1 atm, 300 K.	102
3.7a	Calculated temperature profiles for a blast wave in a nozzle.	108

LIST OF FIGURES (Cont.)

<u>Figure</u>		<u>Page</u>
3.7b	Calculated pressure profiles for a blast wave in a nozzle.	109
3.7c	Calculated velocity profiles for a blast wave in a nozzle.	110
3.8a	Calculated temperature profiles for blast wave in a nozzle.	111
3.8b	Calculated pressure profiles for a blast wave in a nozzle.	112
3.8c	Calculated velocity profiles for a blast wave in a nozzle.	113
3.9	Correlation of shock trajectory for a blast wave in a nozzle.	115
3.10	Correlation of shock trajectory for a blast wave in a nozzle.	117
3.11	Correlation of shock trajectory for a blast wave in a nozzle.	119
3.12	Time interval between shock passage at two stations as a function of energy, for blast wave in a nozzle.	121
3.13a	Calculated pressure profiles for laser absorption in a nozzle.	123
3.13b	Calculated temperature profiles for laser absorption in a nozzle.	124
3.13c	Calculated power profiles for laser absorption in a nozzle.	125
3.14	Absorption coefficient for 10.6 μm and 0.353 μm radiation in multiply-ionized argon.	165
3.14a	Pressure profiles for LSD wave in a conical nozzle.	168
3.14b	Density profiles for LSD wave in a conical nozzle, $P_{\text{st}} = 7 \text{ atm}$, $T_{\text{st}} = 300 \text{ K}$, laser energy 3 J, pulse time 0.5 μs , multiply-ionized argon.	169

LIST OF FIGURES (Cont.)

<u>Figure</u>		<u>Page</u>
3.14c	Temperature profiles for LSD wave in a conical nozzle.	170
3.15	Laser power profile for LSD wave in a conical nozzle.	171
3.16a	Pressure profiles for shock wave in a conical nozzle.	172
3.16b	Density profiles for shock wave in a conical nozzle.	173
3.16c	Temperature profiles for shock wave in a conical nozzle.	174
3.17a	Pressure profile for shock wave in a conical nozzle.	176
3.17b	Density profiles for shock wave in a conical nozzle.	177
3.17c	Temperature profiles for shock wave in a conical nozzle.	178
3.18	Shock location as a function of time in similarity variables.	180
3.19	Shock location as a function of peak shock pressure in similarity variables.	182
4.1	Parabolic rocket schematic.	189
4.2	Blast wave energy vs. \dot{m} .	194
4.3	Measured blast wave energy vs. \dot{m} in argon.	195
4.4	Blast wave energy in argon for different throat sizes.	196
4.5	I_{sp} vs. Δm for argon; Δt is the delay time between the firing of the first and second laser pulse.	198
4.6	I_{sp} vs. Δm for hydrogen.	199
4.7	Mean laser absorptance in argon vs. \dot{m} .	204
4.8	Mean laser absorptance in hydrogen vs. \dot{m} .	205
4.9	Comparison of optical absorptance and blast wave conversion efficiencies in argon.	206

LIST OF FIGURES (Cont.)

<u>Figure</u>		<u>Page</u>
4.10	Comparison of optical absorptance and blast wave conversion efficiencies in hydrogen.	207
4.11	Time history of return (unabsorbed) laser intensity $\dot{m} = 0$ vs. $\dot{m} = .93$ g/s, argon.	209
4.12	Time history of return (unabsorbed) laser intensity $\dot{m} = 0$ vs. $\dot{m} = 12.7$ g/s, argon.	210
4.13	Time history of laser absorptance $\dot{m} = .93$ g/s, argon.	211
4.14	Time history of laser absorptance $\dot{m} = 12.7$ g/s, argon.	212
4.15	Comparison of mean laser absorptance in argon as determined from calorimetric and time-resolved measurements.	214
4.16	Comparison of experimental measurements of the propellant optical absorption efficiency with the measured blast wave conversion efficiency, argon propellant, $\lambda = 10.6$ μm .	216
4.17	Experimental set-up for radiometric measurements of the nozzle exhaust temperature.	218
4.18	Observed emission intensity of the argon $4s(3/2) \leftrightarrow 4p'(1/2)$ transition in the laser-heated nozzle exhaust.	220
4.19	Observed emission intensity of the continuum of argon in the laser-heated nozzle exhaust, monochromator setting is 7465 \AA .	222
4.20	Argon energy level diagram.	223
4.21	Observed argon emission lines and their relative intensities.	225
4.22	Schematic diagram of experimental set-up used for absorption physics studies.	230

LIST OF FIGURES (Cont.)

<u>Figure</u>		<u>Page</u>
4.23	Comparison of experimentally measured breakdown thresholds in argon with PSI's theory predictions, $\lambda = 10.6 \mu\text{m}$, $\tau_p = 10^{-7}$ s.	223
4.24	Comparison of experimentally measured breakdown thresholds in hydrogen with PSI theory predictions, $\lambda = 10.6 \mu\text{m}$, $\tau_p = 10^{-7}$ s.	234
4.25	Fraction of $10.6 \mu\text{m}$ laser pulse energy absorbed in argon breakdown plasma as a function of the initial gas pressure.	236
4.26	Argon laser induced breakdown threshold at $0.35 \mu\text{m}$.	240
4.27	Laser-induced breakdown threshold for argon, $\lambda = 0.35 \mu\text{m}$ $P = 1$ atm.	243
4.28	Laser induced breakdown threshold in argon vs. wavelength ($P = 1$ atm).	244
4.29	Experimental laser-induced breakdown thresholds for several gases at $\lambda = 0.35 \mu\text{m}$, $\tau_p = 0.5 \mu\text{s}$.	245
4.30	Fraction of laser pulse energy absorbed in argon breakdown plasma, $0.35 \mu\text{m}$ vs. $10.6 \mu\text{m}$.	247
4.31	Experimental determinations of fraction of XeF laser pulse energy deposited in breakdown gas.	249
4.32	Schematic of nozzle experiment for $0.35 \mu\text{m}$ energy conversion efficiency measurements.	252
4.33	Design conditions for laboratory experiment to demonstrate 1000 s I_{sp} in argon, $\lambda = 0.35 \mu\text{m}$.	253
4.34	XeF laser to blast wave energy conversion efficiency vs. stagnation pressure. Blast wave energy is inferred from shock transit time measurements in conical nozzle flow.	254

LIST OF TABLES

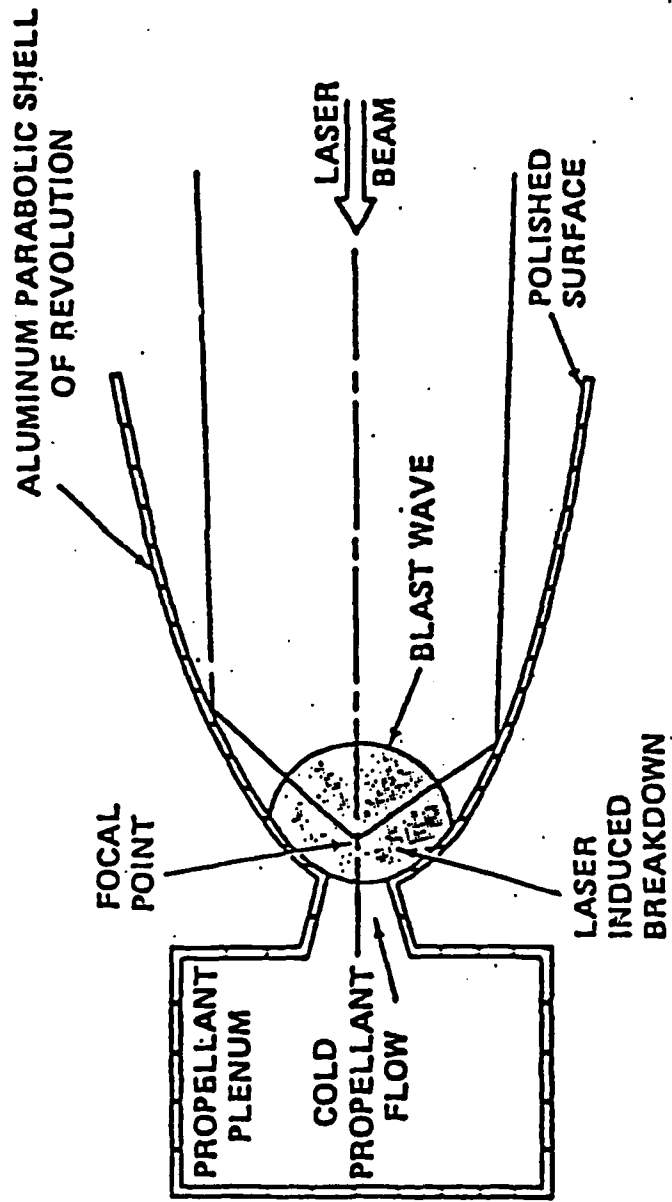
<u>Table</u>		<u>Page</u>
2.1	Contribution of various levels to photoionization cross section of excited states in argon.	39
3.1	Transport scattering cross-section for electron-neutral collisions in argon.	72
3.2	Blast wave runs.	106
3.3	Comparison of present thermodynamic properties with those of Patch.	142
3.4	Argon partition function parameters.	156
3.5	Composition of equilibrium argon.	157
3.6	Thermodynamic properties of equilibrium argon.	158
4.1	Observed emission lines from the excited states of argon.	221
4.2	Population distributions of the excited argon levels and the calculated temperatures.	226

1. INTRODUCTION AND EXECUTIVE SUMMARY

Over the past several years Physical Sciences Inc. (PSI) has been developing, under DARPA support, the technology of pulsed laser propulsion.^{1.1-1.3} Rocket propulsion powered by high energy laser beams, both CW and repetitively pulsed, has been shown to have several potentially desirable features^{1.1-1.3} including: (1) high I_{sp} with high thrust, (2) a remote power source, and (3) high payload to total weight ratio. The studies to date have indicated that pulsed laser propulsion, in particular, is attractive because: (1) I_{sp} 's of 500 to 1000 s have already been demonstrated,^{1.4} (2) it can yield a high thrust to power ratio, (3) it lends itself to simple engine design, (4) the propellant requirements are simple, and (5) it does not have the flow stability constraints associated with CW propulsion.^{1.5}

The basic physics of the PSI pulsed laser propulsion concept is most clearly illustrated in the schematic diagram presented in Fig. 1.1. An incoming laser beam is collected and focused by the interior walls of a parabolic nozzle to yield a breakdown in the propellant gas at the focal point of the parabola. The resulting high pressure plasma is characteristic of detonation wave initiation by high power laser-induced breakdown. With a short duration laser pulse the detonation wave quickly becomes a blast wave, which propagates to the nozzle exit plane converting all of the high pressure of the gas behind it into a force on the nozzle wall. The fluid mechanics of this concept, when operated as a repetitively pulsed device, is discussed in Refs. 1.1-1.3, and it is shown that the strength of the laser-induced blast wave and the laser repetition rate specify the propellant mass flow. The propellant is fed to the focal region from a high pressure plenum chamber as shown, and the laser-induced blast wave stops the propellant flow through the throat until the pressure at the throat weakens to the plenum pressure; then, the propellant flow restarts.

The earliest work on pulsed laser propulsion at PSI involved the development of a theoretical model of the fluid mechanics that was based on blast wave theory of a perfect gas in a conical nozzle.^{1.3} The model provided valuable information about the behavior of the gases, the effect of



- PROPULSION SEQUENCE
- COLD PROPELLANT FLOWS THROUGH THROAT
- LASER ENERGY ABSORBED DOWNSTREAM AT FOCUS
- SHOCKED GAS EXPANDS OUT NOZZLE
- SEQUENCE REPEATS: PROPELLANT USE CONTROLLED BY MASS FLOW AND LASER REPETITION RATE

Fig. 1.1 Repetitively pulsed laser powered thruster.

pulse repetition rate, and the rocket performance to be expected. Using this model the first experiments to test the PSI pulsed laser propulsion concept were specified and designed.

The first experiments to be performed at PSI used pulsed CO₂ lasers and were conducted with small-scale conical and parabolic nozzles. With a background pressure of one atmosphere, a maximum specific impulse of 900 ± 400 s was obtained for helium propellant with an energy conversion efficiency (exhaust energy/laser energy) of ~ 50%. In addition, at a background pressure of 10⁻⁴ atmosphere, a specific impulse of 500 ± 100 s was obtained with a self-focusing parabolic nozzle operating with helium propellant.

The experimental and analytical investigations described in the present report were performed during the period May 1978 through December 1980. The studies carried out are divided into two categories - thruster performance and phenomenology studies, and mission analyses. The studies relating to thruster performance (Vol. I) include: theoretical investigations into the laser-induced gas breakdown process at 10.6 μm and 0.35 μm (Sec. 2); the development of a detailed computer model of the quasi-1D non-steady flow in the nozzle (Sec. 3); and small-scale thruster performance and absorption physics experiments using pulsed CO₂ (10.6 μm) and XeF (0.35 μm) lasers (Sec. 4). The mission analysis section (Vol. II) describes the results of studies performed by the Lockheed Missiles and Space Company (under sub-contract to PSI) and PSI to evaluate the system requirements of some candidate defense-related missions for pulsed laser propulsion. The studies address the problem of orbit to orbit transfer of satellites as well as the launch of a vehicle from earth.

The objective of the first phase of the thruster studies described in this report was to perform more detailed experiments and modeling in order to confirm and better understand the previously obtained 10.6 μm thruster performance results. The theoretical modeling was improved by developing a detailed computer model of the quasi-1D non-steady nozzle flow with laser heat addition. The effects of laser energy absorption, LSD wave growth and propagation, and 'real gas' equilibrium chemistry were included. New thruster.

performance experiments were also carried out for other propellant gas species in addition to helium. The experiments incorporated numerous diagnostic measurements including shock pressure and transit time measurements, ballistic pendulum measurements of impulse, laser optical transmittance, measurements of plasma re-radiation losses, and radiometric determinations of the exhaust gas "electronic" temperature. Thruster performance parameters such as specific impulse (I_{sp}) and laser to propellant energy conversion efficiency were evaluated as a function of propellant delivery pressure, nozzle throat size, and laser interpulse time. These more comprehensive and better diagnosed experiments, coupled with the detailed fluid mechanical model that simulates laser absorption and 'real gas' chemical effects, have led to a more reliable assessment and better understanding of the performance of a pulsed laser-powered thruster.

A second phase of thruster performance experiments addressed wavelength scaling. Since laser propulsion activities are likely to follow advances in laser technology for other applications in space, it has been proposed that pulsed laser propulsion systems utilize visible/UV pulsed lasers. Thus, we sought to determine how the physics of laser-induced gas breakdown and plasma optical absorptance scales in going from 10.6 microns to the visible/UV. To address this question, theoretical predictions were made for the laser-induced gas breakdown threshold and subsequent optical absorptance of argon at 0.35 μm . The model predictions were then compared to experimental measurements performed at PSI using our e-beam pumped XeF laser device. The experimental breakdown measurements were also extended to other gases including nitrogen and methane. In addition to these basic absorption physics studies, preliminary single-pulse thruster performance experiments were performed at 0.35 μm using a conical nozzle with external focusing optics and argon and helium propellants. Shock pressure and transit time measurements in the nozzle were interpreted using the detailed numerical flow code to yield estimates of the laser energy that was deposited in the propellant gas. The results indicate that with a proper choice of plenum delivery pressure and nozzle volume, efficient conversion ($\geq 50\%$) of pulsed 0.35 μm radiant energy into propellant fluid mechanical energy is possible. Of course, since

external focusing optics were used, the question still remains as to whether a self-focusing nozzle can be constructed with walls of sufficient optical quality to focus the incoming vis/UV beam to the necessary power density to achieve gas breakdown.

Volume II of this document presents a brief discussion of several possible missions for a laser propulsion systems. The missions considered include both earth launch of vehicles and orbit to orbit transfer of satellites. The former was analyzed by the Lockheed Missile and Space Company under subcontract to PSI. The results of their analysis, which are contained in a separate report,* indicates that the earth launch of practical payloads will require laser system power levels which probably cannot be expected for several decades. In contrast, orbit to orbit transfer for the repositioning of satellites may be an attractive nearer term mission for a laser propulsion system.

* W. S. Jones and K. C. Sun, Laser Propulsion for Defense Missions System Analysis (U), Final report, PSI subcontract 2532, Lockheed Missile and Space Company report No. LMSC-L040143 (Secret), 25 Feb. 1980. This report is included as part of Volume II of this document.

1.1 References

- 1.1 Pirri, A. N., Simons, G. A., and Nebolsine, P. E., "The Fluid Mechanics of Pulsed Laser Propulsion," PSI TR-60, Physical Sciences Inc., July 1976.
- 1.2 Nebolsine, P. E., Pirri, A. N., Goela, J. S., and Simons, G. A., "Pulsed Laser Propulsion - Final Report," PSI TR-108, Physical Sciences Inc., February 1978.
- 1.3 Nebolsine, P. E., Pirri, A. N., Goela, J. S., Simons, G. A., and Rosen, D. I., "Pulsed Laser Propulsion," Physical Sciences Inc. TR-142; presented at the AIAA Conference on Fluid Dynamics of High-Power Lasers, Oct. 1978. See also Simons, G. A. and Pirri, A. N., "The Fluid Mechanics of Pulsed Laser Propulsion, AIAA Journal, Vol. 15, No. 6, June 1977, pp. 835-842.
- 1.4 Nebolsine, P. E., Pirri, A. N., Goela, J. S., and Simons, G. A., "Pulsed Laser Propulsion," AIAA Journal, Vol. 19, January 1981, pp. 127-128.
- 1.5 Caledonia, G. E., Wu, P. K. S., and Pirri, A. N., "Radiant Energy Absorption Studies for Laser Propulsion," NASA Report CR-134809, Physical Sciences Inc. Report TR-20, March 1975; also Wu, P. K. S. and Pirri, A. N., "Stability of Laser Heated Flows," AIAA Journal, Vol. 14, March 1976, pp. 390-392.

2. THEORETICAL STUDIES OF LASER-INDUCED GAS BREAKDOWN

2.1 Introduction

We are concerned in this section with the early stages of the laser/gas interaction. During this time the gas goes from a state of very low absorption, low temperature and ambient pressure to a state where there is strong absorption of the laser radiation, a high degree of ionization, high gas pressure and temperature.

We are interested in calculating the induction time for gas breakdown as a function of the following experimental parameters: laser intensity at focus, focal size, pulse length and gas density. The gases of interest are air, Ar, H₂ and H₂O. The laser wavelengths that we are concerned with are 10.6 μm (CO₂ laser) and 0.35 μm (XeF). We also are interested in determining the absorption coefficient in the laser-produced plasma in order to determine minimum depths of focus and gas pressures required for significant absorption of the laser energy.

Early in the laser pulse low ionization impurities, dust particles or ambient ionization due to cosmic rays yield the primary electrons from which a cascade breakdown can develop.^{2.1} These electrons heat up by inverse bremsstrahlung absorption of the laser flux, excite and ionize the gas. Breakdown at 10.6 μm is similar to microwave breakdown, which has been studied in great detail both experimentally and theoretically.^{2.2,2.3} The photon energy $h\nu$ (≈ 0.12 eV) is much smaller than the average electron energy (2-5 eV) so that the electrons are heated up continuously, and a classical treatment of the absorption process is appropriate. Secondary electrons are produced by direct impact ionization of the gas molecules (or atoms) by those electrons that have reached an energy greater than the ionization threshold ϵ_I . The situation at 0.35 μm is quite different, however. The photon energy $h\nu$ (≈ 3.5 eV) is of the order of or larger than the average electron energy. Finite quantum effects therefore cannot be neglected. Only a small number of quanta (3-5) need be absorbed for an electron to reach an energy larger than

either the first excited state or the ionization threshold of the carrier gas where inelastic collisions leading to gas excitation and ionization will occur. We find, as shall be shown below, that a cascade develops by photoionization of the excited states formed rather than by direct electron impact ionization. Non-linear effects (multi-photon processes) also become important at the fluxes ($I \geq 10^{10}$ W/cm² or $\Phi \geq 10^{28}$ photons/cm²·s) considered.

Our approach has been to use a Boltzmann code that solves for the electron distribution function as a function of the laser power input to the electron gas. We can then derive from the code the rates at which various excited and ionized species are formed. The rate equations for the various species are then solved and the gas history during the breakdown obtained. The code results are correct only for an infinite and homogeneous medium. In reality, because of the finite focal volume, electrons will diffuse out of the breakdown region. The breakdown times will therefore be longer than those that one would predict for a uniformly irradiated gas. A general discussion of the breakdown process and of the effect of diffusion losses is given in the next sub-section. Particular results at 10.6 μ m and 0.35 μ m are given in Sub-sections 2.3 and 2.4.

2.2 General Considerations

Electrons will gain energy from the electric field when they collide with neutrals and lose energy through inelastic processes such as vibration and rotational excitation (for polyatomic gases), electronic excitation of atoms (and molecules), elastic collisions with neutrals and ionization. A simple model of breakdown can be formulated by looking at the energy equation for electrons

$$\frac{d}{dt} [n_e (\epsilon + \epsilon_I)] = kI - \sum \epsilon_j \frac{dn_j}{dt} - (\epsilon - \frac{3}{2} kT) \frac{2m}{M} v n_e \quad (2.2.1)$$

where ϵ is the average electron energy, n_e the electron density, n , T the gas density and temperature and ϵ_j and n_j refer to the energy and

density of various excited states of the gas particles. The first term on the right-hand side represents energy gained from the laser field, k being the absorption coefficient and I the intensity. The second term represents losses due to excitation of the gas and the last term represents heating of the gas due to elastic collisions of electrons with the gas particles at a frequency ν , m/M being the ratio of electron to heavy particle mass. During the breakdown process the electron energy remains fairly constant and the ionization rate is obtained by looking at the balance of energy gained by the electrons from the field to energy lost by all processes except ionization, the ionization rate being

$$v_i = \frac{1}{n_e (\epsilon + \epsilon_I)} \times (\text{Energy gained in unit volume and time} - \text{Energy losses per unit volume and time}).$$

In order to calculate the avalanche rate v_{av} we must subtract from v_i the losses due to attachment (if any) at a rate v_a and the loss of electrons from the focal volume. We will have

$$v_{av} = v_i - v_a - \frac{D}{\Lambda^2} \quad (2.2.2)$$

where Λ is proportional to the transverse (smallest) dimension of the focal volume and D is the diffusion coefficient. For a top hat intensity profile of diameter D , it can be shown^{2.4} that $\Lambda = D/4.8$. At early times, when the electron density is small, the diffusion coefficient is the free electron diffusion coefficient $D = (\lambda V_e)/3$, where λ is the mean free path of the electron and V_e is the electron mean velocity. We estimate this diffusion coefficient at one amagat neutral density, using a gas kinetic cross-section of 10^{-15} cm^2 and electron energy of 3 eV, to be $\sim 3000 \text{ cm}^2/\text{s}$.

At later times the diffusion becomes ambipolar and the diffusion coefficient, D_a , is reduced by a factor $(M/m)^{1/2} \approx 250$. Ambipolar diffusion occurs when the electric field built up by charge separation is large

enough to prevent electrons from diffusing freely. Ions must be carried along with them. A condition for ambipolar diffusion is that the electron Debye length be smaller than the focal spot size. The electron density above which this occurs is given by

$$n_{es} = \frac{kT_e}{4\pi e^2 \Lambda^2}$$

This density is plotted as a function of Λ in Fig. 2.1 for various electron temperatures. In the laboratory experiments performed at Physical Sciences Inc. (see Sec. 4.3) the focal spot size was around 50 μm at 0.35 μm wavelength and 100 μm at 10.6 μm and the electron energies during the breakdown are estimated to be in the range 2-5 eV. Under these conditions we expect ambipolar diffusion to occur when the electron density exceeds 10^{10} particle/cm³.

Breakdown will have occurred by the time the electron density has exponentiated 20 to 40 times, i.e. when the cascade has raised the electron density from $n_e = 10^2 - 10^4 \text{ cm}^{-3}$ to $n_e = 10^{16} - 10^{18} \text{ cm}^{-3}$. We thus require as a condition for breakdown that the pulse length τ_p satisfy the inequality.

$$\tau_p > \frac{20 \text{ to } 40}{v_{av}} \quad (2.2.3)$$

We note that with the neglect of three body processes, all terms on the right-hand side of Eq. (2.2.1) scale proportionately with pressure, i.e., v_i will be proportional to pressure. The diffusion coefficient, however, scales as $1/p$. Solution of the Boltzmann equation will yield v_i as a function of intensity and over a given intensity range we will always be able to write

$$v_i(p, I) = v_{i0} p I^m \quad (2.2.4)$$

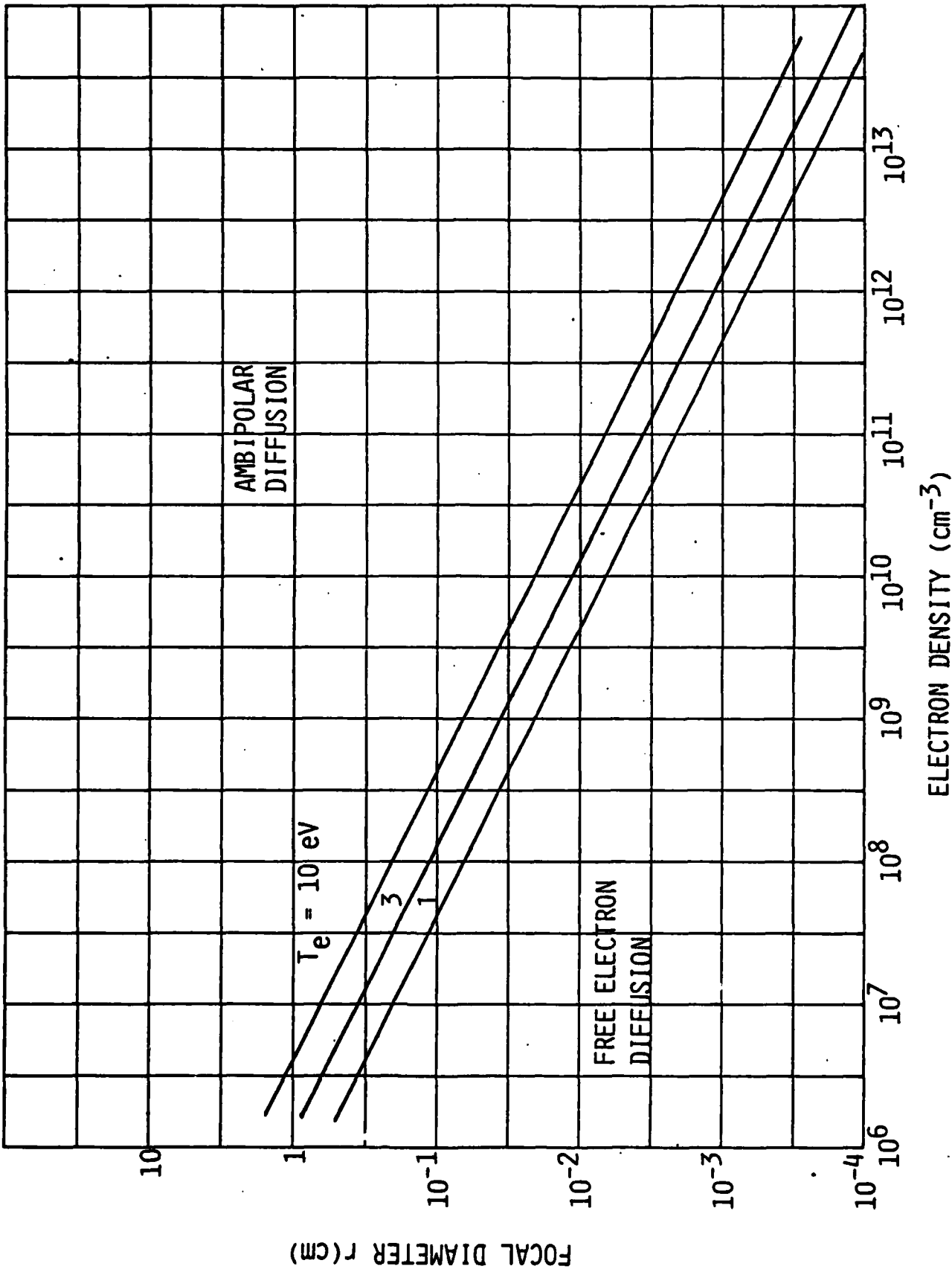


Fig. 2.1 Electron density for transition from free diffusion to ambipolar diffusion.

where $m \geq 1$. The breakdown threshold criteria, given by Eq. (2.2.3) will lead to a relation between I , p and τ_p that must be satisfied. We distinguish three regimes.

1) Large focal size (no diffusion losses) and no attachment, then $v_i = v_{av}$ and combination of Eq. (2.2.3) and Eq. (2.2.4) leads to

$$I_{th} \propto \left(\frac{40}{\tau_p p} \right)^{1/m} \quad (2.2.5)$$

2) Small focal size (diffusion losses) but negligible attachment. Equating v_i to D/r^2 , we obtain

$$I_{th} \propto (\Lambda p)^{-2m} \quad (2.2.6)$$

where we used the fact that D scales as $1/p$.

3) Electron losses by attachment just about balance ionization gain. We will have in this case a threshold independent of pressure.

$$I_{th} = I_0 \quad (2.2.7)$$

The last regime occurs when the ionization rate is fast enough so that, in the absence of attachment, breakdown would have occurred well within the pulse, i.e.

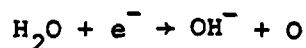
$$\tau_p \gg \frac{40}{v_i(I_{th})}$$

At $0.35 \mu\text{m}$ the photon energy is 3.5 eV and is large enough that one and two photon photoionization of excited states is possible. A laser

flux of 10^9 W/cm² corresponds to a photon flux of 1.7×10^{27} cm⁻² s⁻¹. Assuming photoionization cross-sections of order 10^{-17} cm² we see that single photoionization of an excited state will occur in less than 10^{-10} s. This time is several orders of magnitude shorter than the XeF pulse length. We therefore expect that electron impact excitation of an excited state lying less than 3.5 eV from the ionization continuum is equivalent to an ionization event at the laser fluxes that we are considering. Equation (2.2.1) can still be used to describe the cascade process except that ϵ_I must be replaced by $\epsilon_I - h\nu$ and the sum over excited states on the right-hand side must extend only to those states lying below $\epsilon_I - h\nu$. For laser fluxes larger than 10^{10} W/cm², two photon ionization processes of excited states becomes probable, as we shall show in Sub-section 2.4. The simple treatment given above does not hold and the scaling of threshold with pressure and pulse length becomes more complex. The treatment for two photon ionization of argon is given in Sub-section 2.4.

2.3 Breakdown at 10.6 μm

Calculation of the net ionization rate, $(\nu_i - \nu_a)$, with the neglect of diffusion losses was carried out by Weyl^{2.5} for air, N_2 , H_2 and He. We have used the same procedure and the same Boltzmann code for argon and water vapor. The cross-sections for water vapor and argon were obtained from the AVCO cross-section tape. The cross-sections for water vapor include the processes of vibrational excitation (energy loss ~ 0.2 eV), excitation of electronic levels with threshold 5, 6.3, 9, 12 and 12.6 eV, and the dissociative attachment reaction



with threshold at 5.6 eV. The cross-sections for argon contain the effects of excitation of the 11.6 eV (4s) and 13.2 eV (4p) excited states of argon, and electron impact ionization at electron energies above 15.7 eV.

A verification of the code results was obtained by making DC breakdown calculations and comparing the ionization rates to the well known Townsend first ionization coefficient for the gases. The first Townsend ionization coefficient α is defined by the spatial growth of the electron distribution in an electron discharge

$$\frac{dn_e}{dx} = \alpha n_e \quad (2.3.1)$$

The temporal growth is obtained by transforming to the frame of the electrons which are moving in the x direction at the drift velocities v_D . We have

$$\begin{aligned} \frac{dn_e}{dt} &= v_{av} n_e \\ &= \frac{dn_e}{dx} \frac{dx}{dt} = v_D \frac{dn_e}{dx} \end{aligned}$$

We must therefore have

$$v_{av} = \alpha/v_D \quad (2.3.2)$$

The quantities v_{av}/p , α/p and v_D are functions of E/p . We show in Figs. 2.2 and 2.3 comparison between calculated and measured v_{av}/p . The measurements compared with were those of Golden and Fisher^{2.6} for argon and Golden et al.^{2.7} for H_2 . We also compare in Figs. 2.2 and 2.3 the calculated and measured^{2.8,2.9} drift velocities. We see that there is an excellent agreement between measured and calculated v_{av}/p , but that the drift velocities in argon differ by a factor of 1.5.

We have plotted in Fig. 2.4 the avalanche rates at $p = 1$ atm for the four gases studied. These rates vary linearly with pressure. Attachment and ionization rates are equal in H_2 , H_2O and air at the laser fluxes $I = 9 \times 10^8$, 5.5×10^9 and 3.5×10^9 W/cm^2 , respectively, which represent the long pulse length, large focal spot, breakdown thresholds for these gases. The absorption coefficient to the laser flux can be written as a function of an effective collision frequency ν_{eff} by use of the relation:

$$k_{en} = \frac{\omega_p^2}{\omega^2} \frac{\nu_{eff}}{c} = 3.38 \times 10^{-30} n_e \nu_{eff} \quad (cm^{-1}) \quad (2.3.3)$$

where ω_p is the electron plasma frequency and in the last step we chose $\omega = 1.77 \times 10^{14} s^{-1}$ corresponding to $\lambda = 10.6 \mu m$. Equation (2.3.3) is valid for $\omega \gg \nu_{eff}$, as is the case at pressures of interest. A plot of ν_{eff}/N (N is the gas density) as a function of laser intensity is shown in Fig. 2.5. The frequency ν_{eff} is an effective collision frequency averaged over the electron distribution function. This distribution function is far from Maxwellian during the early stages of the breakdown but when the electron density has reached $10^{13} cm^{-3}$ electron-electron collisions start to dominate, tending to make the distribution function Maxwellian. Thus

ARGON, DC BREAKDOWN

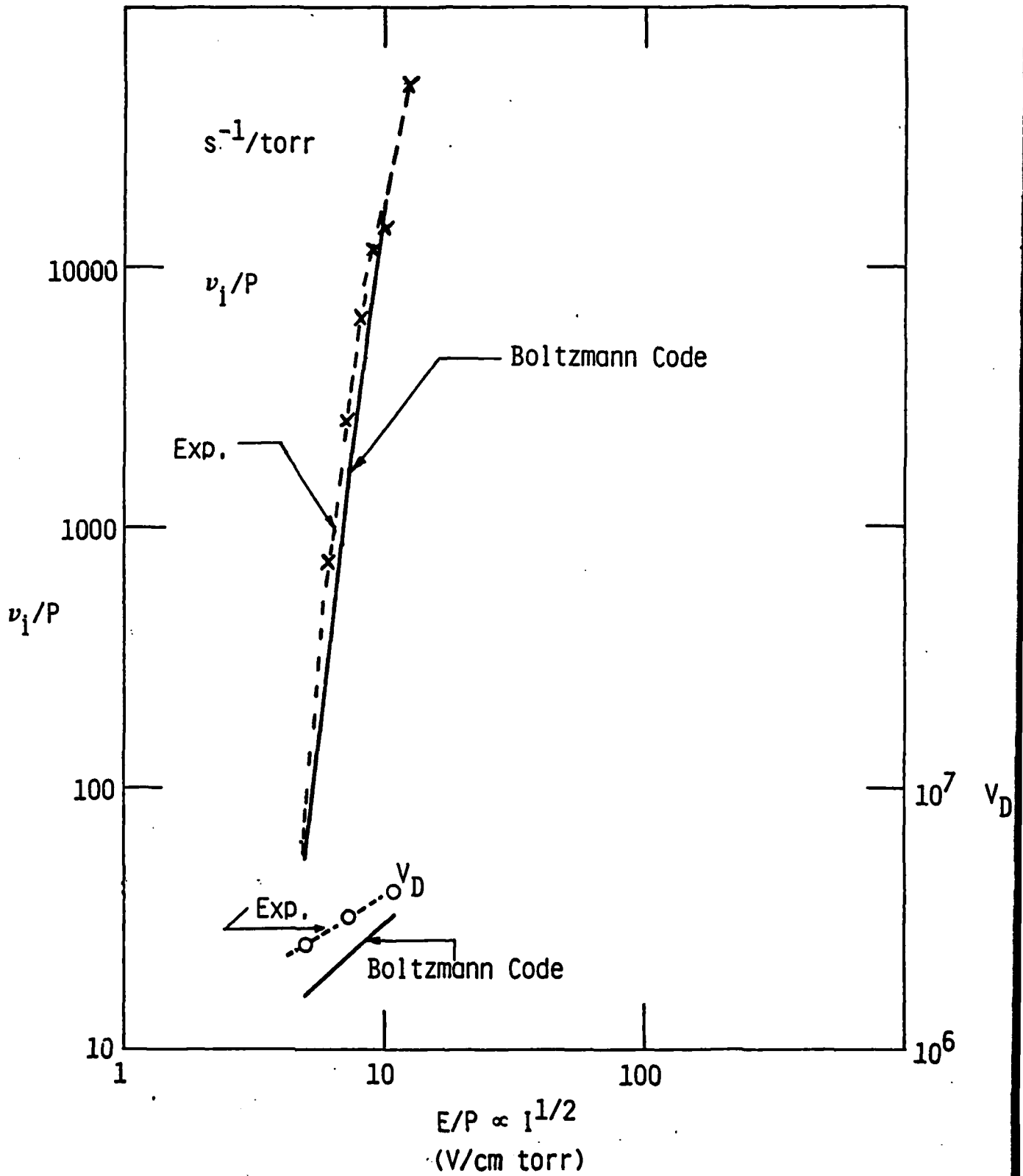


Fig. 2.2 Comparison of Boltzmann code with DC breakdown measurements in Argon
 — ionization rate; - - - drift velocity.

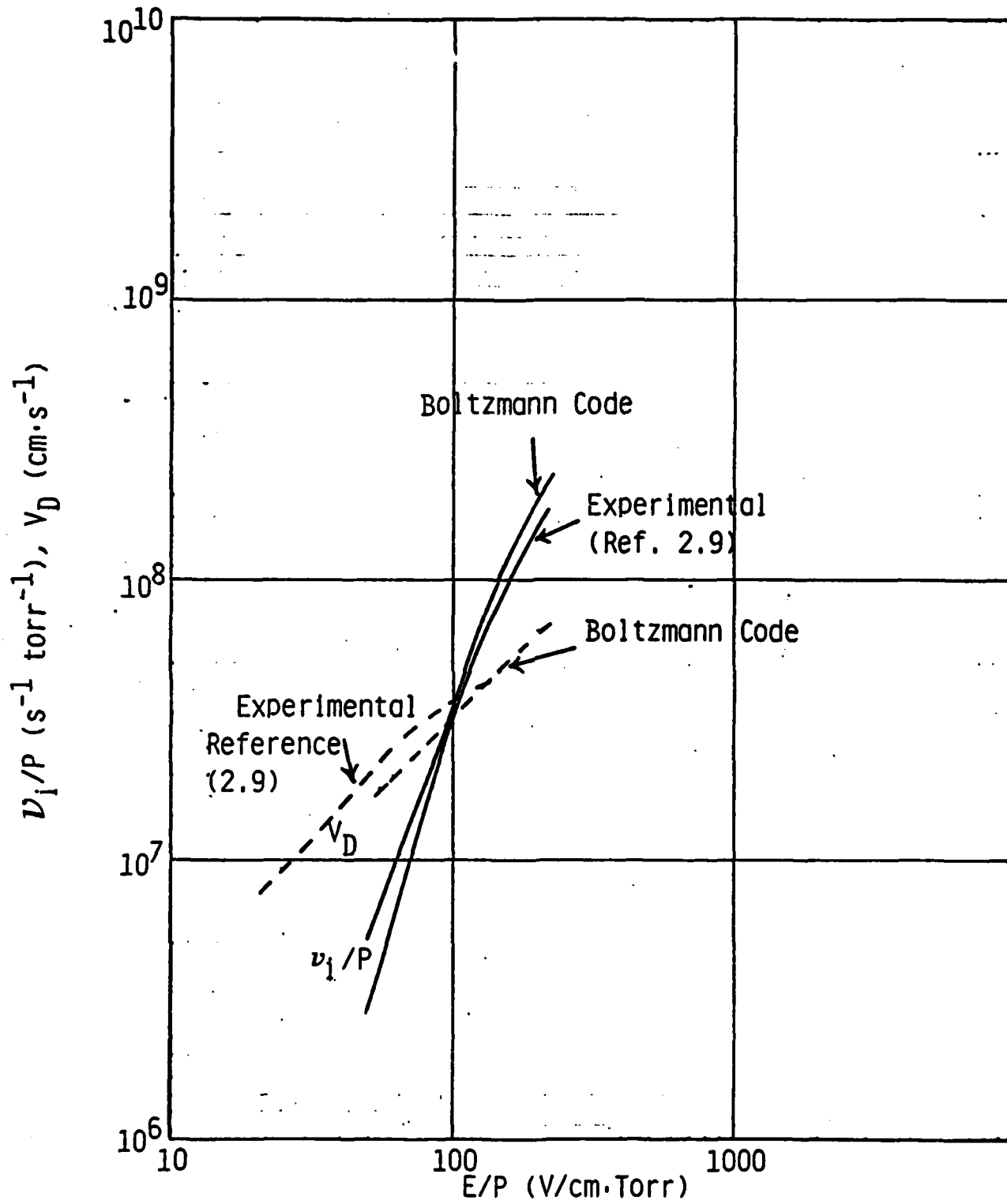


Fig. 2.3 Comparison of Boltzmann code with DC breakdown results in hydrogen.

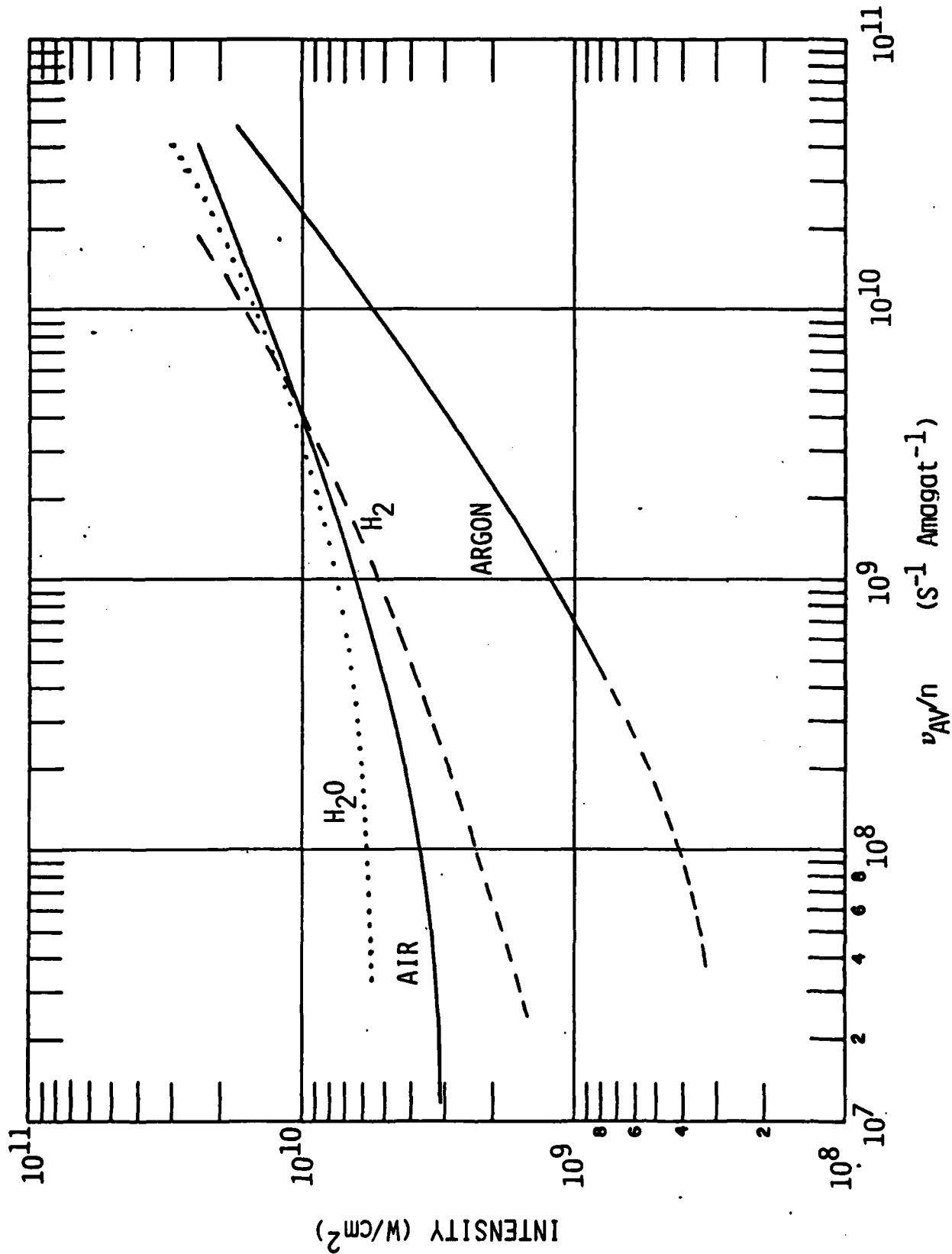


Fig. 2.4 Avalanche rate in H₂O, H₂, Ar and air as a function of 10.6 μm laser intensity.

EFFECTIVE COLLISION FREQUENCIES

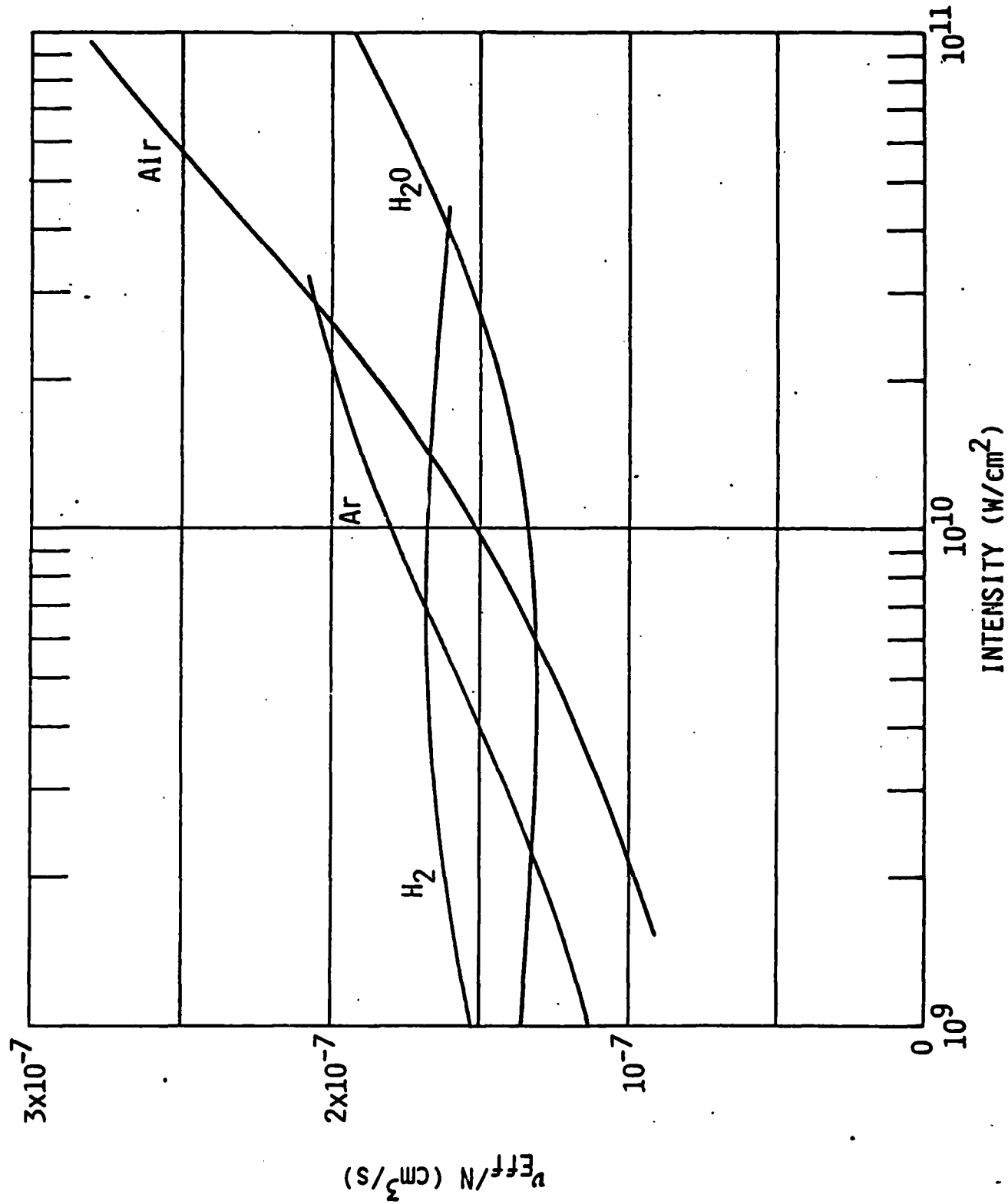


Fig. 2.5 Electron-neutral collision frequency in H₂, H₂O, air and Ar as a function of 10.6 μm laser intensity.

ν_{eff} , which was constant up to this point starts varying. At late times when the degree of ionization of the gas exceeds a few percent, then absorption due to electron-ion collisions becomes important, the absorption coefficient being given by^{2.10}

$$k_e = \frac{32\pi^3}{3} \left(\frac{2\pi}{3mkT_e} \right)^{\frac{3}{2}} \frac{Z^2 e^6}{hc\omega^3 m} n_e^2 \left(1 - e^{-\hbar\omega/kT_e} \right) \bar{G}. \quad (2.3.4a)$$

The Gaunt factor \bar{G} is discussed in detail in Shkarovsky's book.^{2.11} The derivation of the Gaunt factor is very complex and involves a) calculation of the radiation spectrum during a collision as a function of impact parameter and incident electron energy and b) performing an integration over impact parameters and an averaging over the electron distribution function. When the frequency is such that $\hbar\omega \ll kT_e$ and when the electron thermal energy is much less than $Z^2 R$ (Z = ion charge, R = 1 Rydberg = 13.6 eV), a derivation of the radiation using classical mechanics is valid. Due to the long range of the coulomb potential, most of the radiation comes from distant collisions where a straight line approximation to the electron trajectory is adequate and one obtains Kramers result.

$$\bar{G} = \frac{\sqrt{3}}{\pi} \ln \left[\frac{(1.79kT/m)^{\frac{3}{2}}}{\omega(Ze^2/kT)} \right]. \quad (2.3.4b)$$

Equation (2.3.4b) was derived with the neglect of collective plasma effects and is only valid for $\omega \gg \omega_p$. As ω approaches ω_p a correction factor due to the plasma dielectric response arises and one must multiply Eq. (2.3.4b) by $(1 - \omega_p^2/\omega^2)^{-\frac{1}{2}}$ (Ref. 2.12). For the application at hand where $\hbar\omega \approx 0.12$ eV and $kT_e \approx 1-2$ eV, the ratio of photon energy to average electron energy is not so small that quantum effects can be neglected. Rather than using Eq. (2.3.4b) it is preferable to use the numerical results of Karzas and Latter^{2.13} which are based on suitable averaging over the electron distribution of the quantum mechanical results of Sommerfeld. We show in Fig.

2.6 the Gaunt factor derived by Karzas and Latter.^{2.13} The curves plotted are parameterized with the parameter $(b_H/b_0)^2 = kT/Z^2R$ which is the square of the ratio of the de Broglie wavelength of the electron (b_H) to the impact parameter for 90° deflection (b_0). The dashed lines in Fig. 2.6 are plots of Eq. (2.3.4b). We see for $\hbar\omega = 0.12$ eV, $kT = 1.36$ eV and $Z = 1$ that the curve $(b_H/b_0)^2 = 0.1$ give a Gaunt factor $\bar{G} = 1.5$ while Eq. (2.3.4b) would give $\bar{G} = 0.68$ which is too low a value by a factor of more than 2.

Combining Eqs. (2.3.3) and (2.3.4a), expanding the exponential for small values of $\hbar\omega/kT_e$, letting $\omega = 1.77 \times 10^{14} \text{ s}^{-1}$, and expressing T_e in eV, we obtain the following expression for the total absorption coefficient at 10.6 μm .

$$k = N^2 x_e \left[3.38 \times 10^{-30} \frac{\nu_{\text{eff}}}{N} + \frac{1.8 \times 10^{-35} x_e \bar{G}}{(1 - 1.01 \times 10^{-19} N x_e)^{1/2} T_e^{3/2}} \right] \quad (2.3.5)$$

where x_e is the degree of ionization ($x_e < 1$). We now apply our results to laboratory conditions where breakdown in Ar and H₂ was measured (see Sec. 4.3). The beam was focused by a $f = 20$ cm Germanium lens and had a diffraction limited Gaussian profile at focus of $1/e$ radius equal to 40 μm . Breakdown was found to occur within the gain switched spike. The spike width at half maximum was 80 ns. For the threshold calculations, we approximate the spike by a square profile of width $\tau_p = 80$ ns and intensity \bar{I} .

2.3.1 Argon

The breakdown condition $\nu_{\text{av}} \tau_p \geq 40$, can be written using Eqs. (2.2.2) - (2.2.4)

$$\left(\nu_0 i_p^m - \left(\frac{2.405}{a} \right)^2 \frac{D_0(i)}{p} \right) \tau_p \geq 40 \quad (2.3.6)$$

where i is the intensity normalized to 10^{10} W/cm^2 , D_0 is the diffusion coefficient at 1 amagat density, a is the focal radius and p the pressure in atmospheres. From our Boltzmann code results shown in Fig. 2.4 we have

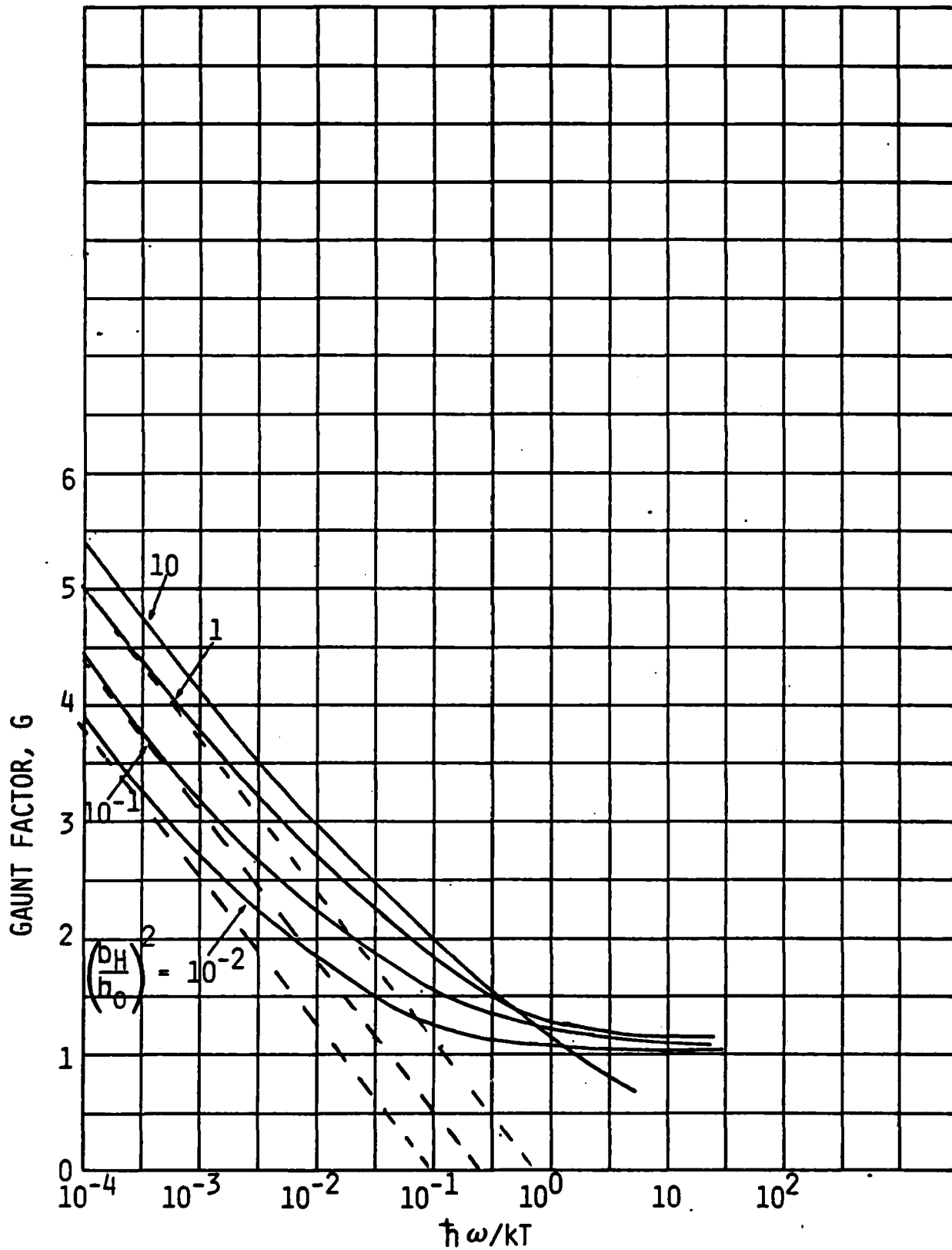


Fig. 2.6 Gaunt factor for electron-ion bremsstrahlung absorption following Karzas and Latter.

$m = 1.5$, $v_0 = 2.5 \times 10^{10} \text{ s}^{-1} \text{ Ama}^{-1}$. We solve Eq. (2.3.6) for i as a function of \ddot{p} , for fixed a . Over the intensity range considered, we used the fact that D_0 varied from $7 \times 10^3 \text{ (cm}^2/\text{s)}$ at $i = 0.1$ to 3.6×10^3 at $i = 10$ with a value of 5×10^3 at $i = 1$. The results for $a = 40 \text{ }\mu\text{m}$, $100 \text{ }\mu\text{m}$ and ∞ (no diffusion) have been plotted in Fig. 2.7. The agreement with measurements is satisfactory though we somewhat underestimate threshold at the larger focal radii at which Hill^{2.14} and Cohn et al.^{2.3} operated. In Section 4.3.2, predictions of the theoretical model will be further compared with the experimental threshold measurements obtained at PSI.

2.3.2 Hydrogen

We apply Eq. (2.3.6) to hydrogen. From Fig. 2.4 we see that at $I = 10^{10} \text{ W/cm}^2$ ($i=1$), $m = 2$ and $v_0 = 4 \times 10^9 \text{ s}^{-1} \text{ Ama}^{-1}$. We use the following formula for D_0 derived from the Boltzmann code results

$$D_0 = (1.6 + 0.4i) \times 10^3 \text{ (cm}^2/\text{s Ama)}$$

That breakdown threshold versus pressure that we calculate is plotted in Fig. 2.8 and is in excellent agreement with our experimental data and the data of Hill^{2.14} and of Cohn et al.^{2.3} The calculated breakdown threshold in hydrogen will also be shown to be in very good agreement with the data obtained at PSI (see Section 4.3.2).

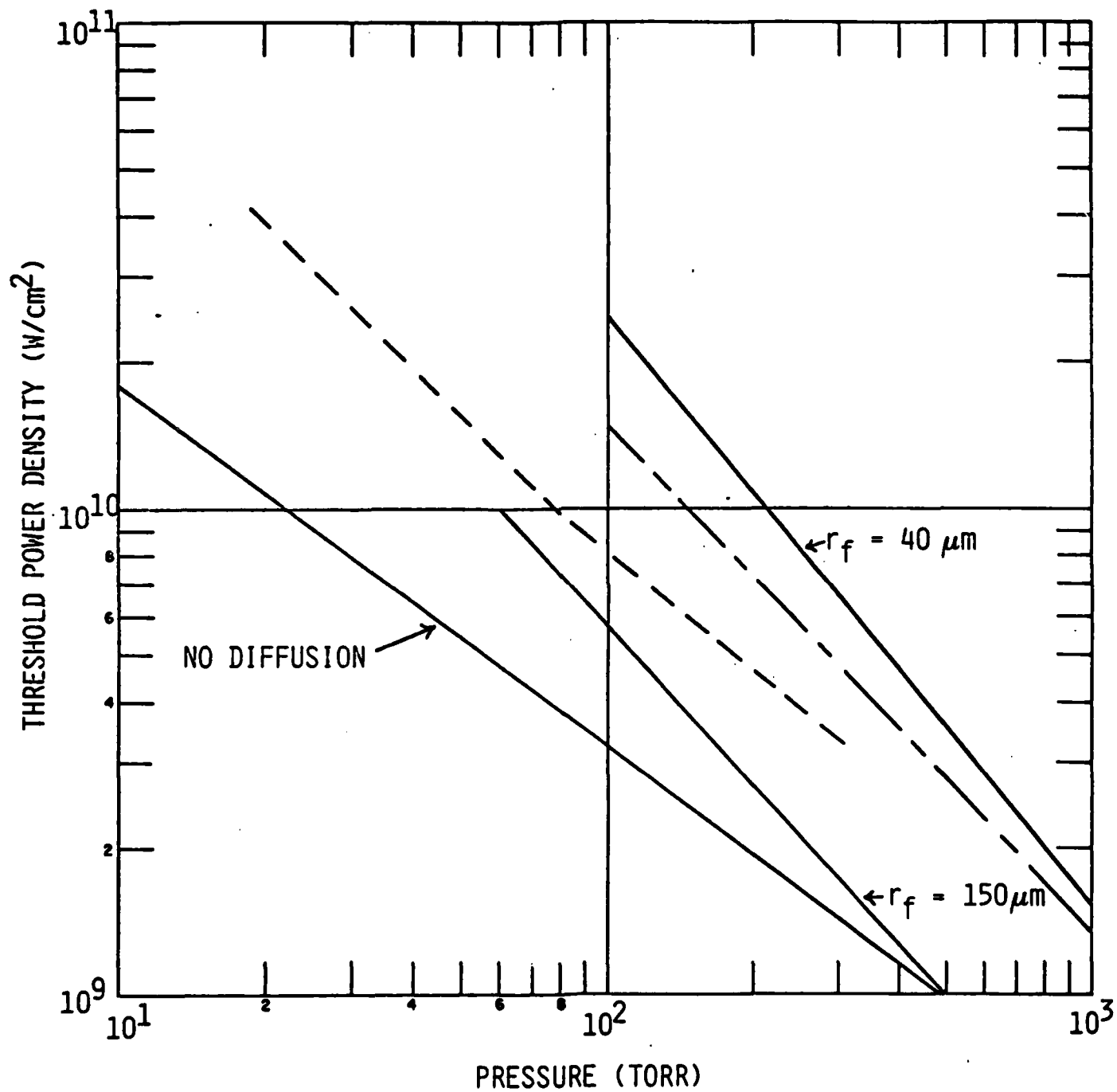


Fig. 2.7 10.6 μm breakdown thresholds in Argon --- measurements of Cohn Hacker et al. ($r_f = 155 \mu\text{m}$), - - - measurements of Hill et al. ($r_f = 100 \mu\text{m}$). — Theory for $\tau_p = 80 \text{ ns}$.

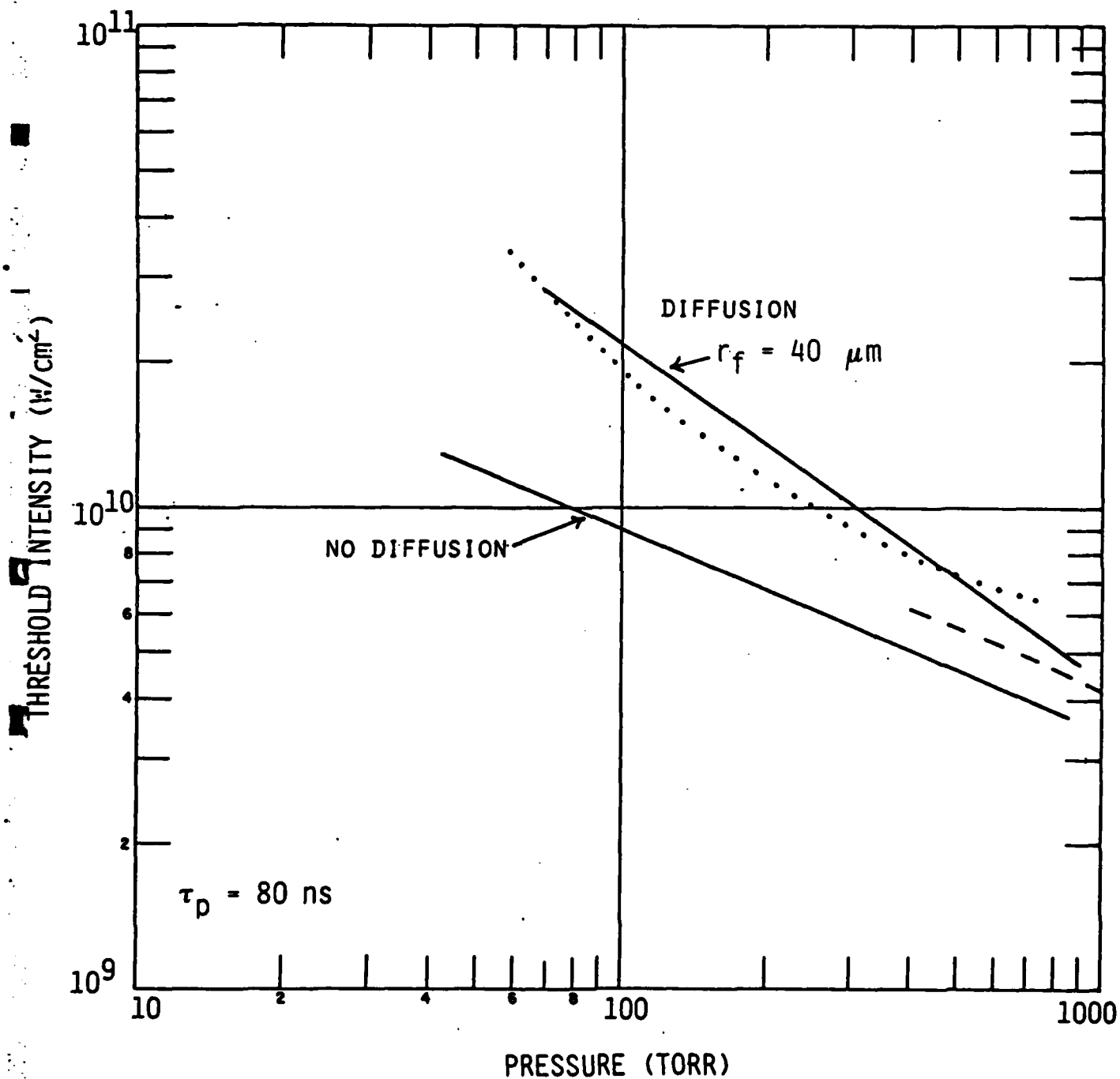


Fig. 2.8 10.6 μm breakdown threshold in hydrogen :... data of Cohn, Hacker et al. ($r_f = 150 \mu\text{m}$), --- Hill et al. ($r_f = 100 \mu\text{m}$). -- Theory for $\tau_p = 80 \text{ ns}$.

2.4. Breakdown at 0.35 μm

Breakdown at 0.35 μm involves many more processes than at 10.6 μm due to the high energy of the photons involved. We can have direct multi-photon ionization of the gas and of impurities in the gas which would yield a large electron concentration in the absence of an electron cascade. As is the case for 10.6 μm radiation, the electrons that absorb energy from the radiation field create excited states through inelastic collisions with neutrals. Photoionization of these excited states, as we stated in Section 2.3, can lead to ionization since these excited states can absorb one or more photons and become photoionized. The combination of these last two processes can lead to a cascade breakdown. Because of the complexity of the problem we have limited our analysis to argon, which does not have vibrational and rotational energy loss processes as molecular gases do.

The energy levels of argon are shown in Fig. 2.9. One sees from this figure that an electron must absorb 4 photons before it has enough energy to excite the 4s states (Ar^*) at 11.6 eV and 4p states (Ar^{**}) between 13.2 and 13.6 eV. Photoionization of Ar^{**} by absorption of one photon is possible. Two photons, however, are required to photoionize Ar^* , while photoionization of the ground state requires simultaneous absorption of five photons.

2.4.1 Early Time Breakdown Analysis for Argon

We model the physical processes leading to breakdown in argon at early time through the following set of reactions.

Direct multiphoton ionization



Electron inverse bremsstrahlung absorption



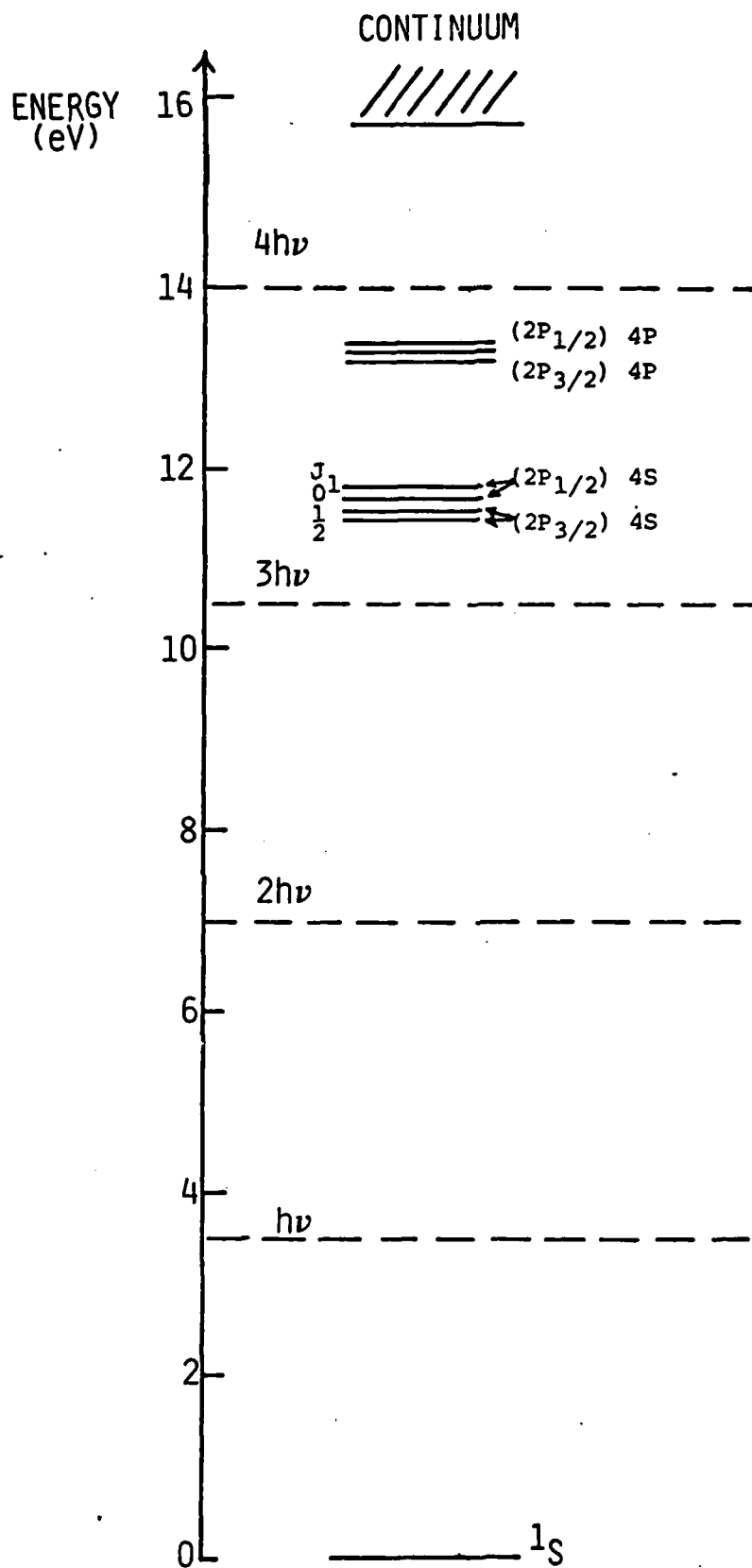
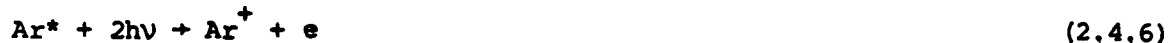


Fig. 2.9 Energy levels in Argon.

Electron impact excitation of Ar



Photoionization of the excited state



We analyze each of the above processes below.

a. Direct Multiphoton Ionization

The probability that an atom absorbs m photons to become ionized can be calculated quantum mechanically using m^{th} order perturbation theory. One finds that the lifetime varies as I^{-m} . A review of the work done until 1976 can be found in Ref. 2.16. The problem in getting quantitative answers is that one has to perform a multiple summation over intermediate states and that subtle interference effects between terms can occur. Also, the wave functions required for calculating the matrix elements are not that well known except for the simplest atoms. Calculated and measured lifetimes can differ by many orders of magnitude.^{2.16} There has been no theoretical calculation for multiphoton ionization in argon at the XeF wavelength. Experimental studies of breakdown in argon and N_2 at doubled ruby frequency ($\lambda/2 = 3470 \text{ \AA}$) in the pressure range 400-500 torr were carried out by Krasnyuk and Pashinin.^{2.17} The pulse length was in the range $3-5 \times 10^{-11} \text{ s}$ and the focal area at half intensity was $1.4 \times 10^{-5} \text{ cm}^2$. The beam was focused using a lens of focal length 1.8 cm and breakdown threshold was defined as that intensity which produced a faint glow to the eye in the focal region. The data is shown in Fig. 2.10. The threshold curve is practically independent of P and is consistent with the scaling $I \propto p^{-1/5}$ as one would expect for a multiphoton ionization threshold corresponding to a fixed number of ions in the focal volume. The fact that the threshold did not correspond to a sharp breakdown transition is also an indication that breakdown was not associated with an electron cascade.

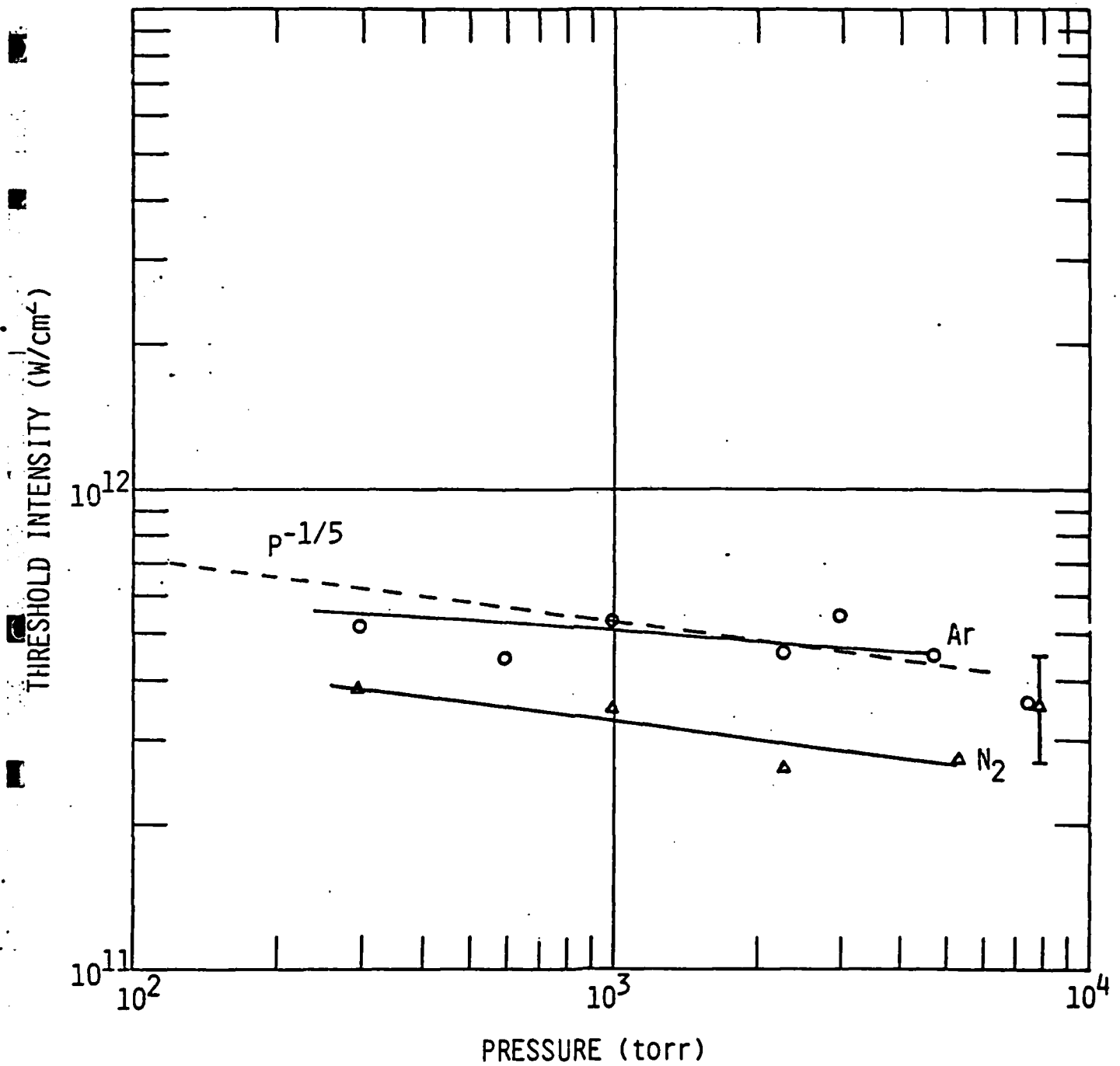


Fig. 2.10 Multiphoton ionization threshold in Argon and Nitrogen (data of Krasyuk and Pashinin, Ref. 2.17).

We can obtain an estimate of the multiphoton ionization cross section from the data of Krasyuk and Pashinin as follows. Let the cross section Q be defined by

$$\frac{dn^+}{dt} = Q\phi^5 n$$

where ϕ is the photon flux in $\text{cm}^{-2} \text{s}^{-1}$. A faint glow corresponds to ≈ 100 photons reaching the eye. If V_{eff} is the effective focal volume, n the gas density and δ the degree of ionization, the number of photons reaching the eye is $\approx n\delta V_{\text{eff}}\Omega$, where Ω is the solid angle subtended by the eye. We have assumed one visible photon emitted per recombination event.

The effective focal volume is

$$V_{\text{eff}} = \frac{\int I^5(\vec{r}) d^3r}{I_{\text{max}}^5}$$

If we assume that the beam has a diffraction limited Gaussian profile near focus, one readily derives an expression for V_{eff} as a function of the Gaussian $1/e^2$ radius at focus W_F ,

$$V_{\text{eff}} = \frac{3}{48} \frac{\pi^3 W_F^4}{\lambda}$$

where λ is the wavelength. Letting $\lambda = 0.35 \times 10^{-4} \text{ cm}$ and $(0.5\pi W_F^2) = 1.4 \times 10^{-5} \text{ cm}^2$, we obtain $V_{\text{eff}} = 5 \times 10^{-6} \text{ cm}^3$ under the conditions of Krasyuk and Pashinin's experiment. We also estimate under the conditions of the experiment that $\Omega = \pi(0.2 \text{ cm})^2 / 4\pi(100 \text{ cm})^2 = 3 \times 10^{-7}$. Finally, the experiments were performed near atmospheric pressure so that $n \approx 2 \times 10^{19} \text{ cm}^{-3}$.

$$\delta = \frac{100}{nV_{\text{eff}}\Omega} = \frac{100}{(2 \times 10^{19}) \times (5 \times 10^{-6}) \times (3 \times 10^{-7})} = 3 \times 10^{-6}$$

At the end of the pulse, $n^+/n = \delta = Q\phi^5 \tau_p$, so that for $\phi = 2 \times 10^{29} \text{ cm}^{-2} \text{s}^{-1}$ ($I = 5 \times 10^{11} \text{ W/cm}^2$) and $\tau_p = 3 \times 10^{-11} \text{ s}$, we have: $Q = 1.6 \times 10^{-145} \text{ cm}^{10} \text{ s}^4$.

We note in closing this subsection that any gas will contain a certain number of impurities, in particular organic vapors which have relatively low ionization potential (8-10 eV). At the fluxes where multiphoton ionization is an important process in argon, these organic impurities will become ionized very early in the pulse.

b. Electron-Neutral Inverse Bremsstrahlung Absorption at 0.35 μm

The inverse bremsstrahlung absorption cross section is usually derived by calculating bremsstrahlung emission and using the principle of detailed balance.^{2.18} We are concerned with electrons whose average energy is of the order of or smaller than $h\nu$. A proper treatment of the emission and absorption must be quantum-mechanical. There is some confusion in the literature on the proper absorption cross section to use. Zel'dovich and Raizer^{2.18} and Kroll and Watson^{2.19} use the following absorption coefficient per unit electron and neutral density, which can be derived classically.

$$K_a = \frac{8\pi e^2}{3mc\omega^2} \left[\frac{2(\epsilon + h\nu)}{m} \right]^{1/2} \left(\frac{\epsilon + h\nu}{\epsilon} \right)^{1/2} \left(\frac{\epsilon + h\nu}{h\nu} \right) \sigma_s(\epsilon + h\nu) \quad (2.4.8a)$$

where ϵ = electron energy before absorption and $\sigma_s(\epsilon)$ is the momentum transfer cross section at ϵ . Phelps^{2.20} uses the following formula for K_a . (2.4.8b)

$$K_a = \frac{8\pi e^2}{3mc\omega^2} \left[\frac{2(\epsilon + h\nu)}{m} \right]^{1/2} \frac{(\epsilon + h\nu/2)}{h\nu} \sigma_s(\epsilon + h\nu/2). \quad (2.4.8b)$$

Finally, Dalgarno and Lane^{2.21} solve the quantum mechanical scattering problem by partial wave expansion and obtain, keeping only the s and p wave contributions,

$$K_a = \frac{4\pi e^2}{3mc\omega^2} \left[\frac{2(\epsilon + h\nu)}{m} \right]^{1/2} \left[\frac{(\epsilon + h\nu)}{h\nu} \sigma_s(\epsilon) + \frac{\epsilon}{h\nu} \sigma_s(\epsilon + h\nu) \right]. \quad (2.4.8c)$$

We note that Eqs. (2.4.8b) and (2.4.8c) are identical if σ_g is independent of energy and that all expressions are equivalent in the limiting case $\epsilon \gg h\nu$. The formula derived by Zel'dovich and Raizer has a singularity at zero energy.

We have used Eq. (2.4.8c) for K_a because it is on a firmer theoretical basis rather than Eqs. (2.4.8a) and (2.4.8b). The formulas (2.4.8a) - (2.4.8c) give significantly different answers in the case of argon when used in a Boltzmann code. At fluxes of 10^{10} - 10^{11} W/cm² the heating rate using Eq. (2.4.8c) was found to be about a factor of 2 smaller than that using Eq. (2.4.8a). The reason for the discrepancy is the low value of electron average energy (2-3 eV) and the very strong dependence on energy of the momentum transfer cross section, (see Fig. 2.11).

The stimulated emission coefficient K_e is obtained from detailed balancing

$$K_e(\epsilon) = K_a(\epsilon - h\nu) \left(\frac{\epsilon - h\nu}{\epsilon} \right)^{1/2} \quad \epsilon > h\nu$$

$$K_e(\epsilon) = 0 \quad \epsilon < h\nu$$

If one has a Boltzmann distribution of electrons corresponding to a temperature T , then the net absorption cross section averaged over the distribution function is

$$\bar{K} = \int_0^{\infty} f(\epsilon) d\epsilon (K_a(\epsilon) - K_e(\epsilon)) = (1 - e^{-h\nu/kT}) \int_0^{\infty} f(\epsilon) d\epsilon K_a(\epsilon).$$

It is easy to verify that, when $h\nu \ll kT$ and when the collision frequency $\nu_c = n_e (2\epsilon/m)^{1/2} \sigma(\epsilon)$ is independent of ϵ , the absorption coefficient $k = \bar{K} n_e$ reduces to the expression given by Eq. (2.3.3) with $\nu_{eff} = \nu$. The net absorption cross section \bar{K} for argon as a function of electron temperature T is plotted in Fig. 2.11.

5047

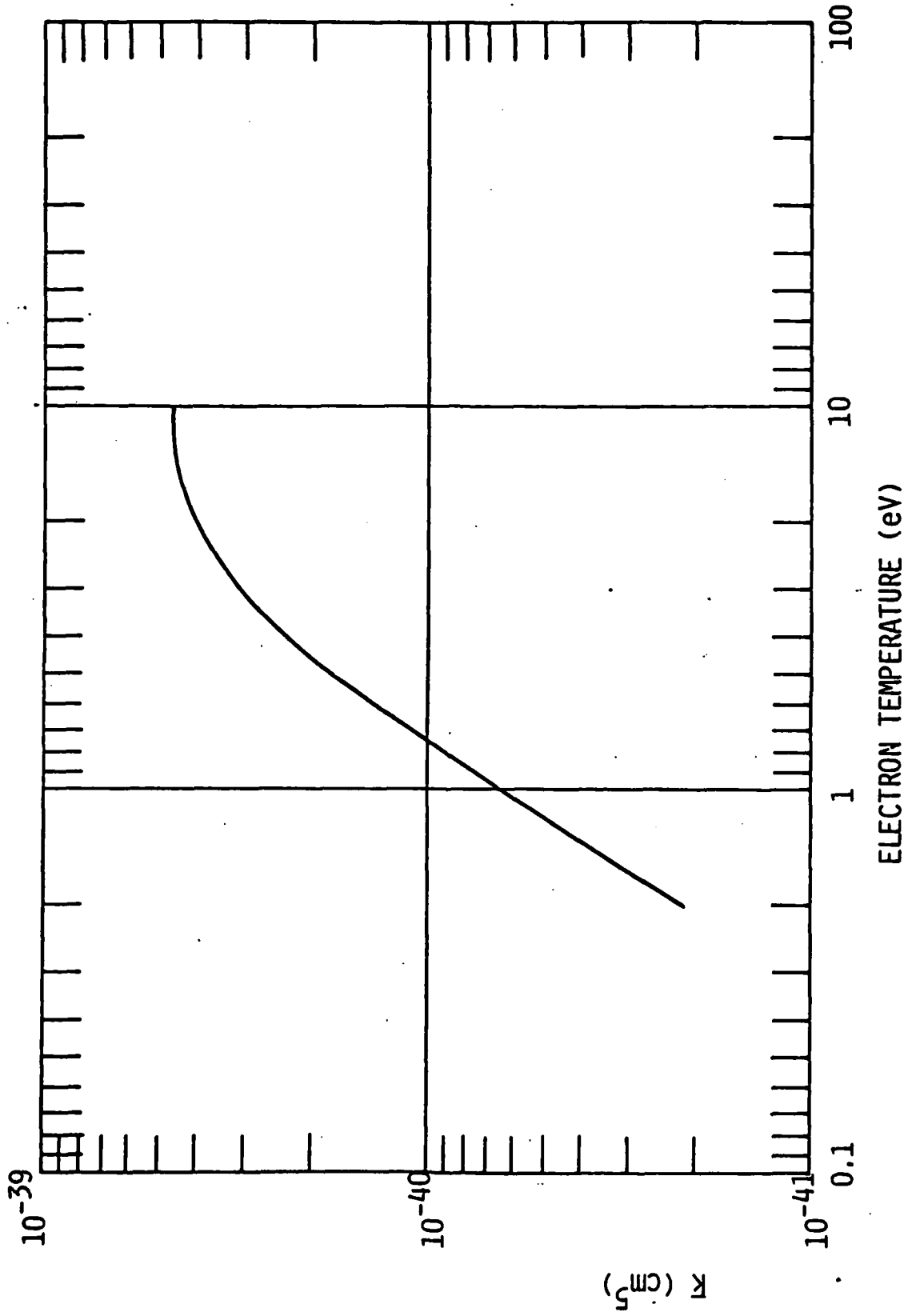


Fig. 2.11 Electron-neutral inverse Bremsstrahlung cross section \bar{K} in Argon, $h\nu = 3.4 \text{ eV}$.

c. Electron Impact Excitation of Argon

The inelastic cross sections for excitation of electronic states of argon have been reviewed by Eggarter.^{2.22} Jacob and Mangano^{2.23} have used the cross sections suggested by Eggarter to calculate, by use of a Boltzmann code, the first Townsend ionization coefficient in argon and found that these had to be reduced by a factor of ~ 2 in order to obtain agreement with the data. The cross sections that gave the best fit were 10% larger than those measured by Shaper and Scheibner.^{2.24} These cross sections, however, represent excitation of both 4s and 4p states of argon. Since it is important, in order to model breakdown at 0.35 μm , to break up the cross section into excitation of the 4s and 4p states separately, we have used the cross sections furnished by R. Center^{2.25} and adjusted them in order to fit the first Townsend ionization coefficient data. The adjustment factor was found to be 0.8. The cross sections have been plotted in Fig. 2.12. The sum of the cross sections is in good agreement with the data of Shaper and Scheibner^{2.24} at energies below 13.5 eV and is in good agreement with Eggarter's total cross section estimate^{2.23} above 14 eV.

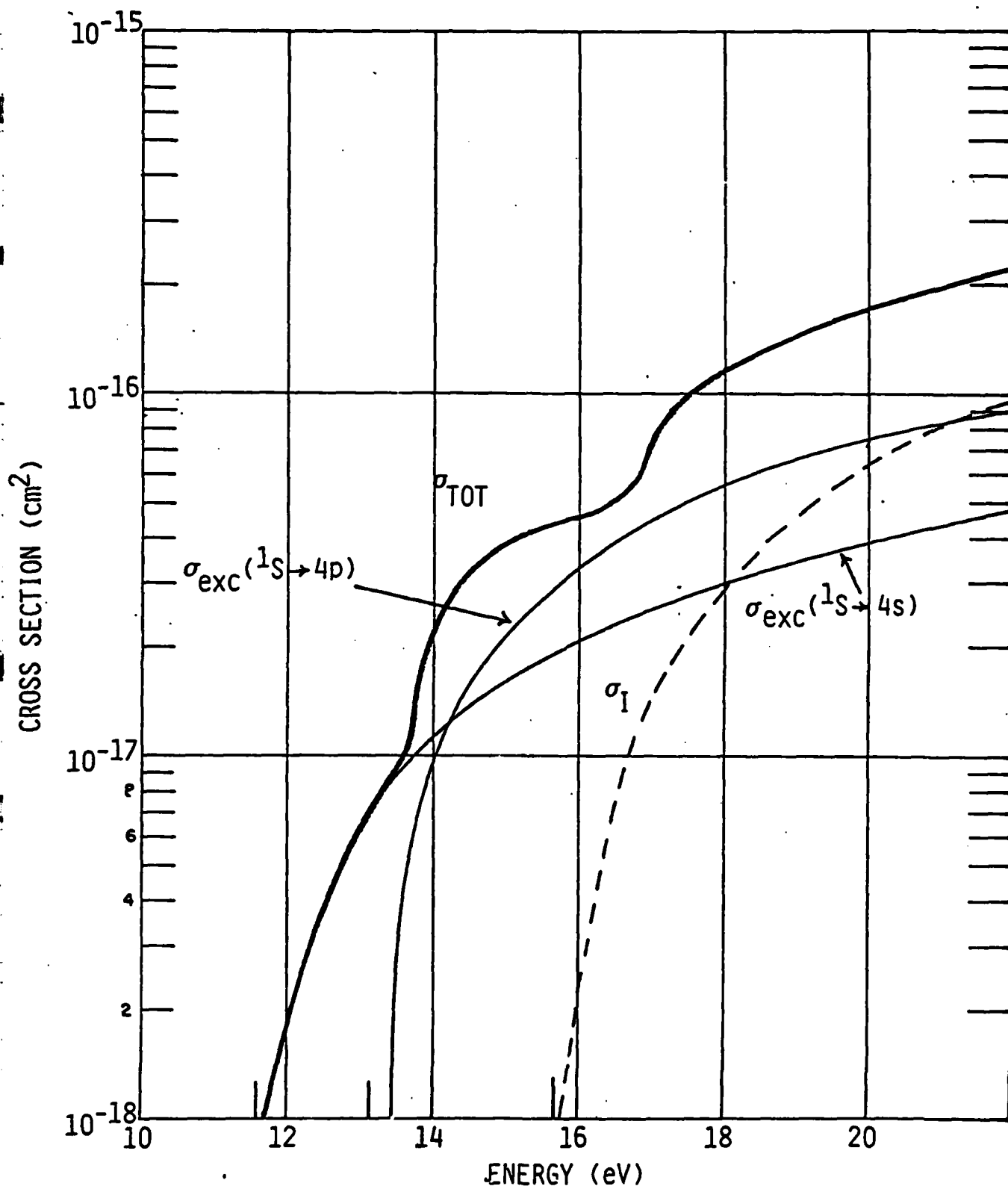


Fig. 2.12 Electron inelastic cross sections in Argon

d) Photoionization of excited states of Argon

The 4p states and higher lying states are within $h\nu$ of the ionization continuum and can be photoionized by absorbing one photon. One estimates the cross-section σ_{phi} to be of the order of 10^{-17} cm^2 so that the lifetime of these states in the laser beam is:

$$\tau = \frac{h\nu}{\sigma_{\text{phi}} I} \approx 5 \times 10^{-2} I^{-1} \text{ s}$$

where I is in W/cm^2 . The radiative lifetime for allowed transitions to the ground state is $3 \times 10^{-9} \text{ s}$ or longer^{2.26} so that at fluxes $I > 10^7 \text{ W/cm}^2$ photoionization is more probable than radiative decay. Also any radiation to the ground state is strongly reabsorbed, resulting in trapping of the radiation. The effective lifetime may be as long as a few microseconds depending on the focal spot size and the operating pressure. Radiative decay to the lower lying 4s state, resulting in radiation that is not trapped, occurs with lifetimes $\tau > 5 \times 10^{-8} \text{ s}$. We can therefore assume, in our model for breakdown, that at fluxes larger than 10^6 - 10^7 W/cm^2 the excitation of the 4p and higher lying states is immediately followed by photoionization.

The 4s states in the energy range 11.6 - 11.8 eV above the ground state, see Fig. 2.9, require the simultaneous absorption of two 3.5 eV photons in order for ionization to occur. We estimate below the probability for 2 photon absorption to occur.

The transition rate for two photon absorption is obtained from second order perturbation theory with the interaction Hamiltonian

$$\Delta H = \frac{-e}{mc} \vec{A}_0 \cdot \vec{p} \cos \omega t = e \vec{E}_0 \cdot \hat{e} \cdot \vec{r} \cos \omega t \quad (2.4.9)$$

with $\vec{A}_0 \cos \omega t$ and $\vec{E}_0 \cos \omega t$ the vector potential and electric field of the electromagnetic wave respectively. The unit vector \hat{e} is the polarization vector which we take to be in the x direction. The transition rate between the lower state (m) and the upper (continuum) state (ℓ) is:^{2.27}

$$W_{ml} = \frac{\pi}{8\pi^2} \int \rho(2\omega + \omega_m) \left| \sum_j \frac{\Delta H_{lj} \Delta H_{jm}}{(\omega - \omega_{jm})} \right|^2 d\Omega. \quad (2.4.10)$$

The integration is carried over solid angle Ω , ρ being the density of final states (per unit ω) and $\omega_{jm} = (E_j - E_m)/\hbar$. The sum is over all intermediate states of energy E_j .

We evaluate Eq. (2.4.10) under the condition where only one intermediate state j is predominant in the sum (to be justified later). We use the \vec{r} representation of the interaction Hamiltonian to evaluate the matrix element between the two bound states m and j and the \vec{p} representation between the bound state and the free state. Using the fact that $|\vec{E}_0\rangle = \frac{\omega}{c} |\vec{A}_0\rangle$, we obtain:

$$W_{ml} = \frac{\pi}{8\pi^4} \frac{\rho(2\omega + \omega_m)}{(\omega - \omega_{mj})^2} \frac{e^4 E_0^4 \pi^2}{m^2 \omega^2} \int d\Omega x_{mj}^2 \left| \langle \psi_j \frac{\partial}{\partial x} \psi_l \rangle \right|^2. \quad (2.4.11)$$

We can express the matrix element x_{mj} in terms of the oscillator strength, f_{mj} , of the transition

$$x_{mj}^2 = \frac{\pi}{2m\omega} f_{mj}. \quad (2.4.12)$$

The other matrix element can be related to the photoionization cross-section of the intermediate state. From Bethe-Salpeter, the cross-section is:^{2.28}

$$\sigma_{\text{phi}} = \frac{2\pi e^2 \pi^2}{m^2 c v} \left| \int u_n^* \left(\sum_i e^{i\vec{k} \cdot \vec{r}_i} \frac{\partial u_n}{\partial x_i} \right) d\tau \right|^2 \quad (2.4.13)$$

where \vec{r}_i is the position of the i^{th} electron, $v = \omega/2\pi$, and the integral extends over the configuration space of all electrons. The wave functions ψ_n are normalized per unit energy interval, while the wave functions in Eq. (2.4.13) are normalized per unit volume. We thus have

$$u_n = \psi_n \sqrt{\frac{\rho(\omega_n)}{\pi}}. \quad (2.4.14)$$

Combining Eqs. (2.4.11)-(2.4.14) we obtain ($I = cE_0^2/8\pi$)

$$W_{ml} = \frac{\pi e^2}{(h\nu)^2 (\omega - \omega_{jm})^2 mc} I^2 \sigma_{\text{phi}} f_{mj} .$$

Expressing I in W/cm^2 , σ_{phi} in cm^2 and energies in eV, we obtain

$$W_{ml} = \frac{5 \times 10^5 I^2 \sigma_{\text{phi}} f_{mj}}{(h\nu)^2 (h\nu - \epsilon_{jm})^2} . \quad (2.4.15)$$

A tabulation of ϵ_{jm} and f_{mj} for allowed transitions can be found in Ref. 2.28. We have reproduced in Table 1 the states that contribute the most to the sum in Eq. (2.4.10). The contribution is large either because there is a near resonance $\epsilon_{jm} \approx h\nu$, or because f_{mj} is large. The ionization cross-section σ_{phi} , can be estimated from the relation^{2.29}

$$\sigma_{\text{phi}} = 7.91 \times 10^{-18} \frac{n}{Z^2} \left(\frac{\nu_n}{\nu} \right)^3 \quad (\text{cm}^2) \quad (2.4.16)$$

where ν_n is the frequency at the photoionization edge, ν the photon frequency, Z the ionic charge and n the principal quantum number of the state j . The quantity $(\sigma_{\text{phi}})_{jl} f_{mj} / (h\nu - \epsilon_{jm})$ is shown in the last column of Table 1. One sees that the near resonant states contribute insignificantly to the sum since f_{mj} and σ_{phi} are both small. Lumping all the 4p states together, with $\sigma_{\text{phi}} = 1.1 \times 10^{-17} \text{ cm}^2$, $f_{mj} = 1$, we obtain the following estimate of the photoionization rate

$$W_{ml} = 1.1 \times 10^{-13} I^2 (\text{W}/\text{cm}^2) \text{ s}^{-1} . \quad (2.4.17)$$

The above formula predicts a lifetime of the 4s state of 10^{-8} s at $10^{10} \text{ W}/\text{cm}^2$, 10^{-9} s at $3 \times 10^{10} \text{ W}/\text{cm}^2$ and 10^{-10} s at $10^{11} \text{ W}/\text{cm}^2$.

TABLE 2.1

CONTRIBUTION OF VARIOUS LEVELS TO PHOTOIONIZATION CROSS-SECTION OF EXCITED STATES IN ARGON

LOWER LEVEL m	E_l (ev)	UPPER LEVEL j	$h\nu - E_j + E_m$ (ev)	f_{mj}	σ_{phi} (10^{-16} cm^2)	$\frac{\sigma_{\text{phi}} f_{mj}}{(E_j - E_l - h\nu)^2}$ ($\text{cm}^2/\text{ev}^2 \times 10^{18}$)
4s(3/2) ^o	11.544	4p(1/2)	2.15	0.212	0.16	0.714
		4p(5/2)	1.98	0.366	0.141	1.31
		4p(3/2)	1.89	0.274	0.126	0.971
		6p(3/2)	0.0247	5.5×10^{-4}	0.0042	0.37
4s(3/2) ^o	11.620	4p'(5/2)	2.04	0.413	0.138	1.36
		4p(3/2)	1.98	0.273	0.129	0.897
		4p(1/2)	1.86	0.121	0.112	0.39
		6p(1/2)	0.075	5.3×10^{-4}	0.0037	0.03
4s'(1/2) ^o	11.72	4p'(3/2)	1.95	0.56	0.11	1.6
		4p'(1/2)	1.90	0.341	0.11	1.0
		6p(3/2)	0.034	7.4×10^{-4}	0.002	0.12
4s'(1/2)	11.82	4p'(3/2)	2.06	0.160	0.11	0.42
		4p'(3/2)	2.04	0.431	0.11	1.1
		4p'(1/2)	2.01	0.172	0.11	0.45
		4p'(1/2)	1.86	0.133	0.080	0.33
		6p(1/2)	0.0424	3.4×10^{-4}	0.0013	0.024

e. Early Time Cascade Development

The early time cascade development can be analyzed by writing rate equations for reactions (2.4.1)-(2.4.7). Let n , n^* and n_e be the density of Ar, Ar* and electrons. We will have the following rate equations for the formation of electrons and 4s excited states.

$$\frac{dn_e}{dt} = W_{m1} n^* + k_2 n_e n + S \quad (2.4.18)$$

$$\frac{dn^*}{dt} = k_1 n_e n - W_{m1} n^* \quad (2.4.19)$$

where k_1 is the rate of formation of Ar* corresponding to reaction (2.4.4), k_2 is the rate of formation of Ar** by reaction (2.4.5) and we assumed that Ar** is immediately photoionized by reaction (2.4.7). From Eq. (2.4.17) we have $W_{m1} = AI^2$ with $A \approx 1.1 \times 10^{-13} \text{ sec}^{-1} (\text{W/cm}^2)^{-2}$. The term S represents sources and sinks of electrons, the source being multiphoton ionization of Ar (reaction (2.4.1)) and multiphoton ionization of impurities. The sink of electrons would include a diffusion loss term of the form $-\frac{D}{\Lambda^2} n_e$. We solve Eq. (2.4.18) and (2.4.19) with the neglect of diffusion losses and the initial condition $n_e = n^* = 0$. The result is found to be, after some algebra

$$n_e = \frac{S}{(k_2 + k_1)n} \left[a_+ e^{\alpha_+ t} + a_- e^{\alpha_- t} - 1 \right] \quad (2.4.20)$$

with

$$a_{\pm} = \frac{(k_2 + k_1)n + \alpha_{\pm}}{\alpha_{\pm} - \alpha_{\mp}} \quad (2.4.21)$$

$$\alpha_{\pm} = \frac{-W_{m1} \pm \sqrt{W_{m1}^2 + 4W_{m1}(k_2 + k_1)n}}{2} \quad (2.4.22)$$

The growth of n_e versus t given by Eq. (2.4.20) is shown in Fig. 2.13. The exponential growth at late times is due to the first term in Eq. (2.4.20). Curves of constant α_+ , shown in Fig. 2.14, indicate that α_+ (or breakdown time) will be a function of I_p^m where $0.5 < m < 0.7$ over the range of parameters considered. The rates k_1 and k_2 used in our calculations were

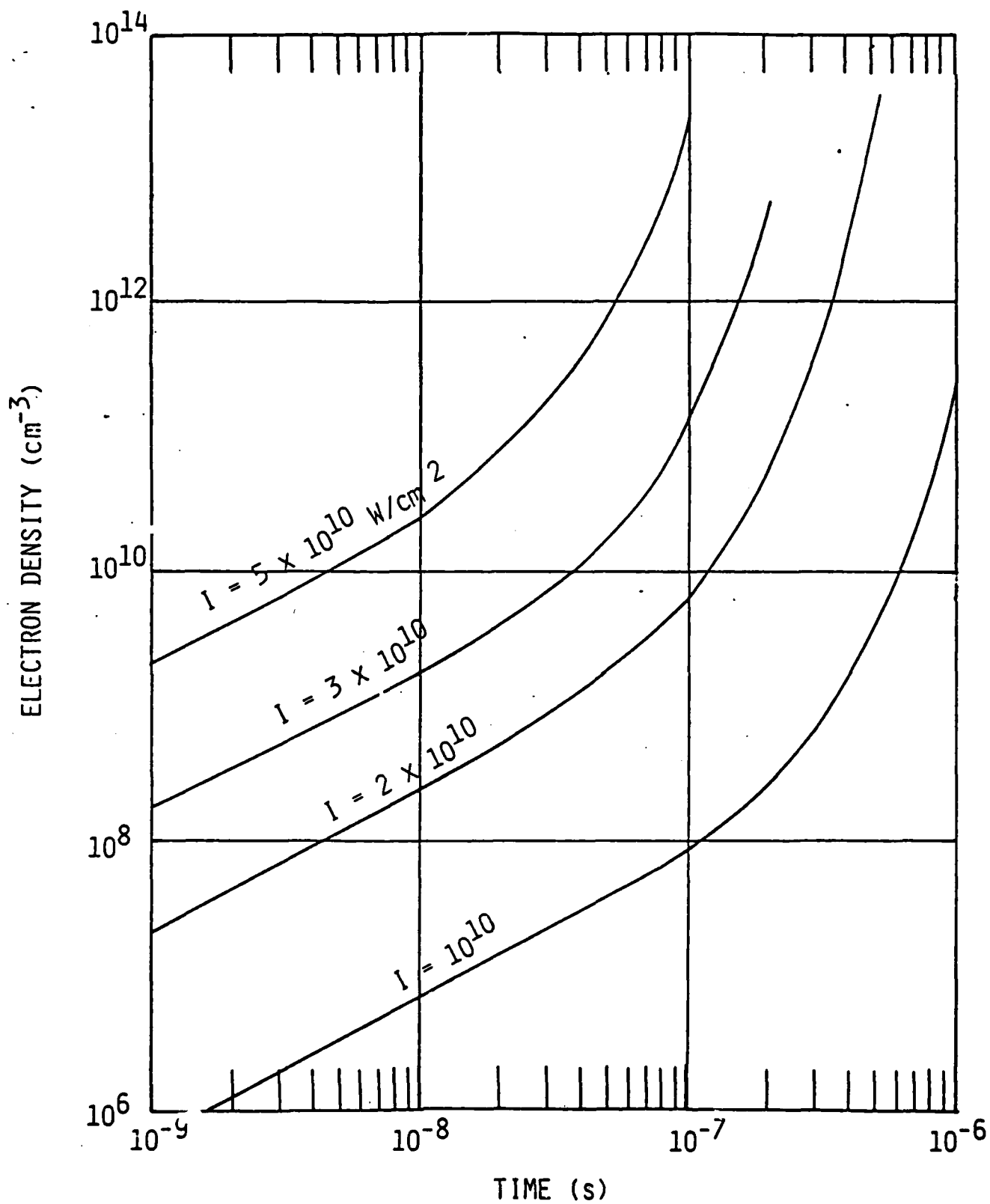


Fig. 2.13 Growth of electron population with time, Argon at standard density.

AVALANCHE RATE IN ARGON

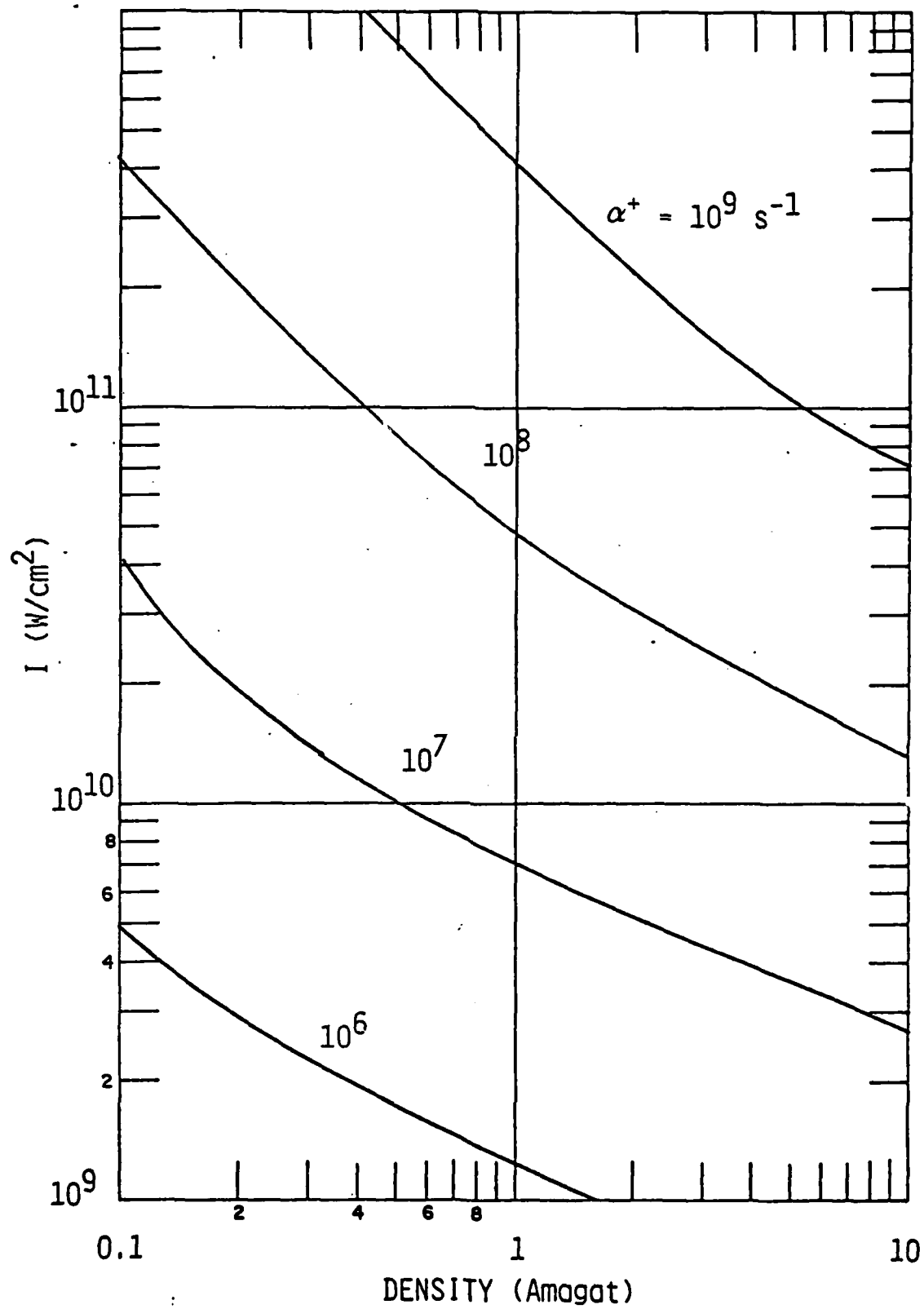


Fig. 2,14 Cascade rate coefficient α_+ as a function of laser intensity for early time cascade growth in argon, $h\nu = 3.5 \text{ eV}$.

derived from a Boltzmann code written by Morgan at JILA. We used in the code the cross sections for excitation that were described previously. The momentum transfer cross section was taken from the data of Frost and Phelps^{2.30} and the total ionization cross section from the data of Rapp and Englander Golden.^{2.31} The inverse bremsstrahlung cross section used was that suggested by Lane and Dalgarno,^{2.21} given by Eq. (2.4.8c). The excitation rates obtained in the intensity range 10^{10} - 10^{11} W/cm² could be fitted by the relations

$$k_1 = 5 \times 10^{-23} I \quad (\text{cm}^3/\text{s}) \quad (2.4.23)$$

$$k_2 = \frac{2.5 \times 10^{-23} (I/10^{10})^{1.28}}{1 + \left(\frac{I}{10^{10}}\right)^{0.28}} \quad (\text{cm}^3/\text{s}) \quad (2.4.24)$$

where I is in (W/cm²). The resulting electron distribution functions at 10^{10} and 10^{11} W/cm² are shown in Fig. 2.15. The total excitation rate in the intensity range 10^{10} - 10^{11} W/cm² using Eq. (2.4.8c) is a factor of 2 lower than that using Eq. (2.4.8b) and a factor of 7 lower than the excitation rate obtained by Friedland^{2.32} who used the Raizer formula for k_a , i.e., Eq. (2.4.8a). The discrepancy is entirely due to the difference in heating rate using the various formulae, since the bulk (>80%) of the energy absorbed goes into excitation of electronic states.

2.4.2 Late Time Breakdown Analysis for Argon

When the electron concentration exceeds some critical value, electron-electron collisions become dominant, tending to make the electron distribution function Maxwellian. The equilibration time due to electron-electron collisions is:^{2.33}

$$t_{ee} = \frac{0.26 T_e^{3/2}}{n_e \ln \Omega} \approx \frac{3.8 \times 10^4}{n_e} \text{ s} \quad (2.4.25)$$

where in the last step we made $T_e = 10,000^\circ\text{K}$, and took a value of 6 for the Coulomb logarithm. This time is to be compared with the electron heating time and the excitation time. Let $\bar{\epsilon}$ ($=3/2 kT_e$) be the average electron energy. The electron heating time is

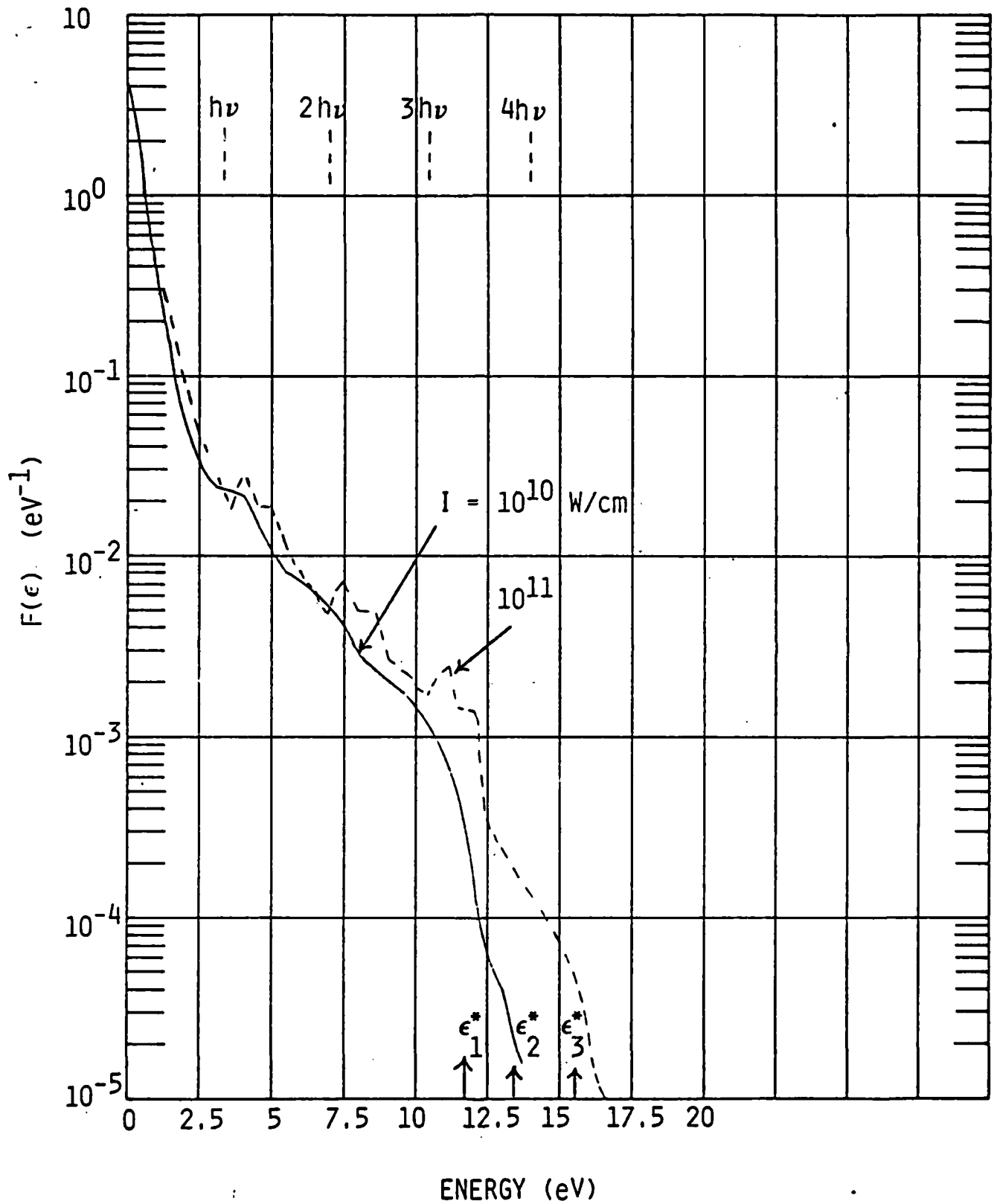


Fig. 2.15 Electron distribution function in Argon at two laser fluxes.

$$t_H = \frac{\bar{\epsilon}}{KnI} = 6 \times 10^{-8} \left(\frac{10^{10}}{I} \right) p^{-1} \text{ s} \quad (2.4.26)$$

where in the last step we took $\bar{\epsilon} = 1.2 \text{ eV}$, $n = 2.5 \times 10^{19} \text{ cm}^{-3}$, $\bar{K} = 4.5 \times 10^{-41} \text{ cm}^5$. I is in W/cm^2 and p is the pressure in atmospheres. The excitation time is obtained from Eqs. (2.4.23) and (2.4.24)

$$t_{\text{exc}} = \frac{1}{(k_1 + k_2)n} \approx 6 \times 10^{-8} \left(\frac{10^{10}}{I} \right) p^{-1} \text{ s.} \quad (2.4.27)$$

For $I \approx 10^{10} \text{ W/cm}^2$ and $p \leq 1 \text{ atm}$, we find that the condition $t_{ee} < t_H, t_{\text{exc}}$ occurs when n_e exceeds 10^{13} cm^{-3} . The Boltzmann code written by Morgan allows for the inclusion of electron-electron collisions. The effect of electron-electron collisions on the electron distribution and on the heating rate (or effective absorption coefficient) is dramatic. We show in Fig. 2.16 two electron distribution functions obtained with and without electron-electron collisions, when $n_e = 10^{14} \text{ cm}^{-3}$. The heating rate when electron-electron collisions are included is two to three times larger than when they are not.

We model the late time breakdown by assuming that we have a two temperature gas. Let T_e be the electron temperature; $\bar{\epsilon} = 3/2 kT_e$, the average electron energy, and T the heavy particle temperature. The rates for reactions (2.4.4) and (2.4.5) are obtained by a suitable averaging of the cross sections over the distribution function. Electron-ion recombination must be included in the model when the electron density gets to be large enough. Also, electron impact ionization of excited states becomes important as the population of excited states builds up. We must, therefore, add to the series of reactions (2.4.1)-(2.4.5) the following reactions



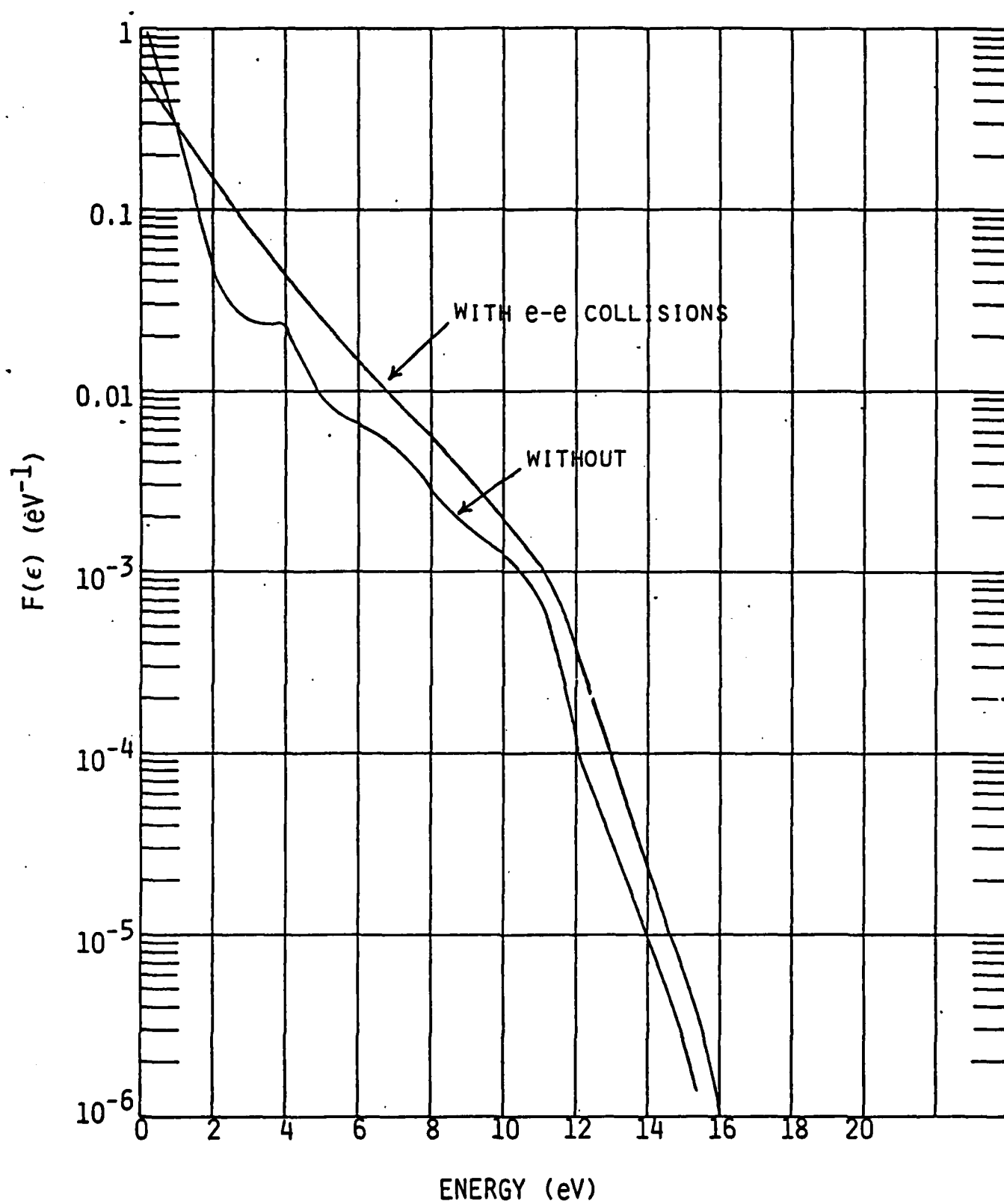
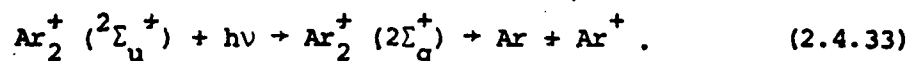


Fig. 2.16 Effect of electron-electron collisions on the distribution function of electrons.



Reaction (2.4.28) is very fast at atmospheric pressure, having a rate coefficient of $3 \times 10^{-31} \text{ cm}^6/\text{s}$. It leads to the formation of ion dimers which very rapidly recombine with electrons through reaction (2.4.29). Reaction (2.4.29) has a rate coefficient^{2.34} of $0.1 \times 10^{-7} (300/T_e)^{0.61} \text{ cm}^3/\text{s}$ where T_e is in °K. Shui and Biondi^{2.34} experimentally observed that reaction (2.4.29) leads to excited argon atoms principally in the 4p state.

We expect, at the high XeF laser fluxes that we are considering, that the photodissociation of Ar_2^+ will be faster than reaction (2.4.29). We show in Fig. 2.17 the potential energy curves for Ar_2^+ and other excited states of the Ar_2 dimer as derived by Lorentz and Olsen.^{2.35} The binding energy of Ar_2^+ is 1.24 eV. Photodissociation will occur through the channel.



We therefore combine reactions (2.4.28) and (2.4.33) into the following overall reaction which results in heating of the gas.



The rate limiting step for (2.4.28a) being reaction (2.4.28), we use the rate for reaction (2.4.28) in reaction (2.4.28a). In a similar way we replace reaction (2.4.30) by



The three body recombination reaction (2.4.32) is extremely important in the late stages of the breakdown processes since it leads to the formation of excited states of argon which are rapidly photoionized. It leads to an effective plasma absorption coefficient larger than that due to electron-ion and electron-neutral inverse bremsstrahlung in two body collisions. We replace reaction (2.4.32) by

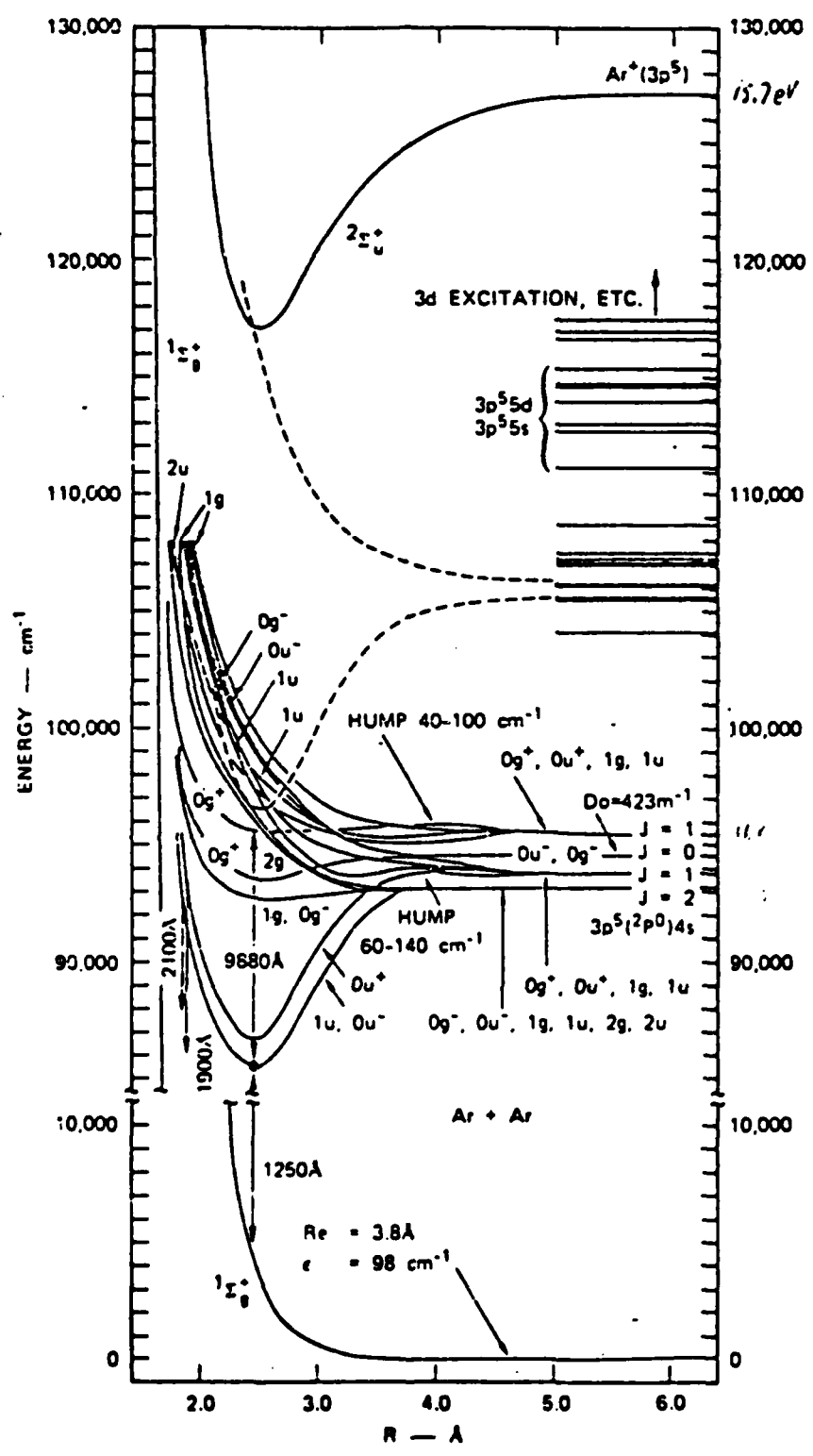


Fig. 2.17 - Potential energy curves for the system Ar + Ar.



The three body recombination rate for reaction (2.4.32) has been studied by Gurevich and Petaevskii^{2.37} and by Bates et al.^{2.38}

We model the breakdown by adding to the inverse bremsstrahlung absorption by the electrons, the effects of reactions (2.4.28a), (2.4.30a), (2.4.31) and (2.4.32a). We have three species - electrons, Ar and Ar* - and two temperatures - T_e and T_g . Let x_e , x and x^* be the densities of electrons, Ar and Ar* normalized to the initial gas density n . Let $\bar{\epsilon}$ be the average electron energy ($= 3.2 kT_e$). The five equations describing the breakdown at late times are the following

Species conservation:

$$x_e + x + x^* = 1. \quad (2.4.34)$$

Rate of growth of electrons and Ar*

$$\frac{dx_e}{dt} = \nu' x_e x^* + W_{m1} x^* + \nu^{**} x_e x. \quad (2.4.35)$$

$$\frac{dx^*}{dt} = \nu^* x_e x - W_{m1} x^* - \nu' x_e x^*. \quad (2.4.36)$$

Energy equation for electrons and excited states

$$\begin{aligned} \frac{d}{dt} \left[(\bar{\epsilon} + \epsilon_I) x_e + \epsilon^* x^* \right] = & \left[(\bar{K}_{en} x_e x + \bar{K}_{ei} x_e^2) n \phi + x_e (\nu' + \nu^* x^* + \nu^{**} x) \right. \\ & \left. + 2W_{m1} x^* - \frac{2m}{M} \nu_m x_e \left(\bar{\epsilon} - \frac{3}{2} kT \right) + \mu x_e^3 \right] h\nu; \quad (2.4.37) \end{aligned}$$

Energy equation for the heavy particles

$$\frac{3}{2} k \frac{d}{dt} T = \frac{2m}{M} \nu_m (\bar{\epsilon} - \frac{3}{2} kT) x_e + (k_R x_e x^2 n^2) h\nu. \quad (2.4.38)$$

In the above, ν^* , ν^{**} and ν' are the excitation rates corresponding to reactions (2.4.4), (2.4.5) and (2.4.30), $\epsilon_I (=15.755 \text{ eV})$ is the ionization potential of argon, \bar{K}_{en} and \bar{K}_{ei} are the inverse bremsstrahlung absorption coefficients for electron-neutral and electron-ion collisions averaged over a Boltzmann distribution of electrons, ν_m is the momentum transfer collision frequency

between electrons and heavy particles, μ is the rate corresponding to reaction (2.4.32) and k_R the rate coefficient for reaction (2.4.28). ϕ is the photon flux in units of (area \times time)⁻¹. Following Zel'dovich and Raizer,^{2.39} we approximate the excitation cross section near threshold by $\sigma_{exc}(\epsilon) = C(\epsilon - \epsilon_{th})$ for $\epsilon > \epsilon_{th}$. After averaging over a Maxwellian distribution we obtain an excitation rate

$$\nu_{exc} = 3.23 \times 10^7 n C \bar{\epsilon}^{-3/2} \left(\frac{3}{2} \frac{\epsilon_{th}}{\bar{\epsilon}} + 2 \right) \exp \left(-\frac{3}{2} \frac{\epsilon_{th}}{\bar{\epsilon}} \right) \text{ (s}^{-1}\text{)} \quad (2.4.39)$$

where C is in cm²/eV, n in cm⁻³ and $\bar{\epsilon}$ in eV. We use for argon $C = 10^{-17}$ cm²/eV and obtain ν^* , ν^{**} and ν' by letting ϵ_{th} be ϵ^* , ϵ^{**} and $(\epsilon^{**} - \epsilon^*)$, respectively.

\bar{K}_{en} is obtained by taking the average of $K_a (1 - \exp(-\frac{2h\nu}{3\epsilon}))$ over a Boltzmann distribution of ϵ , where K_a is given by Eq. (2.4.8c). \bar{K}_{ei} is k_e/n^2 where k_e is given by Eq. (2.3.4a). Using a Gaunt factor of 1.2 (see Fig. 2.6 for $h\nu/kT_e \approx 1$ and kT_e in the range 1-5 eV), we have

$$K_{ei} = \frac{3.5 \times 10^{-37}}{\bar{\epsilon}^{-1/2} (h\nu)^3} (1 - \exp(-\frac{3}{2} \frac{h\nu}{\bar{\epsilon}})) \text{ (cm}^5\text{)} \quad (2.4.40)$$

where $h\nu$ and $\bar{\epsilon}$ are expressed in eV.

The collision frequency for momentum transfer ν_m has contributions due to electron-neutral and electron-ion collisions. We have

$$\nu_m = (x+x^*)\nu_a + x_e \nu_e \quad (2.4.41)$$

where

$$\nu_a = n \left(\frac{2\epsilon}{m} \right)^{1/2} \sigma_s(\epsilon) = 4.84 \times 10^7 n \epsilon(\text{eV})^{1/2} \sigma_s(\epsilon) \quad (2.4.42)$$

and

$$\nu_e = \frac{n \ln \Omega}{0.266 T(\text{K})^{3/2}} = \frac{5.54 \times 10^{-6}}{\bar{\epsilon}^{-3/2}} n \ln \left(\frac{8.4 \times 10^9 \bar{\epsilon}^{-3/2}}{n^{1/2}} \right) \text{ s}^{-1}. \quad (2.4.43)$$

In the last step, n is in cm^{-3} and $\bar{\epsilon}$ in eV.

The three body electron ion recombination rate is given by^{2,37, 2.40}

$$\mu = \frac{4\pi(2\pi)^{1/2}}{9} \frac{n^2 e^{10} \ln\Lambda}{m^{1/2} (kT)^{9/2}} = \frac{5.6 \times 10^{-26} n^2 \Lambda}{(\bar{\epsilon})^{9/2}} \quad (2.4.44)$$

where $\ln\Lambda$ is a Coulomb logarithm of a special kind of order unity.^{2.40}

The system of differential equations (2.4.35)-(2.4.38) subject to the constraint given by Eq. (2.4.34) was numerically integrated. Results for the case $p = 1 \text{ atm}$, $I = 10^{10} \text{ W/cm}^2$ with initial electron concentration $x_{e0} = 10^{-6}$ ($n_{e0} = 2.5 \times 10^{13} \text{ cm}^{-3}$) are shown in Figs. 2.18-2.20. The breakdown time is calculated to be 800 ns. The gas temperature and electron temperature remain constant during most of the induction time to breakdown, see Fig. 2.18. The build-up of the electron and excited state argon population is shown in Fig. 2.19. The absorption coefficients due to the various absorption mechanisms are shown in Fig. 2.20. The two most important absorption mechanisms during most of the delay time to breakdown are electron-neutral inverse bremsstrahlung and photodissociation of the dimer Ar_2^+ , the first mechanism being the one that determines the time evolution of the cascade. Most of the energy is deposited into the gas in the very last stages of the breakdown and the absorption mechanisms, in order of importance, are: photoionization of Ar^{**} formed either by three body recombination reaction (2.4.32), or by electron impact excitation on Ar^* ; electron-ion inverse bremsstrahlung, and electron-neutral inverse bremsstrahlung. For the case studied the absorption coefficient reaches a maximum of 30 cm^{-1} at $t = 0.786 \mu\text{s}$ and decreases thereafter with increasing electron temperature. It is interesting to note that the electron-ion inverse bremsstrahlung absorption coefficient peaks at a value of 0.6 cm^{-1} , i.e., is 50 times lower than the recombination absorption.

The two-photon ionization of $\text{Ar}^*(4s)$ plays an important role in the breakdown process. The rate that we used, given by Eq. (2.4.17), is of the order of the electron cascade time at $I = 10^{10} \text{ W/cm}^2$, and the value of this rate constant, for which we have just obtained an approximate value, should

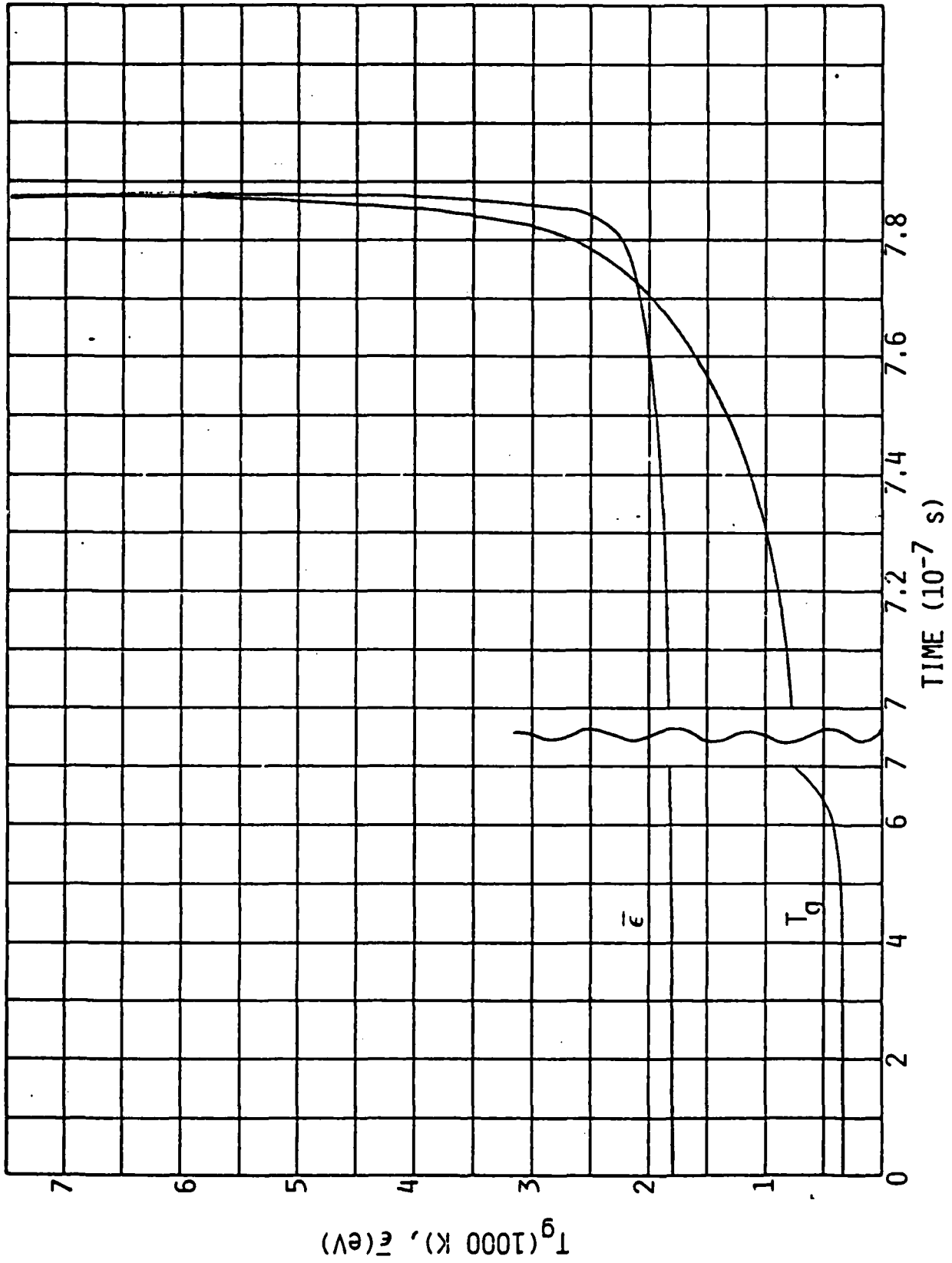


Fig. 2.18 Electron energy and gas temperature during breakdown, $n = 1$ amagat, $I = 10^{10}$ W/cm².

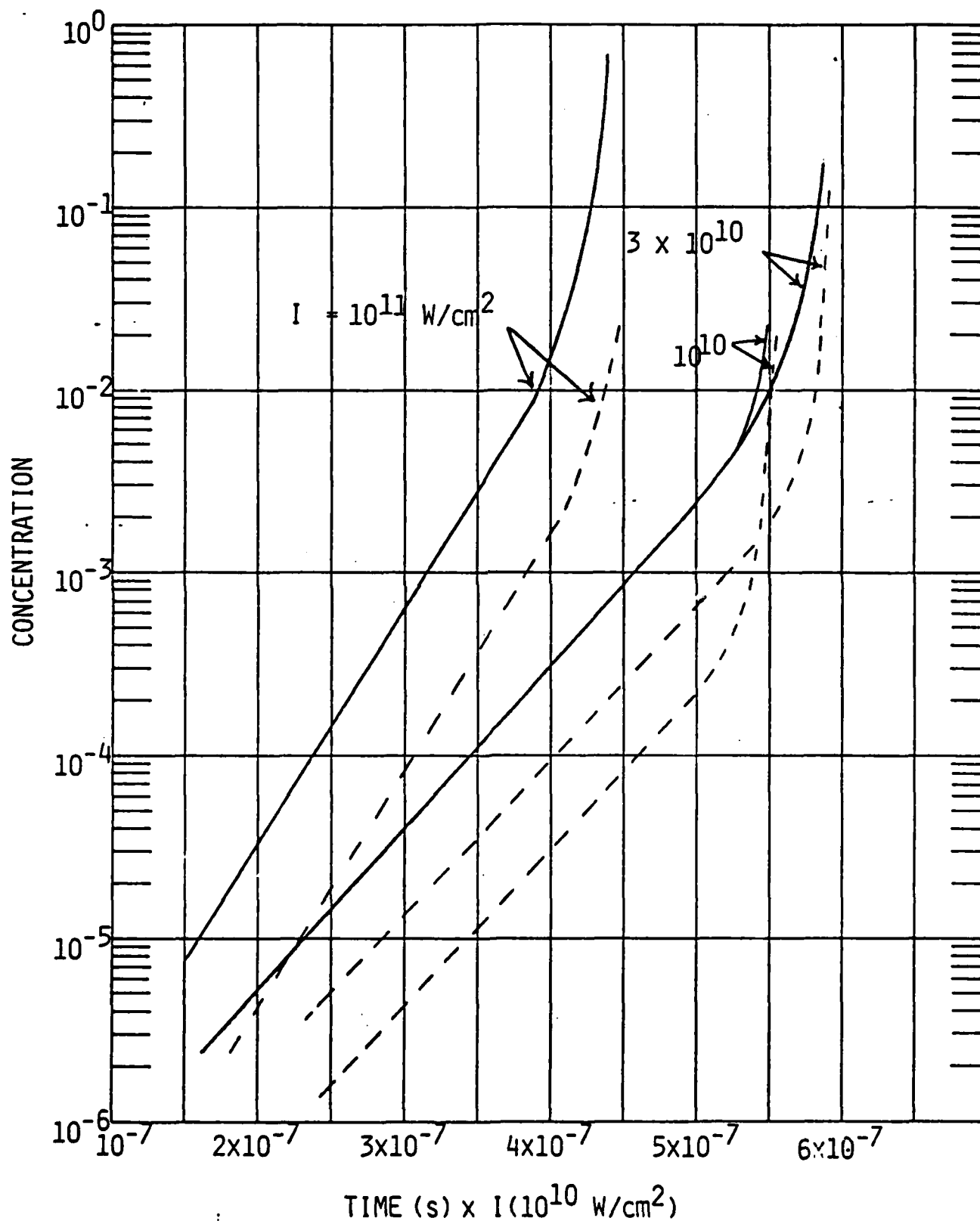


Fig. 2.19 Growth of electron concentration (—) and first excited state concentration (---) in the late time breakdown of Argon.

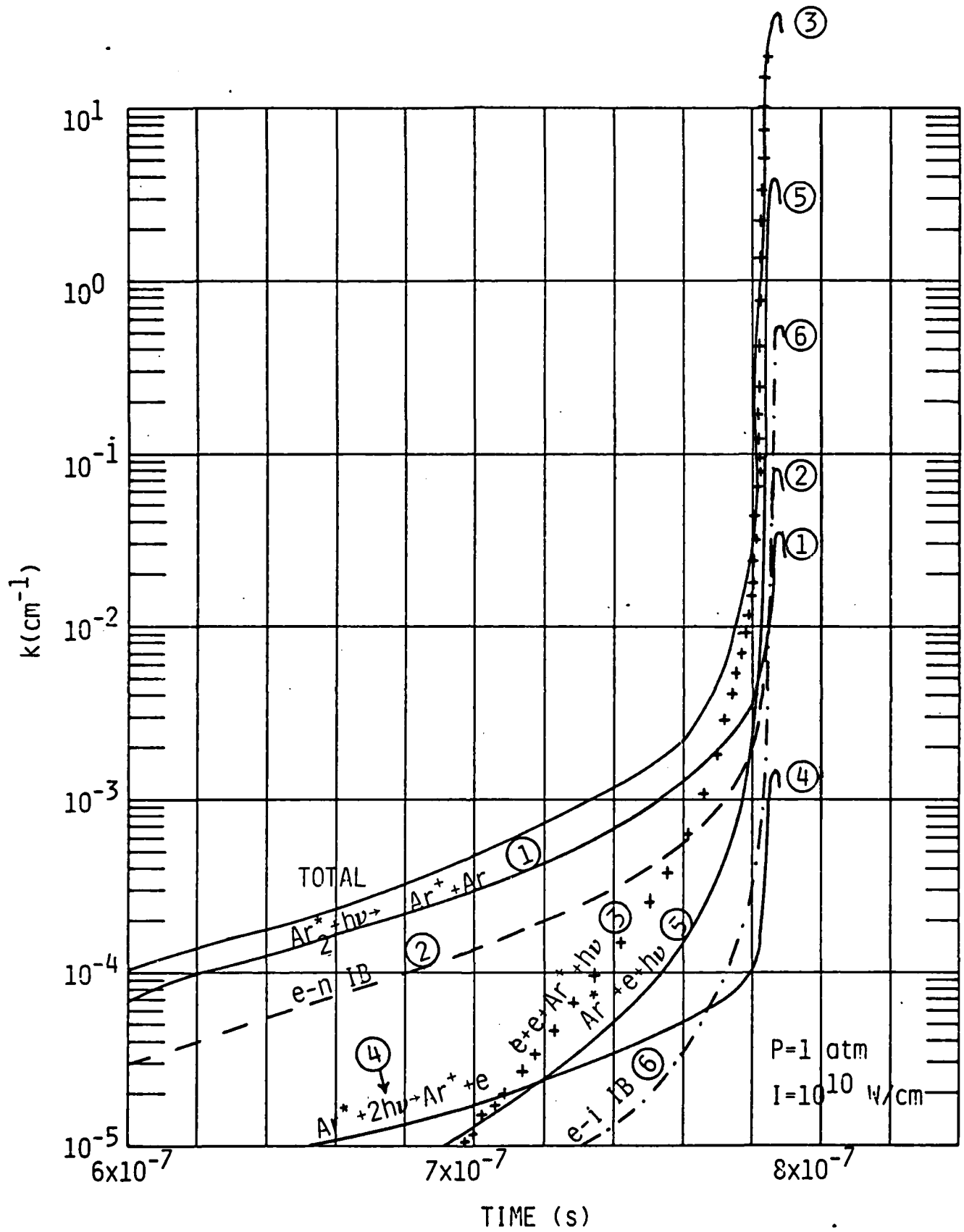


Fig. 2.20 Various absorption mechanisms in Argon.

influence the breakdown time in a significant way. It is possible that W_{ml} could be 10 to 20 times larger than the value used due to constructive interference of many intermediate states. When we multiply W_{ml} by 10 we find the breakdown to be 5.8×10^{-7} s instead of 7.8×10^{-7} s. At very large values of W_{ml} the breakdown time reaches its asymptotic value of 5×10^{-7} s. As I is increased beyond 10^{10} W/cm² for $p = 1$ atm, the breakdown time scales as I^{-1} .

2.5 REFERENCES

- 2.1. C. Grey Morgan, Rep. Progr. Phys. 38, 621 (1975).
- 2.2. Sanford Brown, Microwave Breakdown in Gases.
- 2.3. H. Cohn, M. Hacker, B. Lax and W. Halverson, J. Appl. Phys. 46, 668 (1974).
- 2.4. F. Morgan, L. Evans and C. Grey Morgan, J. Phys. D. Appl. Physics 4, 225 (1971).
- 2.5. G. Weyl, J. Phys. D. Appl. Phys. 12, 33 (1979).
- 2.6. D. Golden and L. Fisher, Phys. Rev. 123, 1079 (1961).
- 2.7. D. Golden, H. Nakamo and F. Fisher, Phys. Rev. 138, 1613 (1965).
- 2.8. J. Anderson, Phys. Fl. 7, 1517 (1964).
- 2.9. S. C. Brown, Basic Data of Plasma Physics, Second Revised Edition, The MIT Press (1967).
- 2.10. Ya. B. Zel'dovich and Yu. P. Raizer, Physics of Shock Waves and High Temperature Hydrodynamic Phenomena, Vol. I, Academic Press, New York (1966), p. 259.
- 2.11. I. Shkarovsky, T. Johnston and M. Bachynski, The Particle Kinetics of Plasmas, Addison Wesley, Reading, Mass. (1966), Chapter 6, pp. 202-241.
- 2.12. T. Johnston and J. Dawson, Phys. Fluids, 16, 722 (1973).
- 2.13. W. T. Karzas and R. Latter, Astrophys. J. Suppl. Series 6, 167 (1961).
- 2.14. G. Hill, D. James and S. Ramsden, J. Phys. D. Appl. Phys. 5, 155 (1972).
- 2.15. F. Mehr and M. Biondi, Phys. Rev. 176, 322 (1968).
- 2.16. P. Lambropoulos, "Topics on Multiphoton Ionization in Gases" in Advances in Atomic and Molecular Physics, Vol. 14 (1977) pp. 87-163.
- 2.17. I. Krasnyuk and P. Pashinin, ZhETF Dis. Red 15, 471 (1972).
- 2.18. Ya. Zel'dovich and Yu. Raizer, Sov. Phys. JETP 20, 722 (1965).
- 2.19. N. Kroll and K. Watson, Phys. Rev. A5, 1883 (1972).

- 2.20. A. Phelps, "Theory of Growth of Ionization During Laser Breakdown," in Physics of Quantum Electronics, P. L. Kelley, B. Lax and P. Tannenwald Ed, McGraw Hill, New York (1966), p. 538.
- 2.21. A. Dalgarno and N. Lane, Astrophys. J. 145, 623 (1966).
- 2.22. E. Eggarter, J. Chem. Phys. 62, 833 (1974).
- 2.23. J. Jacob and J. Mansano, J. Appl. Phys. 79, 467 (1976).
- 2.24. M. Shaper and H. Scheibner, Beil. Plasma Phys. 9, 45 (1969).
- 2.25. R. Center (unpublished).
- 2.26. W. Wiese, M. Smith and B. Miles, Atomic Transition Probabilities Vol. II, Sodium Through Calcium, National Bureau of Standards NSRDS=NBS22 (1969).
- 2.27. A. Yariv, Quantum Electronics, Joan Wiley and Sons, New York (1967) p. 358.
- 2.28. H. Bethe and E. Salpeter, Quantum Mechanics of One and Two Electron Atoms, Academic Press Inc., New York (1957), p. 296.
- 2.29. Same as reference 2.9, p. 265.
- 2.30. L. Frost and A. Phelps, Phys. Rev. A 136, 1538 (1964).
- 2.31. Rapp and Englander Golden, J. Chem. Physics, 43, 1464 (1965).
- 2.32. L. Friedland, Phys. Rev. A 12, 2024 (1975).
- 2.33. L. Spitzer, Physics of Fully Ionized Gases, J. Wiley and Sons, New York (1962), p. 133.
- 2.34. Y. Shiu and M. Biondi, Phys. Rev. A 17, 868 (1978).
- 2.35. D. Lorentz and R. Olsen, "Excimer formation and decay process," Stanford Research Institute Report dated Nov. 27, 1972, Contract N00014-72-C-0457, Menlo Park, Calif. 94025.
- 2.36. H. Michels, R. Hobbs and L. Wright, J. Chem. Phys. 71, 5053 (1978).
- 2.37. A. Gurevich and L. Pitaevskii, Sov. Phys. JETP 19, 870 (1964).
- 2.38. D. Bates, A. Kingston and R. McWhirter, Proc. Roy. Soc. (London) A267, 297 (1962).
- 2.39. See reference 2.10, p. 390.
- 2.40. Id., p. 407.

3. DETAILED MODEL OF QUASI-ONE-DIMENSIONAL FLOW OF A REAL GAS WITH LASER ENERGY ABSORPTION

3.1 Introduction

This chapter deals with computer modeling of single-pulse experiments, and presents work performed over the period from June 1978 through October 1980.

The early theoretical work on the fluid mechanics pulsed laser propulsion at PSI was based on blast wave theory of a perfect gas in a conical nozzle, Ref. 3.1. It provided valuable information about the behavior of the gases, the effect of pulse repetition rate, the rocket performance to be expected, and the interpretation of the experiments. However, it dealt entirely with the gas motion after all the laser energy had been deposited (blast wave mode). It did not consider the absorption process and resulting LSD wave. It was restricted to "constant γ " gases, so that real gas effects could only be considered by taking small values of γ , the specific heat ratio. Radiation from the gas was not considered, and it would have been difficult to fit into the constant γ framework, since the chemical composition of the gas was not calculated.

In order to improve the modeling, and remedy some of these defects, a more elaborate computer model of the non-steady flow was constructed. It was based on the familiar use of quasi-one-dimensional non-steady, inviscid flow in the nozzle, which leads to partial differential equations in axial distance and time. The effects of laser energy absorption and chemical equilibrium of the gases were included. The numerical algorithm used was a simple version of a shock-capturing scheme, which produced LSD waves or shock waves at the appropriate locations in the nozzle. While radiation losses have not as yet been included, the gas composition is calculated, so radiation-loss models can be implemented when developed. A further restriction of the work, so far, has been to single-pulse operation. Multiple-pulse capability can be added fairly easily, and is a task for future work.

The main emphasis so far has been on developing a computational model that would be useful to aide in the more realistic interpretation of single-pulse experimental data, with special emphasis on calculation of the energy absorbed from pressure and shock transit time measurements.

The work described in this chapter dealt with the equations of motion, the equilibrium thermodynamics of argon and hydrogen, the absorption coefficients of these gases at 10.6 and 0.353 μm , the numerical method of solving the equations, the calculated results, and their correlation for the purpose of interpreting the experimental results.

The work was performed over a period of several years, and some of the writing was also done as the work was completed. Therefore, the material in this chapter follows a chronological order, and reflects the improvement of various aspects as the work progressed. Section 3.2 presents the equations of motion used to describe the quasi-one-dimensional inviscid flow, with laser energy addition, of a real gas. Section 3.3 describes an early model of singly-ionized argon, and Section 3.4 the corresponding absorption coefficient for 10.6 μm radiation. The steady flow of a perfect gas in a nozzle, which is the initial condition for the flow, is recalled in Sec. 3.5. The jump conditions across an LSD wave are set forth in Sec. 3.6, since the pulsed-propulsion flow involves LSD waves when the laser is on. In Sec. 3.7 a set of similarity variables are defined which are useful in the correlation of the numerical results. The numerical scheme used to solve the equations is described in Sec. 3.8. The numerical results obtained with perfect gases and singly-ionized argon are presented in Sec. 3.9, including LSD waves in a constant area channel and single-pulse flow in a parabolic nozzle. The last five sections represent improvements over the previous work. Interest in hydrogen as a possible propellant prompted the adaptation of an existing model of dissociating and ionizing equilibrium hydrogen, presented in Sec. 3.10. Improvements in the absorption coefficient for singly-ionized argon, and the additional 10.6 μm absorption coefficients for hydrogen are given

in Section 3.11. An improved model of argon, which includes multiple-ionization up to the third ion, is described in Sec. 3.12, and the associated absorption coefficients are given in Sec. 3.13, including both 10.6 μm and 0.353 μm radiation. Finally, some early results of calculations for multiply-ionized argon at 0.353 μm are presented and correlated in Sec. 3.14.

3.2 Equations Of Motion

We are considering nonsteady flow in a nozzle, in the quasi-one-dimensional approximation, where all quantities may depend on the time t and the axial distance x . The cross-sectional area A of the nozzle depends only on x , while the flow speed u , pressure p , density ρ and internal energy per unit mass e depend on both x and t . The gas is heated by a laser beam of power P propagating in the negative x direction (upstream). This beam power may change with time because the laser has a time-varying output, but as far as the fluid flow is concerned, only x variations of P need be considered. Changes in P with time occur at the speed of light, and so may be taken to occur instantaneously at all locations in the nozzle. This means that time is only a parameter in the laser power term, and no time derivatives of P appear.

With this model of the flow, the conservation equations for mass, momentum and energy of the gas in the nozzle are

$$\frac{\partial}{\partial t} (\rho A) + \frac{\partial}{\partial x} (\rho u A) = 0 \quad , \quad (3.2.1)$$

$$\frac{\partial}{\partial t} (\rho u A) + \frac{\partial}{\partial x} [A (p + \rho u^2)] = p \frac{dA}{dx} \quad (3.2.2)$$

$$\frac{\partial}{\partial t} \left[\rho A \left(e + \frac{u^2}{2} \right) \right] + \frac{\partial}{\partial x} \left[\rho u A \left(e + \frac{p}{\rho} + \frac{u^2}{2} \right) \right] = \frac{dP}{dx} \quad . \quad (3.2.3)$$

These are written in so-called conservation form, with only derivative terms except for the right side of Eq. (3.2.2), which has a source term proportional to the given gradient of the nozzle area.

The laser power obeys the radiation transport equation in the absence of emission

$$\frac{dP}{dx} = k_L P \quad , \quad (3.2.4)$$

where the right side is the absorption by the gas of laser energy, with absorption coefficient k_L . The sign is chosen so that the beam propagates in the negative x direction while being absorbed, so the slope is positive because both P and x decrease together. From Eq. (3.2.4) the right side of the energy equation (3.2.3) can be written $k_L P$, exhibiting the absorbed laser power as a source term.

The laser radiation transport equation (3.2.4) can be integrated from $x = \infty$, where the incoming laser power is P_0 , to give

$$P = P_0 \exp\left(-\int_x^{\infty} k_L dx\right) . \quad (3.2.5)$$

To these four equations must be added specifications of the area distribution $A(x)$, the laser absorption coefficient k_L , the thermal and caloric equations of state $p(\rho, T)$ and $e(\rho, T)$, and the boundary and initial conditions on the variables ρ , u , p and P . They will complete the definition of the mathematical problem whose solution will give the response of the gas flow in the nozzle to the absorption of laser energy.

The choice of dependent variables in the solution of Eqs. (3.2.1 - 3.2.3) and (3.2.5) is somewhat arbitrary. The calculations made in the present work used ρ , u , e and P , with the variables p , T and k_L determined from them by the equations of state and the absorption coefficient formulas.

3.3 Simplified Equilibrium Properties of Single-Ionized Argon

One of the major purposes of the computer program is to include real gas effects. To this end, the equilibrium state of the working fluid is needed. So far the working fluid has been argon although the limiting case of a perfect gas is also available in the computer program. This section will present the argon properties used. For other gases a similar approach can be easily implemented.

An ionizing monatomic gas like argon needs only one reaction coordinate, which is conveniently taken as the degree of ionization

$$\alpha = n_I / (n_I + n_A) . \quad (3.3.1)$$

We only consider singly ionized ions so that $n_I = n_E$. This limits the accuracy of the thermodynamic model somewhat. Reference 3.1 has a detailed calculation of argon equilibrium up to 5 atm, 35,000 K, including third ionization. It shows that the second ion becomes 1% of the number of atoms at 15,500 K at 0.1 atm and 19,400 K at 5 atm. This indicates the region in which the assumption of single ionization is valid.

The mass density of the gas is the sum of the masses of the atoms $n_A m_A$ and the ions $n_I m_A$, where we have neglected the electron mass and the difference between the ion and atom mass.

$$\rho = m_A (n_I + n_A) . \quad (3.3.2)$$

The number densities can then be expressed in terms of ρ and α as

$$n_I = \frac{\rho \alpha}{m_A} , \quad n_A = \frac{(1-\alpha) \rho}{m_A} . \quad (3.3.3)$$

The pressure is the sum of the partial pressures of the three species

$$\begin{aligned} P &= (n_A + n_I + n_E) kT = (n_A + 2n_I) kT \\ &= (1+\alpha) \rho RT , \quad R \equiv k/m_A \end{aligned} \quad (3.3.4)$$

where R is the atomic gas constant.

The composition α is found from the Law of Mass Action for ionization, the so-called Saha equation, which is

$$\frac{P_I P_E}{P_A} = \left(\frac{2\pi m_E}{h_P^2} \right)^{3/2} (kT)^{5/2} \frac{Q_{eI} Q_{eE}}{Q_{eA}} e^{-h_I^0 m_A / kT}$$

in terms of the partial pressures p_i , Planck's constant h_p , the ionization energy h_I^0 per unit mass, and the electronic partition functions Q_{eli} . In terms of the number densities, this is

$$\frac{n_I n_E}{n_A} = \frac{\beta T^{3/2}}{m_A} e^{-h_I^0 m_A / kT} \quad (3.3.5)$$

where

$$\beta \equiv m_A \left(\frac{2\pi m_E i}{h_p^2} \right)^{3/2} \frac{Q_{elI} Q_{elE}}{Q_{elA}} \quad (3.3.6)$$

When n_i is replaced by α from Eq. (3.3.3), the familiar Saha form appears as

$$\frac{\alpha^2}{1-\alpha} = \frac{\beta T^{3/2}}{\rho} e^{-T_I/T}, \quad T_I = \frac{h_I^0 m_A}{k} \quad (3.3.7)$$

The partition function of electrons is 2. Those of the atom and ion are more complicated, being sums over the energy states. The first terms are the ground state degeneracies

$$Q_{elA} = 1, \quad Q_{elI} = 6 \quad (3.3.8)$$

When these terms are used the partition function factor is 12 and $\beta = 1.94E-6$ in cgs units. The ionization temperature is 15.755 ev which gives $T_I = 182,837$ K. These constants lead to

$$\frac{\alpha^2}{1-\alpha} = 1.94E-6 \frac{T^{3/2}}{\rho} e^{-182,837/T} \quad (3.3.9)$$

This set of constants is approximate in that two effects are omitted: the effect of higher states in the atom and ion electronic partition function, and the lowering of the ionization potential due to the effect of the free

electrons on electrons bound in high energy levels of the atom. These two effects can be roughly taken into account by changing the constants in Eq. (3.3.9). In the calculations to be discussed later, the Saha equation was used in the form

$$\frac{\alpha^2}{1-\alpha} = 1.61E-6 \frac{T^{3/2}}{\rho} e^{-182,214/T} \equiv Y \quad (3.3.10)$$

Comparison with the elaborate calculations in Ref. 3.2 shows Eq. (3.3.10) to be accurate to better than 6% for 2 and 5 atm up to temperatures where second ion density becomes 1% of the atom density.

The combination of Eqs. (3.3.4) and (3.3.10) provide the thermal equation of state $p(\rho, T)$. The explicit expression of α as a function of ρ and T is the solution of the quadratic equation

$$\alpha^2 + Y\alpha - Y = 0,$$

where Y is the right side of Eq. (3.3.10). The appropriate solution is

$$\alpha = -Y/2 + (Y^2/4 + Y)^{1/2} \quad (3.3.11)$$

The caloric equation of state is obtained from summing the contributions to the internal energy of the various particles. The atoms contribute $3kT/2$ per particle, as do the electrons and ions. In addition, the ions carry the ionization energy per unit mass h_I° . Thus

$$pe = 3kT(n_I + n_A + n_E)/2 + n_I h_I^\circ m_A,$$

where e is the internal energy per unit mass. Then use of Eq. (3.3.3) shows that

$$e = 3RT(1+\alpha)/2 + \alpha h_I^\circ \quad (3.3.12)$$

The enthalpy per unit mass is found from the equation of state Eq. (3.3.4) as

$$h = e + p/\rho = 5 RT(1+\alpha)/2 + \alpha h_I^0 . \quad (3.3.13)$$

These two expressions provide the caloric equation of state as $e(\rho, T)$ when Eq. (3.3.11) is used for α .

Finally, the speed of sound is needed in the numerical integration to control the relation between the step size in x and t . The definition of the speed of sound for equilibrium is

$$a^2 = \left(\frac{\partial p}{\partial \rho} \right)_{\text{entropy}} .$$

By the use of standard thermodynamic derivatives this can be expressed as

$$a^2 = \left[\left(\frac{\partial \rho}{\partial p} \right)_T - \frac{1}{c_p T} \left(\frac{\partial \ln \rho}{\partial \ln T} \right)_p \right]^{-1} , \quad c_p = \left(\frac{\partial h}{\partial T} \right)_p . \quad (3.3.14)$$

From the equation of state Eq. (3.3.4), we find

$$\left(\frac{\partial \rho}{\partial p} \right)_T = \frac{\rho}{p} \left[1 - \left(\frac{\partial \ln(1+\alpha)}{\partial \ln \bar{p}} \right)_T \right] , \quad (3.3.15a)$$

$$\left(\frac{\partial \ln \rho}{\partial \ln T} \right)_p = -1 - \left(\frac{\partial \ln(1+\alpha)}{\partial \ln T} \right)_p , \quad (3.3.15b)$$

while c_p from Eq. (3.3.13) is

$$c_p = \frac{5}{2} R \left[1 + \alpha + \left(1 + \frac{2h_I^0}{5RT} \right) \left(\frac{\partial \alpha}{\partial \ln T} \right)_p \right] . \quad (3.3.16)$$

The derivatives of α are found by expressing Eq. (3.3.10) in terms of p and T , by replacing ρ by the equation of state, yielding

$$\frac{\alpha^2}{1-\alpha^2} = \frac{f(T)}{p}, \quad f = CT^{5/2} e^{-182214/T}, \quad C = 1.64E-6R \quad (3.3.17a)$$

or

$$\alpha = (1 + p/f)^{-1/2} . \quad (3.3.17b)$$

Differentiation of this, and use of Eq. (3.3.17a) gives

$$\left(\frac{\partial \ln(1+\alpha)}{\partial \ln p} \right)_T = \frac{-\alpha(1-\alpha)}{2} \quad (3.3.18a)$$

$$\left(\frac{\partial \ln(1+\alpha)}{\partial \ln T} \right)_p = \frac{\alpha(1-\alpha)}{2} \left(\frac{5}{2} + \frac{h_I^0}{RT} \right) \quad (3.3.18b)$$

$$\left(\frac{\partial \alpha}{\partial \ln T} \right)_p = \frac{\alpha(1-\alpha^2)}{2} \left(\frac{5}{2} + \frac{h_I^0}{RT} \right) . \quad (3.3.18c)$$

Using the latter derivative, c_p from Eq. (3.3.16) becomes

$$c_p = \frac{5}{2} R (1+\alpha) \left[1 + \frac{\alpha(1-\alpha)}{2} \frac{2}{5} \left(\frac{5}{2} + \frac{h_I^0}{RT} \right)^2 \right] . \quad (3.3.19)$$

Substituting the first two derivatives into Eqs. (3.3.15), and those into Eq. (3.3.14) together with c_p , we finally find for the speed of sound

$$a^2 = G p/\rho = G(1+\alpha)RT \quad (3.3.20a)$$

where

$$\frac{1}{G} = 1 + \frac{\alpha(1-\alpha)}{2} - \frac{\frac{2}{5} \left[1 + \frac{\alpha(1-\alpha)}{2} \left(\frac{5}{2} + \frac{h_I^o}{RT} \right) \right]^2}{1 + \frac{\alpha(1-\alpha)}{2} \frac{2}{5} \left(\frac{5}{2} + \frac{h_I^o}{RT} \right)^2} \quad (3.3.20b)$$

The quantity G replaces the specific heat ratio γ in the perfect gas speed of sound. We note that for a perfect gas, $\alpha = 0$, Eq. (3.3.20b) reduces to

$$\frac{1}{G} = 1 - \frac{2}{5} = \frac{3}{5} ,$$

so that $G = 5/3$, the correct value of the specific heat ratio for a monatomic perfect gas like argon.

3.4 Absorption Coefficient for Singly-Ionized Argon

The laser energy absorption coefficient k_L depends on the absorption mechanism by which the working fluid absorbs laser energy. For the present case of pulsed laser propulsion, with gases such as argon, absorption is by inverse Bremsstrahlung, depending on interactions between electrons and neutrals or electrons and ions. The electrons are initially produced by gas breakdown at the focus of the laser near the nozzle throat.

The absorption coefficient then is the sum of the electron-neutral and electron-ion contribution.

$$k_L = k_{LEN} + k_{LEI} \quad (3.4.1)$$

The electron-ion contribution is the classical Kramers radiation, whose absorption coefficient at any frequency ν is

$$k_\nu = \sigma_{EI} n_E n_I e^{\frac{h_p \nu}{kT}} \left(1 - e^{-\frac{h_p \nu}{kT}} \right) \quad (3.4.2)$$

including stimulated emission. The cross-section is

$$\begin{aligned}\sigma_{EI} &= \frac{4}{3} \left(\frac{2\pi}{3m_E kT} \right)^{1/2} \frac{z^2 e^6}{h_p c m_E v^3} \\ &= 3.69E8/T^{1/2} v^3 \text{ (cm}^5\text{)}\end{aligned}$$

where $Z = 1$ is the charge and e the unit charge. The frequency is related to wavelength by $\nu = c/\lambda$, and for $\lambda = 10.6 \mu\text{m}$ ($10.6E-4 \text{ cm}$) the cross-section becomes

$$\sigma_{EI} = 1.63E-32/T^{1/2} \quad (3.4.3)$$

The number densities can be written in terms of ρ and α from Eq. (3.3.3), which introduces a factor m_A in the denominator. For argon, $m_A = 6.685E-23 \text{ g}$ so Eq. (3.4.2) becomes

$$k_{LEI} = 3.65E12 \frac{\rho^2 \alpha^2}{T^{1/2}} \left(e^{1357/T} - 1 \right) \quad (3.4.4)$$

where we have used $h_p \nu/k = h_p c/\lambda k = 1357$.

This result does not include quantum-mechanical effects, which are usually approximated by a so-called Gaunt factor applied to k_{LEI} . For the temperature range of interest, a Gaunt factor of 1.6 is an average value. When this is applied to Eq. (3.4.4), the final expression for absorption of $10.6 \mu\text{m}$ radiation by electron-ion interaction is

$$k_{LEI} = 5.84E12 \frac{\rho^2 \alpha^2}{T^{1/2}} \left(e^{1357/T} - 1 \right) \quad (3.4.5)$$

The electron-neutral contribution has the form

$$k_\nu = \sigma_{EN} n_E n_A \left(1 - e^{-h_p \nu/kT} \right) \quad (3.4.6)$$

which again includes stimulated emission. The cross-section is taken from Eq. (5.57) of Ref. 3.2, which is

$$\sigma_{EN} = \frac{e^2 \sigma_{tr}(E)}{m_E e v^2} \left(\frac{2E}{m_E} \right)^{1/2} \frac{2}{3} \frac{E}{h_p v} \left(1 + \frac{h_p v}{E} \right)^2 \frac{\sigma_{tr}(E + h_p v)}{\sigma_{tr}(E)}$$

We ignore the difference between the transport scattering cross-section σ_{tr} at E and $E + h_p v$, and replace E by kT and v by c/λ . Then the electron-neutral cross-section is

$$\sigma_{EN} = 9.09E-28 \sigma_{tr} T^{3/2} \left(1 + \frac{h_p c}{\lambda kT} \right)^2 \quad (3.4.7)$$

By using n_A and $n_E = n_I$ from Eq. (3.3.3), and including the factor m_A^2 in the constant we find for $\lambda = 10.6 \mu\text{m}$ that Eq. (3.4.6) becomes

$$k_{LEN} = 2.04E17 \sigma_{tr} \rho^2 \alpha(1-\alpha) T^{3/2} \times \left(1 + \frac{1357}{T} \right)^2 \left(1 - e^{-1357/T} \right) \quad (3.4.8)$$

Finally, the cross-section σ_{tr} is taken from the work reported in Ref. 3.4. The authors kindly supplied a table for argon, which is reproduced in Table 3.1.

The total absorption coefficient of argon is then the sum of Eqs. (3.4.5) and (3.4.8) according to Eq. (3.4.1).

3.5 Steady Flow in Nozzle

The starting condition for single pulse laser propulsion is steady flow in the nozzle. The equations for isentropic flow of a perfect gas in a nozzle of given area distribution $A(x)$ are well-known. It is convenient to specify them in terms of the stagnation conditions in the chamber which feeds the nozzle, as defined by the stagnation pressure and temperature p_{st} and T_{st} .

TABLE 3.1

 TRANSPORT SCATTERING CROSS-SECTION FOR
 ELECTRON-NEUTRAL COLLISIONS IN ARGON

T(eV)	$\sigma_{tr} \times 10^{16} (\text{cm}^2)$	T(eV)	$\sigma_{tr} \times 10^{16} (\text{cm}^2)$
0.0	8.05	0.65	0.470
0.01	6.10	0.8	0.68
0.02	3.74	1.0	1.05
0.03	2.80	1.5	1.74
0.04	2.29	2.0	2.48
0.05	1.84	3.0	4.07
0.07	1.14	4.0	5.8
0.09	0.56	6.0	8.7
0.11	0.342	8.0	11.7
0.14	0.235	10.0	13.8
0.17	0.196	12.0	14.5
0.20	0.177	15.0	13.2
0.25	0.156	20.0	10.4
0.35	0.151	26.0	8.3
0.40	0.182	30.0	7.2
0.50	0.283		

The density is found from the gas law:

$$\rho_{st} = p_{st} / RT_{st} \quad (3.5.1)$$

The internal energy and enthalpy are

$$e_{st} = c_v T_{st}, \quad h_{st} = e_{st} + p_{st} / \rho_{st} \quad (3.5.2)$$

A convenient reference speed is the limiting speed at which the stagnation enthalpy is converted completely to velocity.

$$u_\ell = (2h_{st})^{1/2} = (2c_p T_{st})^{1/2} \quad (3.5.3)$$

The usual isentropic relations for a perfect gas with specific heat ratio γ are

$$\frac{\rho_{st}}{\rho} = \left(1 + \frac{\gamma-1}{2} M^2\right)^{1/(\gamma-1)}, \quad \frac{p_{st}}{p} = \left(1 + \frac{\gamma-1}{2} M^2\right)^{\gamma/(\gamma-1)} \quad (3.5.4)$$

where M is the Mach number.

To find the mass flow we use the mass conservation equation evaluated at the sonic condition (throat) $M = 1$. Denoting quantities at this state by a superscript $*$, we have

$$\dot{m} = \rho^* u^* A^* \quad (3.5.5)$$

The density is found from Eq. (3.5.4) as

$$\rho^* = \left(\rho_{st} \frac{2}{\gamma+1}\right)^{1/(\gamma-1)}$$

The speed is found from the energy conservation equation as

$$\frac{1}{2} u_\ell^2 = c_p T^* + \frac{1}{2} u^{*2} + \frac{1}{2} u^{*2} = \frac{u^{*2}}{\gamma-1} + \frac{u^{*2}}{2}$$

$$u^* = u_\ell \left(\frac{\gamma-1}{\gamma+1} \right)^{1/2}$$

so that the mass flow rate is

$$\dot{m} = \rho_{st} u^* A^* \left(\frac{2}{\gamma+1} \right)^{1/(\gamma-1)} \left(\frac{\gamma-1}{\gamma+1} \right)^{1/2}$$

A more convenient form in terms of p_{st} is obtained by using (3.5.1) and (3.5.3) to eliminate ρ_{st} and T_{st} , giving

$$\dot{m} = \frac{p_{st} A^*}{u_\ell} \gamma \left(\frac{2}{\gamma-1} \right)^{1/2} \left(\frac{2}{\gamma+1} \right)^{(\gamma+1)/2(\gamma-1)} \quad (3.5.6)$$

To find the distribution of properties along the nozzle one needs the Mach number distribution. This can be related to the area distribution by the well-known relation

$$\left(\frac{A}{A^*} \right)^2 = \frac{1}{M^2} \left[\frac{2}{\gamma+1} \left(1 + \frac{\gamma-1}{2} M^2 \right) \right]^{(\gamma+1)/(\gamma-1)}$$

For a given $A(x)$, this can be solved (iteratively) for $M(x)$. Then all other properties follow. The density and pressure have already been given in Eqs. (3.5.4). The temperature and internal energy are found from the energy conservation equation as

$$\frac{T_{st}}{T} = 1 + \frac{\gamma-1}{2} M^2, \quad e = c_v T \quad (3.5.7)$$

This same conservation equation gives the velocity, using Eqs. (3.5.3) and (3.5.7), as

$$u^2 = 2c_p (T_{st} - T) = u_\ell^2 \left[1 + \left(\frac{\gamma-1}{2} M^2 \right)^{-1} \right]^{-1} \quad (3.5.8)$$

These relations completely specify the steady flow in a nozzle of given shape $A(x)$ when the stagnation pressure and temperature are given, and provide the starting conditions for the laser-driven wave pulse.

3.6 One-Dimensional LSD Wave

The pulsed laser propulsion scheme discussed in this report drives a laser-supported detonation (LSD) wave down the nozzle. This wave is analogous to an ordinary shock wave, but in addition includes the absorption of laser-energy into the gas. It is useful to consider the jump conditions which can be reached by absorbing energy, as well as to provide a simple case for verifying the correctness and accuracy of the computer program constructed to solve the equations of motion presented in Section 3.2.

We will therefore look at the jump conditions across an LSD wave in the same way the jump conditions across ordinary shock wave are studied. If we consider a stationary LSD wave with conditions $()_1$ in front and conditions $()_2$ in back, the usual conservation of mass and momentum hold:

$$\rho_1 v_1 = \rho_2 v_2 \quad (3.6.1)$$

$$p_1 + \rho_1 v_1^2 = p_2 + \rho_2 v_2^2 \quad (3.6.2)$$

Here we have used v for velocity because we are using a steady coordinate system which differs from the laboratory-fixed system in which the non-steady flow occurs. The relation between u in the laboratory system and v in the steady wave-fixed system is

$$|v| = u_s - u \quad (3.6.3)$$

where u_s is the velocity of the wave in the laboratory system.

From Eq. (3.6.1) we find

$$v_1 = \frac{\rho_2 v_2}{\rho_1}, \quad u_s = \frac{u_2 - \rho_1 u_1 / \rho_2}{1 - \rho_1 / \rho_2} \quad (3.6.4)$$

while from Eq. (3.6.2), using Eq. (3.6.1) we have

$$v_1^2 = (u_s - u_1)^2 = \frac{P_2 - P_1}{\rho_1(1 - \rho_1/\rho_2)} \quad (3.6.5)$$

The energy conservation equation includes contributions from gas enthalpy h , kinetic energy $v^2/2$ and the laser intensity I (power per unit area):

$$I_1/\rho_1 v_1 + h_1 + v_1^2/2 = I_2/\rho_2 v_2 + h_2 + v_2^2/2 \quad (3.6.6)$$

By using Eq. (3.6.1), this can be written

$$v_1^2 = \frac{h_2 - h_1 - \Delta I/\rho_1 v_1}{(1 - \rho_1^2/\rho_2^2)/2} \quad (3.6.7a)$$

$$(u_s - u_1)^2 = \frac{h_2 - h_1 - \Delta I/\rho_1 (u_s - u_1)}{(1 - \rho_1^2/\rho_2^2)/2} \quad (3.6.7b)$$

where the change in intensity is defined as

$$\Delta I = I_1 - I_2 \quad (3.6.8)$$

If the laser energy is fully absorbed, $\Delta I = I_1$, but we will also be interested in cases of partial absorption, where $I_2 \neq 0$.

To the three conservation equations must be added the equations of state, which for the present case of argon is given in Eqs. (3.3.4) and (3.3.13) as

$$p = (1+\alpha)\rho RT \quad (3.6.9a)$$

$$h = 5RT(1+\alpha)/2 + \alpha h_I^0 \quad (3.6.9b)$$

where α is given by the Saha relation, used in the form Eq. (3.3.17).

The solution of these jump conditions provides the state behind the LSD wave when the state in front is given, including the amount of laser energy absorbed, ΔI . As in an ordinary shock wave, the speed of the incoming flow must be specified, which is equivalent to specifying the shock speed. However, in the laser propulsion application, this speed is not known. The situation is completely analogous to combustion waves, where the chemical heat release takes the place of the laser energy absorbed, and an additional condition is required to specify the wave speed. In combustion wave theory, this added condition is the Chapman-Jouquet (CJ) condition that the speed behind the wave is equal to the sound speed there, so that disturbances cannot catch the wave from behind. This condition can be applied to LSD waves for the same reason, and serves to determine the inflow speed v_1 , or the shock speed u_s in the laboratory system $u_s = |v_1| + u_1$, if the flow speed in front, u_1 , is known in that system.

Although for a perfect gas ($\alpha = 0$) the solution can be obtained algebraically, for a real gas it must be found iteratively. A convenient method is as follows: Eliminate $v_1^2(1 - \rho_1/\rho_2)$ between momentum conservation Eq. (3.6.5) and energy conservation Eq. (3.6.7a). Then use the thermal equation of state Eq. (3.6.9a) to eliminate p_2 . The result is a quadratic equation for ρ_2/ρ_1 :

$$A \left(\frac{\rho_2}{\rho_1} \right)^2 + B \frac{\rho_2}{\rho_1} + C = 0$$

$$A = (1 + \alpha_2) RT_2, \quad C = -p_1/\rho_1$$

$$B = (1 + \alpha_2) RT_2 - p_1/\rho_1 - 2(h_2 - h_1 - \Delta I/\rho_1 v_1)$$

The appropriate solution is

$$\frac{\rho_2}{\rho_1} = -\frac{B}{2A} + \left[\left(\frac{B}{2A} \right)^2 - \frac{C}{A} \right]^{1/2} \quad (3.6.10)$$

where the sign of the radical is determined from the ordinary shock case
 $\alpha = \Delta I = 0$.

The solution procedure is to assume

$$p_1, T_1, T_2 \text{ and } I_1/v_1 \text{ with } I_2 = 0$$

and calculate all ()₁ thermodynamic quantities.

Then we guess p_2 , find α_2 and h_2 from Eqs. (3.3.17a) and Eq. (3.6.9b), find ρ_2 from Eq. (3.6.10), and use it to find p_2 from Eq. (3.6.9a). We iterate on p_2 until the guessed value equals the computed value. Then v_1 can be found from Eq. (3.6.5) and I_1 from the assumed value of I_1/v_1 . This gives an LSD wave for the assumed value of T_2 and I_1/v_1 which has v_2 from Eq. (3.6.4) and a speed of sound a_2 from Eq. (3.3.20). It will not necessarily satisfy the CJ condition. We can then iterate on either T_2 or I_1/v_1 to find a solution which has $v_2 = a_2$.

A computer program to find LSD waves satisfying the CJ condition has been written following this procedure, and the iterations can be made to converge satisfactorily.

For a perfect gas, the solution can be accomplished algebraically. For that purpose we use Eq. (3.6.9b) in the form ($\alpha = 0$)

$$h = \gamma p / (\gamma - 1) \rho$$

in Eq. (3.6.7a) and substitute for p_2 from Eq. (3.6.5). This leads to the quadratic for the density ratio in the form

$$\frac{\gamma-1}{\gamma} \left[\frac{1}{2} + \frac{\Delta I}{\rho_1 v_1^3} + \frac{\gamma}{\gamma-1} \frac{p_1}{\rho_1 v_1^2} \right] \left(\frac{\rho_2}{\rho_1} \right)^2 - \frac{\rho_2}{\rho_1} \left(1 + \frac{\rho_1}{\rho_1 v_1^2} \right) + \frac{\gamma+1}{2\gamma} = 0 \quad (3.6.11)$$

The CJ condition can be written, using the perfect gas form of the speed of sound and Eqs. (3.6.4) and Eq. (3.6.5), as

$$a_2^2 = \frac{\gamma p_2}{\rho_2} = \frac{\gamma}{\rho_2} \left[p_1 + \rho_1 v_1^2 \left(1 - \frac{\rho_1}{\rho_2} \right) \right] = v_2^2 = \frac{v_1^2 \rho_1^2}{\rho_2^2}$$

Solving for ρ_2/ρ_1 gives

$$\frac{\rho_2}{\rho_1} = \frac{\gamma^{-1} + 1}{1 + p_1/\rho_1 v_1^2}$$

If this is used to eliminate ρ_2/ρ_1 in Eq. (3.6.11) the result is

$$\frac{\Delta I}{\rho_1 v_1^3} = \frac{1}{2} \frac{1}{\gamma^2 - 1} \left(\frac{1}{1 - M_1^{-2}} \right)^2$$

where $M_1 = v_1^2/(\gamma p_1/\rho_1)$ is the wave Mach number. For high speed waves, $M_1 \gg 1$, the last term is unity and the wave speed v_1 is found to be

$$v_1 = \left[2I_1(\gamma^2 - 1)/\rho_1 \right]^{1/3} \quad (3.6.12)$$

This is the result found by Raizer in Ref. 3.5 for hypersonic LSD waves in a perfect gas, showing that the speed varies as the cube root of the absorbed laser power.

The procedure outlined above will find the jump conditions across an LSD wave for given gas properties in front, and given T_2 or I_1/v_1 . It can also be used to find the state of the gas in the LSD wave after only a portion of the laser energy is absorbed. For this purpose, we treat the state $()_2$ as an intermediate state where only part of the laser power, ΔI , has been absorbed. But the wave speed v_1 is already found under the condition that all the laser power I_1 has been absorbed. Thus we can use the procedure outlined above for given values of ΔI and v_1 to specify $\Delta I/v_1$ and iterate on T_2 until the correct known value of v_1 is obtained. If we do this for a range of values of ΔI from 0 to I_1 , we can find a kind of structure of the LSD wave as a function of absorbed power. Notice that the

solution for the value $\Delta I = 0$ is an ordinary shock wave travelling at the LSD wave speed, before any power has been absorbed.

A number of LSD wave solutions in real argon have been found. Figure 3.1 shows a plot of T_2 and wave speed $v_1 = v_{\text{LSD}}$ vs laser intensity I_1 . The initial state is $p_1 = 1$ atm, $T_1 = 300$ K. The wave speeds are lower than the perfect gas argon speed from Eq. (3.6.12), also shown, but the dependence is close to $I_1^{1/3}$ since the two speed curves are nearly parallel. The reduction in speed is a result of energy going into internal degrees of freedom rather than into driving the wave; i.e., γ is lower than 5/3 in Eq. (3.6.12). The temperatures are quite high, reaching about 18,500 K at 10 MW/cm². The structure of one of these waves is shown in Fig. 3.2 as a function of the percent of the laser energy absorbed. The initial ordinary shock wave produces large jumps in p and ρ_1 which then decay as the wave absorbs energy. The temperature continues to increase, however, reaching a very slight peak near the back of the wave before decreasing to its final value. We expect this same behavior in the waves driven down the nozzle in the nozzle in the unsteady laser propulsion case.

3.7 Similarity Variables

One of the purposes for solving for the flow in the nozzle is to aid in the interpretation of the experimental data. Measurements of the arrival of the LSD wave pressure pulse at stations near the end of the nozzle are being used to infer the energy put into the gas by the laser. The flow solutions trace the time history of the LSD wave location for a given laser power. If we can extract from the flow solutions a simple relation between laser energy and arrival of the shock at the measuring station, we can infer the energy put into the gas in a particular experimental shot. In other words, we need a method for correlating the $x-t$ trace of the wave location as a function of the controlling physical variables.

A useful guide to such a correlation is found in the similarity solutions for blast waves in hypersonic tunnels, Ref. 3.6, by Mirels and

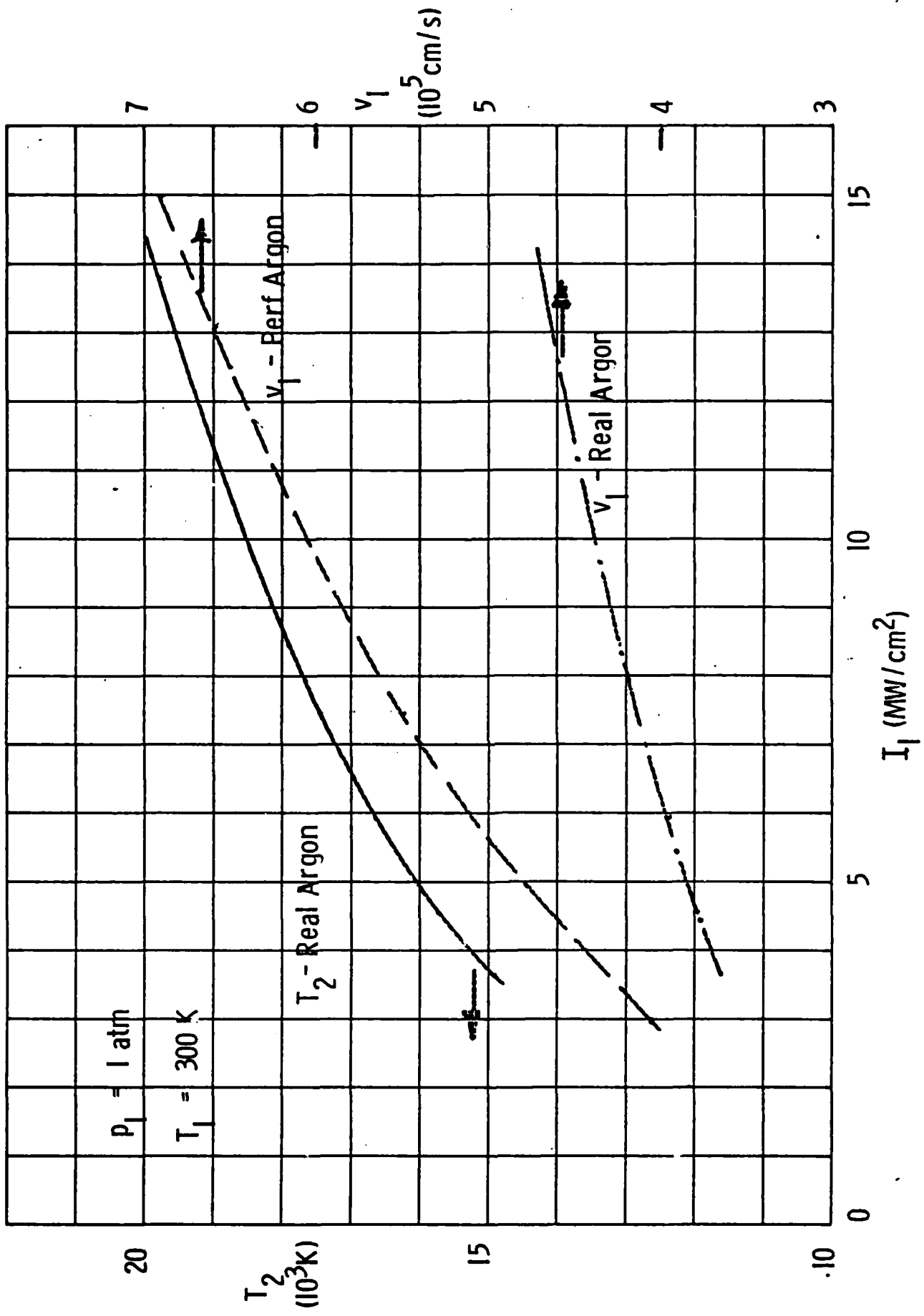


Fig. 3.1 Dependence on initial laser intensity I_1 of LSD wave velocity and temperature behind LSD wave. Perfect and real argon.

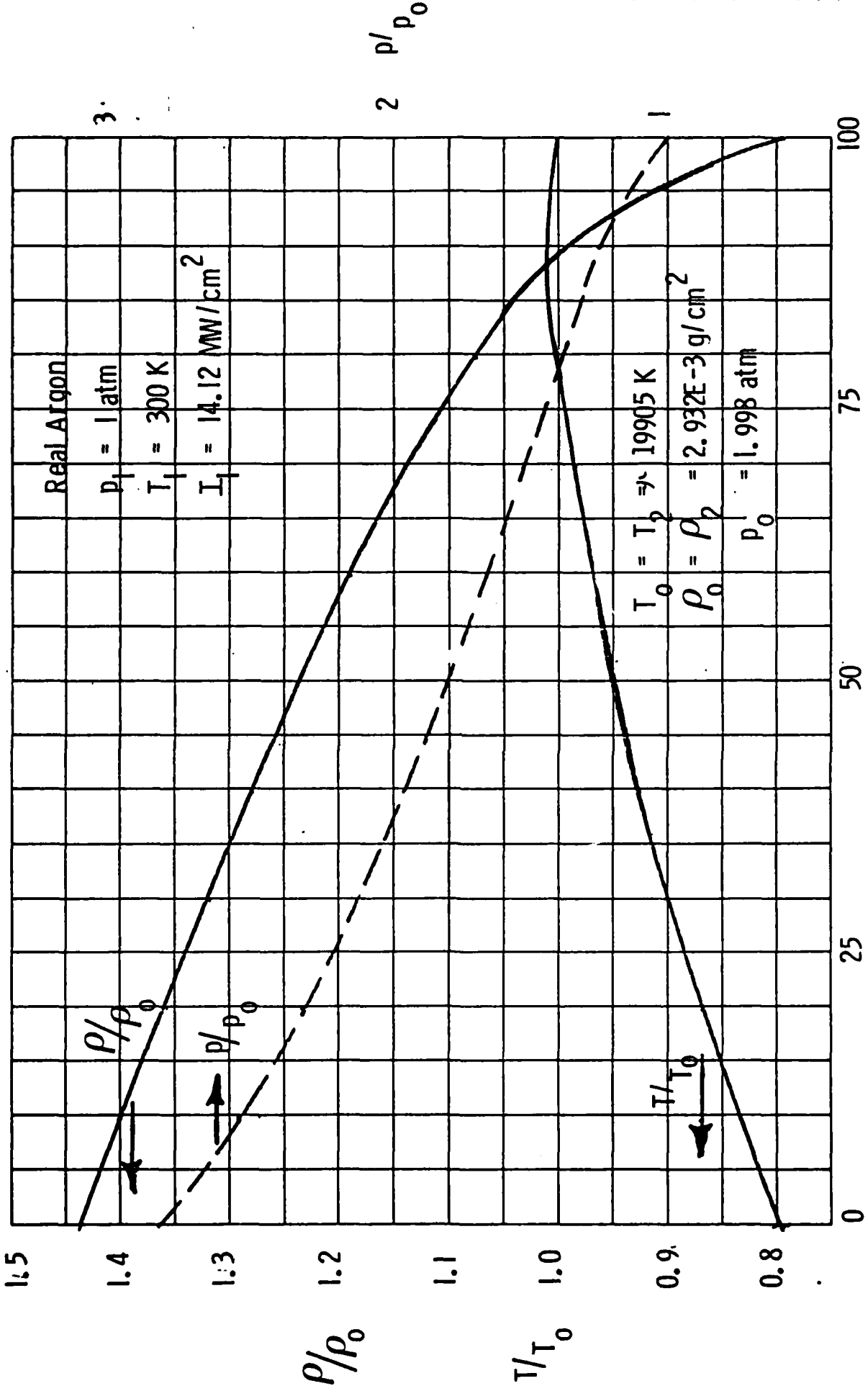


Fig. 3.2 Structure of LSD wave as a function of percent of laser energy absorbed. Real argon.

Mullen, and in the previous work on fluid mechanics in the present program, Ref. 3.1, by Simons and Pirri. In these studies, solutions were obtained for the hypersonic flow in a nozzle generated by an instantaneous deposition of energy just downstream of the throat. The flow equations are the present Eqs. (3.2.1) and (3.2.2), plus the condition of isentropic flow behind the shock wave, which replaces the energy conservation relation, Eq. (3.2.3), because the laser energy is assumed to be all absorbed instantaneously at time zero. A perfect gas (constant γ) is assumed. The jump conditions across the blast wave (an ordinary hypersonic shock wave) are the usual Rankine-Hugoniot equations in the limit of high shock Mach number.

The geometry of the nozzle is taken to be a power law variation of A with x , i.e.,

$$A(x) = \delta x^\sigma . \quad (3.7.1)$$

For a conical nozzle, $\sigma = 2$, and for a parabolic nozzle, $\sigma = 1$, for example. Both cases were considered in Ref. 3.6, while only the cone was considered in Ref. 3.1.

The problem as formulated above has a similarity solution in terms of only one independent variable x/x_s , where x_s is the position of the shock wave, given by

$$x_s = Ct^{2/3} , \quad c = \left(\frac{9}{4I_b} \frac{Eu_\ell}{\dot{m}} \right)^{1/3} \quad (3.7.2)$$

where E is the energy deposited to create the blast wave, and u_ℓ and \dot{m} are the limiting velocity and mass flow rate of the flow in the nozzle before the blast is set off, as introduced in Section 3.5. The quantity I_b is a function only of γ and σ , the gas properties and nozzle shape.

For a given nozzle shape and gas, then, the shock trajectory depends only on the energy deposited, E and the ratio \dot{m}/u_ℓ . This latter ratio characterizes the mass in the nozzle up to x_s , because the continuity equation for the nozzle flow before the blast is $\dot{m} = \rho u A$. But $u = u_\ell$ in the hypersonic flow approximation so $\rho A = \dot{m}/u_\ell$, a constant.

A dimensionless form of the shock trajectory equation can be found by dividing Eq. (3.7.2) by $E/\dot{m}u_\ell$. The result is

$$\xi_s = \left(9/4I_b\right)^{1/3} \tau^{2/3} \quad (3.7.3)$$

where the dimensionless distance and time variables are

$$\xi = x/(E/\dot{m}u_\ell) , \quad \tau = t/(E/\dot{m}u_\ell^2) . \quad (3.7.4)$$

In this similarity variable form, the shock wave trajectory depends only on γ and σ , but not on E , \dot{m} or u_ℓ , which is to say, not on the stagnation conditions or energy deposited, but only on the gas and the nozzle shape.

The calculations performed in the present work include real gas effects in argon, and make no assumption of hypersonic flow. They also have different initial conditions than this ideal blast wave theory, which assumes all the energy is put into a point of zero volume. Nevertheless, it proved possible to correlate the computed shock trajectories by use of the variables ξ and τ defined above, for different values of E and \dot{m} , as we shall see in Section 3.9.

An approximate correction to the shock trajectory to account for the flow speed in the nozzle ahead of the shock can be made. We can assume that the shock moves relative to the flow rather than relative to the walls. Over most of the nozzle the flow speed is nearly u_ℓ , so to account for the flow we can re-write Eq. (3.7.2) as

$$x_s = u_\ell t + Ct^{2/3} . \quad (3.7.5)$$

In the similarity variables of Eq. (3.7.4) this is

$$\xi_s = \tau + \left(9/4I_b\right)^{1/3} \tau^{2/3} . \quad (3.7.6)$$

This shows that for small τ , which means small t , large E , small \dot{m} or small u_ℓ , the ideal blast wave theory dominates, the first term being small.

However, for large τ , which means large t , small E , large m or large u_0 , the corrective term τ dominates. The shock is weak and just drifts along at nearly the flow speed u_0 . In a nozzle with expanding area the shock weakens continuously, and eventually the τ term will dominate. Of course, Eq. (3.7.6) is an ad hoc correction, rather than an exact result, but it gives the correct limits and should be a correct guide to what we expect from the computed results.

3.8 Numerical Method

The method for solving the partial differential equations (3.2.1 - 3.2.4) that we chose is a so-called "shock-capturing" method, in which the conservation form of the equations is represented in finite difference form in such a way that shock waves are generated automatically, with a thickness of a few mesh points in x . There are a number of such finite difference schemes, of varying degrees of complexity, with accuracy usually increasing with the complexity. We have chosen to use one of the simplest ones, known as the Lax method, and first set forth in Ref. 3.7.

In one space dimension, the Lax method deals with an equation of the form

$$\frac{\partial w}{\partial t} + \frac{\partial F(w)}{\partial x} = S .$$

The space derivative is represented by a first central difference

$$\left(\frac{\partial F}{\partial x}\right)_i = (F_{i+1} - F_{i-1})/2\Delta x \quad (3.8.1)$$

where the subscript denotes the value at the x location. The source term S is represented similarly by

$$s_i = \frac{1}{2}[s_{i+1} + s_{i-1}] . \quad (3.8.2)$$

Finally, the time derivative is represented as

$$\left(\frac{\partial w}{\partial t}\right)_i = (w_i^{n+1} - w_i^n)/\Delta t$$

where the superscript is the time location, and

$$\bar{w}_i^n = \left(w_{i+1}^n + w_{i-1}^n \right) / 2 = w_i^n + \left(w_{i+1}^n - 2w_i^n + w_{i-1}^n \right) / 2 .$$

The use of \bar{w}_i^n instead of w_i^n in the time derivative introduces a viscosity-like dissipation term which enables the shock-capturing to occur. This can be seen by writing out the time derivative in detail as

$$(\partial w / \partial t)_i = \left(w_i^{n+1} - w_i^n \right) / \Delta t - \left(w_{i+1}^n - 2w_i^n + w_{i-1}^n \right) / 2\Delta t .$$

The second term is a central difference representation of $\partial^2 w / \partial x^2$ times $(\Delta x)^2 / \Delta t$. Such a term would arise from a viscous-like dissipation term with "viscosity" $(\Delta x)^2 / \Delta t$, so we expect the diffusion of the shock over several mesh points to depend on this ratio.

All the terms in Eqs. (3.2.1) - (3.2.3) are of the form of one of the three terms in Eqs. (3.8.1) - (3.8.3) so they can be written in finite difference form. Eq. (3.2.1) becomes

$$\begin{aligned} & \left[A_i \rho_i^{n+1} - \left(A_{i+1} \rho_{i+1} + A_{i-1} \rho_{i-1} \right) / 2 \right] / \Delta t \\ & + \left[A_{i+1} \rho_{i+1}^n u_{i+1}^n - A_{i-1} \rho_{i-1}^n u_{i-1}^n \right] / 2\Delta x = 0 \end{aligned}$$

while Eq. (3.2.2) is

$$\begin{aligned} & \left[A_i \rho_i^{n+1} u_i^{n+1} - \left(A_{i+1} \rho_{i+1}^n u_{i+1}^n + A_{i-1} \rho_{i-1}^n u_{i-1}^n \right) / 2 \right] / \Delta t \\ & + \left[A_{i+1} \left(p_{i+1}^n + \rho_{i+1}^n u_{i+1}^{n2} \right) - A_{i-1} \left(p_{i-1}^n + \rho_{i-1}^n u_{i-1}^{n2} \right) \right] / 2\Delta x \\ & = \left[\left(dA/dx \right)_{i+1} p_{i+1}^n + \left(dA/dx \right)_{i-1} p_{i-1}^n \right] / 2 . \end{aligned}$$

The first of these can be solved for ρ_i^{n+1} as

$$\rho_i^{n+1} = \left(A_{i+1} \rho_{i+1}^n + A_{i-1} \rho_{i-1}^n \right) / 2A_i$$

$$- \left[A_{i+1} \rho_{i+1}^n u_{i+1}^n - A_{i-1} \rho_{i-1}^n u_{i-1}^n \right] \Delta t / 2\Delta x A_i \quad (3.8.4)$$

while the second can be solved for u_i^{n+1} as

$$u_i^{n+1} = \left(A_{i+1} \rho_{i+1}^n u_{i+1}^n + A_{i-1} \rho_{i-1}^n u_{i-1}^n \right) / 2A_i \rho_i^{n+1}$$

$$- \left[A_{i+1} \left(p_{i+1}^n + \rho_{i+1}^n u_{i+1}^{n2} \right) - A_{i-1} \left(p_{i-1}^n + \rho_{i-1}^n u_{i-1}^{n2} \right) \right] \Delta t / 2\Delta x A_i \rho_i^{n+1}$$

$$+ \left[\left(dA/dx \right)_{i+1} p_{i+1}^n + \left(dA/dx \right)_{i-1} p_{i-1}^n \right] \Delta t / 2A_i \rho_i^{n+1} \quad (3.8.5)$$

These equations enable us to advance ρ and u by one time step if all conditions are known at the previous time step.

The energy equation can be treated similarly. The term on the right is the laser heat addition term, and can be treated in several ways. We have chosen to write it as a derivative according to Eq. (3.8.1) so that Eq. (3.2.2) is

$$\left\{ A_i \rho_i^{n+1} \left(e_i^{n+1} + \left(u_i^{n+1} \right)^2 / 2 \right) - \left[A_{i+1} \rho_{i+1}^n \left(e_{i+1}^n + u_{i+1}^{n2} / 2 \right) \right. \right.$$

$$\left. \left. + A_{i-1} \rho_{i-1}^n \left(e_{i-1}^n + u_{i-1}^{n2} / 2 \right) \right] / 2 \right\} / \Delta t$$

$$+ \left[A_{i+1} \rho_{i+1}^n \left(e_{i+1}^n + p_{i+1}^n / \rho_{i+1}^n + u_{i+1}^{n2} / 2 \right) \right.$$

$$\left. - A_{i-1} \rho_{i-1}^n u_{i-1}^n \left(e_{i-1}^n + p_{i-1}^n / \rho_{i-1}^n + u_{i-1}^{n2} / 2 \right) \right] / 2\Delta x$$

$$= \left(p_{i+1}^n - p_{i-1}^n \right) / 2\Delta x \quad .$$

This is solved for e_i^{n+1} as

$$\begin{aligned}
e_i^{n+1} = & -\left(u_i^{n+1}\right)^2 / 2 + \left(P_{i+1}^n - P_{i-1}^n\right) \Delta t / 2 \Delta x A_i \rho_i^{n+1} \\
& + \left[A_{i+1} \rho_{i+1}^n \left(e_{i+1}^n + u_{i+1}^{n2} / 2 \right) + A_{i-1} \rho_{i-1}^n \left(e_{i-1}^n + u_{i-1}^{n2} / 2 \right) \right] / 2 A_i \rho_i^{n+1} \\
& - \left[A_{i+1} \rho_{i+1}^n u_{i+1}^n \left(e_{i+1}^n + P_{i+1}^n / \rho_{i+1}^n + u_{i+1}^{n2} / 2 \right) \right. \\
& \left. - A_{i-1} \rho_{i-1}^n u_{i-1}^n \left(e_{i-1}^n + P_{i-1}^n / \rho_{i-1}^n + u_{i-1}^{n2} / 2 \right) \right] \Delta t / 2 \Delta x A_i \rho_i^{n+1}. \quad (3.8.6)
\end{aligned}$$

We can now advance e by one time step.

With e and ρ known, the thermodynamic relations of Section 3.3 now enable us to find α , T and p , completely defining the state of the gas at time t_{n+1} at x_i . The remaining variable which must be advanced is the laser power P , which is found from Eq. (3.2.5). This can be written in the form

$$P_{i-1} = P_i \exp\left(-\int_{x_{i-1}}^{x_i} k_L dx\right)$$

whose finite difference expression is

$$P_{i-1} = P_i \exp\left[-\left(k_{Li} + k_{Li-1}\right) \Delta x / 2\right]. \quad (3.8.7)$$

Once the thermodynamic properties of the gas are known at t_{n+1} , the expressions in Section 3.4 define k_L at that time. Then the field of $P(x)$ can be determined from Eq. (3.8.7), beginning at an x station greater than the current shock position, where $P = P_0$, the incoming laser power, and moving toward $x = 0$ by successively reducing i . Notice that P_0 can be a function of time if the laser power varies with time. Changes of P with time propagate with the speed of light, which is instantaneously on the time scale of the flow, so that such changes are accomplished merely by starting the difference equation (3.8.7) with the value of P_0 at the new time.

We have now described the relations used to specify the variables at each point in space and time. To advance a step in time the finite difference expressions for ρ , u and e must be swept simultaneously through the range of x from $x = 0$ to a value $x = x_f$ which the shock wave has not yet reached, so the values there are still the initial conditions. This gives a criteria for stopping the x integration. Then Eq. (3.8.7) for P is swept backwards from x_f to $x = 0$, using $P_0(t)$ as the value of P at x_f .

The point $x = 0$ is taken to be the nozzle throat. A boundary condition at this point is needed to start each sweep over x . In actuality there are fluid mechanical effects felt upstream of the throat. However, the high pressures induced by laser absorption will effectively stop the flow through the throat until the wave has advanced far enough so the pressure at the throat has fallen below the unchoking value. Therefore, the throat will behave like a wall, so we impose a reflection boundary condition there. This means that we introduce a fictitious station at $x = -\Delta x$, and set all the thermodynamic variables there to be the same as those at $x = \Delta x$, except that u is the negative of its value at Δx . Then we can use the finite difference equations (3.8.4) - (3.8.6) starting at $x_i = 0$, with the $x_{i-1} = -\Delta x$ values so specified. There is no need for such a condition on P , since it obeys only a one-step difference relation, Eq. (3.8.7), and is swept backwards to $x = 0$, where a value is found. If this value is greater than zero, some of the laser energy has penetrated the gas and been lost. The computer program keeps track of this lost energy.

A choice of Δx and Δt must be made. These quantities are not independent since they must satisfy the Courant condition

$$\Delta t < \Delta x / (u+a) \quad (3.8.8)$$

for each interval Δx . This condition states that in the time interval Δt a wave moving at the sound speed a relative to the local flow speed u will not cross an interval Δx . It is a requirement for stability in the type of time-marching problem being considered here. To be in accord with this requirement, Δt is chosen by calculating $u+a$ at each x_i , finding the largest

of these sums. This is then multiplied by 1.1, and divided into Δx to find Δt for the next time step.

The main difficulty in implementing this Lax scheme in the present calculation is the continually expanding regime of x . As the wave moves downstream, the sweep in x must cover the distance from $x = 0$ to $x = x_f$ past the shock at each step, a distance which continually increases. If Δx remains fixed, we must continually add more x stations which takes more and more computer time and capacity. Furthermore, the smaller Δx , the smaller the time step allowed by Eq. (3.8.8), and the more machine time needed for the shock to reach a given distance.

To overcome these difficulties and perform the calculations in a reasonable time on a moderate-sized computer, we used a scheme in which the number of x stations were fixed, and when the x scale had to be expanded Δx was increased. We used 500 x stations and began with a Δx such that the 500 stations covered a distance twice the length of the hot region used to initiate the laser absorption, which is described below. When the shock reached the edge of this x region, then Δx was doubled, the x stations in the original region were thinned to 250 by eliminating every other one, and 250 new x stations were added, so the x region now covered was twice as large as the first region. The calculation continued until the shock reached the edge of the new region, when the doubling and thinning process took place again. The calculation proceeded this way with a number of doublings of Δx , until it was large enough to encompass the full x distance desired in 500 stations. At each doubling, the allowable Δt also increased according to Eq. (3.8.8), and so did the distance over which the shock transition occurred, since it is always several values of Δx . However, in the calculations to be presented, the largest value of Δx is 0.0512 cm, so the shock thickness is not a significant problem.

The starting conditions in the nozzle were those of steady flow from a given set of stagnation conditions, as described in Section 3.5. However, this is cold flow, since the stagnation temperature is room temperature. Some method for initiating laser absorption is needed.

In the experiments performed, this was accomplished by focussing the laser to a small spot just downstream of the throat to cause gas breakdown. To simulate this in the calculations, a short region of the nozzle starting at the throat was filled at $t = 0$ with a high temperature, high pressure gas, which would absorb laser energy. This region was short enough so that the energy it contained was a negligible fraction of the laser energy in a pulse. The absorption occurring in this initiation region was enough to start the LSD wave formation process and allow the calculation to proceed. The initial Δx was chosen as $1/250$ the length of this hot initiation region, so the initial x region, with 500 stations, was twice the initiation length.

3.9 Results for Perfect Gases and Singly-Ionized Argon

A computer program LSDNS was constructed to solve Eqs. (3.2.1) - (3.2.4) by the method described in Section 3.8. It accepts a given nozzle area distribution $A(x)$. The gas properties for a laser energy absorption case are those of equilibrium argon given in Section 3.3, with the $10.6 \mu\text{m}$ absorption properties given in Section 3.4. The program will also compute blast wave solutions with no laser absorption, starting from a hot, high temperature initiation region at the throat. For this purpose, the gas can be either real argon or a perfect gas of constant γ .

The program has been exercised in both modes. In the absorbing mode it has been used to study the way $10.6 \mu\text{m}$ radiation is absorbed in real argon as a wave is driven down the nozzle. In the non-absorbing mode it has been used to study the difference between the ideal blast wave theory of Refs. 3.6 and 3.1 and the present theory, which includes non-hypersonic shock-waves, a finite hot gas initiation zone, and real gas effects.

In order to check the code and the numerical method, some calculations were made in a constant area channel for a constant-strength LSD wave, to see if the code could reproduce the properties of such a wave. These check runs will be described first, before turning to variable area calculations pertinent to single-pulse laser propulsion.

3.9.1 Constant Area LSD Waves

To produce a steady LSD wave, the area distribution was set equal to a constant. The boundary condition at $x = 0$ was changed from the reflection condition described above to one in which the properties at $x = 0$ were held fixed at the conditions behind the LSD wave it was desired to reproduce. These conditions were obtained by solving the equations given in Section 3.6. The calculation was begun with all x stations (except $x = 0$) at the conditions in front of the wave (with $u = 0$ there). The program then produced a wave which progressed down the channel, and this wave was analyzed to see if it was the expected LSD wave.

The first case run was an ordinary shock wave with no laser flux, moving into argon at 1 atm, 300 K. The wave strength was such that the temperature behind the wave was 14,931 K. The speed of the wave calculated from the jump conditions was 4.46E5 cm/s. In the LSDNS program, Δx was taken as 1.E-3 cm. A sample of the results is shown in Fig. 3.3 as profiles of T and p vs x , at 6 different values of time (TMD) as listed on the plots in μs . As in all the LSD wave plots to be shown, T is normalized by the value behind the wave (14,931 K in this case) while p is normalized with the density behind the wave ($7.97E-3 \text{ g/cm}^3$) and the perfect gas speed of sound at the normalizing temperature. It is seen that a very steady wave is produced quickly. There is a slight (1%) overshoot in T at early times, whose amplitude dies out at later times. The pressure has an undershoot of similar size near $x = 0$. To calculate the wave speed one must choose a point on the profile and follow it in time. Since the profiles are very flat, choosing a point to follow is difficult. If one chooses the point at which ρ is a maximum, the average speed of this point over the time interval from 0.1639 to 0.8118 μs is 4.36E5 cm/s, which compares very well with the value 4.46E5 cm/s found from the jump conditions. So it appears that the program can develop a correct shock wave.

We then calculated an LSD wave in real argon by the same method. We chose a case with laser intensity $I_0 = 14.12E6 \text{ W/cm}^2$, for which the jump conditions of Section 3.6 give $T_2 = 19,905 \text{ K}$ and a wave speed of 4.71E5 cm/s,

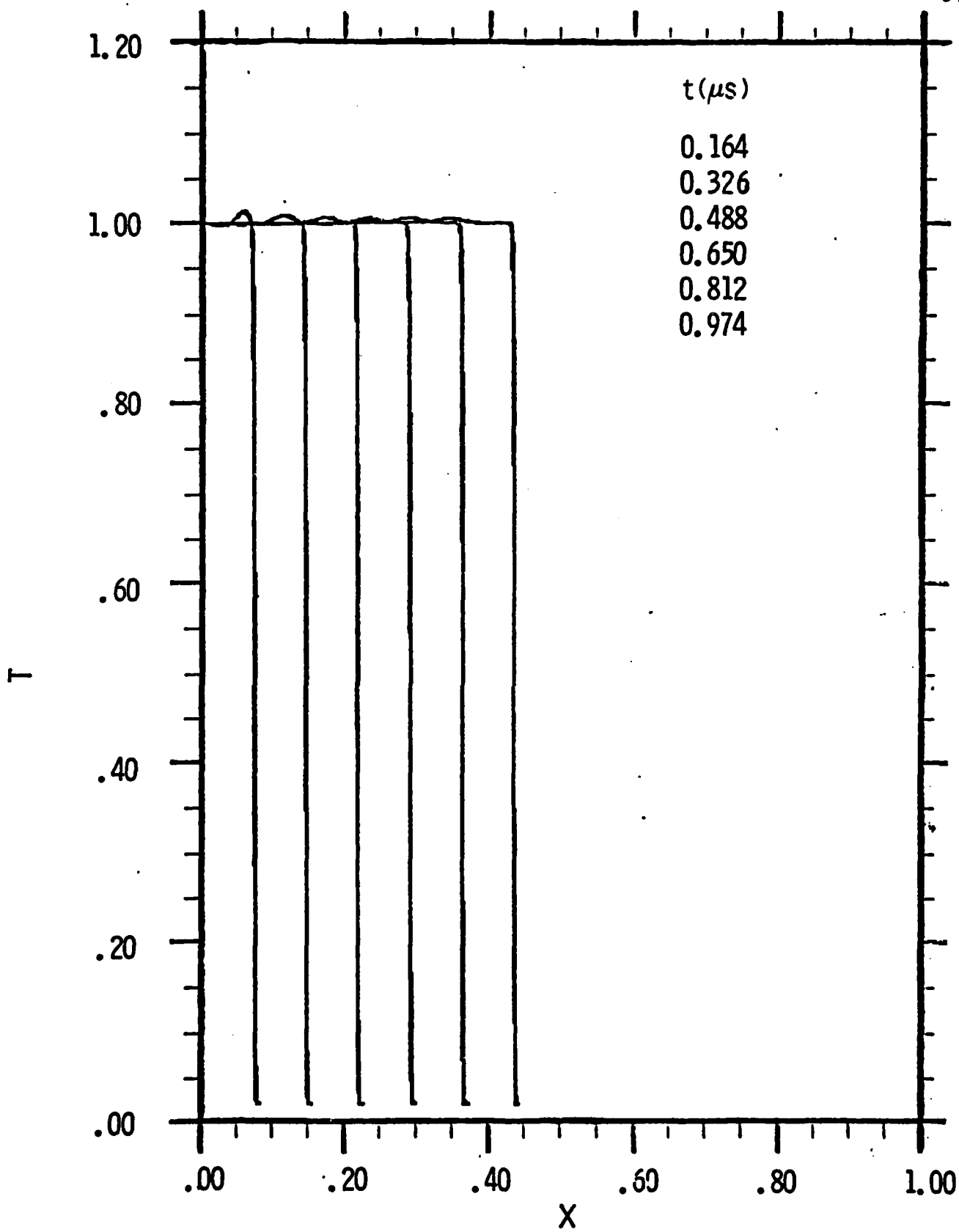


Fig. 3.3a Calculated temperature profiles for an ordinary shock wave in real argon, initially at 1 atm, 300 K.

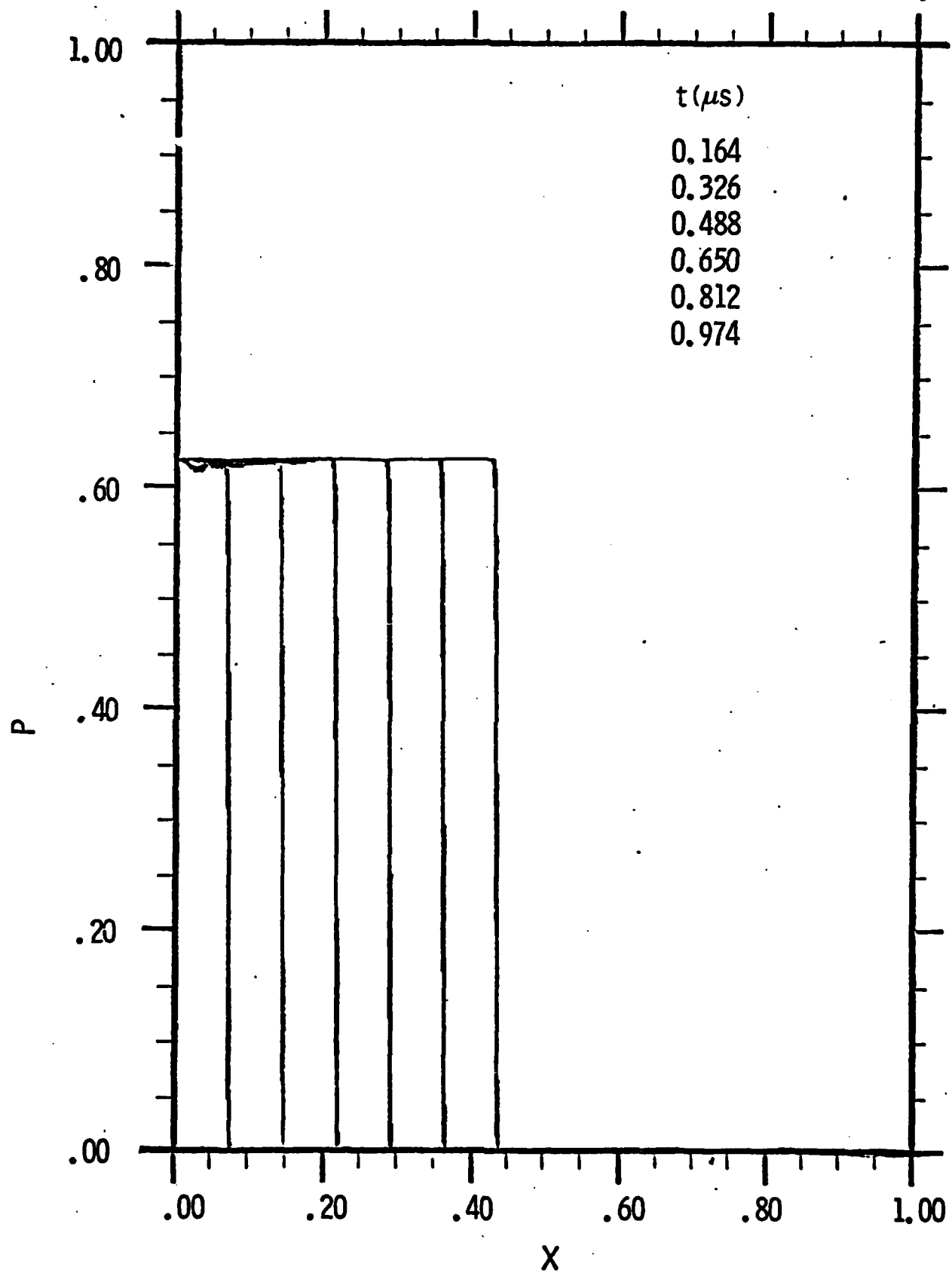


Fig. 3.3b Calculated pressure profiles for an ordinary shock wave in real argon, initially at 1 atm, 300 K.

starting with 1 atm, 300 K. The results of a calculation for this case are shown in Fig. 3.4, using $\Delta x = 1.E-3$ cm in LSDNS. There is now a 1.6% overshoot in T at the shock front, and a 22.4% overshoot in p. The jump conditions give profiles which indicate a 0.9% overshoot in T when the laser is 90% absorbed and an 80% overshoot in p before any absorption has occurred. LSDNS is not able to resolve the shock well enough to show the large pressure overshoot, but does produce some overshoot after laser absorption, which occurs in about three Δx steps. The wave speed can be followed using the pressure peak location, and from 0.1811 to 0.8872 μs gives $4.70E5$, which is almost exactly the jump condition value. Again LSDNS has given a steady wave, this time with laser absorption, at the correct speed. It is not able to correctly produce the details of the wave profile during absorption, but this is not to be expected, since the shock-capturing numerical method includes an artificial viscosity, mentioned in Section 3.8, which falsifies the actual wave structure. The important feature is the ability to produce the correct wave speed and settle down to the correct jump conditions when the laser energy is completely absorbed.

The results for one more constant area case are instructive. This is a lower intensity case of $I_0 = 3.65E6$ W/cm² into 1 atm and 300 K which gives $T_2 = 14,931$ and a speed of $3.65E5$ cm/s, according to the jump conditions. The profiles are presented in Fig. 3.5, for $\Delta x = 1.E-3$ cm and show a much different character than before. The profile is not steady, but develops an increasingly pronounced temperature plateau with a further increase to another plateau at 10% above the final LSD wave value. The pressure rises to a plateau and then drops when the second temperature increase occurs. This character, which is quite different from that seen in Fig. 3.4, develops in time from a profile at the earliest time plotted which is more like the one shown in Fig. 3.3. The later profiles show a delay in laser absorption, which takes place about 0.05 cm behind the shock front, instead of simultaneously with it. During the absorption, the pressure is nearly constant. The speed of the shock wave for the last three time steps is

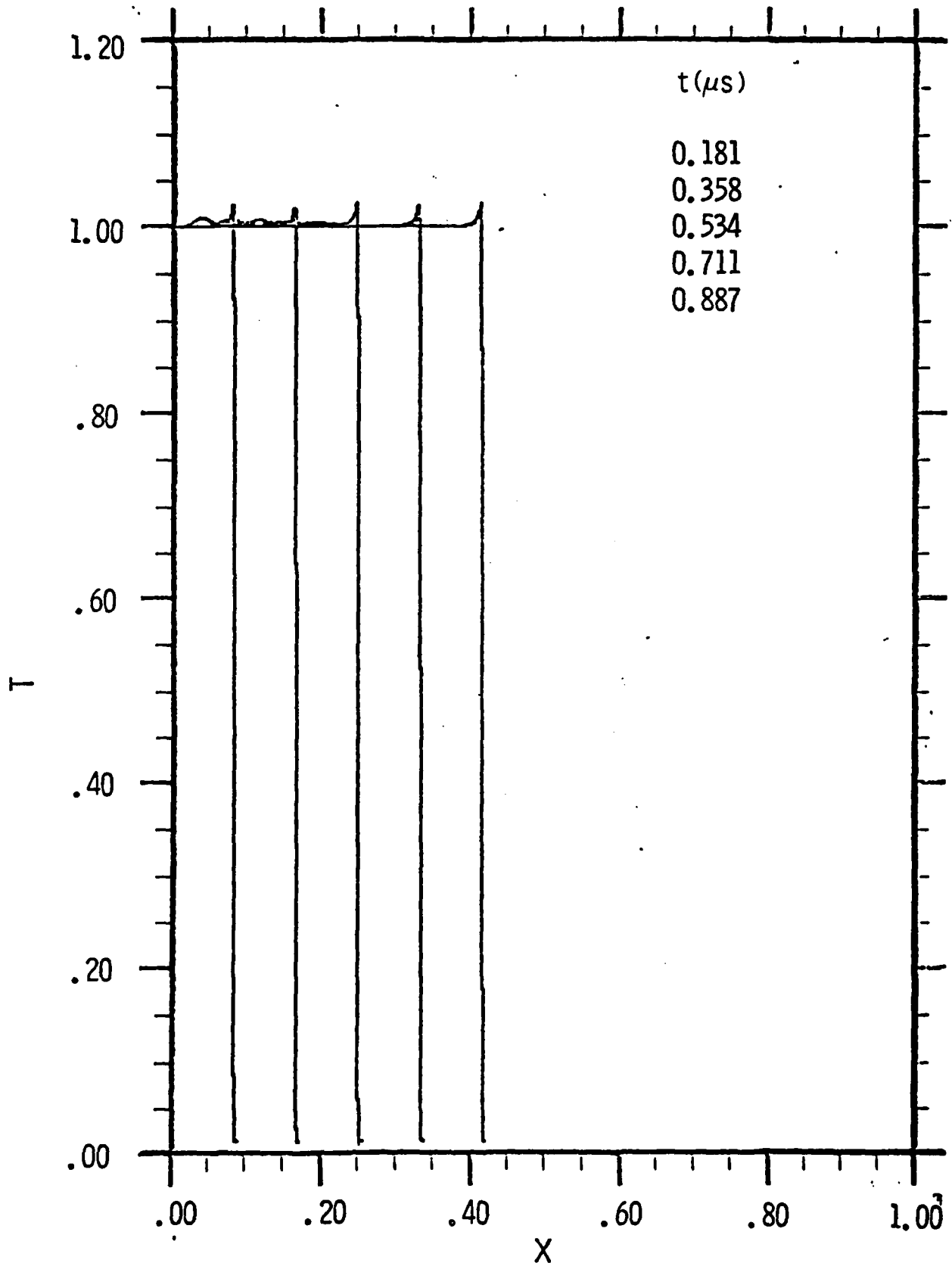


Fig. 3.4a Calculated temperature profiles for an LSD wave in real argon initially at 1 atm, 300 K. $I_1 = 14.12 \text{ MW/cm}^2$, $\Delta x = 1.E-3 \text{ cm}$.

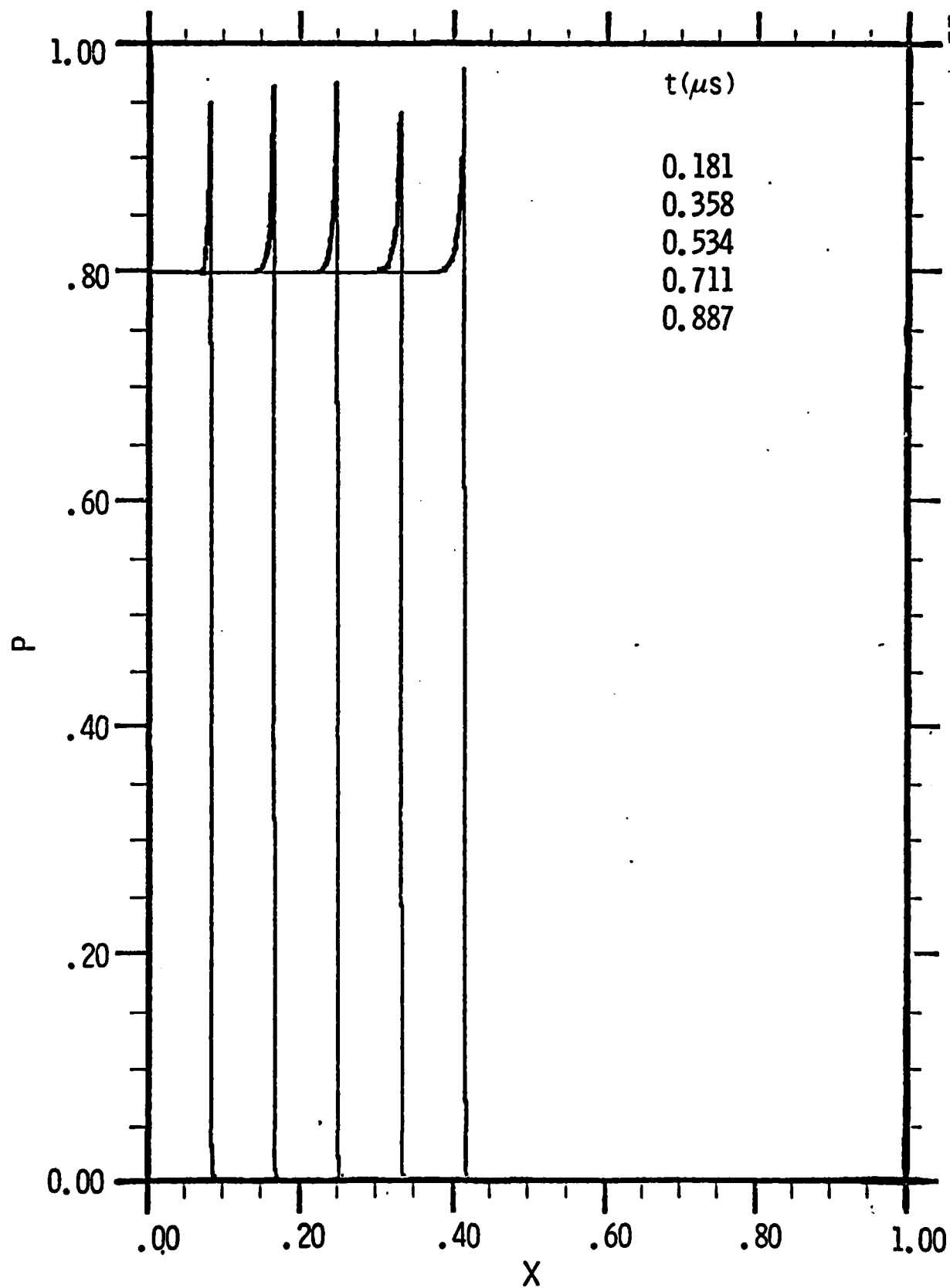


Fig. 3.4b Calculated pressure profiles for an LSD wave in real argon, initially at 1 atm, 300 K. $I_1 = 14.12 \text{ MW/cm}^2$, $\Delta x = 1.E-3 \text{ cm}$.

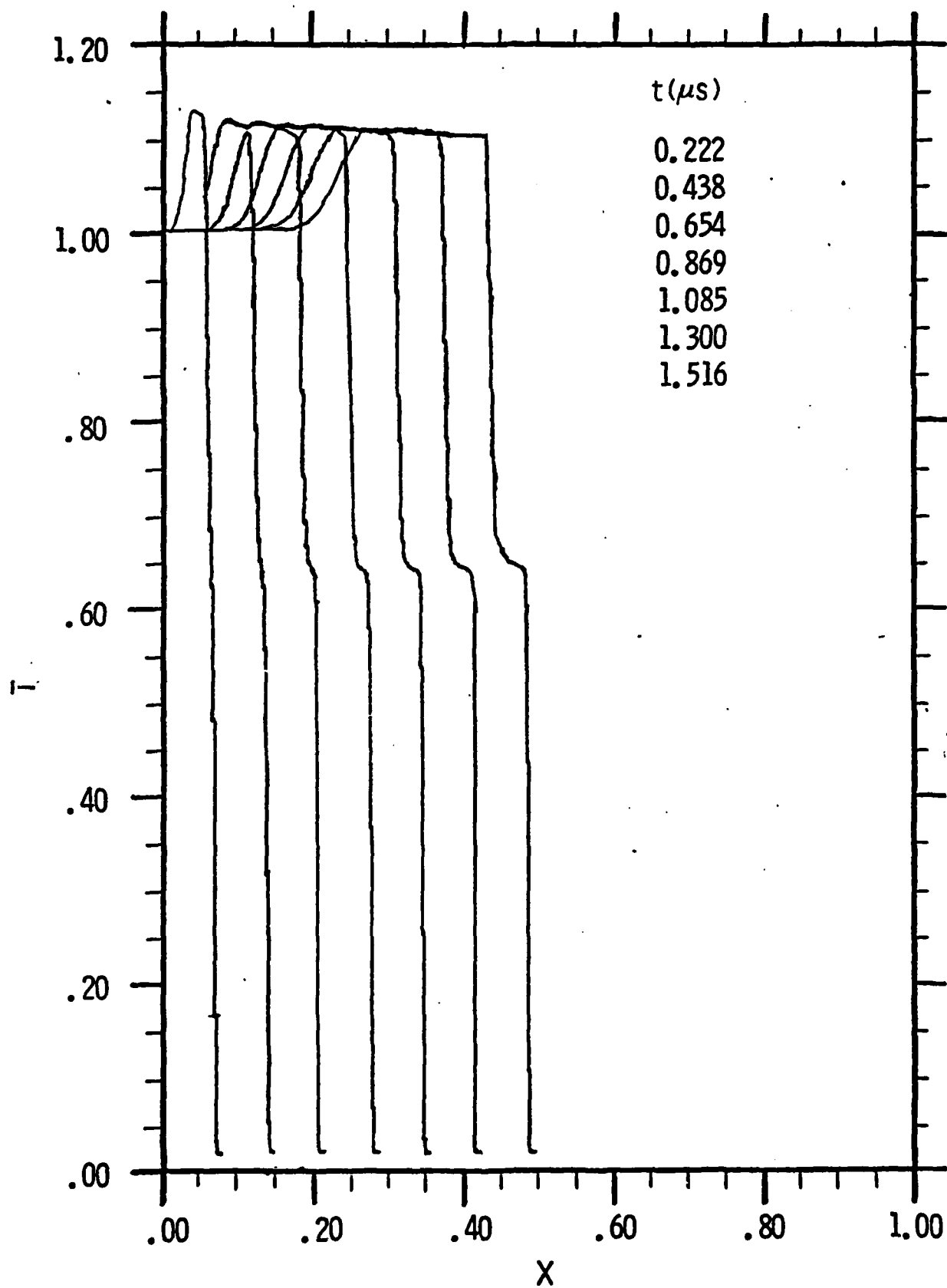


Fig. 3.5a Calculated temperature profiles for an LSD wave in real argon, initially at 1 atm, 300 K. $I_1 = 3.65 \text{ MW/cm}^2$, $\Delta x = 1.E-3 \text{ cm}$.

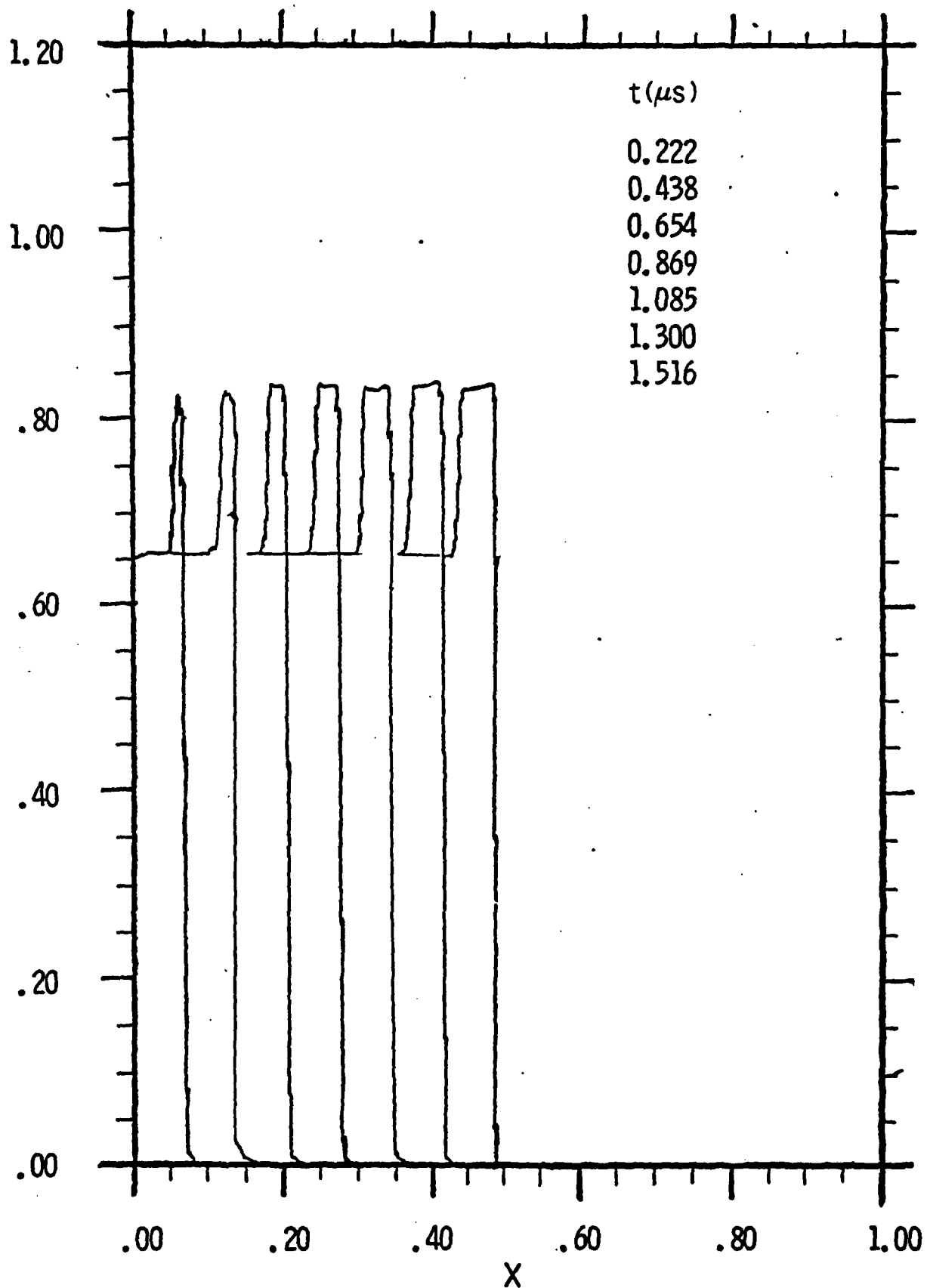


Fig. 3.5b Calculated pressure profiles for an LSD wave in real argon, initially at 1 atm, 300 K. $I_1 = 3.65 \text{ MW/cm}^2$, $\Delta x = 1.E-3\text{cm}$.

calculated from the maximum pressure or density point to be $3.24E5$ cm/s which is significantly lower than the $3.65E5$ cm/s given by the jump conditions for an LSD wave. However, the flow may not yet have reached steady state.

Clearly, the program is not producing a sharp LSD wave in this case, but is approaching a configuration more like an ordinary shock wave followed by a constant pressure absorption zone. We do not know if this configuration will reach a steady state, or will change to some other configuration as the wave progresses down the channel.

The same calculation was repeated with only one change, $\Delta x = 2.E-3$ cm instead of $1.E-3$ cm, and the resulting profiles are shown on the same scale in Fig. 3.6. Here we see a return to the LSD type of profile with a combined shock and absorption zone, small overshoot in T and large overshoot in p. This wave travels at $3.65E5$ cm/s, the same speed calculated from the jump conditions, and is clearly an LSD wave. So at this low intensity, $3.65E6$ W/cm², we have been able to produce both an LSD wave configuration and one where the shock and absorption zone become separated, merely by changing Δx by a factor of two. In both cases, however, the laser energy was absorbed. The location of the absorption zone changed, not the over-all amount of absorption.

This dependence on Δx is a reflection of the presence of the absorption length scale in the LSD wave. The laser energy is absorbed in a length whose order is the inverse of the absorption coefficient k_L . For all the energy to be absorbed in the shock wave, the thickness of the shock must be comparable to this absorption length. The thickness of the computed shock depends on the ratio $(\Delta x)^2/\Delta T$, which appears as an artificial kinematic viscosity in the numerical method, as pointed out in Section 3.8. In fact, using the relation between viscosity and mean free path, and remembering that a shock is a few mean free paths thick, we can write the shock thickness as

$$\delta_s = K_1 (\Delta x)^2 / a \Delta t$$

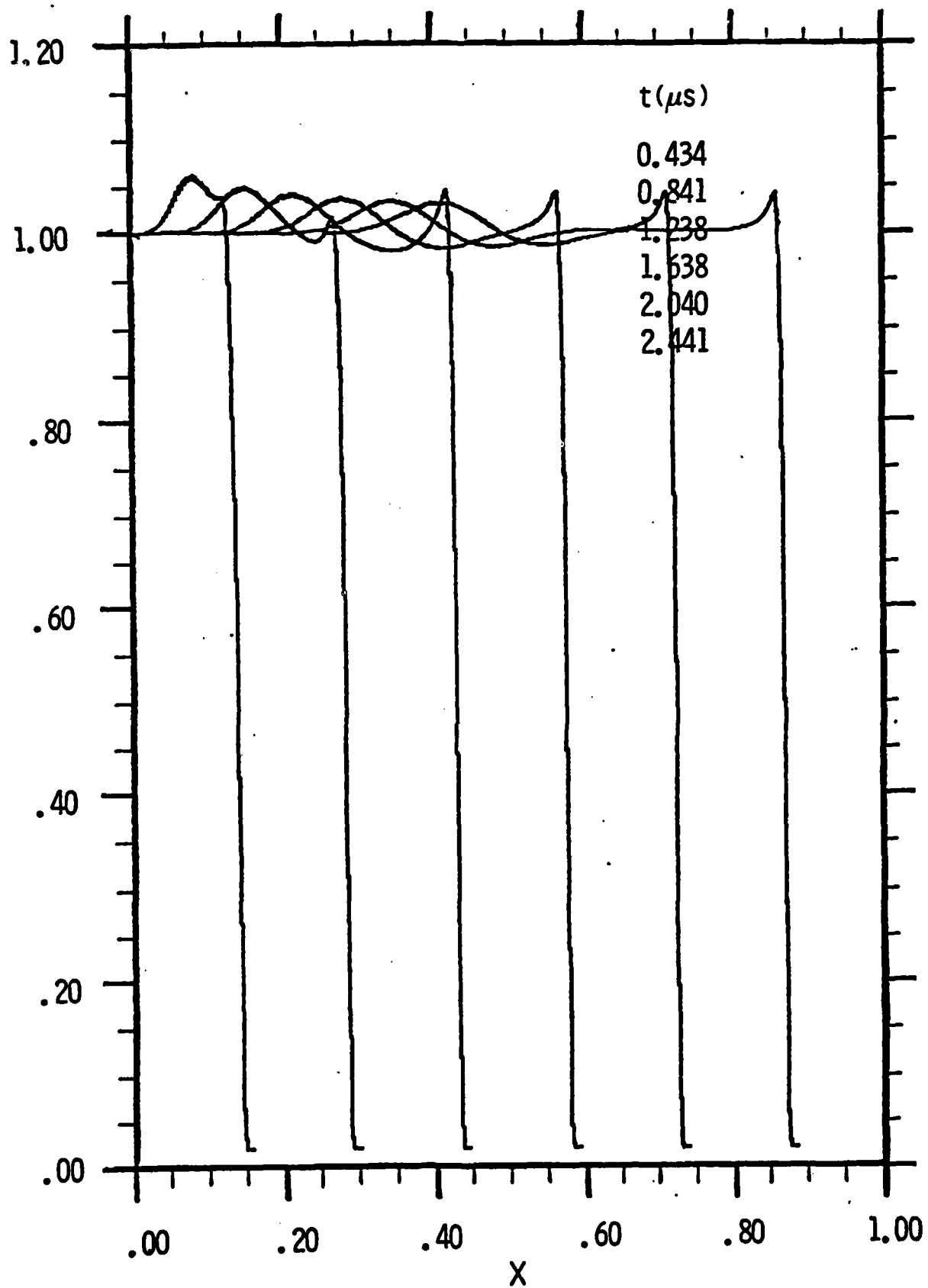


Fig. 3.6a Calculated temperature profiles for an LSD wave in real argon, initially at 1 atm, 300 K. $I_1 = 3.65 \text{ MW/cm}^2$, $\Delta x = 2.E-3 \text{ cm}$.

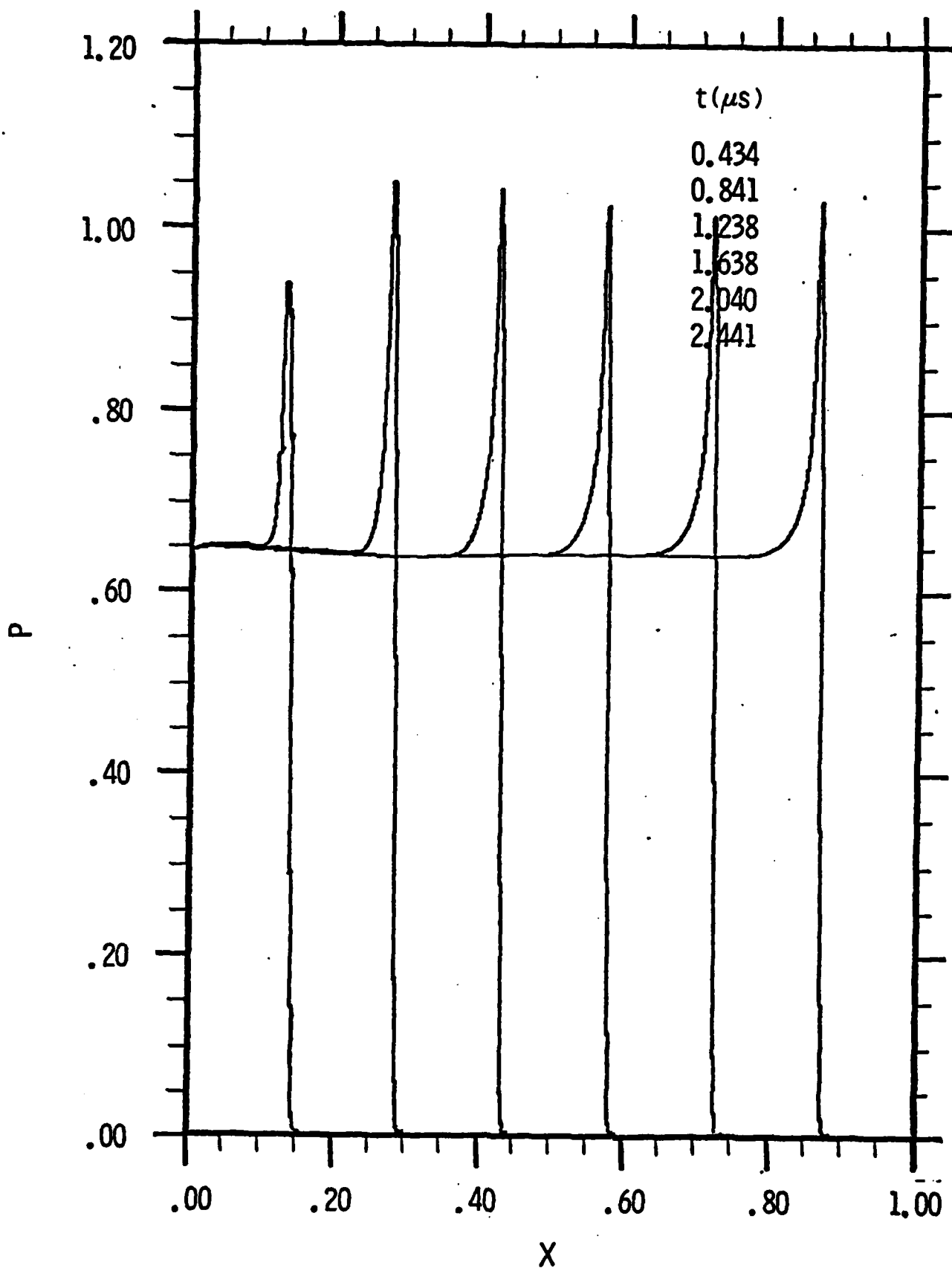


Fig. 3.6b Calculated pressure profiles for an LSD wave in real argon, initially at 1 atm, 300 K. $I_1 = 3.65 \text{ MW/cm}^2$, $\Delta x = 2.E-3 \text{ cm}$.

where a is the speed of sound behind the shock, and K_1 is a constant of order unity. But we have also had to use the Courant condition Eq. (3.8.8) to relate Δx and Δt to insure the stability of the numerical procedure. This may be written

$$\Delta x = K_2 (u+a) \Delta t$$

where K_2 is a constant slightly larger than unity. Combining these two shows that

$$\delta_s = K_1 K_2 (u+a) \Delta x / a$$

which means that the shock thickness is proportional to Δx .

To absorb all the laser energy within the shock wave requires the thickness δ_s to be of the order $1/k_L$, or $\delta_s k_L \sim O(1)$. Since $\delta_s \sim O(\Delta x)$, this means that $k_L \Delta x$ cannot be too small, or the absorption will not occur in the shock wave. In the high intensity case of Fig. 3.5, k_L in the absorption zone is about $3.E3$ so the product $k_L \Delta x = 3$. In the low intensity case of Figs. 3.5 and 3.6, k_L is $2.E2$ to $5.E2$. For the case which behaved like an LSD wave, Fig. 3.6, $k_L \Delta x = 0.4$ to 1 , while for the case which absorbed behind the shock, Fig. 3.5, $k_L \Delta x = 0.2$ to 0.5 . This gives some indication that LSD wave solutions require $k_L \Delta x$ close to unity or above. The lower the intensity, the cooler the wave and the lower k_L . Therefore, larger Δx will be required to make the absorption occur within the shock wave.

3.9.2 Variable Area Nozzle Blast Wave Calculations

We next turned to calculations in a nozzle shape in which experiments were made. The shape of the nozzle was initially parabolic, so the square of the cross-sectional radius was proportional to the axial distance, measured from zero radius. The throat radius r_{th} occurs at $x = 0$ in the coordinates used for the calculations so

$$r_p^2 = Cx + r_{th}^2, \quad A_p = \pi Cx = \pi r_{th}^2. \quad (3.9.1)$$

The particular experimental nozzle for which calculations have been done had $C = 1.27$ cm, $r_{th} = 0.09906$ cm so that

$$A_p(x) = 3.9898x + 3.0828E-2 \quad (3.9.2)$$

$$dA_p/dx = \pi C = 3.9898.$$

In addition to the parabola, some calculations were made with a conical extension to the parabola at $x = x_m$, which matched the radius r_m and slope. This case then has the equations

$$r_C = C(x-x_m)/2r_m + r_m, \quad r_m = (Cx_m + r_{th}^2)^{1/2}$$

$$A_C(x) = \pi r_C^2, \quad \frac{dA_C}{dx} = \pi C \left[\frac{C(x-x_m)}{2r_m^2} + 1 \right]. \quad (3.9.3)$$

The only new parameter required to add the cone is the matching station x_m . In the calculation reported here, the value of x_m was set at 10 cm, the value used in the PSI experiments.

The time dependence of the laser pulse coming into the nozzle was defined to be either a constant flux from $t = 0$ to a cut-off time, or a linearly decreasing pulse from an initial value at $t = 0$ to zero at the cut-off time.

As described above, the starting state of the flow in the nozzle was isentropic flow of a perfect gas with specified stagnation pressure and temperature, which then determined the mass flow rate \dot{m} in the nozzle. To initiate the wave, a region of the nozzle from $x = 0$ to $x = XIC$ was filled with hot gas at some specified initial state, and then the program was turned on.

If a blast wave type of calculation was desired, enough initial hot gas was inserted to contain the desired amount of energy E which would generate the blast wave. No laser power P was used for this type of calculation, since the energy in the initial hot gas represents instantaneous deposition of the laser energy before the calculation starts. If an LSD wave calculation was desired, a very small amount of hot gas was used, just enough to start laser absorption, but with an insignificant amount of energy compared to that to be deposited by the laser.

Most of the runs made so far were of the blast wave type, because we were interested in finding a relation between the energy deposited and the time of the shock arrival at a measuring station. The idea was to infer the energy deposited in the gas from the measurements.

A table of the runs made in the blast wave mode is given in Table 3.2. The heated zone distance was always chosen at $XIC = 0.1$ cm. The densities in the heated zone, ρ_{IC} , were chosen in various ways. For Run 1, it was chosen as approximately the value at $x = 0.1$ cm in the starting cold flow state. In Runs 2 and 3 it was taken as the value in the cold flow at the throat. In Runs 5-11 it was chosen as twice the density in the cold flow at $x = 0.1$ cm. The internal energy of the hot gas was then chosen so as to give the desired total energy in the hot gas slab. Given these two thermodynamic quantities, the state of the hot gas was completely defined, and the pressure and temperature could then be calculated from the perfect gas law or from the equilibrium argon relations given in Section 3.3. The resulting initial temperatures and pressures are quite high since a large amount of energy is contained in this gas, whose volume is only 0.023032 cm^3 for the nozzle described above. For real argon, the temperatures are far above the validity of the singly-ionized model of Section 3.3, but the correct energy is included, and the properties of Section 3.3 are used consistently throughout the calculation. The gas cools rapidly after the calculation starts, and most of the flow is in a regime where single ionization is a good approximation.

TABLE 3.2

BLAST WAVE RUNS

Run	Gas	Energy (J)	Pst (atm)	T _{st} (K)	\dot{m} (g/s)	XIC (cm)	ρ_{IC3} (g/cm ³)	PIC (atm)	T _{IC} (K)	u_g (cm/s)
1	Perf. Ar	1.05	2	300	1.816	0.1	7.288E-5	300	2.004E6	5.587E4
2	Real Ar	1.05	2	300	1.816	0.1	2.108E-5	114.7	1.959E4	5.587E4
3	Perf. Ar	1.05	2	300	1.816	0.1	2.108E-5	300	6.928E4	5.587E4
5	Perf. H ₂	2	11.86	300	2.281	0.1	4.065E-5	342.8	2.072E5	2.943E5
6	Perf. H ₂	2	0.1186	3	0.2281	0.1	4.965E-5	342.8	2.072E5	2.943E4
7	Perf. H ₂	1	11.86	300	2.281	0.1	4.065E-5	171.4	1.036E5	2.943E5
8	Real Ar	4	1.3	300	1.180	0.1	1.027E-4	1117	2.647E6	5.587E4
9	Real Ar	2	1.3	300	1.180	0.1	1.027E-4	545.7	1.293E6	5.587E4
10	Perf. Ar	2	1.3	300	1.180	0.1	1.027E-4	571.3	2.708E6	5.587E4
11	Real Ar	4	18.01	300	16.35	0.1	1.423E-4	787.7	1.348E5	5.587E4

Some sample results from these calculations are shown in Figs. 3.7 and 3.8. They are profiles of T, p and u vs x at several times, as listed in μ s at the upper right of each figure. The temperatures are given in 10^4 K, the pressures are normalized by 34.2 atm and the velocities by $1.86E5$ cm/s, while x is in cm. The progress and decay of strength of the blast wave as it moves down the nozzle are shown. The thickness of the shock jump increases as it moves because Δx increases, starting at $4.E-4$ cm at $t = 0$. The shock near $x = 4$ has $\Delta x = 1.28E-3$, the one near $x = 11$ has $\Delta x = 2.56E-3$, and the one near $x = 20$ has $\Delta x = 5.12E-3$.

Figure 3.7 is from Run 10 in perfect argon, while Fig. 3.8 is from Run 9 in real argon. The energy, stagnation conditions and initial hot gas density are the same, though the hot gas temperatures and pressures differ, as shown in Table 3.2. They both show similar character. There is rapid decay of pressure level as the flow moves into the rapidly expanding nozzle, with the perfect gas case having higher pressure. There is some difference in the temperature profiles, which is to be expected because the internal degrees of freedom in real argon absorb energy which must appear as temperature in the perfect argon. The latter shows a rather flat temperature plateau behind the shock for a large portion of the distance, while the real argon shows a small plateau followed by a slow rise in temperature. The velocity profiles are quite similar, though the perfect gas run has a higher velocity level, since it does not have the internal energy sink.

The flow in the nozzle is initiated by a hot gas region, and the location of the interface between the initially hot and cold gas can be followed by mass conservation. This interface is similar to the contact surface in a shock-tube flow, and in fact the present flow is much like a shock tube flow with a very thin driver section and an expanding nozzle for the driven section. The location of the interface is marked on each profile in Figs. 3.7 and 3.8 by a tic mark. It progresses down the nozzle, but much more slowly than the shock wave.

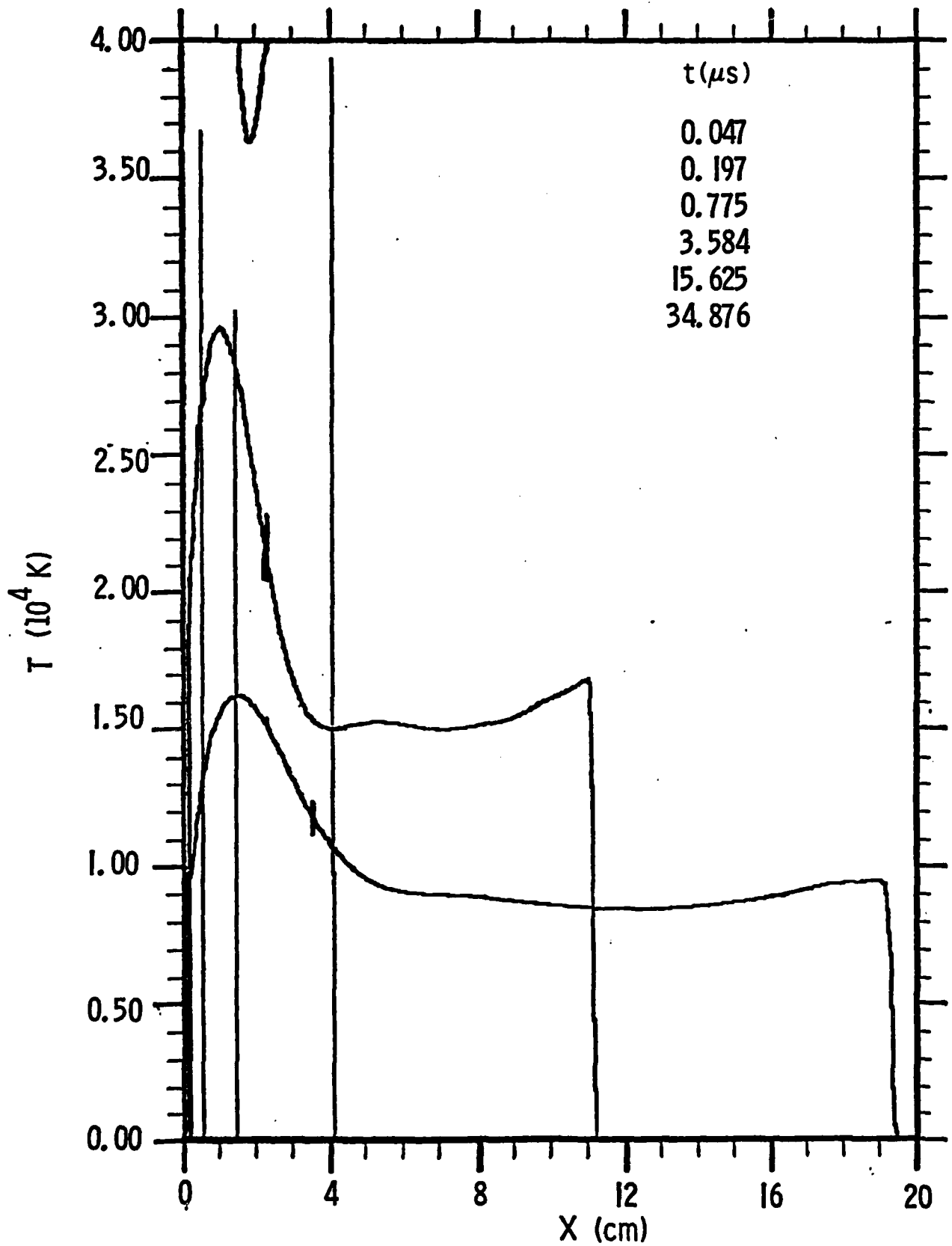


Fig. 3.7a Calculated temperature profiles for a blast wave in a nozzle. Perfect argon, with starting stagnation conditions of 1.3 atm, 300 K. Run 10

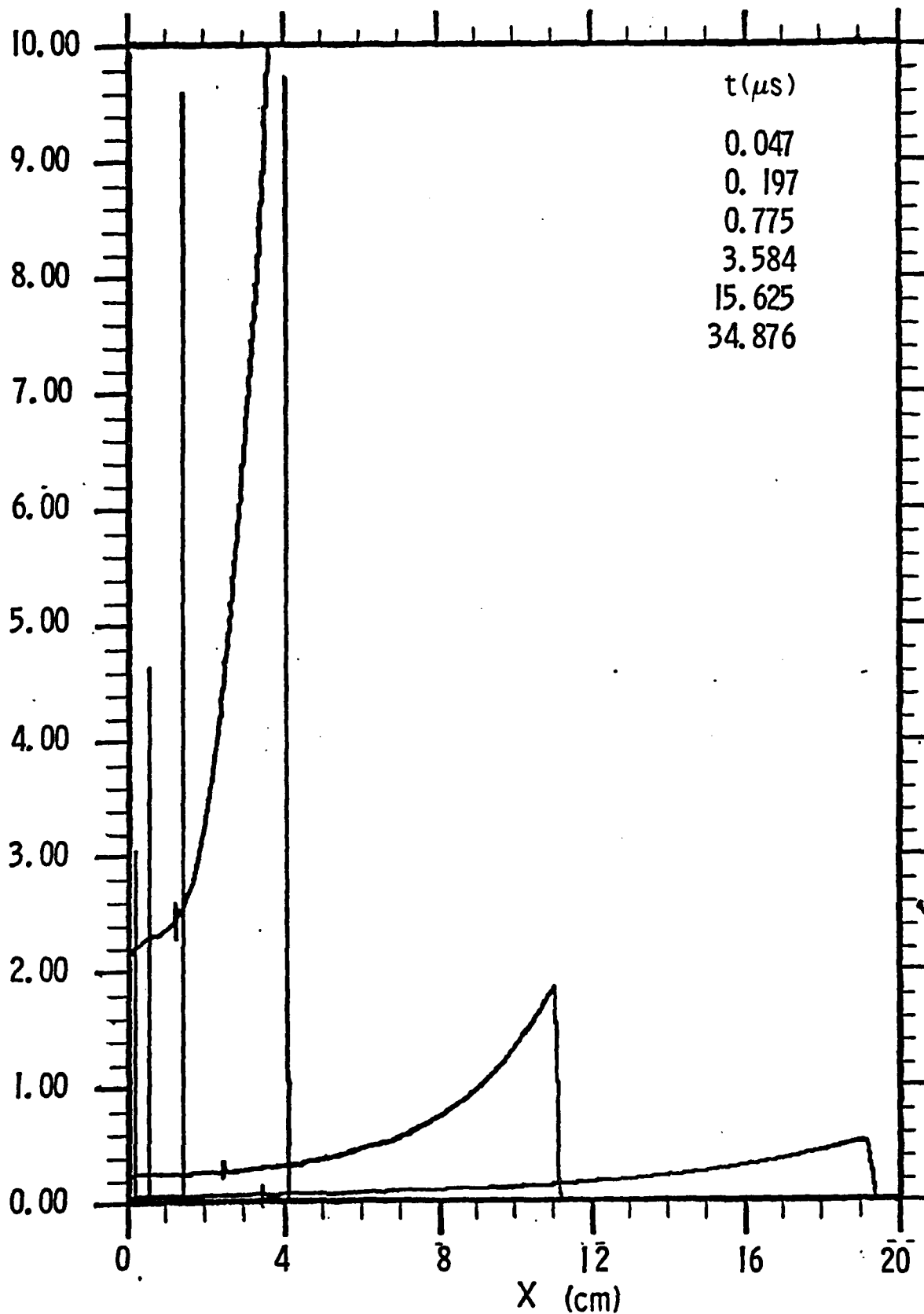


Fig. 3.7b Calculated pressure profiles for a blast wave in a nozzle. Perfect argon, with starting stagnation conditions of 1.3 atm, 300 K. Run 10

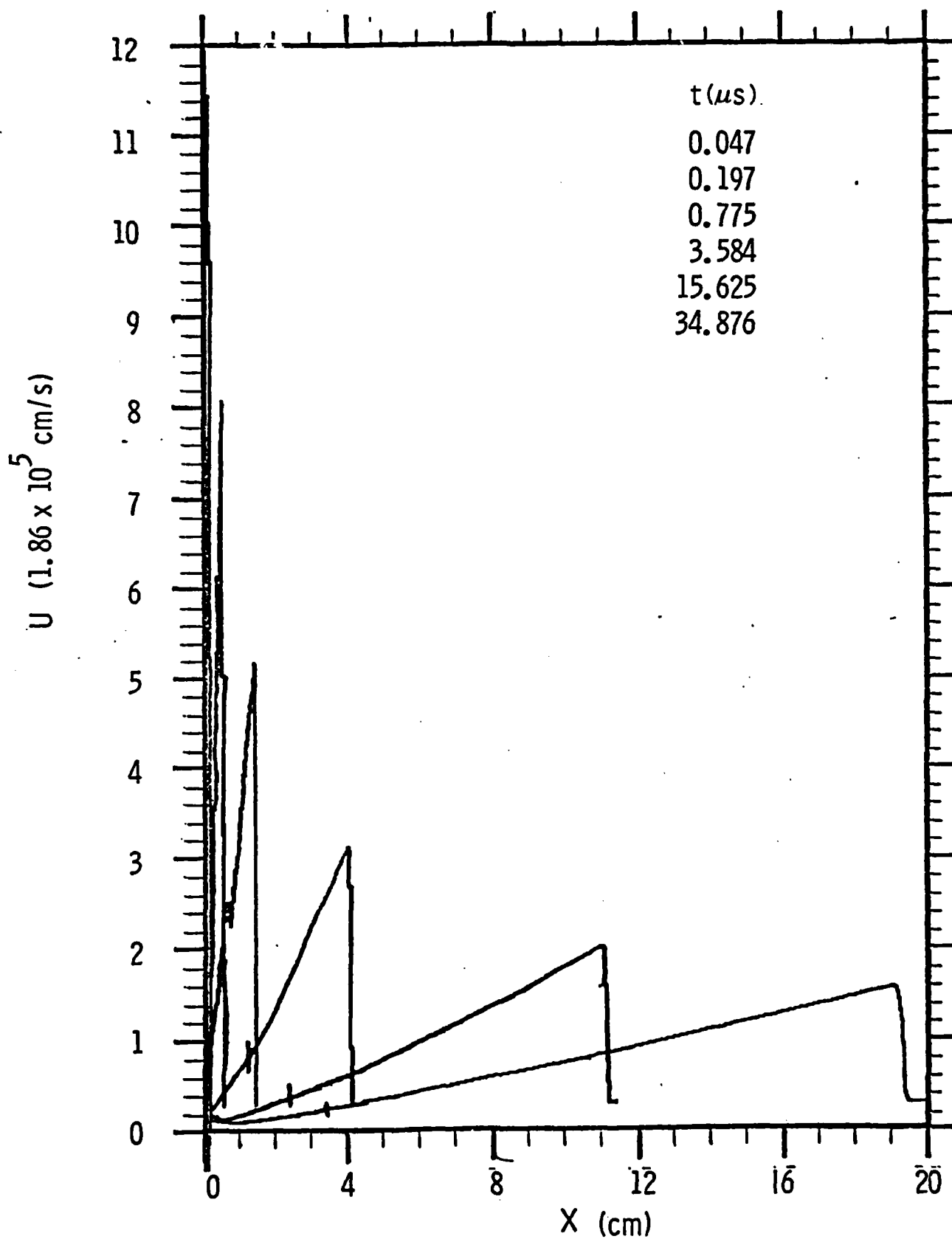


Fig. 3.7c Calculated velocity profiles for a blast wave in a nozzle. Perfect argon, with starting stagnation conditions of .1.3 atm, 300 K. Run 10

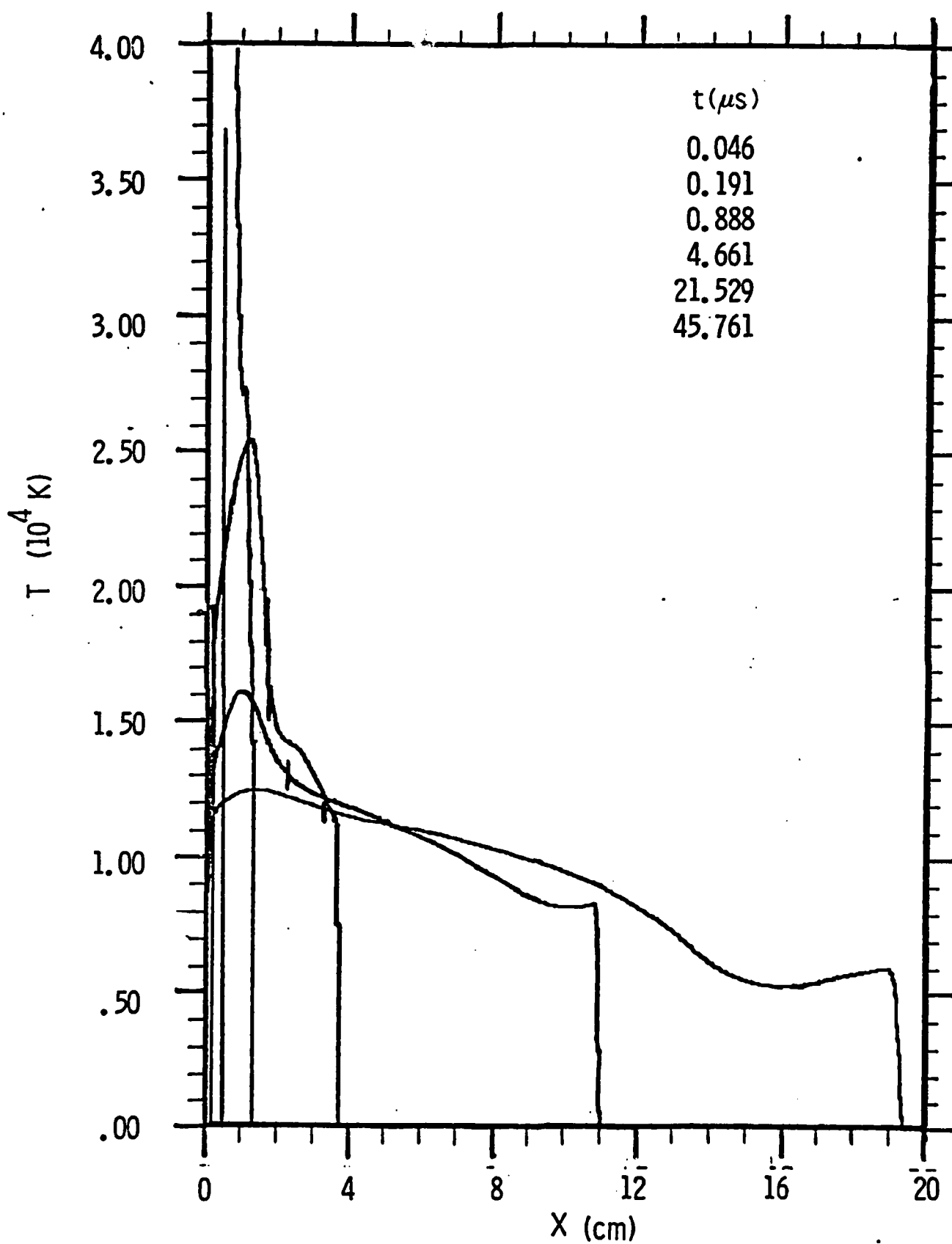


Fig. 3.8a Calculated temperature profiles for blast wave in a nozzle. Real argon, with starting stagnation conditions of 1.3 atm, 300 K. Run 9.

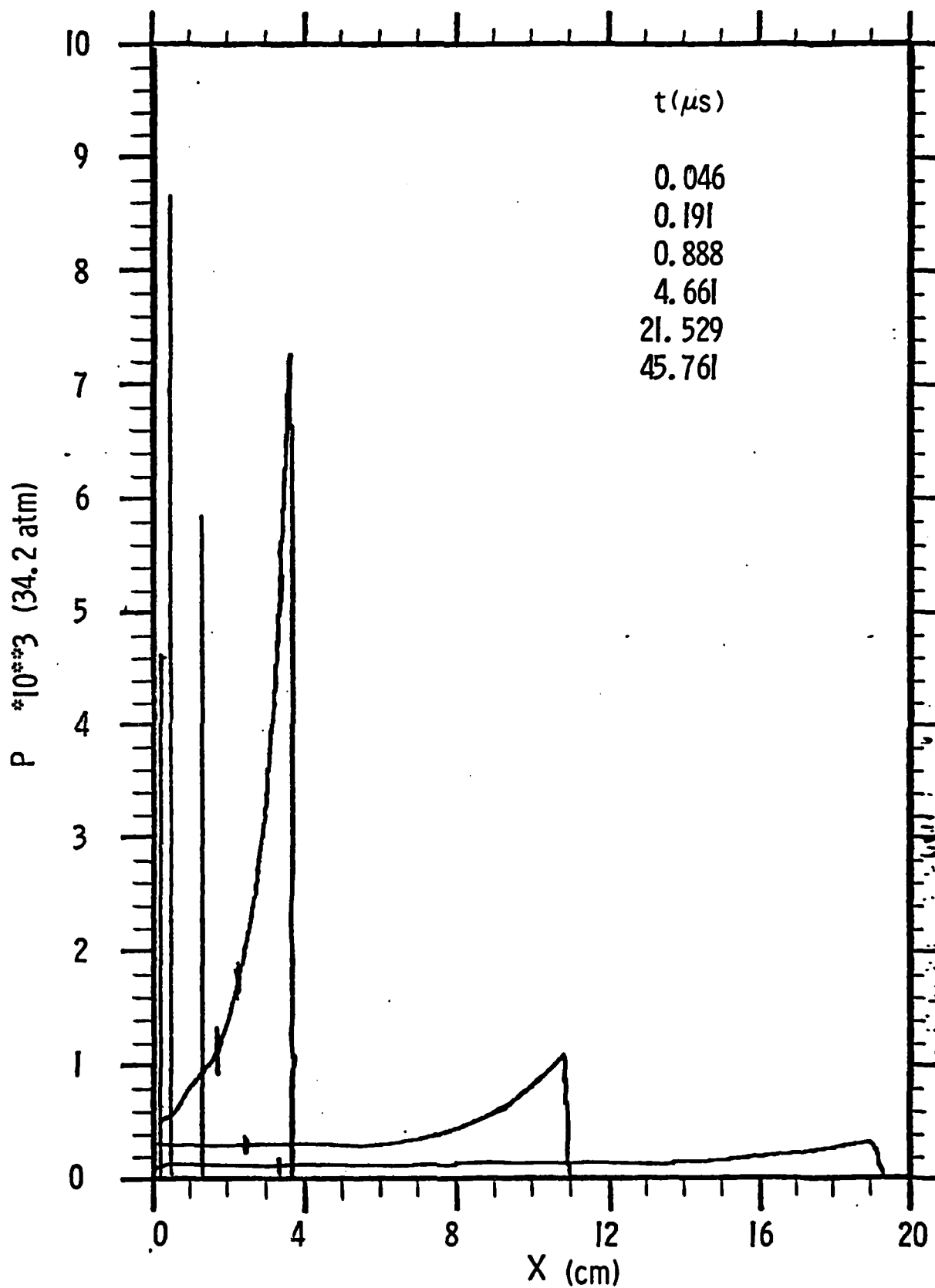


Fig. 3.8b Calculated pressure profiles for a blast wave in a nozzle. Real argon, with starting stagnation conditions of 1.3 atm, 300 K. Run 9.

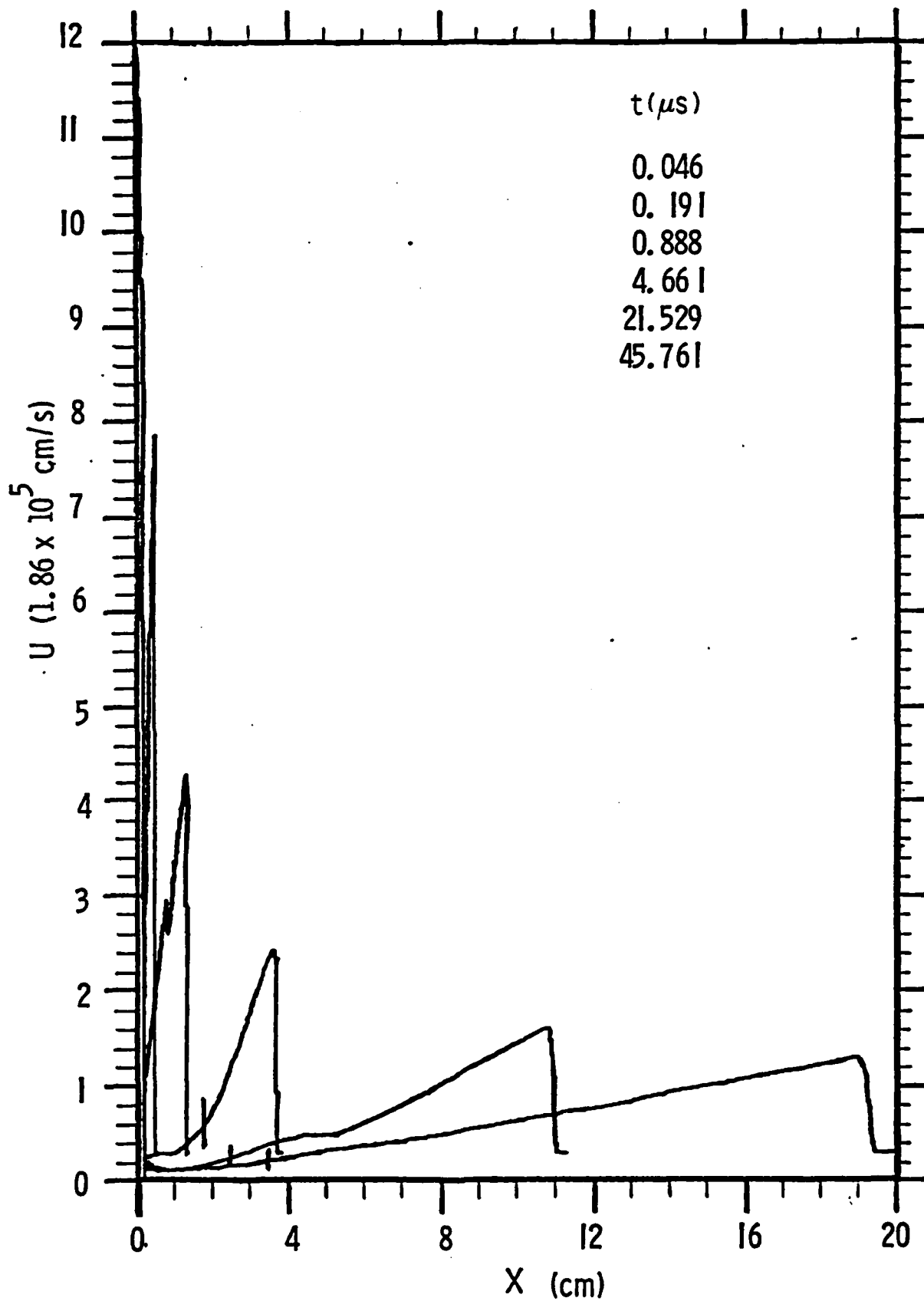


Fig. 3.8c Calculated velocity profiles for a blast wave in a nozzle.
 Real argon, with starting stagnation conditions of 1.3 atm,
 300 K. Run 9.

The most noticeable difference between the real and perfect gas cases is the time for the shock to reach a given point. The perfect gas shock moves much faster, reaching 19 cm in 35 μ s, while the real gas shock takes 46 μ s to reach that station. This again can be attributed to the investment of energy in the internal modes in a real gas, leaving less energy in the form of pressure to drive the shock wave.

Our interest in these blast calculations is primarily in the shock wave trajectory, as pointed out above, since we have made experiments measuring shock arrival at certain nozzle stations, as indicated by a steep rise in observed pressure. Therefore, the time history of the maximum pressure point was correlated, using the similarity variables described in Section 3.7. As given in Eq. (3.7.4), these are

$$\xi = x / (E / \dot{m} u_{\ell}) \quad , \quad \tau = t / (E / \dot{m} u_{\ell}^2) \quad (3.9.1)$$

The energy, mass flow rate and limiting velocity are given in Table 3.2 for each run, so the similarity variables can be found from t and x_p at the maximum pressure point.

A log-log plot of ξ_p vs τ is shown in Fig. 3.9 for the three perfect hydrogen runs, 5, 6 and 7, which were all made with the parabolic nozzle without the conical extension. The points for Runs 5 and 7, which differ only in having $E = 2$ and 1 joule, fall almost on top of each other. The points for Run 6, which has low values of p_{st} and T_{st} , and therefore, low values of \dot{m} and u_{ℓ} , fall at much smaller values of ξ_p and τ . However, all three cases fall quite well on a single curve over six decades in τ and four decades in ξ . This confirms the scaling in E over a factor of two, in \dot{m} over a factor of 10 and in u_{ℓ} over a factor of 10 indicated by the use of the similarity variables.

Based on the "corrected" expression for the shock trajectory suggested in Eq. (3.7.6), we have made a least squares fit to the calculated points using the two terms τ and $\tau^{2/3}$. The result is

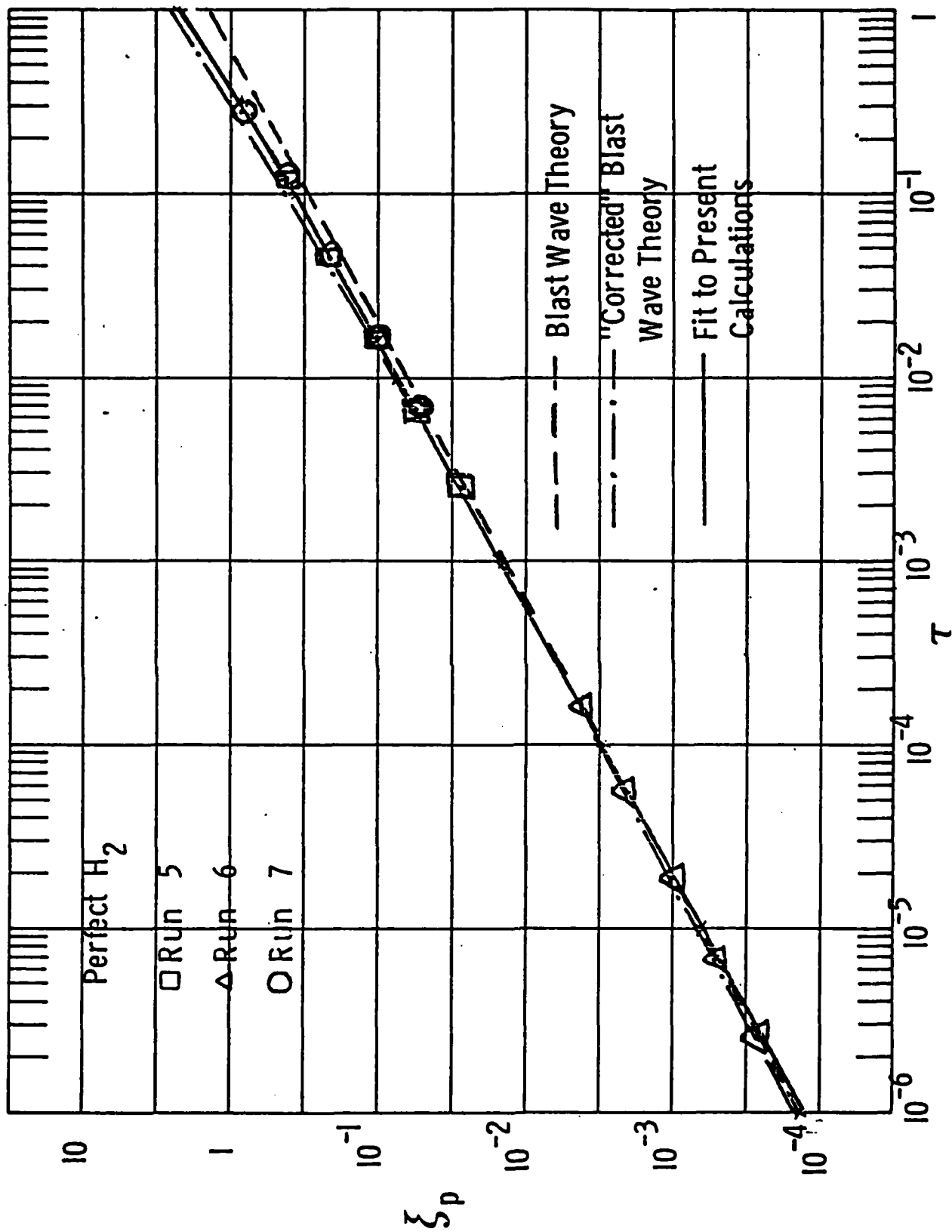


Fig. 3.9 Correlation of shock trajectory for a blast wave in a nozzle. Perfect hydrogen.

$$\xi_p = 1.353\tau^{2/3} + 0.8212\tau \quad (3.9.2)$$

which is shown in Fig. 3.9 as the solid curve. The "corrected" blast wave relation Eq. (3.7.6) for a diatomic gas is

$$\xi_s = 1.453\tau^{2/3} + \tau \quad (3.9.3)$$

since Ref. 3,5 has $I_p = 0.733$ for $\gamma = 1.4$ and a parabolic nozzle. This is the dash-dot curve in Fig. 3.9, and is quite close to the fitted line but slightly higher. The good agreement between these two curves is an indication that the present perfect gas calculations are a correct solution of the flow problem and that the simple correction to ideal blast wave theory to account for the speed of the flow in front of the shock is a good approximation. That the correction is needed at large τ can be seen by plotting the ideal blast wave trajectory for this case, from Eq. (3.7.3), which is

$$\xi_s = 1.453\tau^{2/3}. \quad (3.9.4)$$

This is the dashed straight line in Fig. 3.9, and shows a divergence from the other two curves above $\tau = 1.E-3$, becoming quite large at the larger τ , where the shock is not hypersonic relative to the flow in front.

A similar plot appears in Fig. 3.10 for perfect argon, from Runs 1, 3 and 10. The first two use the parabolic nozzle, while the third uses the conical extension at $x = 10$, but only the two points at the highest values of τ are in the conical section, one at 12.3 cm and the other at 19.0 cm. The results for Runs 1 and 10 fall very nearly on the same curve, though they differ by a factor of two in energy. The points for Run 3 fall well below the others. This is attributable to the initial density, which for Run 3 was taken very high, namely the sonic density of the cold starting flow. For Runs 1 and 10 this density was taken as much lower, corresponding to the cold flow density at the downstream edge of the hot initial flow for Run 1 and twice this density for Run 10. The lower densities are more

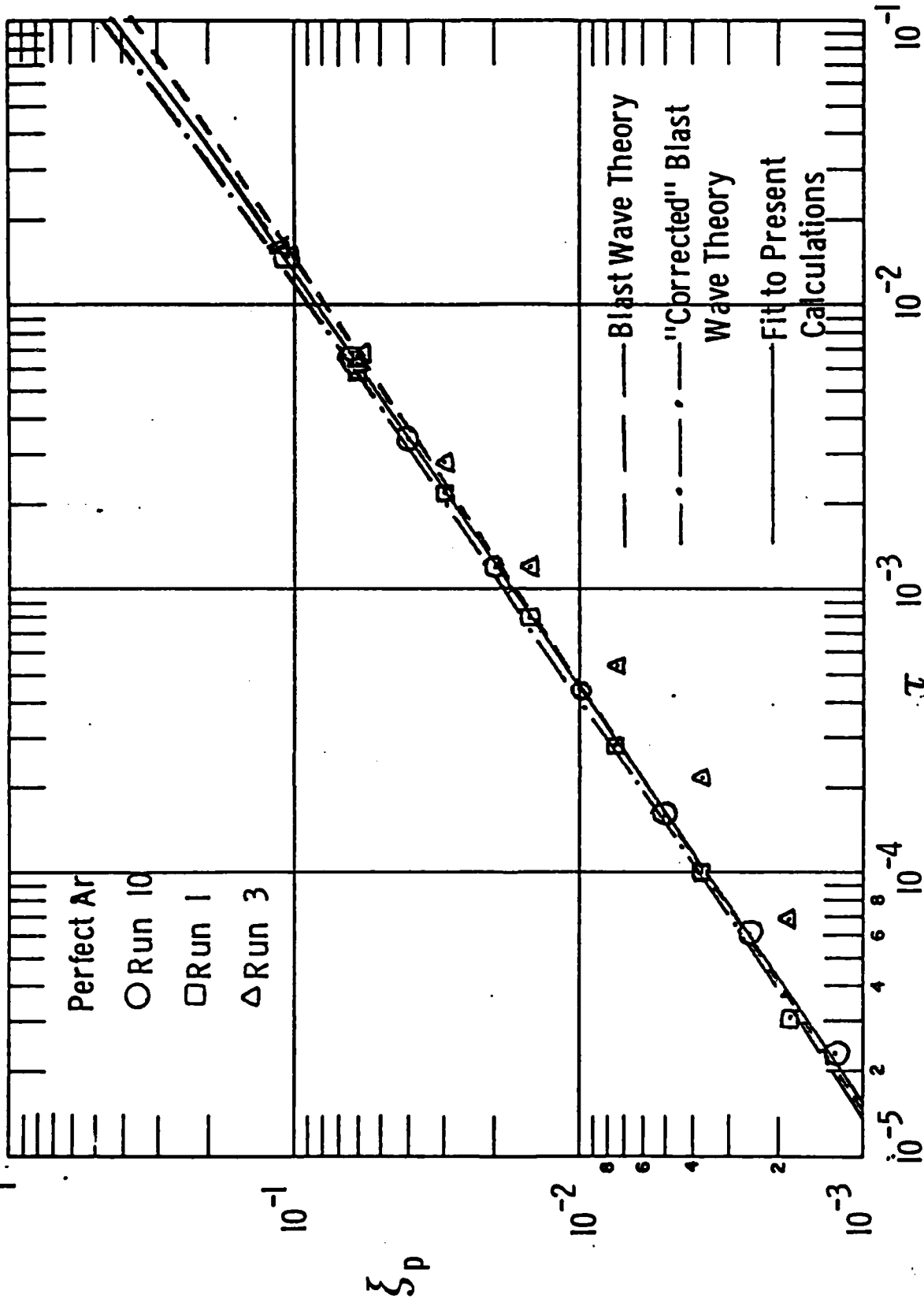


Fig. 3.10 Correlation of shock trajectory for a blast wave in a nozzle. Perfect argon.

realistic as initial conditions, and the points for Run 3 will be ignored, but they do show that a dependence on the initial hot gas conditions can exist if these conditions vary greatly.

A least-square fit to Runs 1 and 10 is shown in Fig. 3.10 as the solid curve. It has the equation

$$\xi_s = 1.674\tau^{2/3} + 0.7499\tau . \quad (3.9.5)$$

The corresponding result from corrected blast wave theory, Ref. 3.5 is found with $I_b = 0.436$ as

$$\xi_s = 1.728\tau^{2/3} + \tau \quad (3.9.6)$$

which is the dash-dot curve in Fig. 3.10. It again shows a slight difference from the fitted curve, being slightly higher, though the differences are not large. If we use the ideal blast wave trajectory, we find

$$\xi_s = 1.728\tau^{2/3} \quad (3.9.7)$$

which is the dashed line in Fig. 3.10. It shows again the discrepancy at the higher values of τ .

The third class of runs is for real argon, and the similarity form of the pressure peak vs time is plotted in Fig. 3.11 for Runs 8, 9, 11 and 2. All but the latter have the conical extension on the nozzle. Again the three runs with low initial density fall together, while Run 2, with initial density at the high throat value, falls low. A least-square fit to runs 8, 9 and 11 is the solid curve, whose equation is

$$\xi_p = 1.358\tau^{2/3} + 0.9746\tau . \quad (3.9.8)$$

To see the difference between real and perfect argon, the fit to the perfect argon calculations, Eq. (3.9.5), has been plotted as the dash-dot curve.

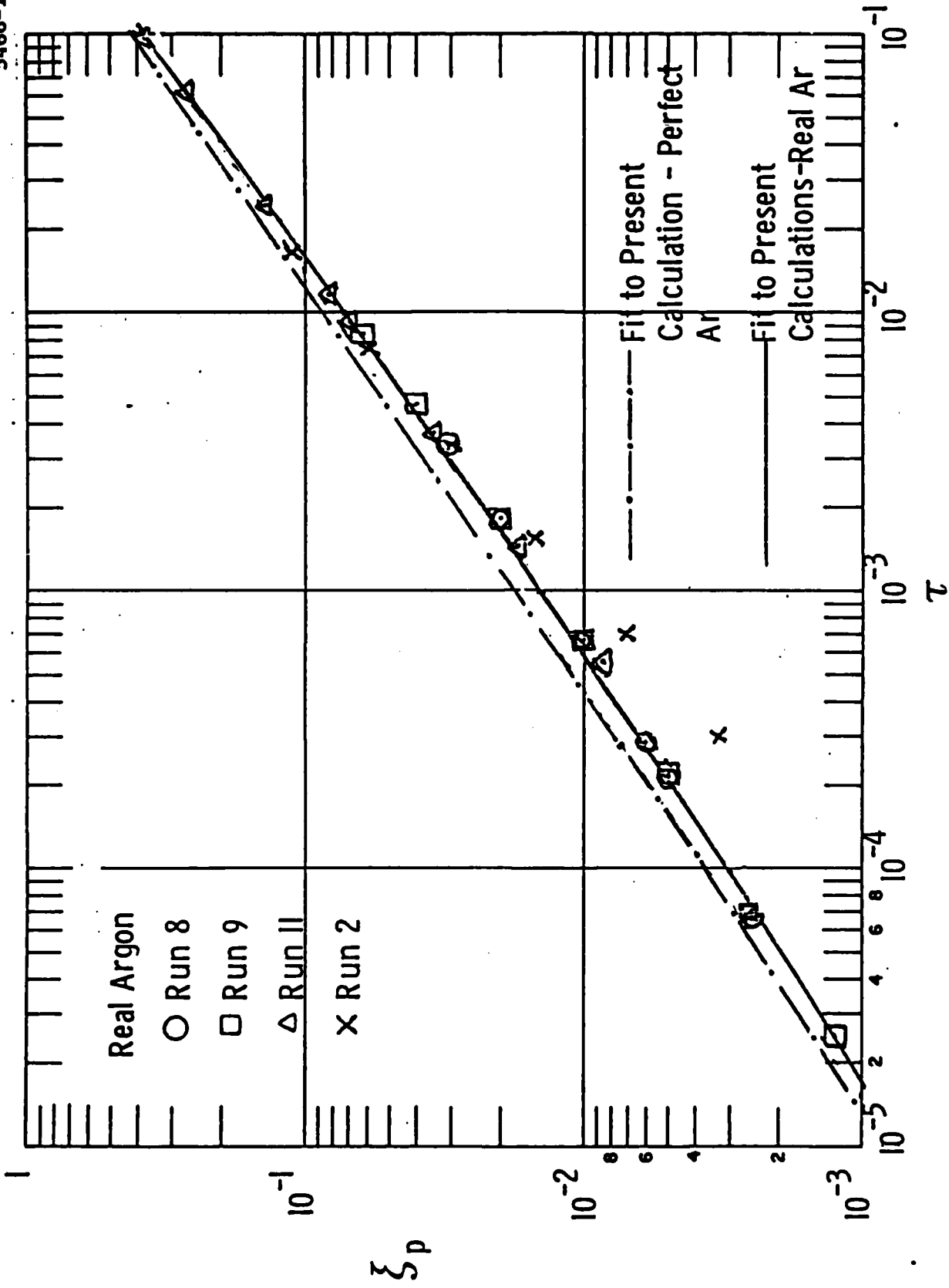


Fig. 3.11 Correlation of shock trajectory for a blast wave in a nozzle. Real argon.

There is a significant difference between the fits for perfect and real argon over the whole range. The corrected blast wave theory curve for perfect argon is even higher than the fitted curve for perfect argon, and so is in worse agreement with the real gas calculations.

Let us now turn to the use of the fitted curves for the purpose of estimating the energy which generated an observed wave. Suppose that the time of arrival of the pressure pulse at each of two stations x_1 and x_2 is measured. The similarity form of the x - t relation we have found is

$$\xi = A\tau^{2/3} + B\tau. \quad (3.9.9)$$

For a given run we know \dot{m} and u_λ . For each E we choose, the values of ξ corresponding to x_1 and x_2 can be found from Eq. (3.9.1). Then Eq. (3.9.9) can be solved to find the values of τ for these values of ξ , and then the values of t follow from Eq. (3.9.1). Thus we can find $\Delta t = t_2 - t_1$ for each E by using the fitted form Eq. (3.9.9). By varying E , a curve of E vs Δt can be constructed. On this curve, the value of E can be read off corresponding to the observed Δt , which tells us what energy was put into the gas to produce the observed Δt between shock arrival at the two measuring stations.

Curves constructed in this way are shown in Fig. 3.12. The case considered is $\dot{m} = 1.180$, $u_\lambda = 5.5875E3$, which corresponds to a nozzle flow with $T_{st} = 300$ K, $p_{st} = 1.3$ atm, the conditions for Runs 8 and 9. The x stations at which ξ is calculated are 17.6 and 12.6 cm. The solid curve is the real argon curve from Eq. (3.9.8), which correlates Runs 8, 9 and 11. The dashed curve is corrected blast wave theory from Eq. (3.9.6), which is for perfect argon. The correlation of the perfect argon calculations, Eq. (3.9.5), is the dash-double-dot curve. The dash-dot curve is also made from a real argon correlation, but of Runs 8 and 9 only, not including the high pressure Run 11. This correlation is

$$\xi_p = 1.300\tau^{2/3} + 0.9336\tau \quad (3.9.10)$$

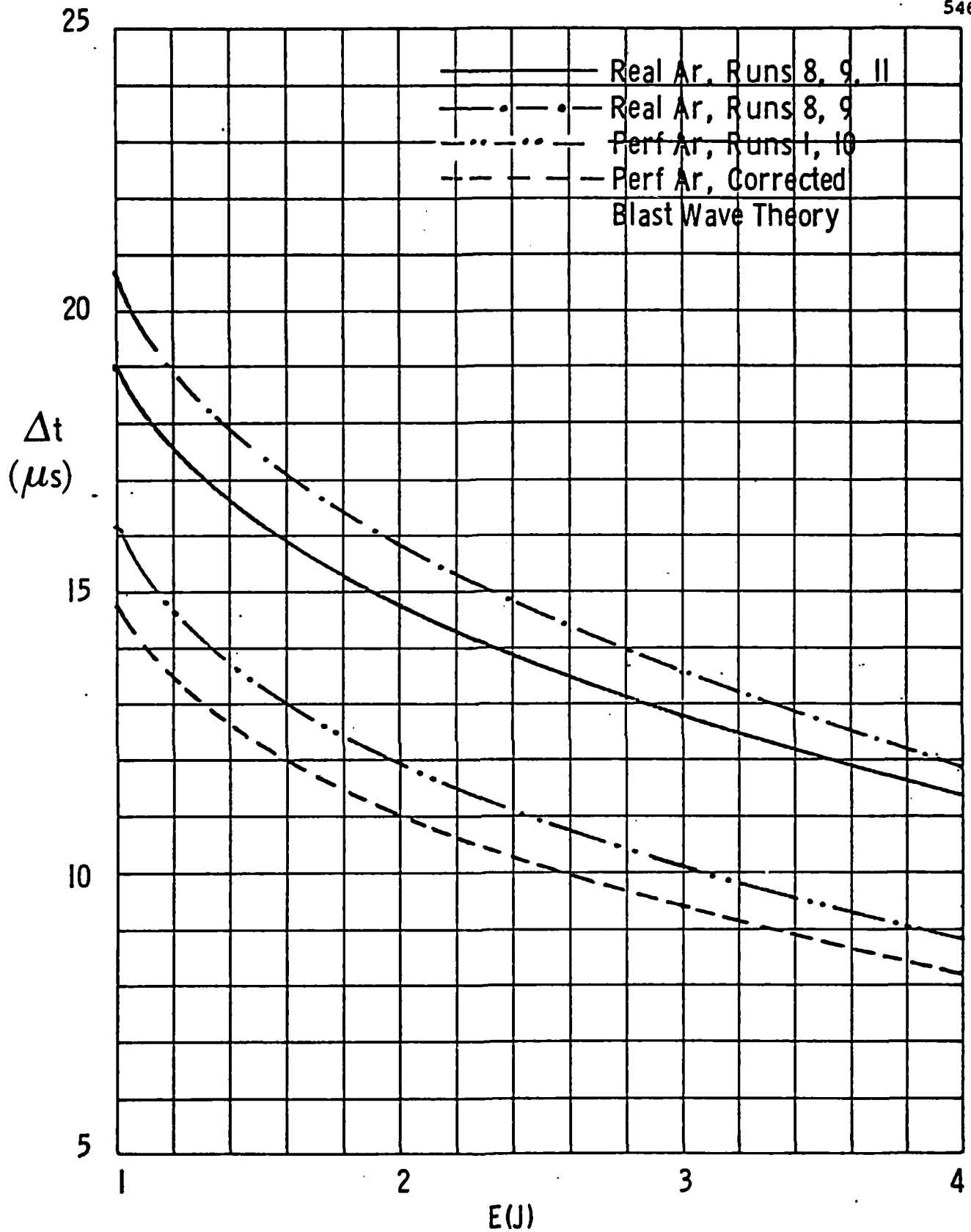


Fig. 3.12 Time interval between shock passage at two stations as a function of energy, for blast wave in a nozzle. $x_1 = 12.6$ cm, $x_2 = 17.6$ cm. Argon with starting stagnation conditions of 1.3 atm, 300 K.

and might be expected to be the best correlation for the present case, since it is made up from runs having the same stagnation conditions and differing only in energy.

The difference between the solid and dash-dot curves in Fig. 3.12 is a measure of the inaccuracies found by using varying m runs to correlate the shock trajectory. This difference varies from 20% at $E = 1$ J to 10% at $E = 4$ J at a fixed Δt .

The errors made by using perfect gas instead of real gas correlations are much larger, nearly a factor of two in energy at a given Δt . It appears that the inclusion of real gas effects in argon are important for the estimation of energy from time of arrival measurements.

3.9.3 Variable Area Nozzle LSD Wave Calculations

So far, only one run has been made with the laser absorption included in the calculation. The laser power started at 5.14 MW and decreased linearly in time to zero at 3.5 μ s. This gives a total laser energy of 9 J. The starting cold flow in the nozzle was generated by stagnation conditions of 1 atm and 300 K. The initial hot gas region, to initiate laser absorption, was at 20,000 K, but at the cold starting flow density, and extended from $x = 0$ to $x = 0.01$ cm, with negligible energy (less than 0.02 J). The conditions of this run in real argon were chosen to approximate an experimental run made at PSI.

The results of this run (Run 4) are shown in Fig. 3.13, where the profiles of temperature, pressure, and laser power (POW) are shown. Of the nine profiles plotted, the first seven are at times when the laser is still on, while the last two are after the laser has turned off.

The pressure in Fig. 9.11a decays very rapidly, as it did in Figs. 3.7b and 3.8b. On the scale plotted, the last two profiles are not visible. (Pressure is normalized here with 34.2 atm.) The temperature, in Fig. 3.13b, is normalized with 10,000 K. Its profile shows a character similar to that of the blast wave profiles of Fig. 3.8a, rather than that of the LSD wave profiles of Fig. 3.4a. Examination of the power profiles of

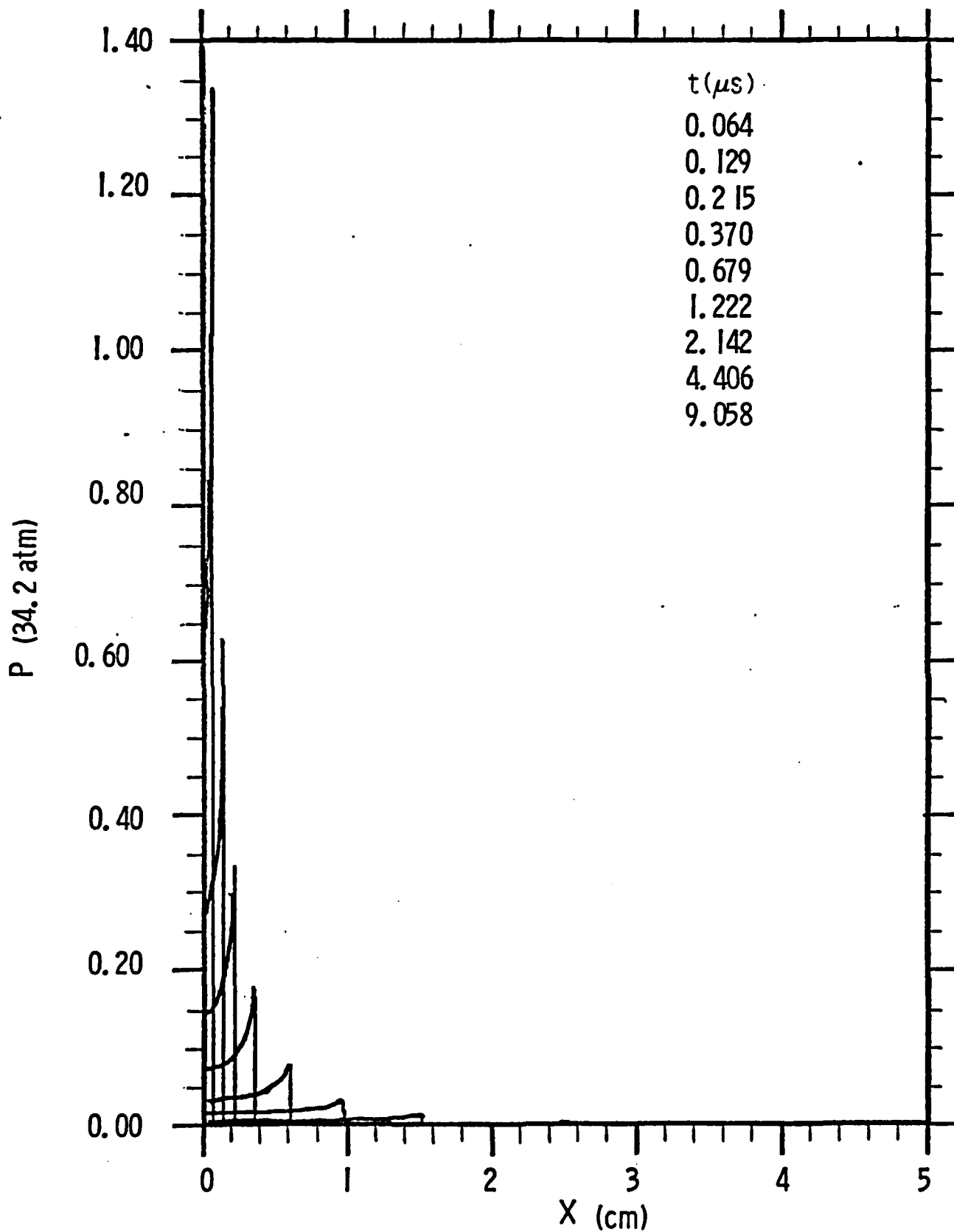


Fig. 3.13a Calculated pressure profiles for laser absorption in a nozzle. Real argon with starting stagnation conditions of 1 atm, 300 K. Triangular laser pulse starting at 5.14 μs and turning off at 3.5 μs .

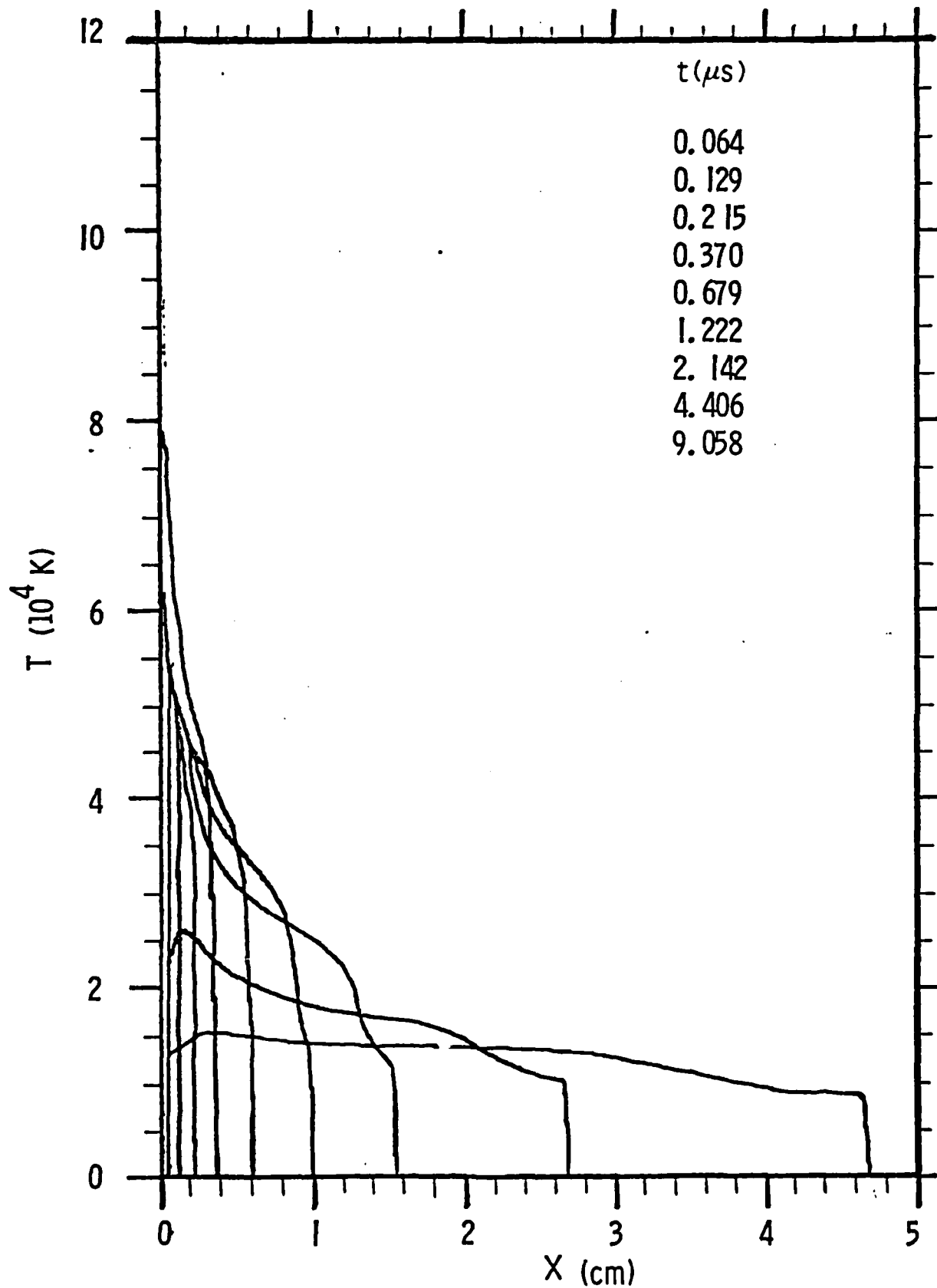


Fig. 3.13b Calculated temperature profiles for laser absorption in a nozzle. Real argon with starting stagnation conditions of 1 atm, 300 K. Triangular laser pulse starting at 5.14 MW and turning off at 3.5 μ s.

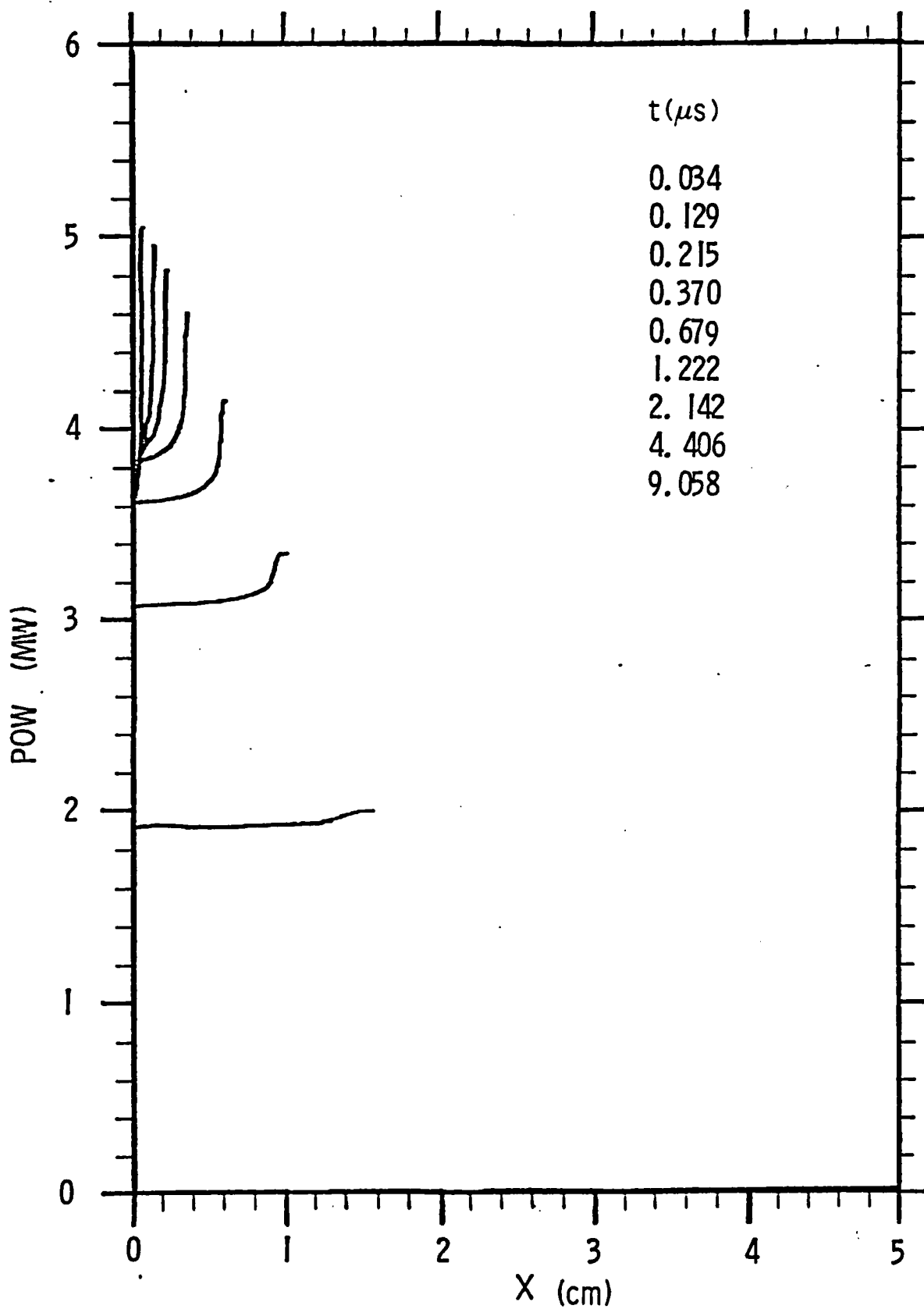


Fig. 3.13c Calculated power profiles for laser absorption in a nozzle. Real argon with starting stagnation conditions of 1 atm, 300 K. Triangular laser pulse starting at 5.14 MW and turning off at 3.5 μs .

Fig. 3.13a (normalized by 1 MW) shows that not much of the laser energy has been absorbed by the gas. For the early time profiles, nearly all the laser energy is absorbed as the beam traverses the gas. However, as the initial hot gas expands and cools, less and less energy is absorbed. By 0.18 μ s, only 29% of the energy has been absorbed by the gas, by 0.92 μ s only 18% has been absorbed, and by the time the laser turns off, the gas has absorbed only 11%. The rest has reached the walls.

The reason for the small amount of absorption must be sought in the gas conditions that prevail for this low pressure ($p_{st} = 1$ atm) case. The starting densities are quite low due to the rapid expansion, varying from $1.054E-3$ g/cm³ at the throat to $8.15E-7$ g/cm³ at $x = 5$ cm. At 0.92 μ s, the maximum density is only $4.E-5$ g/cm³, and over most of the flow it is below $1.E-5$ g/cm³. Although the temperature is as high as 55,000 K, and ionization is complete, the electron-ion Bremsstrahlung absorption goes like density squared, and the absorption coefficient is never larger than 2 cm⁻¹ over a total distance of 0.8 cm. In fact, it is larger than 1 cm⁻¹ over about 0.034 cm, and smaller over the rest of the 0.8 cm. So there is not enough distance with large enough absorption to absorb the laser energy.

The situation is different from the case of Fig. 3.5, where the energy was not absorbed at the shock front, but was absorbed behind it. There was no area change, so the rapid expansion of the gas as it moved down the channel, which occurs in the present case, did not occur there.

It appears that absorption in rapidly expanding nozzles will present a problem unless the stagnation conditions are high enough to keep the density high and provide large absorption coefficients over significant lengths.

3.10 Equilibrium Properties of Hydrogen

Besides argon, another working fluid of interest is hydrogen. In this section we will present a model for the equilibrium properties of hydrogen which has been used to relate the internal energy per unit mass e and density ρ to the pressure temperature, and composition of the gas. As pointed out in Sec. 3.2, the natural variables for the non-steady flow equations include e and ρ . Therefore the equilibrium properties need to be expressed as functions of e and ρ . The model uses ρ and temperature T as independent variables. When ρ and e are given, an iterative solution on e can be used to find T , pressure p , and composition. This iteration is too time-consuming to be used in the flow program, where it would have to be performed as much as a million times. Instead, a separate program was constructed to perform the iteration and produce a table of p , T and composition with e and ρ as the independent variables. The flow program interpolates in this table, which is a very fast procedure, and provides good accuracy for the equilibrium properties of hydrogen.

We characterize the hydrogen as a mixture of perfect gases whose components have number densities: molecules n_M , atoms n_A , ions n_I and electrons n_E . We do not expect to get a temperature where other species are significant, nor are there multiply-ionized atoms, so $n_I = n_E$. As reaction coordinates we use the fraction of molecules dissociated β and the fraction of atoms ionized, α :

$$\beta = \frac{(n_A + n_I)/2}{n_M + (n_A + n_I)/2}, \quad \alpha = \frac{n_I}{n_A + n_I} \quad (3.10.1)$$

In terms of the original number of particles per unit volume,

$$n_0 = n_M + (n_A + n_I)/2 \quad (3.10.2)$$

the number of density of the species are

$$n_M = n_0 (1 - \beta), \quad n_A = 2n_0 \beta (1 - \alpha), \quad n_I = n_E = 2n_0 \beta \alpha \quad (3.10.3)$$

and the corresponding partial pressures are found from

$$p_i = n_i kT \quad (3.10.4)$$

where k is the Boltzmann constant. The partial mass densities are, in terms of the particle masses m_i ,

$$\rho_M = n_M m_M, \quad \rho_A = n_A m_A, \quad \rho_I = n_I m_I, \quad \rho_E = n_E m_E \quad (3.10.5)$$

and the total number and mass densities are

$$n = n_0 [1 + \beta (1 + 2\alpha)], \quad \rho = n_0 m_M \quad (3.10.6)$$

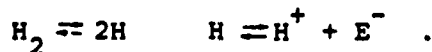
Whenever convenient, we will use the facts that an excellent approximation for hydrogen is $m_A = m_I = m_M/2$.

The equation of state is the sum of the partial pressures,

$$p = \rho Z R_M T, \quad Z = 1 + \beta (1 + 2\alpha), \quad R_M = k/m_M \quad (3.10.7)$$

where Z is the compressibility factor and R_M the gas constant for the molecules. Since ρ and T are the dependent variables, we need α , β in terms of T , ρ .

Since we deal with hydrogen in thermochemical equilibrium, α and β are determined by the Law of Mass Action in terms of the thermodynamic variables of the mixture. There are two reactions occurring, dissociation and ionization:



For each, the equilibrium constant provides a relation between the partial pressures and the partition functions of the species, involving the heat of reaction. These relations are

$$\frac{P_A^2}{P_M} = \left(\frac{\pi m_A}{h_p^2} \right)^{3/2} \frac{(kT)^{5/2} Q_{elA}^2}{Q_c Q_v Q_r Q_{elM}} e^{-h_D^{\circ} m_M / kT} \quad (3.10.8a)$$

$$\frac{P_I P_E}{P_A} = \left(\frac{2\pi m_E}{h_p^2} \right)^{3/2} (kT)^{5/2} \frac{Q_{elI} Q_{elE}}{Q_{elA}} e^{-h_{IL}^{\circ} m_I / kT} \quad (3.10.8b)$$

where h_p is Planck's constant, Q_v and Q_r are the vibrational and rotational partition functions of H_2 , Q_c is a partition function reflecting vibration-rotation coupling, Q_{eli} are the electronic partition functions of the species, h_D° is the heat of dissociation of a molecule per unit mass and h_{IL}° is the heat of ionization of an atom per unit mass. From Eqs. (3.10.3, 4, 5, and 6) the partial pressure ratios are

$$\frac{P_A^2}{P_M} = \frac{4\beta^2 (1 - \alpha)^2}{1 - \beta} n_o kT = \frac{4\beta^2 (a - \alpha)^2}{1 - \beta} \frac{\rho kT}{m_M} \quad (3.10.9a)$$

$$\frac{P_I P_E}{P_A} = \frac{4\beta^2 \alpha^2}{2\beta (1 - \alpha)} n_o kT = \frac{2\beta \alpha^2}{1 - \alpha} \frac{\rho kT}{m_M} \quad (3.10.9b)$$

The electronic partition function for the molecule may be replaced by its ground-state statistical weight 1, since its first excited state lies very high (132,000 K). For the electron $Q_{elE} = 2$ because of the two electron spin states, and for the ion, there are no internal states, $Q_{elI} = 1$.

Using Eq. (3.10.9) in Eq. (3.10.8), we find

$$\frac{\beta^2 (1 - \alpha)^2}{(1 - \beta)} = \frac{g_D(T)}{\rho} \quad (3.10.10a)$$

$$\frac{\beta \alpha^2}{(1 - \alpha)} = \frac{g_I(T)}{\rho} \quad (3.10.10b)$$

where we have defined

$$g_D = \frac{T^{3/2} e^{-\theta_D/T} Q_{elA}^2}{Q_c Q_r Q_v} \frac{Q_{elA}^2}{4} m_M k \left(\frac{\pi m_A k}{h_P^2} \right)^{3/2}, \quad \theta_D = h_D^0 m_M/k \quad (3.10.11a)$$

$$= 51,970 \text{ K}$$

$$g_I = \frac{T^{3/2} e^{-\theta_{IL}/T}}{Q_{elA}} m_M k \left(\frac{2\pi m_E k}{h_P^2} \right)^{3/2}, \quad \theta_{IL} = h_{IL}^0 m_I/k. \quad (3.10.11b)$$

Equations (3.10.10) define α , β in terms of ρ , T , and could be used. However, they are difficult to solve for α and β , and can be simplified considerably for hydrogen without much loss of accuracy. Equilibrium hydrogen dissociates almost completely before it ionizes significantly. We can thus separate the two reactions, and assume α is small during dissociation, while β goes from 0 to 1. Then β is near unity while α increases from near zero. These two approximations are separated by a temperature T^* below which there are molecules and atoms with very few electrons, and above which there are atoms, ions and electrons, with few molecules. Therefore we use

$$T < T^* : \frac{\beta^2}{1 - \beta} = \frac{g_D(T)}{\rho}, \quad \beta \alpha^2 = \frac{g_I(T)}{\rho} \quad (3.10.12a)$$

$$T > T^* : \frac{(1 - \alpha)^2}{(1 - \beta)} = \frac{g_D(T)}{\rho}, \quad \frac{\alpha^2}{1 - \alpha} = \frac{g_I(T)}{\rho}. \quad (3.10.12b)$$

These are easily solved for β and α to yield

$$T < T^* : \beta = \frac{g_D}{2\rho} \left[-1 + \sqrt{1 + \frac{4\rho}{g_D}} \right], \quad \alpha = \left[\frac{g_I}{\beta\rho} \right]^{1/2} \quad (3.10.13a)$$

$$T > T^* : \alpha = \frac{g_I}{2\rho} \left[-1 + \sqrt{1 + \frac{4\rho}{g_I}} \right], \quad 1 - \beta = (1 - \alpha)^2 \frac{\rho}{g_D} \quad (3.10.13b)$$

In general, we will only use β as variable below T^* from Eq. (3.10.13a), and take $\alpha = 0$. Above T^* we will take α as variable, from Eq. (3.10.13b), and take $\beta = 1$. The second expressions in Eq. (3.10.13) will only be used if an estimate which differs from zero is needed for α below T^* , or which differs from unity for β above T^* .

To complete the specification of g_D and g_I we need the partition functions. The combination $Q_c Q_r Q_v$ can be found in Ref. 3.8, p. 163, Eq. (7.39), where it is called Q_{vjm} . It may be divided as follows:

$$Q_r = T/2 \theta_r, \quad Q_v = \left(1 - e^{-\theta_v/T} \right)^{-1} \quad (3.10.14)$$

Rotation has been taken to be fully excited, and the factor 2 in Q_r has been added to Ref. 3.8 because of the symmetry of the hydrogen molecule. The vibrational and rotational temperature constants θ_v and θ_r come from Eqs. (7.32) and (7.33), p. 162, of Ref. 3.8 using the JANNAF spectroscopic constants (in cgs units)

$$B_e = 60.848, \quad \omega_e = 4405.3, \quad x_e = 125.325/4405.3 = .0284$$

$$\delta = 3.0664/60.848 = .0504, \quad \gamma = 60.848/4405.3 = .0138$$

They are

$$\theta_v = \frac{h_p c \omega_e (1 - x_e)}{k}, \quad \theta_r = \frac{h_p c B_e}{k} \left(1 - \frac{\delta}{2}\right)$$

$$\theta_v = 5978 \text{ K} \quad \theta_r = 85.34 \text{ K}.$$

The remaining factor Q_c is the coupling partition function,

$$Q_c = 1 + \frac{\theta_r}{3T} + \frac{8\gamma^2 T}{\theta_r} + \frac{\delta}{e^{\theta_v/T} - 1} + \frac{2x_e \theta_v/T}{\left(e^{\theta_v/T} - 1\right)^2} \quad (3.10.15)$$

$$= 1 + \frac{28.45}{T} + 1.785 \times 10^{-5} T + \frac{5.04 \times 10^{-2}}{e^{\theta_v/T} - 1} + \frac{5.68 \times 10^{-2} \theta_v/T}{\left(e^{\theta_v/T} - 1\right)^2}.$$

The last expression needed is for the electronic partition function of the atoms, which is

$$Q_{elA} = 2S_1 e^{-\theta_{IL}/T}, \quad S_1 = \sum_{j=1}^L j^2 \exp\left(\frac{\theta_{IL}}{Tj^2}\right). \quad (3.10.16)$$

The first term is the ground state weight 2. The subsequent terms account for excited electronic states. The upper limit of the sum must be finite, since the terms grow like j^2 for large j . The finite cut-off means that above some degree of excitation the electron is no longer considered bound to an atom, but is a free electron. Related to this necessity for cutting off the sum is the lowering of the ionization potential. The value of h_{IL}^0 is not that for removing an electron infinitely far from an atom, because in an ionized mixture the electron no longer is considered bound when it is

far enough from the atom to be indistinguishable from other electrons. Thus θ_{IL} is not the value $\theta_I = 157,770$ K obtained from the spectroscopic constants for a very weakly ionized mixture, but a lower value (hence the subscript L). If these two effects are not accounted for, the composition of equilibrium hydrogen at high temperatures and pressure will be noticeably in error, as found in Ref. 3.9, Table 7.1.

The lowering of the ionization potential is discussed in Ref. 3.10. In Eq. (3.85), p. 218, it is suggested that

$$\Delta I = k\Delta\theta_I = 2 e^3 \left(2\pi n_E / kT \right)^{1/2}$$

where e is the charge in esu, and the other units are cgs. For hydrogen, $e = 4.803 \times 10^{-10}$ esu, and we have

$$\Delta I = 4.728 \times 10^{-20} \left[\frac{n_E (\text{cm}^{-3})}{T(\text{K})} \right]^{1/2} \text{ ergs} . \quad (3.10.17)$$

This relates the lowering of the ionization potential to T and the electron density, which is, in turn, related to α by Eq. (3.10.3), and so depends on θ_{IL} through g_I in Eq. (3.10.13b). Thus, the determination of α is an iterative process, requiring iteration on θ_{IL} . It also requires iteration on the upper limit L of the sum in Eq. (3.10-16), which is related to θ_{IL} . There are a number of such relations which can be used. Here we have chosen a simple one, namely to cut off when

$$\theta_I / j^2 > \Delta I / k .$$

In the present work, we have used one step in the iteration, calculating α by the following procedure:

- 1) Find α from Eq. (3.10.13b) using $\theta_{IL} = \theta_I = 157,770$ K, $L = 17$.

- 2) Find n_E from Eqs. (3.10.3) and (3.10.6) using this α .
- 3) Find ΔI from Eq. (3.10.17).
- 4) Calculate $\theta_{IL} = \theta_I - \Delta I / 1.3806 \times 10^{-23}$.
- 5) Calculate a cut-off $L =$ greatest integer in $[\theta_I / (\theta_I - \theta_{IL})]^{1/2}$.
- 6) Recalculate α using θ_{IL} and this L .

The resulting value of α is taken as the correct one. Further iterations could be performed, but it will be seen that this one iteration yields quite accurate results.

This calculation of Q_{elA} is used only for $T > T^*$, where α is the varying reaction coordinate and $\beta = 1$ in general. (However, if an estimate of β different from unity is needed, we may use this Q_{elA} in the second of Eq. (3.10.13b).) For $T < T^*$, there is very little ionization and the temperature is low, so we may take $Q_{elA} = 2$, its ground state value, to calculate the varying reaction coordinate β . The value of α in this region is zero. (If an estimate of α different from zero is needed, we may use the second of Eq. (3.10.13a), with $Q_{elA} = 2$.)

The internal energy is made up of the contributions of the various components. Electrons have no internal degrees of freedom so their internal energy per unit mass is

$$e_E = 3 kT / 2m_E \quad (3.10.18)$$

Hydrogen ions also have no internal degrees of freedom, but they carry the dissociation energy h_D^0 and the ionization energy h_{IL}^0 , so their internal energy per unit mass is

$$e_I = \frac{3kT}{2m_I} + h_D^0 + h_{IL}^0 = \frac{kT}{m_A} \left[\frac{3}{2} + \frac{\theta_D}{2T} + \frac{\theta_{IL}}{T} \right] \quad (3.10.19)$$

Hydrogen atoms have electronic internal degrees of freedom represented by the partition function Q_{elA} defined in Eq. (3.10.16), and carry the dissociation energy. Their internal energy per unit mass is

$$e_A = \frac{3kT}{m_A} + h_D^o + \frac{kT^2}{m_A} \frac{d \ln Q_{elA}}{dT} \quad (3.10.20)$$

$$= \frac{kT}{m_A} \left[\frac{3}{2} + \frac{\theta_D}{2T} + \frac{\theta_{IL}}{T} \left(1 - \frac{S_2}{S_1} \right) \right]$$

where the sum S_1 is defined in Eq. (3.10.16) and the sum S_2 , obtained from the differentiation, is

$$S_2 = \sum_{j=1}^L \exp\left(\theta_{IL}/Tj^2\right). \quad (3.10.21)$$

Finally, the molecules have rotational and vibrational internal degrees of freedom. We take rotation to be fully excited, as before. Then the internal energy per unit mass is

$$e_M = \frac{3kT}{2m_M} + \frac{2kT}{2m_M} + \frac{kT^2}{m_M} \frac{d \ln Q_v}{dT} \quad (3.10.22)$$

$$= \frac{kT}{m_M} \left[\frac{5}{2} + \psi_v \right]$$

where ψ_v is the vibrational contribution obtained by differentiating Q_v from Eq. (3.10.14), and is defined as

$$d \ln Q_v / d \ln T = \psi_v = \left(\theta_v / T \right) / \left(e^{\theta_v / T} - 1 \right). \quad (3.10.23)$$

The internal energy of the mixture is the sum of the species energies, weighted by their mass fractions:

$$e = \sum e_i \rho_i / \rho . \quad (3.10.24)$$

The mass fractions are found in terms of α and β by using Eqs. (3.10.3, 5, and 6):

$$\frac{\rho_M}{\rho} = 1 - \beta, \quad \frac{\rho_A}{\rho} = \beta (1 - \alpha), \quad \frac{\rho_I}{\rho} = \beta \alpha, \quad \frac{\rho_E}{\rho} = \frac{\beta \alpha m_E}{m_I} . \quad (3.10.25)$$

In the low temperature regime there are only molecules and atoms, so we use only those terms, with $\alpha = 0$. In e_A we ignore the last term, since the first terms of the sums S_1 and S_2 are equal. We then find, from Eqs. (3.10.20, 21, 24 and 25), that

$$T < T^* : e = \frac{kT}{m_A} \left[\left(1 - \beta \right) \left(\frac{5}{4} + \frac{\psi_v}{2} \right) + \beta \left(\frac{3}{2} + \frac{\theta_D}{2T} \right) \right] . \quad (3.10.26a)$$

In the high temperature regime there are atoms, ions and electrons, but $\beta = 1$. Then Eqs. (3.10.18, 19, 20, 24 and 25) yield

$$T > T^* : e = \frac{kT}{m_A} \left\{ \frac{3}{2} (1 + \alpha) + \frac{\theta_D}{2T} + \frac{\theta_{IL}}{T} \left[1 - (1 - \alpha) \frac{S_2}{S_1} \right] \right\} . \quad (3.10.26b)$$

The speed of sound is needed to apply the Courant condition in the numerical method. A general thermodynamic expression for the speed of sound is

$$a^2 = \left(\frac{\partial p}{\partial \rho} \right)_{\text{entropy}} = \frac{(\partial h / \partial \rho)_p}{\rho^{-1} - (\partial h / \partial p)_\rho}$$

where h is the gas enthalpy. If we convert the derivatives from the independent variables p, ρ to T, ρ we find

$$a^2 = \frac{(\partial h / \partial \rho)_T (\partial p / \partial T)_\rho - (\partial h / \partial T)_\rho (\partial p / \partial \rho)_T}{\rho^{-1} (\partial p / \partial T)_\rho - (\partial h / \partial T)_\rho} \quad (3.10.27)$$

The pressure derivatives are easily found from the gas law Eq. (3.10.7) as

$$\left(\frac{\partial p}{\partial \rho}\right)_T = R_M T \left[z + \rho \left(\frac{\partial z}{\partial \rho}\right)_T \right] \quad (3.10.28a)$$

$$\left(\frac{\partial p}{\partial T}\right)_\rho = R_M \rho \left[z + T \left(\frac{\partial z}{\partial T}\right)_\rho \right].$$

Although the enthalpy derivatives could be converted to internal energy derivatives, it is perhaps useful to record the enthalpy expressions, so we will use Eq. (3.10.27) as it is. Enthalpy is, of course, obtained from internal energy by the relation

$$h = e + p/\rho \quad (3.10.29)$$

Using the gas law Eq. (3.10.7) and the expressions, Eq. (3.10.26) for e , we find

$$T < T^* : h = \frac{kT}{m_A} \left[(1 - \beta) \left(\frac{7}{4} + \frac{\psi_v}{2} \right) + \beta \left(\frac{5}{2} + \frac{\theta_D}{2T} \right) \right] \quad (3.10.30a)$$

$$T > T^* : h = \frac{kT}{m_A} \left\{ \frac{5}{2} (1 + \alpha) + \frac{\theta_D}{2T} + \frac{\theta_{IL}}{T} \left[1 - (1 - \alpha) \frac{S_2}{S_1} \right] \right\} \quad (3.10.30b)$$

The enthalpy derivatives are then obtained in a straightforward manner

as:

$$T < T^* : \left(\frac{\partial h}{\partial \rho} \right)_T = \frac{kT}{m_A} \left[\frac{3}{4} - \frac{\psi_v}{2} + \frac{\theta_D}{2T} \right] \left(\frac{\partial \beta}{\partial \rho} \right)_T \quad (3.10.31a)$$

$$\begin{aligned} \left(\frac{\partial h}{\partial T} \right)_\rho &= \frac{k}{m_A} \left[(1 - \beta) \left(\frac{7}{4} + \frac{\phi_v}{2} \right) + \frac{5\beta}{2} \right] \\ &+ \frac{kT}{m_A} \left[\frac{3}{4} - \frac{\psi_v}{2} + \frac{\theta_D}{2T} \right] \left(\frac{\partial \beta}{\partial T} \right)_\rho \end{aligned} \quad (3.10.31b)$$

where

$$\phi_v = \frac{dT\psi_v}{dT} = \psi_v^2 e^{\theta_v/T} \quad (3.10.32)$$

$$T > T^* : \left(\frac{\partial h}{\partial \rho} \right)_T = \frac{kT}{m_A} \left[\frac{5}{2} + \frac{\theta_{IL}}{T} \frac{s_2}{s_1} \right] \left(\frac{\partial \alpha}{\partial \rho} \right)_T \quad (3.10.33a)$$

$$\begin{aligned} \left(\frac{\partial h}{\partial T} \right)_\rho &= \frac{k}{m_A} \left[\frac{5}{2} (1 + \alpha) - \frac{\theta_{IL}^2}{T^2} (1 - \alpha) \left(\frac{s_4}{s_1} - \frac{s_2^2}{s_1^2} \right) \right] \\ &+ \frac{kT}{m_A} \left[\frac{5}{2} + \frac{\theta_{IL}}{T} \frac{s_2}{s_1} \right] \left(\frac{\partial \alpha}{\partial T} \right)_\rho \end{aligned} \quad (3.10.33b)$$

where

$$s_4 = \sum_{j=1}^L j^{-2} \exp \left(\theta_{IL}/Tj^2 \right) \quad (3.10.34)$$

and the term containing this sum arises from the differentiation of S_2/S_1 with respect to T .

The derivatives of β and α are found from Eq. (3.10.10). In the process we need the derivatives of g_D and g_I from Eq. (3.10.11). In g_D we remember that $Q_{e1A} = 2$, a constant, in the low temperature regime, and we do not differentiate the small coupling partition function Q_c . Then, by using the definitions in Eq. (3.10.14) we find

$$\frac{d \ln g_D}{dT} = \frac{1}{T} \left(\frac{1}{2} - \psi_v + \frac{\theta_D}{T} \right) \quad (3.10.35a)$$

For g_I , we recall the definitions, Eqs. (3.10.16 and 21) and find

$$\frac{d \ln g_I}{dT} = \frac{1}{T} \left(\frac{3}{2} + \frac{\theta_{IL}}{T} \frac{S_2}{S_1} \right) \quad (3.10.35b)$$

It is then simple to differentiate Eq. (3.10.10). The results are:

$$T < T^* : \left(\frac{\partial \beta}{\partial \rho} \right)_T = \frac{-\beta(1 - \beta)}{\rho(2 - \beta)} \quad (3.10.36a)$$

$$\begin{aligned} \left(\frac{\partial \beta}{\partial T} \right)_\rho &= \frac{\beta(1 - \beta)}{2 - \beta} \frac{d \ln g_D}{dT} \\ &= \frac{\beta(1 - \beta)}{2 - \beta} \frac{1}{T} \left(\frac{1}{2} - \psi_v + \frac{\theta_D}{T} \right) \end{aligned} \quad (3.10.36b)$$

$$T > T^* : \left(\frac{\partial \alpha}{\partial \rho} \right)_T = \frac{-\alpha(1-\alpha)}{\rho(2-\alpha)} \quad (3.10.37a)$$

$$\begin{aligned} \left(\frac{\partial \alpha}{\partial T} \right)_\rho &= \frac{\alpha(1-\alpha)}{2-\alpha} \frac{d \ln g_I}{dT} \\ &= \frac{\alpha(1-\alpha)}{2-\alpha} \frac{1}{T} \left(\frac{3}{2} + \frac{\theta_{IL}}{T} \frac{S_2}{S_1} \right) \end{aligned} \quad (3.10.37b)$$

The pressure derivatives are expressible in terms of the β and α derivatives from Eq. (3.10.28).

$$T < T^* : \quad Z = 1 + \beta$$

$$\left(\frac{\partial p}{\partial \rho} \right)_T = R_M T \left[1 + \beta + \rho \left(\frac{\partial \beta}{\partial \rho} \right)_T \right] \quad (3.10.38a)$$

$$\left(\frac{\partial p}{\partial T} \right)_\rho = R_M \rho \left[1 + \beta + T \left(\frac{\partial \beta}{\partial T} \right)_\rho \right] \quad (3.10.38b)$$

$$T > T^* : \quad Z = 2(1 + \alpha)$$

$$\left(\frac{\partial p}{\partial \rho} \right)_T = 2R_M \left[1 + \alpha + \rho \left(\frac{\partial \alpha}{\partial \rho} \right)_T \right] \quad (3.10.39a)$$

$$\left(\frac{\partial p}{\partial T} \right)_\rho = 2R_M \left[1 + \alpha + T \left(\frac{\partial \alpha}{\partial T} \right)_\rho \right] \quad (3.10.39b)$$

We now have all the terms necessary to find the speed of sound from Eq. (3.10.27) by using Eqs. (3.10.31, 32, 33, 34, 46, 37, 38 and 29) in the proper temperature regimes.

There remains only the specification of T^* , the temperature at which we shift from dissociation with no ionization to ionization with full dissociation. Probably the most accurate compilation of the properties of equilibrium hydrogen is that of Patch, Ref. 3.11. A perusal of his tables shows that the first temperature at which the number of hydrogen molecules is less than the number of electrons is given by the following table:

p (atm) :	1	3	10	30	100
T (10^3 K):	7.3	8	9	10	11

If we take these values as T^* , except using 7000 instead of 7300 at 1 atm, then the relation

$$T^* = 2000 \log_{10} p(\text{atm}) + 7000 \quad (3.10.40)$$

fits $p = 1, 10,$ and $100,$ and is very close to the values at $p = 3, 30.$ We will adopt Eq. (3.10.40) as the definition of $T^*.$

A comparison of some values calculated using the expressions given in this section with those given by Patch is shown in Table 3.3. The enthalpies from Patch have had 2.16×10^8 J/kg added to them because of his use of the atom as the zero of enthalpy, rather than the molecule which is used here.

The comparison shows the present properties to be an excellent approximation to those resulting from Patch's elaborate calculations. The major species are in agreement within a few percent, as are the enthalpies and the specific heats. Only the minor species have serious differences, that is, electrons below T^* and molecules above $T^*.$ It should be noted that Patch has included H_2^+, H_3^+, H^- which are not considered here. He also distinguishes the ground electronic state and excited electronic states of both H_2^+ (H_2 and H_2^*) and H (H^+ , H^*). We have added these in our comparison. He

TABLE 3.3

COMPARISON OF PRESENT THERMODYNAMIC
PROPERTIES WITH THOSE OF PATCH (Ref. 3.11)

T (10 ³ K)	n _M (m ⁻³)		n _A (m ⁻³)		n _E (m ⁻³)		h (J/kg)		c _p (J/kg K)	
	PSI	P	PSI	P	PSI	P	PSI	P	PSI	P
4	4.27 ²³	4.28 ²³	1.41 ²⁴	1.40 ²⁴	7.99 ¹⁶	8.84 ¹⁶	2.09 ⁸	2.12 ⁸	17.6 ⁴	17.3 ⁴
	3.15 ²⁰	3.36 ²⁰	9.13 ²³	9.13 ²⁴	2.09 ²¹	2.09 ²¹	3.84 ⁸	3.84 ⁸	2.55 ⁴	2.55 ⁴
	1.30 ¹⁹	1.44 ¹⁶	4.97 ²³	4.98 ²³	5.71 ²²	5.72 ²²	6.25 ⁸	6.24 ⁸	12.80 ⁴	12.71 ⁴
	2.55 ¹⁷	2.10 ¹⁷	1.13 ²³	1.15 ²³	1.73 ²³	1.74 ²³	15.5 ⁸	15.4 ⁸	27.0 ⁴	25.9 ⁴
	1.75 ¹⁵	3.47 ¹⁵	1.50 ²²	1.50 ²²	1.76 ²³	1.77 ²³	22.3 ⁸	22.2 ⁸	8.86 ⁴	8.88 ⁴
8	1.12 ²⁵	1.12 ²⁵	7.20 ²⁴	7.18 ²⁴	1.81 ¹⁷	4.65 ¹⁷	1.22 ⁸	1.25 ⁸	11.2 ⁴	11.1 ⁴
	3.15 ²²	3.36 ²²	9.13 ²⁴	9.13 ²⁴	6.55 ²¹	6.67 ²¹	3.79 ⁸	3.80 ⁸	2.22 ⁴	2.36 ⁴
	1.72 ²¹	1.90 ²¹	5.72 ²⁴	5.72 ²⁴	1.99 ²³	1.99 ²³	5.16 ⁸	5.16 ⁸	5.64 ⁴	5.61 ⁴
	1.60 ²⁰	1.81 ²⁰	2.78 ²⁴	2.81 ²⁴	9.01 ²³	9.11 ²³	9.58 ⁸	9.51 ⁸	17.3 ⁴	17.1 ⁴
	6.70 ¹⁸	8.54 ¹⁸	7.77 ²³	7.92 ²³	1.45 ²⁴	1.48 ²⁴	17.7 ⁸	17.5 ⁸	19.0 ⁴	19.0 ⁴
12	1.56 ²⁶	1.57 ²⁶	2.70 ²⁵	2.69 ²⁵	3.50 ¹⁷	3.01 ¹⁸	.84 ⁸	.87 ⁸	5.03 ⁴	5.09 ⁴
	2.97 ²⁴	3.16 ²⁴	8.87 ²⁵	8.85 ²⁵	2.04 ²²	2.18 ²²	3.65 ⁸	3.66 ⁸	3.32 ⁴	3.32 ⁴
	1.89 ²³	2.07 ²³	5.96 ²⁵	5.96 ²⁵	6.71 ²³	6.75 ²³	4.81 ⁸	4.79 ⁸	3.29 ⁴	3.32 ⁴
	3.14 ²²	3.35 ²²	3.86 ²⁵	3.88 ²⁵	3.62 ²⁴	3.68 ²⁴	6.92 ⁸	6.90 ⁸	7.80 ⁴	7.79 ⁴
	4.93 ²¹	5.51 ²¹	2.04 ²⁵	2.06 ²⁵	8.16 ²⁴	8.53 ²⁴	11.5 ⁸	11.3 ⁸	14.3 ⁴	14.1 ⁴

also has two cut-offs for Q_{elA} ; one is that used here, the other a distance cut-off. His values of c_p were obtained by numerical differentiation of h .

Considering the relative simplicity of the present model, it provides excellent accuracy for the thermodynamic properties of equilibrium hydrogen.

This model of hydrogen is too complex to include directly in the flow program. We have constructed a table of the properties of hydrogen with e and ρ as independent variables, by choosing ρ and iterating on T to find the desired e . In this table the dependent variables are T , α and β . When e and ρ are calculated in the flow program, these three dependent variables are found from the table by quadratic interpolation. Then p and the speed of sound a are calculated directly from T , α and β .

3.11 Improved Absorption Coefficients for Singly-ionized Argon and Hydrogen

Further study of the laser absorption coefficients for argon and hydrogen have led to expressions which represent an improvement over those presented in Section 3.4 for argon, as well as expressions for the absorption coefficients for hydrogen. One improvement consists of the application of a Gaunt factor to the electron-ion absorption coefficient to account for quantum-mechanical effects. A second improvement for argon is the use of more recent information for the electron-neutral absorption coefficient.

The electron-ion (inverse Bremsstrahlung) absorption coefficient used is the same Kramers formula presented in Section 3.4 at frequency ν

$$k_{\nu EI} = \sigma_{EI} n_E n_I e^{h_p \nu / kT} \left(\frac{e^{-h_p \nu / kT}}{1 - e^{-h_p \nu / kT}} \right) \quad (3.11.1)$$

The last factor accounts for stimulated emission, and the first exponential factor represents the inclusion of both free-free and bound-free absorption. The cross-section is, as in Section 3.4,

$$\sigma_{EI} = \frac{4}{3} \left(\frac{2\pi}{3m_E kT} \right)^{1/2} \frac{Z^2 e^6}{h_p^3 c^3 m_E \nu^3} = \frac{3.69E8}{T^{1/2} \nu^3} \text{ (cm}^5\text{)}.$$

Here Ze is the ion charge, e the electron charge, c the speed of light, and h_p the Planck constant. By converting to wavelength $\lambda = c/\nu$ and using $h_p \nu / k = 1.4388 \text{ cmK}$ we may write Eq. (3.11.1) for singly-charged ions as

$$k_{\lambda EI} = 1.37 \text{ E-23} \frac{\lambda^3 n_I n_E}{T^{1/2}} \left(e^{1.4388/\lambda T} - 1 \right) \text{ (cm}^{-1}\text{)}.$$

The number densities can be replaced by the degree of ionization α , since for both argon from Eq. (3.3.3), and for hydrogen from Eqs. (3.10.3, and 6),

$$n_I = n_E = \alpha \rho / m_A \quad (3.11.2)$$

where for hydrogen, electrons and ions only exist in the high temperature regime where $\beta = 1$.

We may then write the semi-classical electron-ion absorption coefficient as

$$k_{\lambda EI} = \frac{1.37E-23}{m_A^2} \frac{\lambda^3 \rho^2 \alpha^2}{T^{1/2}} \left(e^{1.4388/\lambda T} - 1 \right) \text{ (cm}^{-1}\text{)}. \quad (3.11.3)$$

To account for quantum-mechanical effects we must multiply by a Gaunt factor G , which depends on temperature. This factor is obtained from Ref. 3.12, where a parabola has been fitted to Fig. 5. For $\lambda = 10.6 \mu\text{m}$ the parameters of the figure are $\gamma^2 = 157, 900/T$, $u = h_p c / \lambda k T = 1357/T$. Then Fig. 5 provides the following table:

γ^2	T	u	$\bar{g}_{ff} = G$
3	52633	.0258	2.1
10	15790	.0859	1.55
10^2	1579	.859	1.1

A quadratic has been fitted to this table to provide a Gaunt factor

$$G = 1.04 + 3.74 E-5 T - 3.28 E-10 T^2 \text{ for } \lambda = 10.6 \mu\text{m}. \quad (3.11.4)$$

The contribution of electron-ion absorption is then

$$k_{LEI} = G k_{\lambda EI} \quad (3.11.5)$$

Note that this absorption coefficient is independent of the gas involved, except for the molecular weight of the atom which appears in Eq. (3.11.3) because of the introduction of α . The reason for this is the electromagnetic nature of the interaction between the ion and the electron which is unaffected by the gas species.

If we now turn to the electron-neutral interaction, a dependence on the gas appears, because the interaction now depends on the structure of the neutral particle. Thus we must consider argon and hydrogen separately.

For long wavelength radiation interaction with argon, John (Ref. 3.13) has provided information about the electron-neutral absorption coefficient. His relation may be expressed as

$$k_{\lambda EN} = A(T) \lambda^2 k T n_A n_E \times 10^{16} \quad (3.11.6)$$

where cgs units are used, and A is a function of T related to the momentum transfer cross-section. This expression includes stimulated emission.

John gives a table of A vs. T for a number of species, including argon, from 100 to 25,000 K. A convenient way to incorporate this table into a computer program is by making a fit to TA(T). From Table I of Ref. 3.13, the following fits can be obtained:

$$\begin{aligned} T < 1000 \text{ K: } TA(T) \times 10^{34} &= 861 T^{-.5512} \\ T \geq 1000 \text{ K: } TA(T) \times 10^{34} &= 5.346 \times 10^{-4} T^{1.51} \end{aligned} \quad (3.11.7)$$

These agree with John's values to within 10%.

Introduction of α instead of number densities is accomplished with the help of Eq. (3.3.3) for argon, and with Eqs. (3.10.3 and 6) for hydrogen when $\beta = 1$.

$$n_A = (1-\alpha)\rho/m_A, \quad n_E = \alpha\rho/m_A \quad (3.11.8)$$

Then Eq. (3.11.6) becomes

$$k_{LEN} = \frac{1.3806}{m_A^2} TA(T) \lambda^2 \rho^2 \alpha (1-\alpha) \quad (\text{cm}^{-1}) \quad (3.11.9)$$

which is the final expression for the electron-neutral absorption coefficient for argon, together with Eq. (3.11.7).

For hydrogen, the best available expression seems to be that of Stallcop, (Ref. 3.14) which is

$$k_{\lambda EN} = \sigma_{EN} \frac{n_e n_A}{E_A} [1 - \exp(-h_p c / \lambda k T)]$$

$$\sigma_{EN} = \frac{2.96 \text{ E-45 T}}{1 - \exp(h_p c / \lambda k T)} \left(\frac{\theta_I k \lambda}{h_p c} \right)^2 \left(\frac{\theta_I}{T} \right)^{1/2} e^{-\xi} \text{ (cm}^5\text{)}$$

$$\xi = 4.862 \left(\frac{T}{\theta_I} \right)^{1/2} \left[1 - 0.2096 \left(\frac{T}{\theta_I} \right)^{1/2} + 0.0170 \left(\frac{T}{\theta_I} \right) - 0.00968 \left(\frac{T}{\theta_I} \right)^{3/2} \right]. \quad (3.11.10)$$

If we put σ_{EN} into $k_{\lambda EN}$, use $h_p c / k = 1.4388 \text{ cmK}$ and also use Eq. (3.11.8) we find

$$k_{LEN} = \frac{2.07 \text{ E-45}}{m_A^2} \theta_I^{5/2} T^{1/2} \lambda^2 \rho^2 \alpha (1-\alpha) e^{-\xi} \text{ (cm}^{-1}\text{)}. \quad (3.11.11)$$

This is the final expression for the electron-neutral absorption coefficient for hydrogen, together with Eq. (3.11.10).

The total absorption coefficient is the sum of the electron-ion and electron-neutral contributions:

$$k_L = k_{LEI} + k_{LEN}. \quad (3.11.12)$$

In order to have an idea how the new argon electron-neutral absorption coefficient compares with the older one given above in Section 3.4,

we may compare Eq. (3.11.9) with Eq. (3.4.8). Such a comparison is provided in the following table for $k_{LEN}/\rho^2\alpha(1-\alpha)$:

<u>T(K)</u>	<u>Eq. (3.4.8)</u>	<u>Eq. (3.11.9)</u>
4640	4.94E5	6.38E6
9280	2.20E6	1.82E7
23,200	1.13E7	7.25E7

It appears that new electron-neutral absorption coefficient is an order of magnitude higher than the old one. Since the electron-ion contribution is the same, the total absorption coefficient is not affected that much, but will still be higher.

Of course, the absorption coefficient only enters the calculations when the absorbing mode is used, as in the calculation described at the end of Section 3.9. For all the blast wave mode calculations discussed in connection with Table 3.2, this difference in absorption coefficients has no effect, since those calculations are all made starting with the laser energy already deposited in the gas.

Some confirmation of the validity of Eq. (3.11.9), as opposed to Eq. (3.4.8) can be obtained from Ref. 3.15. Geltman provides a table of cross-sections for various wavelengths and temperatures, not including stimulated emission. At wavelengths of 5 and 10 μm , and temperatures of 10,000 and 20,000 K, his cross-sections are higher than those of John, but by only 31% or less.

3.12 Equilibrium Properties of Multiply-Ionized Argon

As the calculations reported in Sec. 3.9 were made, it became apparent that rather high temperatures were reached in argon, and the rather simple, singly-ionized thermodynamics described in Sec. 3.3 was not a good description. At the same time, a description of equilibrium for a multiply-ionized monotomic gas was developed at PSI under another program. This description used p and T as independent variables, rather than ρ and T as needed for the present work. However, it proved quite easy to convert the description to ρ and T and so make it available for use in the present program. This section will describe the resulting model of equilibrium multiply-ionized argon.

We consider a gas mixture with atoms and up to $N-1$ ions, as well as electrons. The number densities are denoted by $n_A = n_1$, n_i ($i = 2, 3, \dots, N$) and n_E , with corresponding masses $m_A = m_1$, $M_i = m_A - (i - 1) m_E$ and m_E , and charges 0 , $(i - 1)$ and -1 electronic charges. The total number density is

$$n = n_A + n_E + \sum_{i=2}^N n_i \quad (3.12.1)$$

and charge conservation requires

$$-n_E + \sum_{i=2}^N (i - 1) n_i = 0. \quad (3.12.2)$$

The density of the mixture is

$$\rho = m_A n_A + m_E n_E + \sum_{i=2}^N n_i [m_A - (i - 1) m_E].$$

When the charge conservation condition Eq. (3.12.2) is used to eliminate the (i - 1) term we find

$$\rho = m_A \left(n_A + \sum_{i=2}^N n_i \right)$$

and when the definition of n is used from Eq. (3.12.1) the simple result is

$$\rho = m_A n (1 - n_E/n) \quad (3.12.3)$$

The pressure of the mixture is

$$p = nkT = \rho R_A T / (1 - n_E/n), \quad R_A \equiv k/m_A \quad (3.12.4)$$

since each component provides a contribution

$$p_i = n_i kT \quad (3.12.5)$$

The Law of Mass Action provides a relation between the partial pressures of the i-th and (i + 1)-th ion:

$$p_E p_{i+1} / p_i = f_{ip}(T) \quad .$$

Here f_{ip} is an equilibrium constant for the ionization of the i-th ion, which will be defined later. For the atom, this relation is the same as that presented in Sec. 3.3 below Eq. (3.3.4). If we introduce the reaction variables α_i , defined by

$$\alpha_i = n_i/n = p_i/p \quad (3.12.6)$$

then Mass Action becomes

$$\alpha_E \alpha_{i+1} / \alpha_i = f_{ip} / p$$

which is the form appropriate to the use of p and T as independent variables. To shift to ρ and T we replace p by ρ from Eq. (3.12.4) and find

$$\frac{\alpha_E}{1-\alpha_E} \frac{\alpha_{i+1}}{\alpha_i} = \frac{f_{ip}(T)}{\rho R_A T}, \quad i=1,2,\dots,N-1 \quad (3.12.7)$$

(Notice that the α_i as defined by Eq. (3.12.6) for $i=1$ is not the same as the α used in Sec. 3 and defined in Eq. (3.3.1). The relation is $\alpha_1 = \alpha / (1 + \alpha)$.)

For every ionizing reaction there is a relation like Eq. (3.12.7), and since there are $N - 1$ ions, there are $N - 1$ such relations. However, there are $(N + 1)\alpha_i$ variables when α_E and $\alpha_1 = \alpha_A$ are included. The two additional relations needed are total number density Eq. (3.12.1) in the form

$$1 = \alpha_A + \alpha_E + \sum_{i=2}^N \alpha_i \quad (3.12.8)$$

and charge conservation Eq. (3.12.2) in the form

$$-\alpha_E + \sum_{i=2}^N (i - 1) \alpha_i = 0 \quad (3.12.9)$$

Equations (3.12.7, 8 and 9) provide $N + 1$ equations for the $N + 1$ unknowns $\alpha_E, \alpha_i, i = 1,2,\dots,N$, which can be solved for given ρ and T once the equilibrium constants $f_{ip}(T)$ are specified. The solution is carried out by the Newton-Raphson method.

The functions f_{ip} are the partition function ratios where each partition function is composed of a translational part $(2\pi m_i kT/h_p^2)^{3/2}$ and an internal part $Q_{i,int}$. In addition, there is a factor kT for each species. If we ignore the mass ratio m_{i+1}/m_i , the expression for f_{ip} is

$$f_{ip} = \left(\frac{2\pi m_E}{h_p^2} \right)^{3/2} (kT)^{5/2} \frac{Q_{i+1,int} Q_{E,int}}{Q_{i,int}} .$$

The internal partition function of the electron is 2, and on the right side of Eq. (3.12.7) f_{ip} is divided by $\rho R_A T$ where $R_A = k/m_A$. Thus the right side of Eq. (3.13.7) is

$$F_i = \frac{f_{ip}}{\rho R_A T} = \frac{2m_A}{\rho} \left(\frac{2\pi m_E kT}{h_p^2} \right)^{3/2} \frac{Q_{i+1,int}}{Q_{i,int}} . \quad (3.12.10)$$

The internal partition function of the atom or any ion is expressed in terms of the energy states and statistical weights. For the i -th ion we denote the j -th energy level as ϵ_{ij} and the statistical weight as g_{ij} . This energy level is measured from the ground state of the ion, and to it must be added the energy ϵ_i^* to form the ion in its ground state from the atom in its ground state. Thus we find

$$Q_{i,int} = \sum_j g_{ij} \exp \left(- \epsilon_i^*/kT - \epsilon_{ij}/kT \right) . \quad (3.12.11a)$$

The energy ϵ_i^* is the sum of the ionization potentials of all the ions through the $(i-1)$ -th ion. We denote the ionization potential for the i -th ion, including the lowering effect, by I_{Li} , so that

$$\epsilon_i^* = \sum_{j=1}^{i-1} I_{Lj} . \quad (3.12.11b)$$

The lowering of the ionization potential is calculated using the Debye-Huckel theory. The decrement in the potential is given by

$$\Delta I_i = 2ie^3 \left(\frac{\pi}{kT} \right)^{1/2} \left(\sum_{j=2}^N n_j Z_j^2 - n_E \right)^{1/2} \quad (3.12.11c)$$

where e is the electron charge in esu and Z_j is the number of charges on the ion. If ΔI_i is expressed in ergs, $2e^3 \sqrt{\pi/k} = 3.343 \text{ E-20}$, while if it is to be expressed in cm^{-1} , one divides by $h_p c$ so the constant is $2e^3 \sqrt{\pi/k} / h_p c = 1.683 \text{ E-4}$.

Since ΔI_i involves n_i and n_E , while I_{Li} is needed on the right of Eq. (3.12.7) to calculate these quantities, the solution must clearly be iterative. However, solving for the α_i is already iterative because of the complicated form of the equations. The procedure followed was simply to use the current values of n_i and n_E to calculate the ΔI_i used to find the next iteration on the α_i . In view of the approximate nature of the ΔI_i correction, this procedure is sufficiently accurate.

The internal energy per unit mass of each species is expressed in terms of the internal partition function by

$$e_i = \frac{kT}{m_i} \left[\frac{3}{2} + T \frac{d \ln Q_{i,int}}{dT} \right], \quad e_E = \frac{3}{2} \frac{kT}{m_E} \quad (3.12.12)$$

where the first term is the translational part. The mixture internal energy is then

$$e = \sum e_i \rho_i / \rho + e_E \rho_E / \rho, \quad \rho_i = m_i n_i \quad (3.12.13)$$

Using Eq. (3.12.11a) in Eq. (3.12.12), and performing the sum in Eq. (3.12.13), we finally find

$$e = \frac{3}{2} \frac{p}{\rho} + \sum_{i=1}^N \frac{n_i}{\rho} \left[\epsilon_i^* + \frac{\sum_j g_{ij} \epsilon_{ij} e^{-\epsilon_{ij}/kT}}{\sum_j g_{ij} e^{-\epsilon_{ij}/kT}} \right] \quad (3.12.14)$$

The sum over i does not include the electrons because they have no internal energy.

The enthalpy per unit mass is of course related to e by

$$h = e + p/\rho \quad (3.12.15)$$

The speed of sound has already been expressed in terms of enthalpy and pressure derivatives in Eq. (3.10.27) for any equilibrium gas mixture. Since in the present case all the derivatives must be obtained by numerical differentiation, another formulation may be simpler, using the specific heats. The specific heats are defined as

$$c_v = \left(\frac{\partial e}{\partial T} \right)_\rho = \left(\frac{\partial h}{\partial T} \right)_\rho - \frac{1}{\rho} \left(\frac{\partial p}{\partial T} \right)_\rho \quad (3.12.16a)$$

$$c_p = \left(\frac{\partial h}{\partial T} \right)_p = c_v + \left[\left(\frac{\partial h}{\partial \rho} \right)_T - \frac{1}{\rho} \left(\frac{\partial p}{\partial \rho} \right)_T \right] \left(\frac{\partial \rho}{\partial T} \right)_p \quad (3.12.16b)$$

Using these, and the identity

$$\left(\frac{\partial p}{\partial T} \right)_\rho = - \left(\frac{\partial p}{\partial \rho} \right)_T \left(\frac{\partial \rho}{\partial T} \right)_p$$

in Eq. (3.10.27), finally yields the simple expression

$$a^2 = \frac{c_p}{c_v} \left(\frac{\partial p}{\partial \rho} \right)_T \quad (3.12.17)$$

for the square of the sound speed.

Of the three terms in Eq. (3.12.17), only c_p has not yet been expressed entirely in derivatives with respect to ρ and T , since Eq. (3.12.16b) has a derivative holding p fixed. But by using the reciprocal relations of thermodynamics for an equilibrium mixture, Eq. (3.12.16b) can be converted to

$$c_p = c_v + \frac{T}{\rho^2} \left(\frac{\partial p}{\partial T} \right)_\rho^2 / \left(\frac{\partial p}{\partial \rho} \right)_T. \quad (3.12.18)$$

When e and p are known as functions of ρ and T , then Eq. (3.12.17) provides a^2 when Eqs. (3.12.16a) and (3.12.18) are used. As mentioned above, the derivatives are obtained numerically.

Finally, it is necessary to specify the ionization potentials I_i to which the lowering ΔI_i is to be applied, the statistical weights and the energy levels. This information is obtained from experimental spectroscopic data. For argon, there is a great deal of such information available, and the compilations in Ref. 3.16 were used. It is not possible to treat every energy level separately, since there are a large number of them. Instead, we group levels of similar energy together, and use the sum of the degeneracies of the levels in the group and an average energy. The parameters used in the present work are given in Table 3.4, for the neutral atom and the first three ions, which were the heavy species used. The table shows that we took five energy level groups for the atom, nine for the first ion, twelve for the second and eight for the third ion.

Using these parameters, the composition and thermodynamic properties of equilibrium argon were computed with the equations presented in this section. The results can be compared with the published tables from the National Bureau of Standards (Ref. 3.17) and their extensions (Ref. 3.18). Such a comparison is made in Tables 3.5 and 3.6. The first table contains the number fractions α . It shows very good agreement between the present calculations and Ref. 3.17. The major species are usually within one or two percent, with the minor species somewhat further apart. Table 3.6 contains the pressure, internal energy, specific heats and speed of sound. Again the agreement

TABLE 3.4

ARGON PARTITION FUNCTION PARAMETERS

I (ev):	Argon		Argon ⁺		Argon ⁺⁺		Argon ⁺⁺⁺	
	g_{1j}	$\epsilon_{1j}(\text{cm}^{-1})$	g_{2j}	$\epsilon_{2j}(\text{cm}^{-1})$	g_{3j}	$\epsilon_{3j}(\text{cm}^{-1})$	g_{4j}	$\epsilon_{4j}(\text{cm}^{-1})$
		15.76		27.6		40.0		
	1	0	4	0	5	0	4	0
	12	9500	2	1432	3	1112	10	21000
	36	10500	2	109000	1	1570	6	35000
	148	11400	38	134000	5	14000	12	118000
	1268	12300	80	145000	1	33300	10	146000
			54	157000	9	114000	8	170000
			54	172000	43	149000	28	260000
			144	185000	53	185000	78	290000
			174	198000	15	197000		
					60	207000		
					97	230000		
					167	265000		

TABLE 3.6

THERMODYNAMIC PROPERTIES OF EQUILIBRIUM ARGON

T (10 ³ K)	p (atm)		e (erg/g)		C _p (erg/gK)		e _v (erg/gK)		a (cm/s)	
	PSI	NBS	PSI	NBS	PSI	NBS	PSI	NBS	PSI	NBS
	$\rho = 7.090E-7 \text{ g/cm}^3$									
5	7.28E-3	7.29E-3	1.56E10	1.56E10	5.22E6	5.22E6	3.14E6	3.14E6	1.32E5	1.32E5
15	4.29E-2	4.28E-2	4.60E11	4.59E11	2.73E7	2.72E7	2.08E7	2.07E7	2.81E5	2.81E5
25	1.03E-1	1.03E-1	1.17E12	1.17E12	8.47E7	8.55E7	6.74E7	6.82E7	4.21E5	4.19E5
35	1.80E-1	1.80E-1	1.99E12	2.01E12	1.58E8	1.61E8	1.26E8	1.30E8	5.48E5	5.48E5
	$\rho = 7.090E-6 \text{ g/cm}^3$									
5	7.28E-2	7.29E-2	1.56E10	1.56E10	5.21E6	5.21E6	3.13E6	3.14E6	1.32E5	1.32E5
15	3.85E-1	3.83E-1	3.75E11	3.75E11	8.02E7	7.97E7	6.22E7	6.20E7	2.55E5	2.54E5
25	8.76E-1	8.69E-1	8.46E11	8.45E11	1.26E8	1.25E8	9.81E7	9.83E7	3.83E5	3.80E5
35	1.58E0	1.57E0	1.50E12	1.52E12	8.64E7	8.70E7	6.89E7	7.02E7	5.20E5	5.16E5
	$\rho = 7.090E-5 \text{ g/cm}^3$									
5	7.28E-1	7.29E-1	1.56E10	1.56E10	5.20E6	5.21E6	3.12E6	3.13E6	1.32E5	1.32E5
15	3.05E0	3.03E0	2.19E11	2.19E11	8.33E7	8.26E7	6.37E7	6.37E7	2.26E5	2.24E5
25	7.50E0	7.41E0	5.97E11	5.98E11	5.32E7	5.26E7	4.18E7	4.25E7	3.60E5	3.56E5
35	1.43E1	1.39E1	1.24E12	1.24E12	6.98E7	7.10E7	5.26E7	5.41E7	5.04E5	4.94E5
	$\rho = 7.090E-4 \text{ g/cm}^3$									
5	7.28E0	7.29E0	1.56E10	1.56E10	5.20E6	5.21E6	3.12E6	3.13E6	1.32E5	1.32E5
15	2.52E1	2.51E1	1.17E11	1.16E11	4.28E7	4.19E7	3.40E7	3.36E7	2.06E5	2.05E5
25	6.64E1	6.58E1	4.96E11	5.01E11	3.08E7	3.24E7	2.24E7	2.39E7	3.48E5	3.44E5
	$\rho = 7.090E-3 \text{ g/cm}^3$									
5	7.28E1	7.32E1	1.56E10	1.56E10	5.20E6	5.22E6	3.12E6	3.13E6	1.32E5	1.32E5
15	2.31E2	2.30E2	7.50E10	7.40E10	2.16E7	2.04E7	1.74E7	1.88E7	2.00E5	2.00E5

with Refs. 3.17 and 3.18 is very good, with the worst discrepancies (10%) occurring for the specific heats, which we obtained by numerical differentiation ($c_v = (\Delta e / \Delta T)_\rho$, etc.). The speed of sound is better than the specific heat, though it depends on their ratio.

We can conclude that, at least over the range of ρ and T in Tables 3.5 and 3.6, the present model of equilibrium ionizing argon is quite accurate, compared to the most elaborate model for which calculations are available.

To use this argon model in the flow program, we constructed a table of properties as a function of e and ρ , by choosing ρ and iterating on T to get the desired e . In this table, the dependent variables are T , p , a , n_e , n_1 , n_2 , n_3 and n_4 . When e and ρ are calculated in the flow program, these eight dependent variables are found from the table by quadratic interpolation. For all but T and a , the interpolation is done on the logarithm of the dependent variable, rather than the variable itself.

3.13 Absorption Coefficients for Multiply-ionized Argon

When multiply-ionized argon is considered, the absorption coefficients given in Sec. 3.11 must be modified to account for the presence of the higher ions. In addition, the absorption coefficients are needed not only for a laser wave length of 10.6 μm , but also for 0.353 μm . The modified expressions will be presented in this section, for the basic absorption coefficients and for the Gaunt factors.

The electron-ion absorption coefficient has already been expressed in Sec. 3.11. The part associated with the free-free absorption is

$$k_{FF} = \sigma_{EI} n_E n_I \left(1 - e^{-h_{pc}/\lambda kT} \right) \quad (3.13.1)$$

where $\sigma_{EI} = 1.37 \text{ E-}23 (\lambda^3/T^{1/2}) Z^2$. Here Z is the number of charges on the ion, and the stimulated emission factor has been included. The usual approximation for the bound-free absorption is proportional to the free-free absorption:

$$k_{BF} = k_{FF} \left(e^{h_{pc}/\lambda kT} - 1 \right) \quad (3.13.2)$$

The sum of k_{FF} and k_{BF} provides the result

$$k_{\lambda EI} = 1.37 \text{ E-}23 Z^2 \lambda^3 n_E n_I \left(e^{1.4388/\lambda T} - 1 \right) / T^{1/2} \quad (3.13.3)$$

already stated in Sec. 3.11. However, here Z depends on the ion, and a term of the form of Eq. (3.13.3) must be included for each ion.

The quantum-mechanical correction (Gaunt) factor depends on Z, as well as upon the laser wave length λ . According to Karzas and Latter (Ref. 3.12), the parameters plotted in their Fig. 5 are $\gamma^2 = 157894 A^2/T$ and $u = 1.4388/\lambda T$. For $\lambda = 10.6 \mu\text{m}$ the figure yields the following table:

γ^2	Z = 1			Z = 2		
	T(K)	u	$G = \bar{g}_{ff}$	T(K)	u	$G = \bar{g}_{ff}$
3	52631	.0258	2.03	210525	.00645	2.64
10	15789	.0860	1.55	63158	.0215	1.92
10^2	1579	.860	1.10	6316	.215	1.18

γ^2	Z = 3		
	T(K)	u	$G = \bar{g}_{ff}$
10	142104	.00955	2.22
10^2	14210	.0955	1.30
10^3	1421	.955	1.00

Quadratic fits to these three sets of G vs. T yield:

$$Z = 1: G_2 = 1.04 + 3.80E-5T - 3.65E-10T^2$$

$$Z = 2: G_3 = 1.08 + 1.58E-5T - 3.98E-10T^2 \quad (3.13.4)$$

$$Z = 3: G_4 = 0.96 + 2.53E-5T - 1.16E-10T^2$$

(The first of these equations yields essentially the same fit as does Eq. (3.11.4), which was also for Z = 1.)

For $\lambda = 0.353 \mu\text{m}$, the table obtained from Fig. 5 of Ref. 3.12 is as follows:

γ^2	Z = 1			Z = 2		
	T(K)	u	$G = \bar{g}_{ff}$	T(K)	u	$G = \bar{g}_{ff}$
3	52631	.774	1.30	210525	.194	1.51
10	15789	2.58	1.16	63158	.645	1.24
10^2	1579	25.8	1.10	6316	6.45	1.07

γ^2	Z = 3		
	T (K)	u	$G = \bar{g}_{ff}$
10	142104	.287	1.31
10^2	14210	2.87	1.07
10^3	1421	28.7	1.07

Quadratic fits to these three sets of G vs. T yield:

$$Z = 1: G_2 = 1.09 + 4.36E-6T - 8.27E-12T^2$$

$$Z = 2: G_3 = 1.05 + 3.30E-6T - 5.53E-12T^2 \quad (3.13.5)$$

$$Z = 3: G_4 = 1.07 - 9.56E-8T + 1.33E-11T^2$$

The contribution of electron-ion absorption is then

$$k_{LEI} = \frac{1.37E-23 \lambda^3 n_E}{T^{1/2}} \left(e^{1.4388/\lambda T} - 1 \right) \sum_{i=2}^4 n_i (i-1)^2 G_i \quad (3.13.6)$$

where G_i is obtained from Eq. (3.13.4) for $\lambda = 10.6 \mu\text{m}$ and from Eq. (3.13.5) for $\lambda = 0.353 \mu\text{m}$.

The electron-neutral contribution for $10.6 \mu\text{m}$ can be obtained from John (Ref. 3.13) as it was in Sec. 3.11 for hydrogen. His expression is

$$\begin{aligned} k_{LEN} &= A(T) \lambda^2 k_{TA} n_A n_E \times 10^{16} \\ &= 1.38 \lambda^2 n_A n_E TA(T) \end{aligned} \quad (3.13.7)$$

where a fit to his table of TA(T) for argon is as given in Eq. (3.11.7):

$$T < 1000\text{K}: TA(T) \times 10^{34} = 861T^{-.5512}$$

$$T \geq 1000\text{K}: TA(T) \times 10^{34} = 5.346 \times 10^{-4} T^{1.51} \quad (3.13.8)$$

At a wavelength of 0.353 μm , John's expression for electron-neutral absorption is not valid, being developed for the infrared. Some work of Geltman. (Ref. 3.19) is available in this wavelength region. He expresses the absorption coefficient as

$$k_{\text{EN}} = \sigma_{\text{EN}} n_{\text{A}} n_{\text{E}} \left(1 - e^{-h_{\text{p}} c / \lambda k T} \right)$$

and gives σ_{EN} in his Table 4 for various values of λ and T, including 0.5 μm . By converting to 0.353 μm using $\sigma_{\text{EN}} \sim \lambda^3$, and applying the stimulated emission factor, we find from Geltman's 0.5 μm values for argon:

T (K)	5000	10,000	15,000	20,000
$k/n_{\text{A}} n_{\text{E}}$.630E-40	1.40E-40	2.29E-40	3.21E-40

A good fit to these values can be found from a power law in T, and the result is

$$k_{\text{LEN}} = 0.944\text{E-}41 (T/1000)^{1.176} n_{\text{A}} n_{\text{E}} \quad (3.13.9)$$

An alternative expression for this absorption coefficient has been derived by Weyl in Chapter 2 of this report. His values are fitted by

$$\begin{aligned} \frac{k_{\text{LEN}}}{n_{\text{A}} n_{\text{E}}} &= 6.36\text{E-}41 [T(\text{eV})]^{1.4} \\ &= 2.056\text{E-}42 (T/1000)^{1.4} \end{aligned} \quad (3.13.10)$$

which yields values a factor of two or three lower than the values obtained from the fit of Geltman's work, Eq. (3.13.9). In the results presented later, we have used the fit obtained from Geltman.

The effect on the absorption coefficient of multiply-ionized argon by changing from 10.6 μm to 0.353 μm is shown in Fig. 3.14, which presents the total argon absorption coefficient

$$k_L = k_{LEI} + k_{LEN} \quad (3.13.11)$$

for densities of 10^{-1} , 10^{-2} and 10^{-3} g/cm^3 from 12,000 to 35,000 K. The coefficients at 0.353 μm are between two and three orders of magnitude lower than those at 10.6 μm . This difference is primarily due to the effect of the $\lambda^3 [1 - \exp(-1.4388/\lambda T)]$ term in k_{LEI} , which varies slower than λ^3 (a factor of 2.7E4) but faster than λ^2 (a factor of 900).

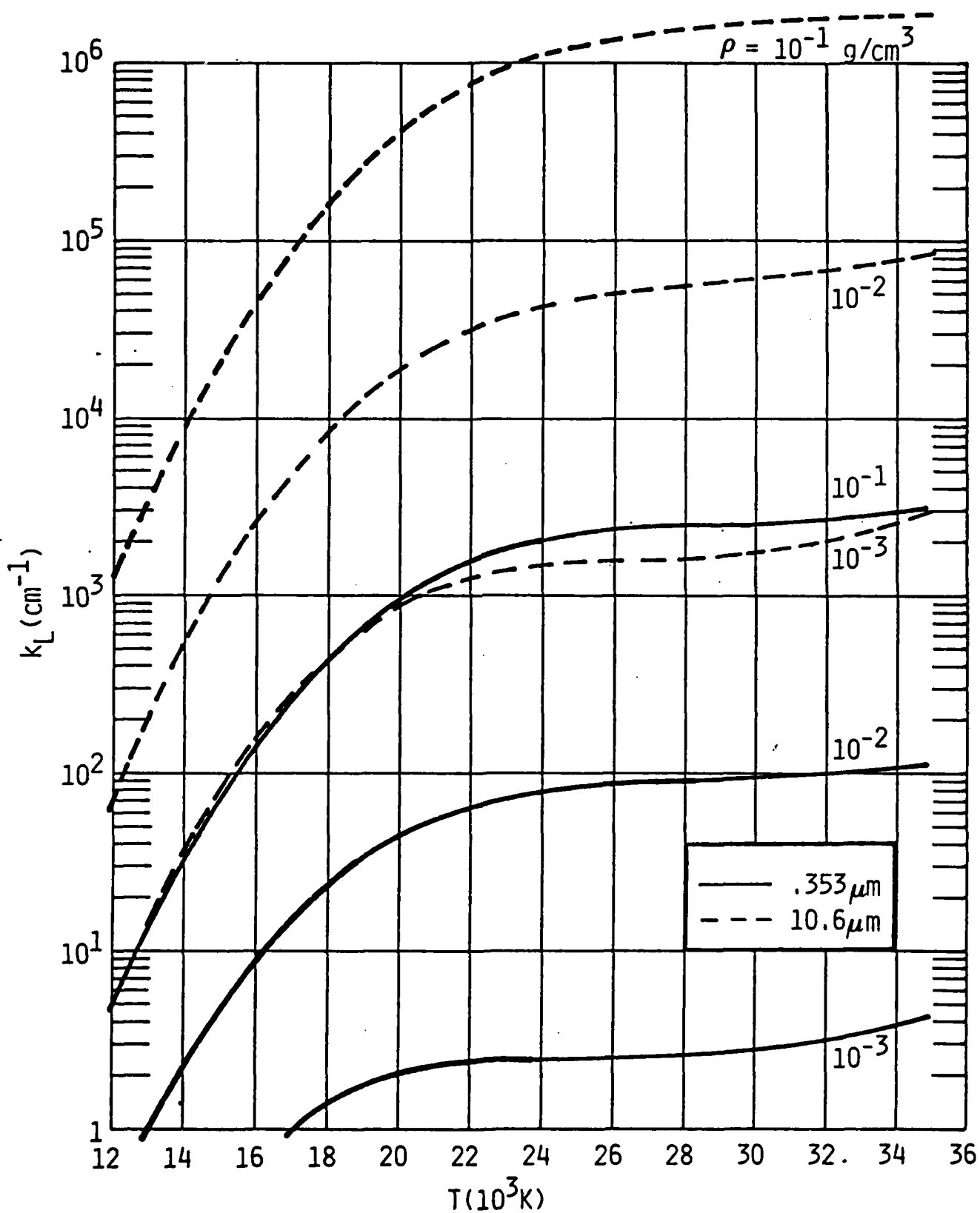


Fig. 3.14 Absorption coefficient for 10.6 μm and 0.353 μm radiation in multiply-ionized argon.

3.14 Results for Multiply-Ionized Argon

Some experiments have been made in argon at 0.353 μm in a conical nozzle, and two computer runs were made to simulate these experiments. The main purpose was to provide a correlation of shock location vs. distance down the nozzle for this combination of gas, wavelength of laser, and geometry.

The nozzle geometry was a cone of 10° half-angle. At the throat end it had a diameter of 0.1016 cm (0.04 inches), and at the large end a diameter of 3.81 cm (1.5 inches). Its length is thus 10.5 cm (4.14 inches), and its area distribution, measured from the throat end, is

$$A = 0.09768 (\chi + 0.2881)^2 . \quad (3.14.1)$$

We used the multiply-ionized argon model described in Sec. 3.12 and the 0.353 μm absorption coefficients described in Sec. 3.13, including the fit to Geltman's electron-neutral values.

The program was run in the absorbing mode, in which the laser was turned on for the first 0.5 μs at a constant power level sufficient to produce the desired amount of energy. After 0.5 μs the laser was turned off and the shock wave coasted down the nozzle. The runs were terminated when the shock reached approximately 12 cm.

To start the laser absorption process, the first 0.01 cm of the nozzle was filled with gas at the cold flow density corresponding to the 7 atm plenum pressure level, but at an internal energy of 3.5E11 erg/g, this corresponds to about 23,000 K in the gas, whose density ranges from 7.37E-3 to 5.65E-3 g/cm³. The amount of energy in this volume of gas is very small. The volume is 8.4E-5 cm², so the energy is about 1.9E5 erg (0.019 J) based on the average density. This is negligible compared to the laser energy, but this small slug of hot gas is sufficient to start the absorption process.

The two runs made were both for stagnation conditions in the plenum of 7 atm and 300 K. The only difference in the runs was the laser energy, which was 3 J for one run and 1 J for the other.

These runs, in the absorbing mode, have two distinct phases. For the first 0.5 μs , while the laser is on, the gas has an LSD wave driving it. After that, the laser is off and there is an ordinary shock wave which coasts.

For the 3 J run, Fig. 3.14 shows profiles of p , ρ and T while the laser is on, at the times indicated on the figure. It shows the LSD wave advancing into the gas with decreasing strength as the nozzle area increases from $8.68\text{E-}3 \text{ cm}^2$ at $X = 0.01 \text{ cm}$ to $6.067\text{E-}2 \text{ cm}^2$ at $X = 0.5 \text{ cm}$. The gas heats from 23,000 K to over 60,000 K initially, and then cools to a maximum of 55,000 K as more gas is ingested. The p and ρ profiles in Figs. 3.14a and 3.14b show the sharply peaked nature typical of LSD waves. The temperature profiles in Fig. 3.14c start sharply peaked at early times, but the peak gradually rounds off as time goes on, indicating that the laser absorption process is not concentrated at the front, but is spread out over the whole region behind the front. Further confirmation of that is provided by Fig. 3.15, which presents the power profiles. It shows the gradual spreading of the absorption region at later times. At 0.49 μs , only half the power has been absorbed in the first 0.04 cm behind the front, while at 0.122 μs , about 98% of the power is absorbed in the first 0.04 cm. However, the power is eventually nearly all absorbed. In fact, for this 3 J run, 97% of the energy is absorbed in the gas, and only 3% escapes through the nozzle throat at $X = 0$.

The laser is shut off at 0.5 μs , and the program continues to run while the shock wave moves from about 0.51 cm to 11.5 cm, at a time of 23 μs . The area of the nozzle goes from $6.22\text{E-}2$ to 13.57 cm^2 in this distance. The p , ρ and T profiles at some of these later times are given in Fig. 3.16. The p and ρ profiles quickly disappear at the bottom of these linear plots because of the huge area increase. The last density profile visible is at 9.29 μs and the last pressure profile is at 2.55 μs . But they continue to

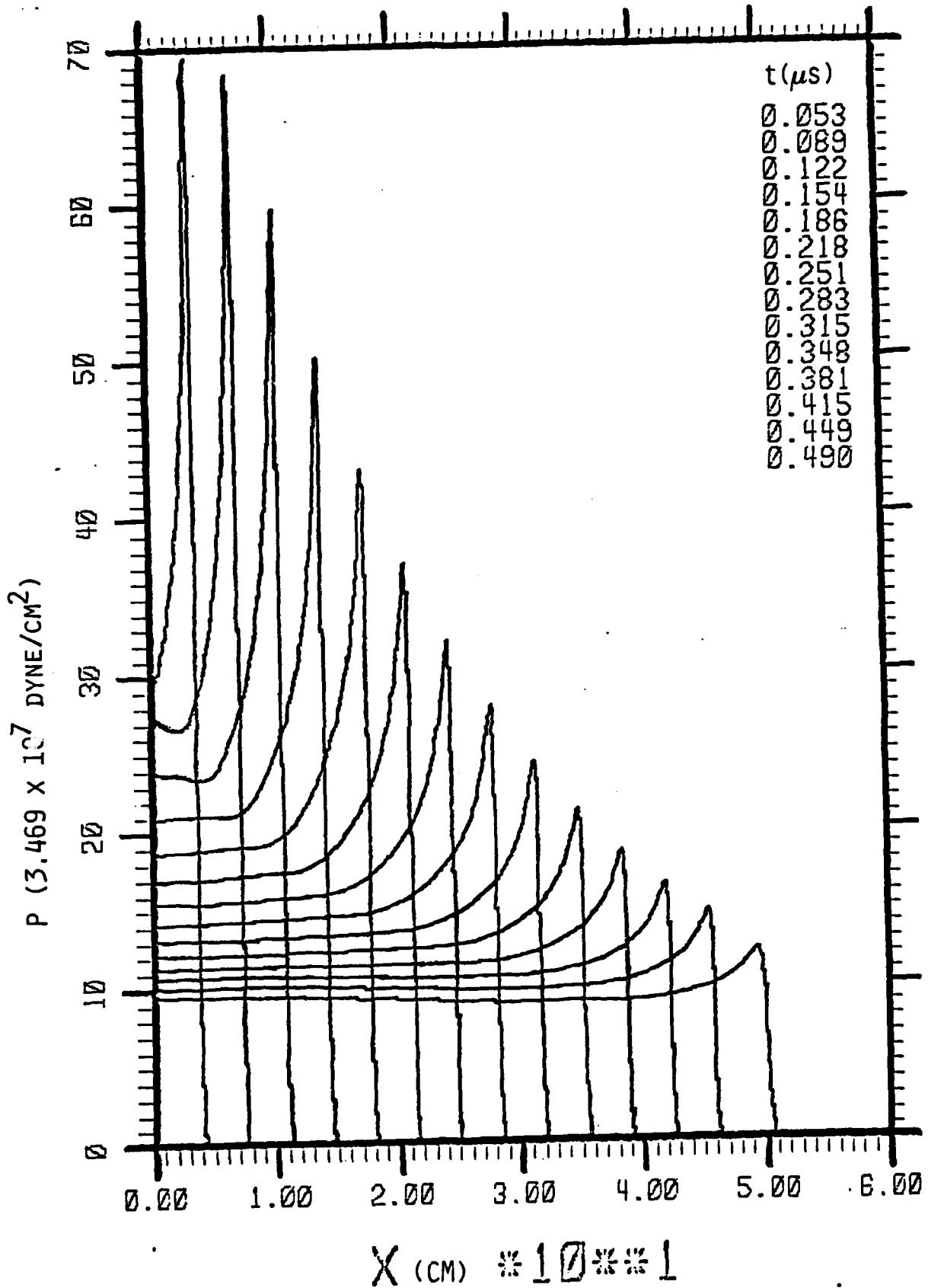


Fig. 3.14a Pressure profiles for LSD wave in a conical nozzle. $P_{st} = 7$ atm, $T_{st} = 300$ K, laser energy 3 J, pulse time 0.5 μ s, multiply-ionized argon.

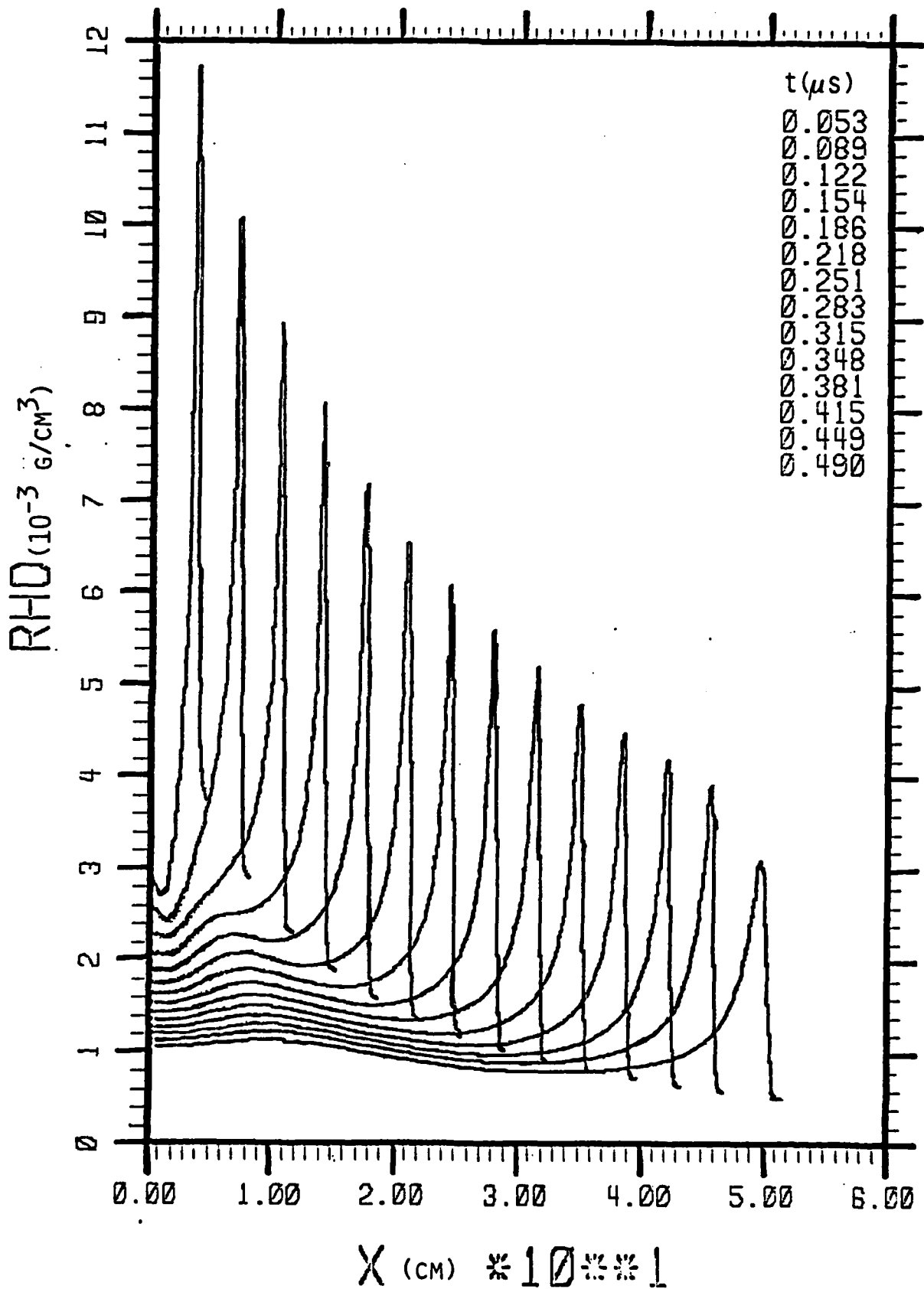


Fig. 3.14b Density profiles for LSD wave in a conical nozzle, $p_{st} = 7 \text{ atm}$, $T_{st} = 300 \text{ K}$, laser energy 3 J, pulse time $0.5 \mu\text{s}$, multiply-ionized argon.

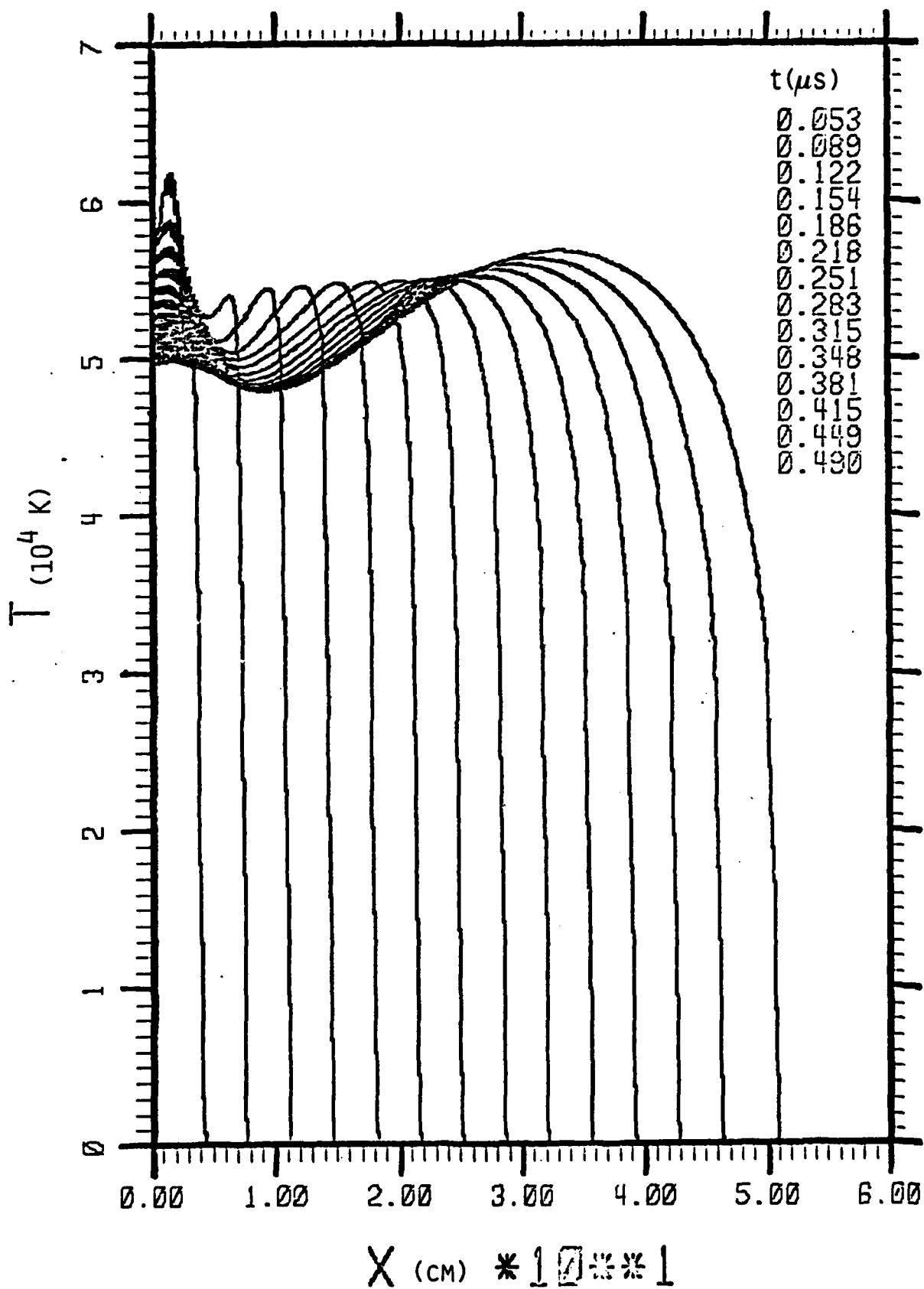


Fig. 3.14c Temperature profiles for LSD wave in a conical nozzle. $p_{st} = 7$ atm
 $T_{st} = 300$ K, laser energy 3 J, pulse time 0.5 μs , multiply-ionized argon.

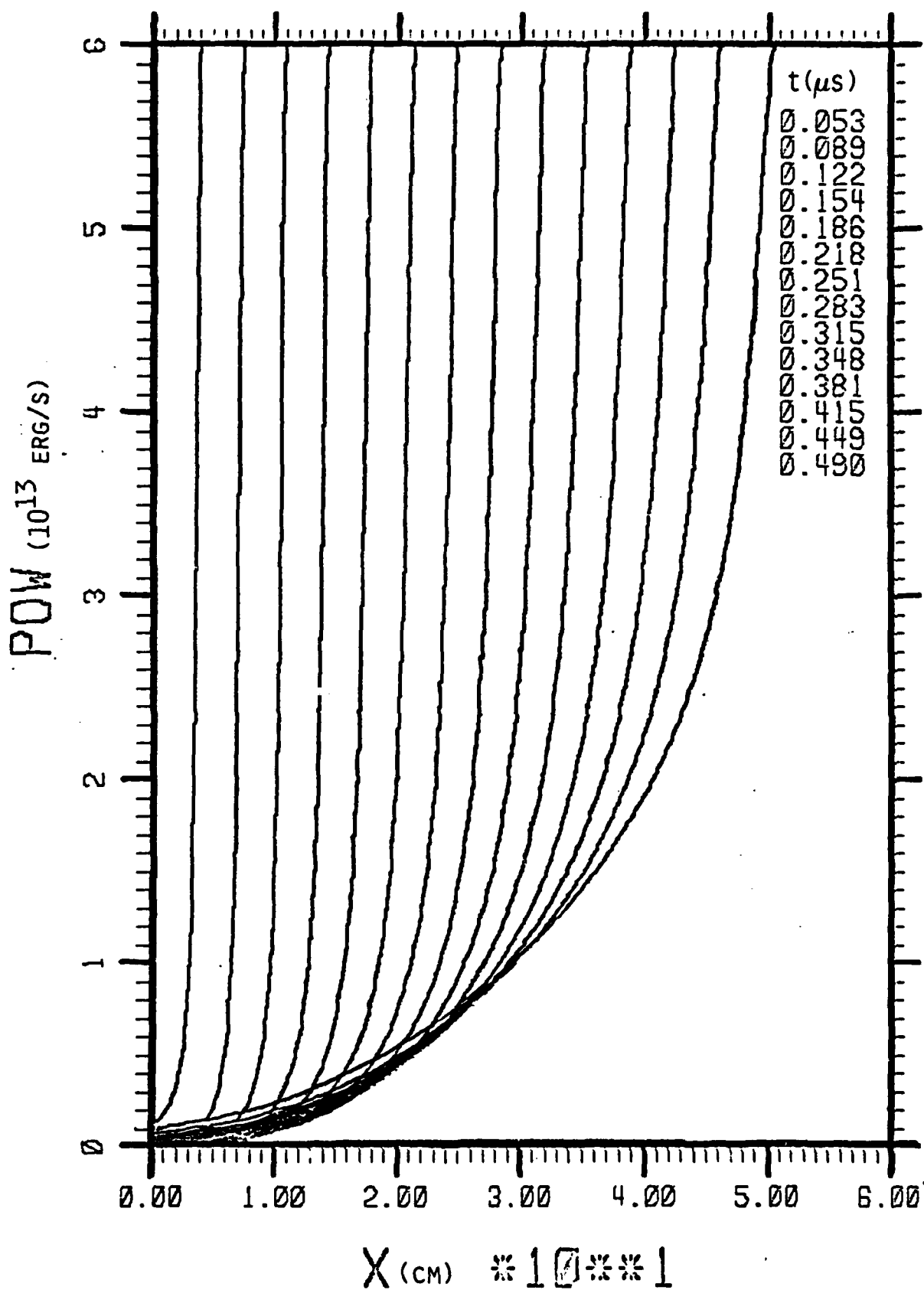


Fig. 3.15 Laser power profile for LSD wave in a conical nozzle. $P_{st} = 7$ atm, $T_{st} = 300$ K, laser energy 3 J, pulse time 0.5 μ s, multiply-ionized argon.

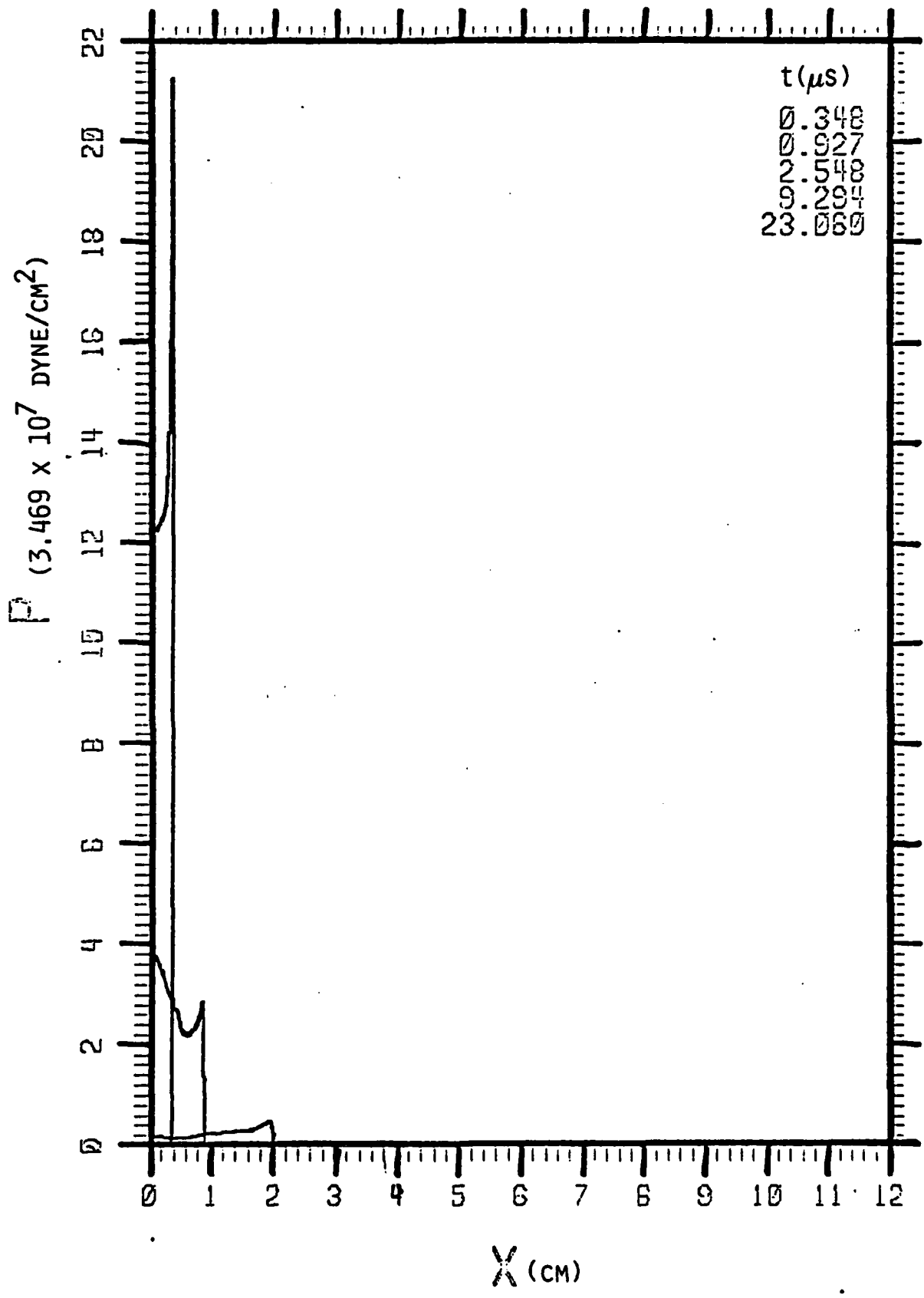


Fig. 3.16a Pressure profiles for shock wave in a conical nozzle. $p_{st} = 7 \text{ atm}$, $T_{st} = 300 \text{ K}$, laser energy 3 J, pulse time 0.5 μs , multiply-ionized argon.

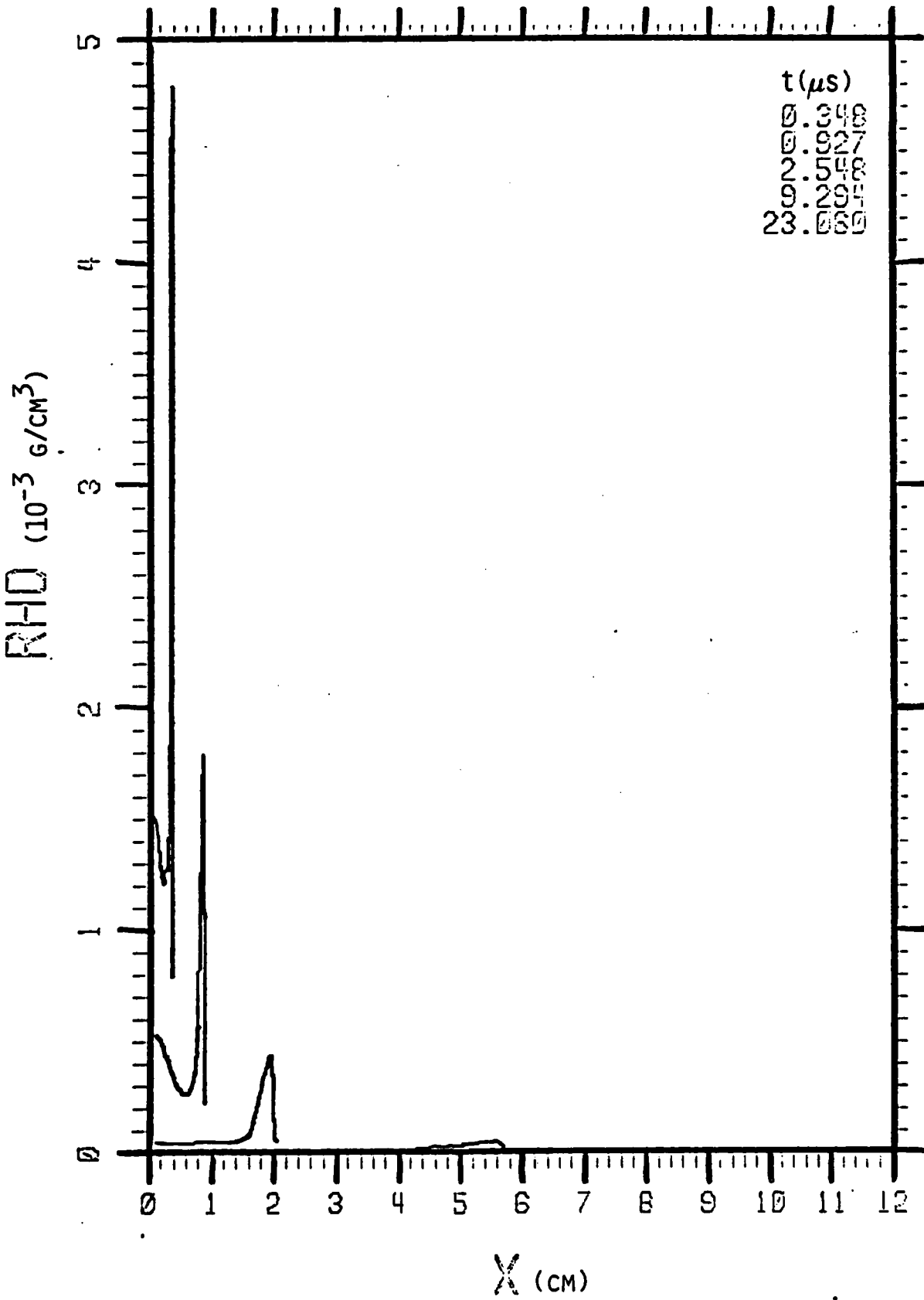


Fig. 3.16b Density profiles for shock wave in a conical nozzle. $p_{st} = 7 \text{ atm}$, $T_{st} = 300 \text{ K}$, laser energy 3 J, pulse time 0.5 μs, multiply-ionized argon.

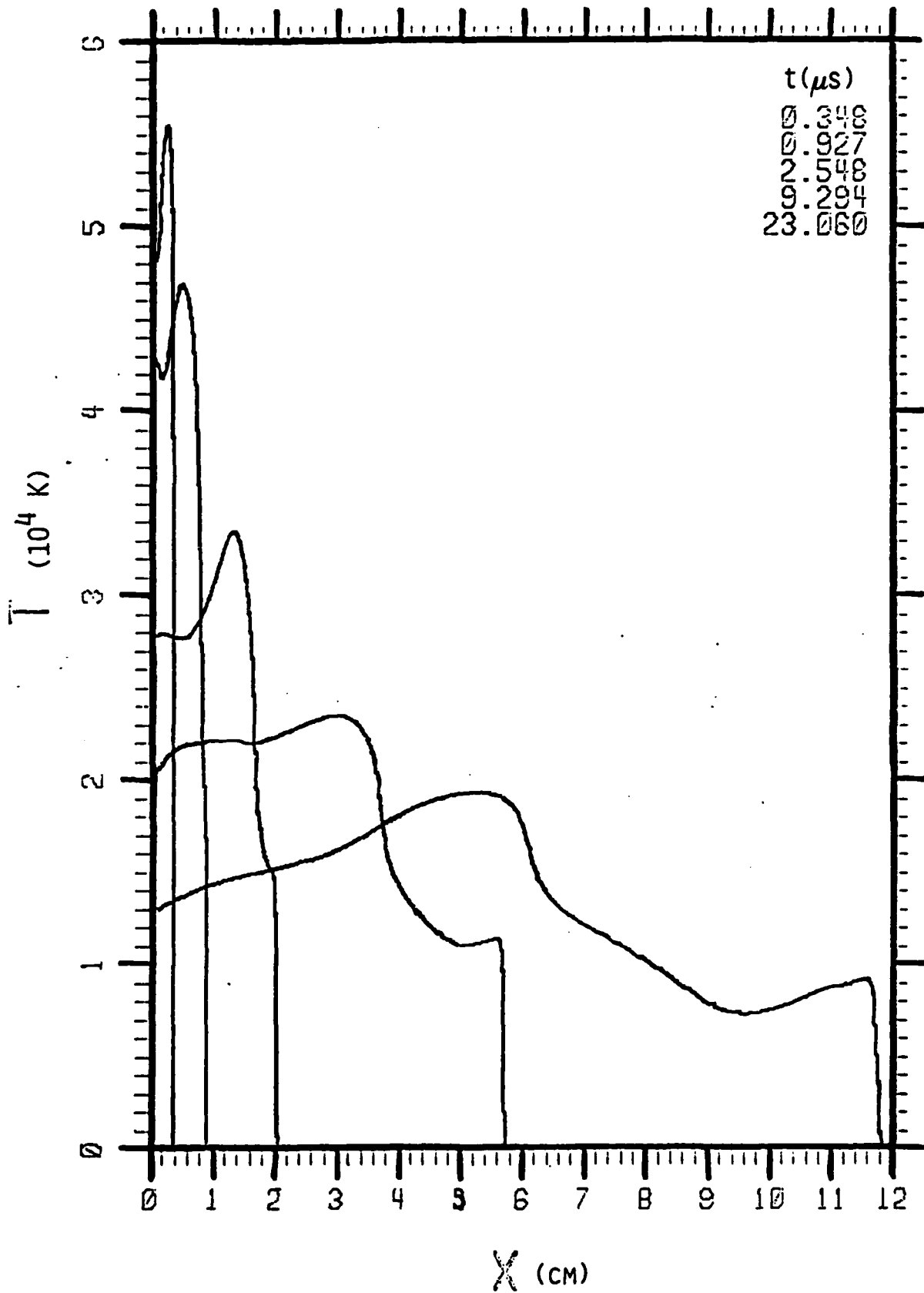


Fig. 3.16c Temperature profiles for shock wave in a conical nozzle.
 $p_{st} = 7$ atm, $T_{st} = 300$ K, laser energy 3 J, pulse time
 0.5 μs , multiply-ionized argon.

show the sharp rise of the shock wave, followed by a decay. The temperature profiles in Fig. 3.16c stay on the graph, since the peak temperature is near 20,000 K even at 23 μ s. The profiles show the sharp rise of the gas dynamic shock, followed by a further rise to the hottest region where the remnants of the laser energy deposition are still visible.

A similar run was made at a lower laser energy of 1 J, still for 0.5 μ s pulse time. All other conditions remained the same. The p, ρ and T profiles for that run are shown in Fig. 3.17. The first profile is at 0.315 μ s, when the laser is still on, but the others are all after the pulse is over. Here the shock wave reached 11.5 cm at 34.8 μ s, which is 11.8 μ s longer than it took with 3 J of energy in the pulse. The slower speed is, of course, caused by the lower energy available to drive the wave. The character of the profiles is the same as those of Fig. 3.16, but the values are lower. The peak temperature of the last profile, for example, is only 13,000 K, rather than 20,000 K. The generally lower levels also prevailed while the pulse was on, as evidenced by the fact that this 1 J case absorbed only 83.7% of the laser energy, in contrast to the 97% absorbed by the 3 J case.

One of the pieces of information desired from these runs is the time of shock arrival at a given nozzle station, as a function of laser energy. This time was measured in some of the experiments.

To obtain such a correlation, use was made of the similarity variables defined in Sec. 3.7 and used for correlation on the earlier data in Sec. 3.9. The similarity distance and time variables are

$$\xi = X / (E / \dot{m} u_{\ell}) , \quad \tau = t / (E / \dot{m} u_{\ell}^2) . \quad (3.14.2)$$

For the present two runs, only E differed, while $\dot{m} = 1.671$ g/s and $u_{\ell} = 5.5875E4$ cm/s for both. For E we used the absorbed energy, which was 97% for the 3 J case, or 2.91E7 erg, and 83.7% for the 1 J case, or 8.37E6 erg.

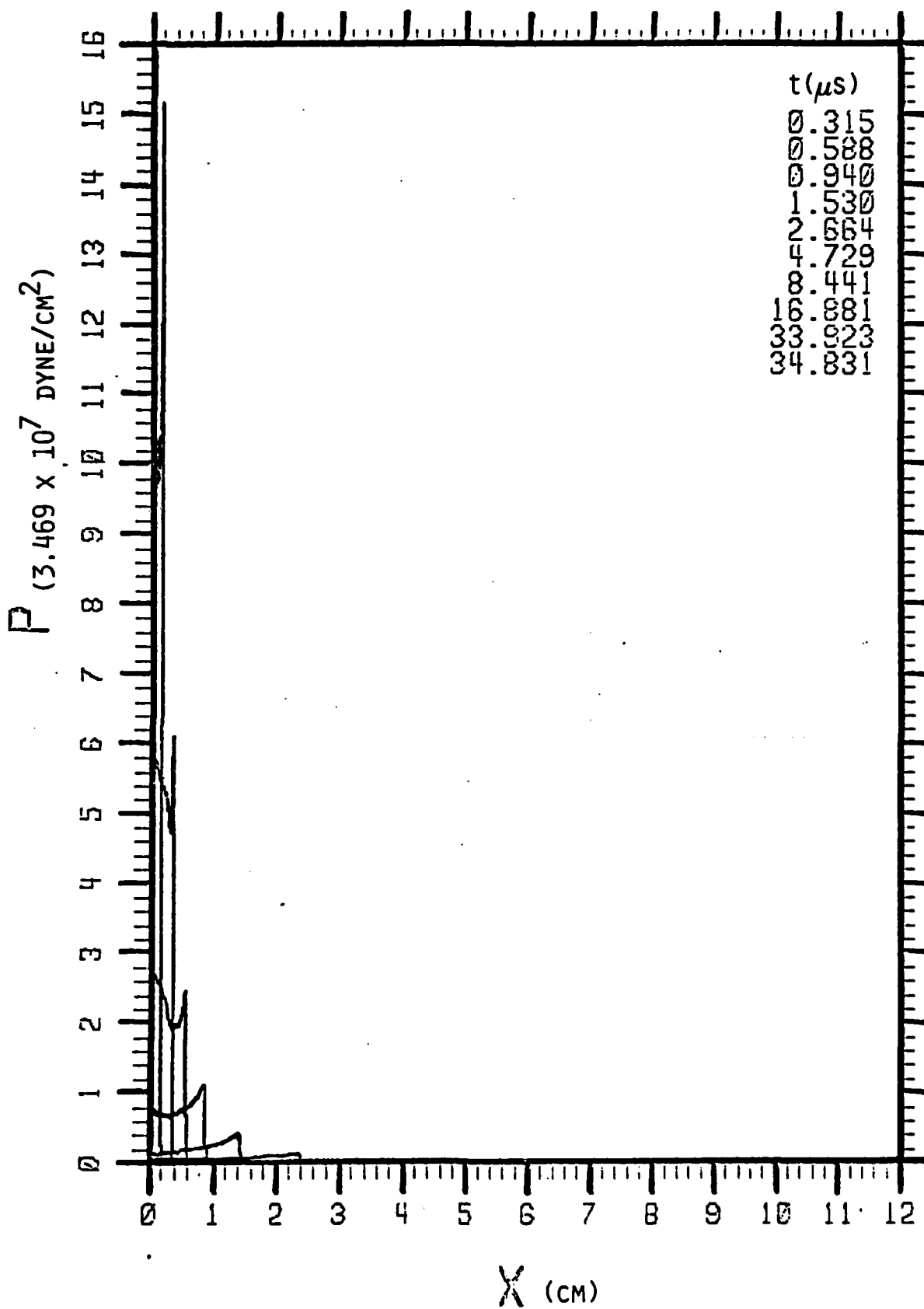


Fig. 3.17a Pressure profile for shock wave in a conical nozzle. $P_{st} = 7 \text{ atm}$, $T_{st} = 300 \text{ K}$, laser energy 1 J, pulse time 0.5 μs , multiply-ionized argon.

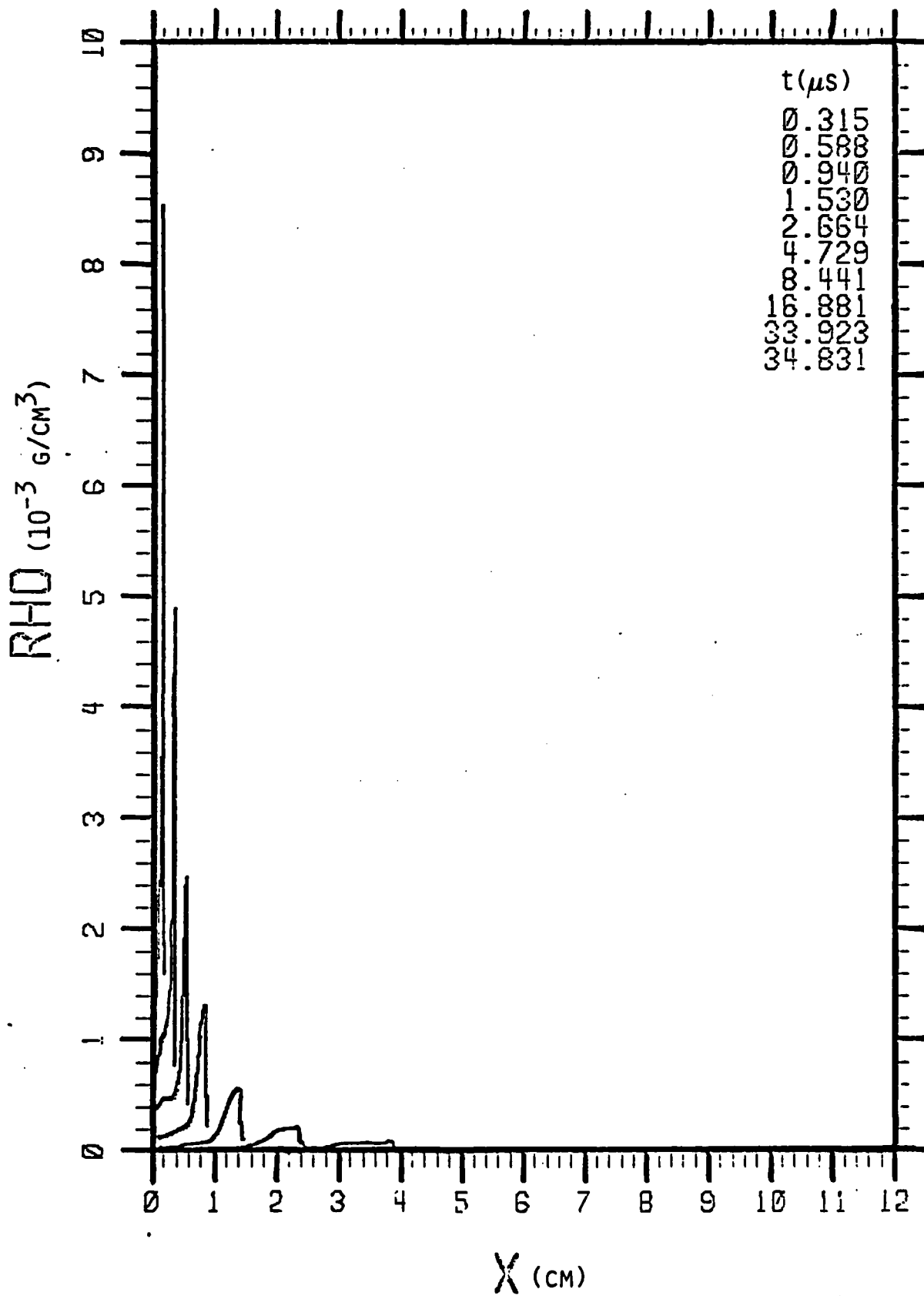


Fig. 3.17b Density profiles for shock wave in a conical nozzle. $P_{st} = 7 \text{ atm}$, $T_{st} = 300 \text{ K}$, laser energy 1 J, pulse time 0.5 μs , multiply-ionized argon.

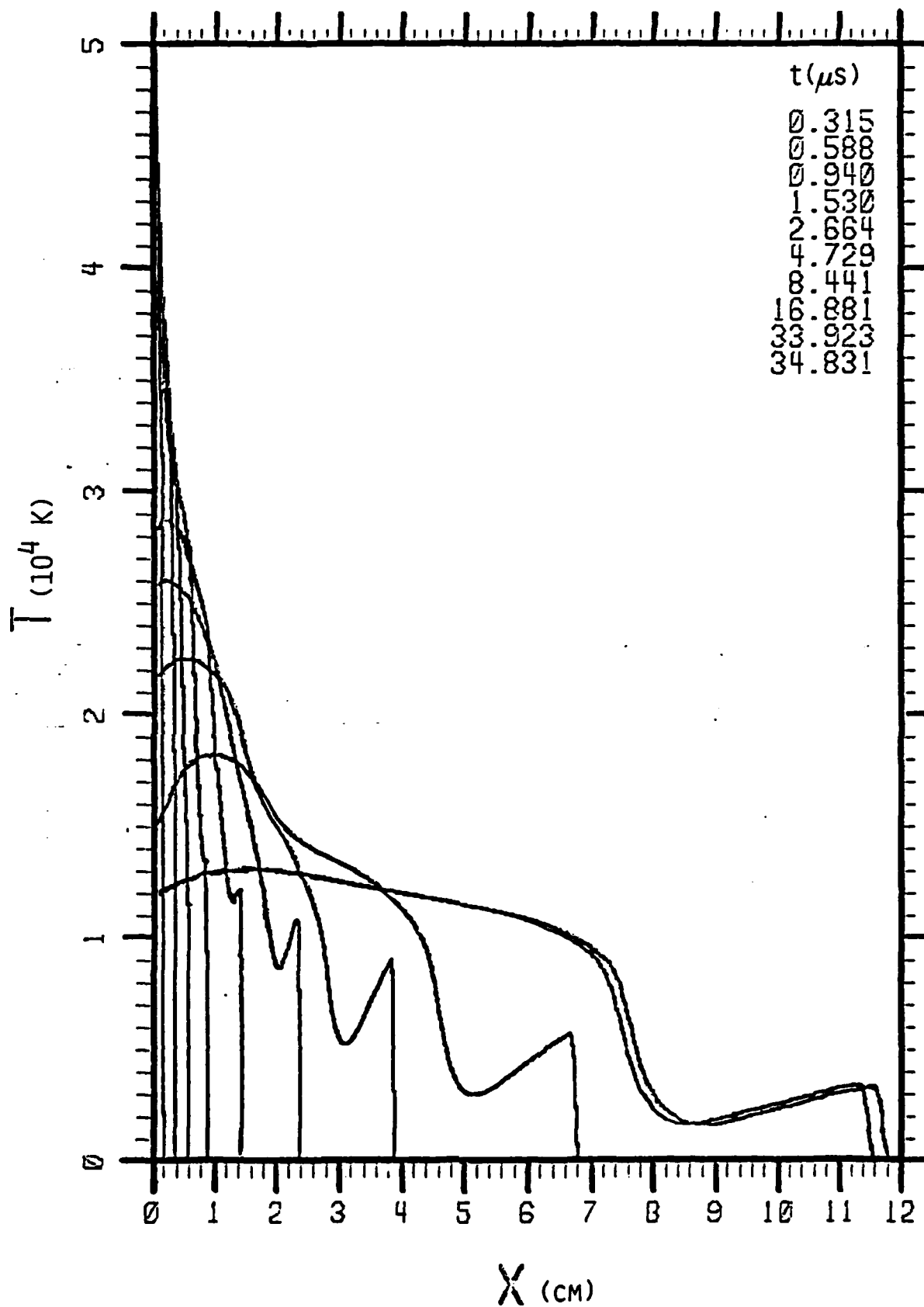


Fig. 3.17c Temperature profiles for shock wave in a conical nozzle.
 $P_{st} = 7 \text{ atm}$, $T_{st} = 300 \text{ K}$, laser energy 1 J, pulse time
 0.5 μs , multiply-ionized argon.

Using these parameters, the location of peak pressure vs. time was converted to ξ_p and τ and plotted in Fig. 3.18. The diagonal lines at the left show the values of τ below which the laser is still on for the two cases. Since the similarity variables are derived from blast wave theory, we would not expect them to be valid while energy was being deposited, or even soon afterward. And in fact, the points for the two laser energy levels are not well-correlated at the early times. However, the regions of interest for the experimental measurements are above $\tau = 10^{-3}$. In fact, measurements were made at $X = 4.3$ cm and 9.4 cm. The symbols with the horizontal tick marks show the values of ξ_p at those values of X . The lower two are for the 3 J case and the upper two for 1 J. It can be seen that in the region of interest for the measurements the circles and triangles both fall on the same line, and the correlation between the two energy levels is very good. The time when the shock reaches 4.3 cm is after 6 μ s for the 3 J case, and after 9 μ s for the 1 J case, which is long after the laser pulse is over. So we would expect the blast wave similarity variables to be applicable to these time periods, as they were for the runs of Sec. 3.9, which were made in the blast wave mode. The good correlation shown in Fig. 3.18 for this time period confirms those expectations.

To represent the points on Fig. 3.18, the straight line shown has been fitted to the four triangles and four circles at the highest values of τ . The equation of that line is

$$\xi_p = 2.499 \tau^{.7717} \quad (3.14.3)$$

For a given mass flow rate and limiting velocity, this is a relation between the location of peak pressure, the time and the energy absorbed. Since mass flow rate is proportional to stagnation pressure p_{st} , and only E/\dot{m} appears in the definition of ξ and τ , the equation can be solved for E/p_{st} . For $p_{st} = 1$ atm and $T_{st} = 300$ K, $\dot{m} = 0.2387$ g/s and $u_\ell = 5.5875E4$ cm/s. We then find

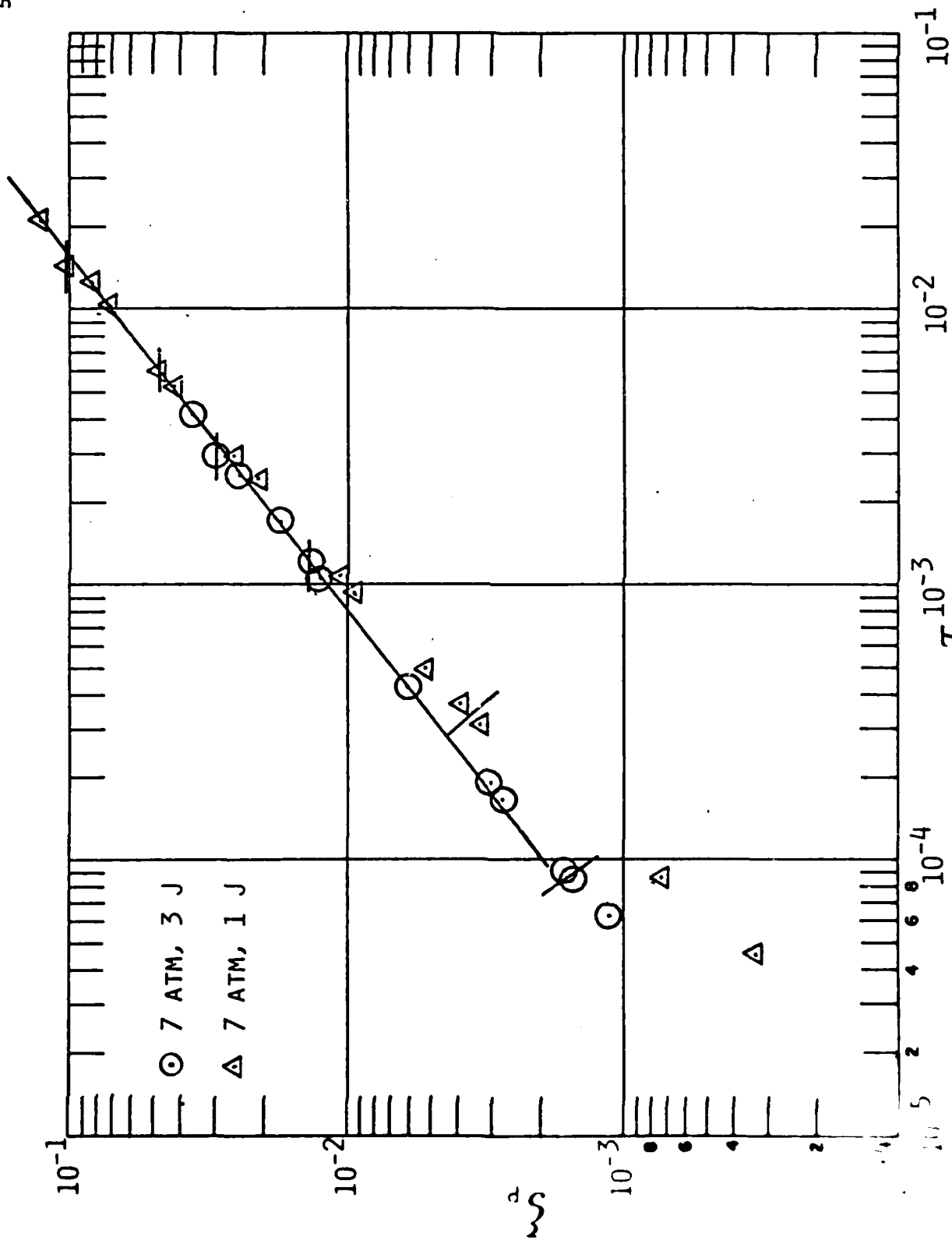


FIG. 1.18 Shock location as a function of time in similarity variables. $p_{st} = 7 \text{ atm}$, $T_{st} = 300 \text{ K}$, multiply-ionized argon.

$$E(\text{J}) = \frac{0.4142 p_{st}(\text{atm}) [x_p(\text{cm})]^{4.38}}{[t(\mu\text{s})]^{3.38}} \quad (3.14.4)$$

which enables us to calculate the energy deposited by the laser in the gas when the stagnation pressure, the measuring station location and the time of shock arrival are known. Equation (3.14.4) is useful for the interpretation of the 7 atm experimental data.

Another correlation of interest is the peak pressure as a function of distance, since pressure measurements may also be made. A similarity variable for pressure is

$$\Pi = p/E(\dot{m}u_\infty/E)^3 \quad (3.14.5)$$

and a plot of this parameter for peak pressure Π_{\max} vs. location ξ_p is given for the 3 J and 1 J cases in Fig. 3.19. The symbols with horizontal bars again show the regions from 4.3 to 9.4 cm. These two cases do not correlate as well as the ones in Fig. 3.18, but they can still be represented with good accuracy by a single line. The solid line is a fit to the four points for each case at the lowest values of Π_{\max} . Its equation is

$$\Pi_{\max} = 14.95 \xi_p^{-2.858} \quad (3.14.6)$$

which then relates peak pressure to its location for given energy, mass flow rate and limiting velocity.

Some idea of the accuracy of this fit can be obtained by fitting the two cases separately. The fit through the four triangles of the 1 J case is almost exactly the same as the solid line on Fig. 3.19. The fit through the four circles of the 3 J case is the dashed line, which is only slightly different from the solid line over the region of interest.

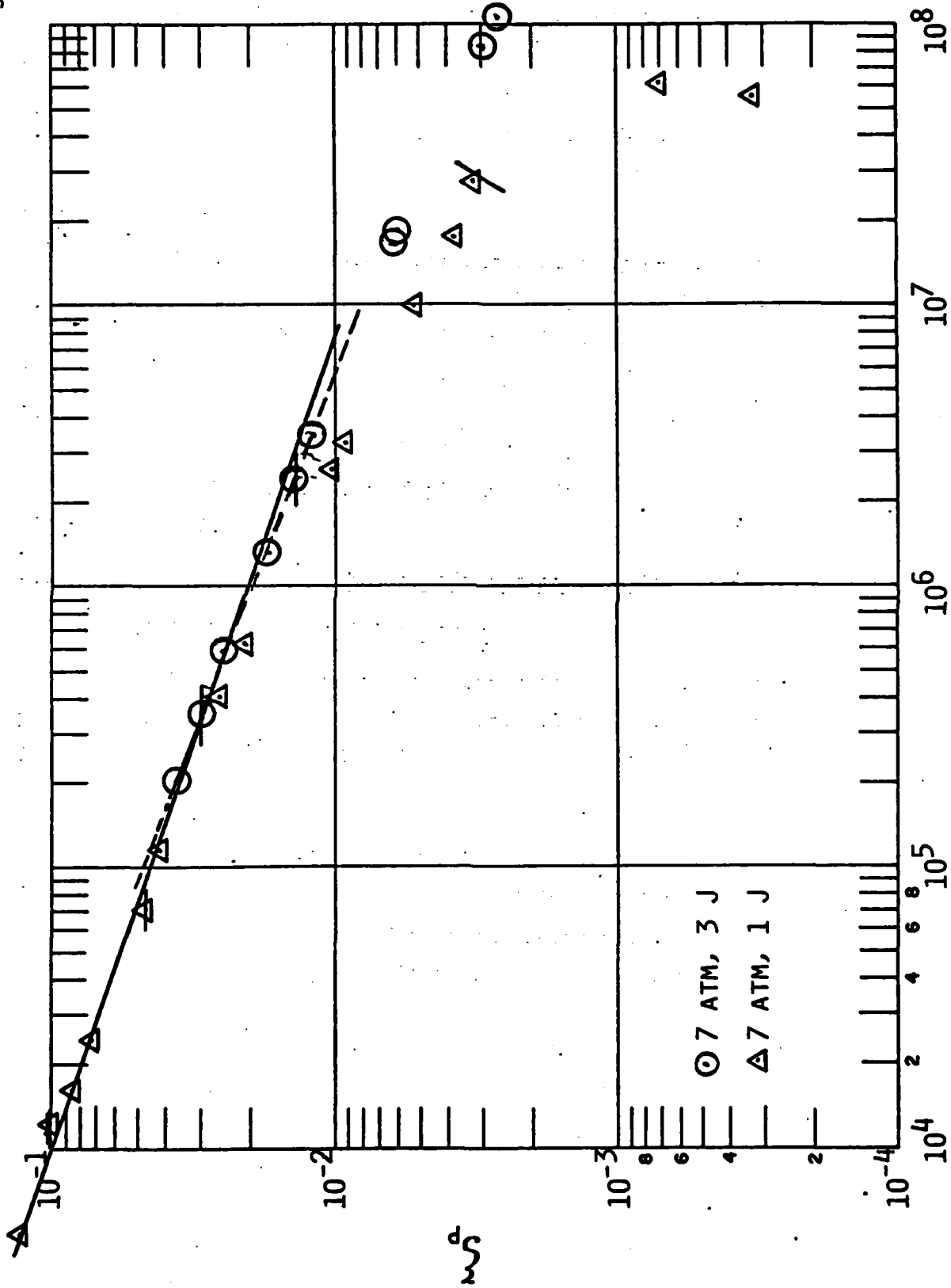


Fig. 3.19 Shock location as a function of peak shock pressure in similarity variables.
 $P_{st} = 7 \text{ atm}$, $T_{st} = \text{multiply-ionizing argon}$.

3.15 References

- 3.1 G. A. Simons and A. N. Pirri, "The Fluid Mechanics of Pulsed Laser Propulsion," AIAA J. 15, 835 (1977).
- 3.2 K. S. Drellishak, G. F. Knopp and A. B. Cambel, "Partition Functions and Thermodynamic Properties of Argon Plasma," AEDC, Tullahoma, TN, AEDC-TDR-63-146, August 1963.
- 3.3 Ya. B. Zeldovich and Yu. P. Raizer, "Physics of Shock Waves and High-Temperature Phenomena," (Academic Press, New York, 1966), Vol. 1, p. 281.
- 3.4 L. S. Frost and A. V. Phelps, "Momentum Transfer Cross-Sections for Slow Electrons in He, Ar, Kr, and Xe from Transport Coefficients," Phys. Rev. 136, A1538 (1964).
- 3.5 Yu. P. Raizer, "Heating of a Gas by a Powerful Light Pulse," JETP 21, 1009 (1965).
- 3.6 H. Mirels and J. F. Mullen, "Aerodynamic Blast Simulation in Hypersonic Tunnels," AIAA J. 3, 2103 (1965).
- 3.7. P. D. Lax, "Weak Solutions of Non-Linear Hyperbolic Equations and Their Numerical Computation," Comm. on Pure and Applied Math. 8, 159 (1954).
- 3.8 J. E. Mayer and M. G. Mayer, "Statistical Mechanics," John Wiley and Sons, Inc., New York, 1940.
- 3.9 N. H. Kemp, R. G. Root, P. K. S. Wu, G. E. Caledonia and A. N. Pirri, "Laser-Heated Rocket Studies," NASA CR-135127 (PSI TR-53), Physical Sciences Inc., Woburn, MA, May 1976.
- 3.10 Ya. B. Zeldovich and Yu. P. Raizer, "Physics of Shock Waves and High-Temperature Hydrodynamic Phenomena," Ed. by Hayes and Probstein, Academic Press, New York, 1966.
- 3.11 R. W. Patch, "Absorption Coefficients for Hydrogen: I, Composition," J. Quant. Spectroscopy and Radiative Transfer, 9, 63 (1969). R. W. Patch, "Thermodynamic Properties and Theoretical Rocket Performance of Hydrogen to 100,000 K and $1.01325 \times 10^8 \text{ N/m}^2$," NASA SP-3069, 1971.
- 3.12 W. J. Karzas and R. Latter, "Electron Radiative Transitions in a Coulomb Field," The Astrophysical Journal, Supplement Series, Supplement Number 55, 6, 167 (1961).
- 3.13 T. L. John, "The Free-Free Transitions of Atomic and Molecular Negative Ions in the Infrared," Monthly Notices of the Royal Astronomical Society, 170, 5 (1975).

- 3.14 J. R. Stalloop, "Absorption of Infrared Radiation by Electrons in the Field of Neutral Hydrogen Atom," *Astrophysical J.*, 187, 179 (1974).
- 3.15 S. Geltman, "Free-Free Radiation in Electron-Neutral Atom Collisions," *J. Quant. Spec. Rad. Transfer*, 13, 601 (1973).
- 3.16 C. E. Moore, "Atomic Energy Levels," National Bureau of Standards NSRDS-NBS 35, Vol. 1, 1971, pp. 211-221.
- 3.17 J. Hilsenrath, C. G. Messina and M. Klein, "Table of Thermodynamic Properties and Chemical Composition of Argon in Chemical Equilibrium Including Second Virial Corrections for 2400°K to 35,000°K," Arnold Engineering Development Center, AEDC-TR-66-248, December 1966.
- 3.18 H. S. Brahinsky and C. A. Neel, "Tables of Equilibrium Thermodynamic Properties of Argon Volume IV. Constant Temperature with Specific Heat and Speed of Sound Data," Arnold Engineering Development Center, AEDC-TR-69-19 Volume IV, March 1969.

4. SMALL-SCALE THRUSTER PERFORMANCE AND ABSORPTION PHYSICS PHENOMENOLOGY EXPERIMENTS

4.1 Introduction

In this section we describe experiments carried out at PSI during the period May 1978 through October 1980 to evaluate the performance of small-scale thrusters powered by pulsed laser radiation.

Reported in Section 4.2 are single and multiple pulse experiments conducted using TEA CO₂ lasers and a self-focusing (parabolic) nozzle. Results are presented for the specific impulse (I_{sp}) achieved using argon and hydrogen propellants, and the energy conversion efficiency (fraction of laser energy converted into propellant fluid mechanical energy) obtained using argon, hydrogen, nitrogen and helium. Specific impulses of 500 s in Ar and 1000 s in H₂ are demonstrated with energy conversion efficiencies $\geq 40\%$. In addition, experiments are described which were performed to assess loss mechanisms that might limit energy conversion efficiency. The loss mechanisms investigated included imperfect laser absorption, plasma re-radiation losses, and losses to exhaust gas heat and "chemistry," i.e., exhaust gas energy in degrees of freedom other than directed kinetic energy. It is shown that for the conditions of the experiments, imperfect laser absorption is generally the dominant loss channel.

In order to understand in more detail the phenomena which control the laser absorption process at 10.6 μm , as well as to establish the scaling of this phenomenology to 0.35 μm , experiments were carried out at 10.6 μm and 0.35 μm to measure laser-induced breakdown thresholds for several gases and the resulting absorption of the laser by the plasma. Using external focusing optics, the output from either a pulsed CO₂ (10.6 μm) or pulsed XeF (0.35 μm) laser was focused into a static, constant density gas background. The principal gases investigated were argon, hydrogen, and nitrogen. Measurements were made, as a function of gas pressure, of the laser intensity threshold to achieve breakdown and the absorption of the laser by the resulting plasma. In general, it was found that thresholds for laser-induced gas breakdown are about a factor of

20 to 30 times higher at 0.35 μm than at 10.6 μm . In addition, the results indicate that to achieve a comparable degree of absorption in the laser-produced plasma, the initial gas pressure must be about a factor of 20 to 30 times higher for 0.35 μm radiation than is required for 10.6 microns. The details of these experiments and their results, along with comparisons to the corresponding predictions of the theory of Section 2, are presented in Section 4.3.

Finally, Section 4.4 describes some single-pulse experiments carried out to measure the efficiency with which a pulse of XeF (0.35 μm) laser energy can be coupled into a nozzle gas flow. To avoid questions of nozzle optical quality, the experiments were performed using external focusing optics and a standard 10° (half angle) conical nozzle. Preliminary results for argon and helium propellants indicate that energy conversion efficiencies $\geq 50\%$ are possible at 0.35 μm if plenum delivery pressures greater than 10 atm are used.

4.2 Thruster Performance Experiments at 10.6 μm

4.2.1 Experimental Apparatus

The basic experimental apparatus is the same as that used in the previous program and described in Refs. 4.1 and 4.2. However, a number of improvements were made and will be described in the following sections.

Lasers

The Lumonics K-101 TEA CO₂ lasers were mounted inside a carefully designed electrically shielded box to minimize EMI noise pickup by the oscilloscopes and associated detection electronics. By shielding against rf radiation, avoiding ground loop problems, and filtering the power line inputs, the electrical noise transients picked up on nearby oscilloscopes when the lasers fired were reduced from a level of several volts to the millivolt level. Another improvement implemented in the operation of the lasers was the use of several digital delay generators manufactured by California Avionics. The delay units enabled accurate and reliable setting of the delay times between the opening of the fast acting propellant feed solenoid valve, the firing of the lasers, and the triggering of the oscilloscope sweeps.

Vacuum Test Chamber

The vacuum test chamber utilized was the same as that described in Ref. 4.1. One improvement made, however, was the addition of a 100 cfm vacuum booster blower before the Welch 17.7 cfm mechanical oil roughing pump. This modification greatly reduced pump down times and, along with careful leak checking of the vacuum system, enabled us to achieve an ultimate vacuum as low as 7×10^{-4} torr which is an order of magnitude better than that obtained previously.

Rocket Nozzle Design and Propellant Feed System

All experimental measurements that will be presented here were made using self-focusing nozzles constructed of aluminum parabolic shells of revolution. The paraboloidal shells were spun so that the inside contour described the parabolic function $y = .787x^2$ (where y and x are given in centimeters). Such a contour has a focus that is 0.32 cm from the apex. The shells were cut to a length of 10 cm which yielded an exit plane diameter of 7.1 cm. The inside surfaces were polished using conventional polishing and buffing techniques to yield mirror like finishes. A detachable nozzle throat assembly was designed that allowed simple changing of the nozzle throat diameter. Throat diameters from 0.2 to 0.5 cm were investigated. A mounting port that could be used for mounting of either a pressure transducer or fast response thermocouple flush with the inside nozzle surface was located 4.4 cm downstream of the throat.

For the purpose of making shock wave transit time measurements a conical skirt extension to the parabolic shell was fabricated. This extension is 10 cm long and has provision for flush mounting of two vibration-isolated pressure transducers separated by an axial distance of 5 cm.

To facilitate a more rapid turn around time between rocket test firings, most of the experimental runs had the propellant mass flow controlled by a fast acting electrically actuated solenoid valve rather than the rupturable latex diaphragm used in previous experiments. For the present experiments, then, the sequence of events was as follows: (1) the propellant feed solenoid valve is triggered to open; (2) several milliseconds later

after steady flow is established, the lasers are fired into the rocket; (3) the oscilloscope sweeps are triggered to record the voltage outputs of the various diagnostic instruments; and, (4) the solenoid valve closes.

A schematic diagram of the parabolic rocket assembly is shown in Fig. 4.1.

4.2.2 Experimental Diagnostics

Pressure Transducers

For most of the experimental measurements, Kistler pressure transducers were used to monitor the laser-induced blast wave arrival times and post shock pressures. For this purpose, the transducers were vibration-isolation mounted inside neoprene rubber stoppers and their sensing elements located flush with the inside surface of the rocket wall. The rise time of the transducers was $\leq 1 \mu\text{s}$ and their responsivity 20-30 millivolts/psi.

For operation with a single laser pulse, the measured shock transit times or post shock pressures were used to infer the energy in the blast wave.^{4.3} (See also Sections 3.9 and 3.14.) With corresponding measurements of the laser energy, energy conversion efficiencies were then determined. Details of these measurements and their results will be discussed in Section 4.2.3.1. For multiple laser pulse operation, the pressure transducers were used to measure the transit time (velocity) of each laser heated mass slug at the exit plane and, hence, determine specific impulse (I_{sp}). The results of these measurements will also be presented in Section 4.2.3.1.

Laser Energy Measurements

Laser pulse energies could be monitored in two ways. First, both prior to and following a set of experimental runs the output of each laser was measured by placing a Lumonics 50D calorimeter before the entrance of the rocket nozzle. In addition, the shot to shot energy of each laser could be monitored by additional calorimeters located to detect that fraction of each laser's energy reflected off the KCl entrance windows to the vacuum tank. The latter calorimeters were constructed from sections of anodized aluminum

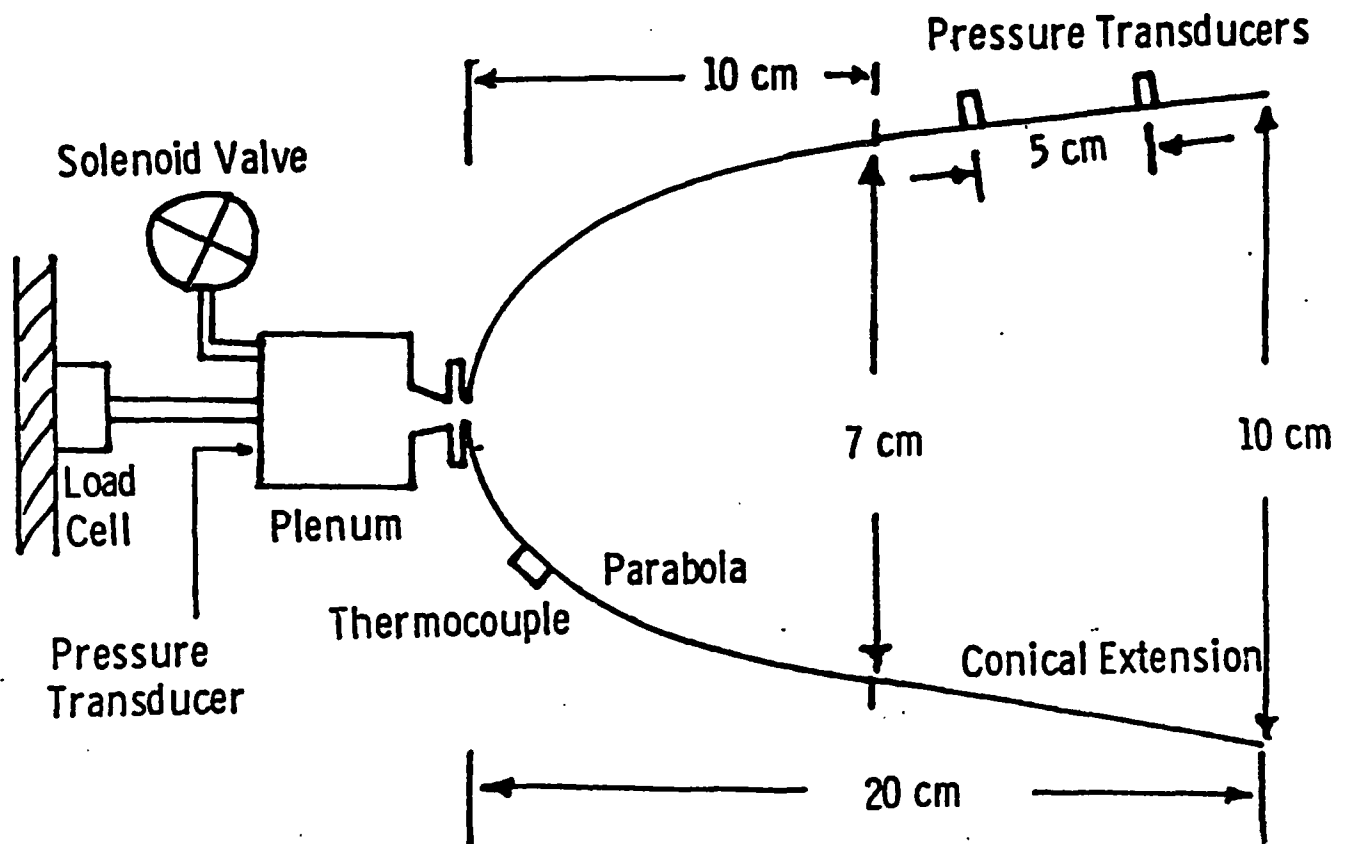


Fig. 4.1 Parabolic rocket schematic

sheet which were backed with an array of thermocouples that followed the temperature rise. Details of the construction and performance of this type of calorimeter are described in Ref. 4.4.

Ballistic Pendulum

As a check on the specific impulse results obtained from the pressure transducer measurements, a limited number of tests were carried out in which the rocket assembly was suspended inside the vacuum tank by a ballistic pendulum. For these measurements, the solenoid valve, because of its excessive weight, had to be replaced by a rupturable latex diaphragm for controlling the propellant mass flow. The details of operation with the latex diaphragm are described in Refs. 4.1 and 4.2.

One significant improvement implemented for the present ballistic pendulum measurements was the use of propellant counterflow to negate the impulse generated by the cold flow in the rocket nozzle. To achieve this a nozzle with an equivalent throat diameter was attached to the back of the rocket plenum chamber so that an equal cold mass flow was ejected to directly oppose the cold mass flow into the laser rocket nozzle. By doing this, the net background impulse from the cold flow was reduced to approximately 5% of that obtained without the use of the counterflow technique. The laser-induced impulse delivered to the rocket was then determined by making separate measurements of the deflection of the pendulum due to the residual unbalanced cold flow alone and cold flow plus laser heating. The increase in the pendulum's deflection observed when the laser was fired into the rocket was then used to determine the laser-induced impulse. The results of the ballistic pendulum measurements are discussed in Section 4.2.3.1.

Radiometric Diagnostics

The Lumonics 50D calorimeter and a Laser Precision energy meter were used to measure the amount of radiant energy that was lost out of the rocket. By using appropriately chosen optical filters, separate determinations were made of both the amount of unabsorbed 10.6 micron laser radiation that was reflected out of the rocket and the amount of UV/visible reradiation that was emitted by the hot gas.

In addition to the time integrated measurements described above, time resolved measurements were also made of the transmitted (unabsorbed) laser radiation using a fast response pyroelectric detector. The results of the radiometric measurements will be presented in Section 4.2.3.2.

4.2.3 Experimental Results

4.2.3.1 Rocket Performance Results

Energy Conversion Measurements - E_{BW}/E_l

An important measurement to make to assess the potential performance of a rocket driven by a pulsed laser is the energy conversion efficiency - that is, what fraction of the laser energy is converted into fluid mechanical energy of the gaseous propellant. In Ref. 4.3, and Section 3.7 of this document, the characteristics of a blast wave driven into a hypersonic flow field are analyzed. In those analyses the energy of the blast wave is related to numerous blast wave parameters including transit time, post shock pressure, and velocity. We have made measurements of these parameters for a blast wave driven by laser detonation into the hypersonic flow field of a small scale rocket nozzle. These measurements, combined with the blast wave analysis, have led to the determination of the efficiency of converting pulsed CO_2 laser energy into fluid mechanical energy for several gaseous propellants. In addition to varying the species of propellant gas, the mass flow of each propellant was varied to assess its effect on the energy conversion process. The mass flow was controlled either by varying the rocket plenum pressure or changing the nozzle throat diameter.

Energy conversion efficiency measurements were made for argon, hydrogen, helium and nitrogen as a function of mass flow. The blast wave energy was determined from pressure transducer measurements. Pressure transducers (Sundstrand 211B4) mounted flush with the rocket wall were used to measure blast wave transit times and post shock pressures. This pressure transducer data was used as input to blast wave theory to deduce blast wave energy. Mirels and Mullen^{4.3} have developed the appropriate formulas (also see Section 3.7 of this document). For the transit time data, the formulas used are:

$$R = Ct^{2/3} \quad (4.2.1)$$

and

$$V_s = \dot{R} = 2/3 Ct^{-1/3} \quad (4.2.2)$$

where R is the shock location, t is the time, V_s is the shock velocity, and C is a constant equal to

$$\left[(9/4 I_B) (E_{BW} V_{\ell}/\dot{m}) \right]^{1/3} \quad (4.2.3)$$

For a parabolic nozzle, I_B is a numerical constant equal to 0.733 for $\gamma = 1.4$ and .436 for $\gamma = 1.67$. The other parameters are the blast wave energy, E_{BW} , the limiting velocity of the "cold" propellant, V_{ℓ} , and the propellant mass flow rate, \dot{m} . The formula used to relate the post shock pressure to the blast wave energy in the parabola is

$$P_s = \frac{1}{(\gamma+1) I_B} \cdot E_{BW}/V \quad (4.2.4)$$

where V is the included volume in the nozzle up to the shock location R_s .

For the strong blast wave cases, where Mirel's and Mullen's analysis only strictly applies, both the pressure and the transit time measurements yielded similar results for the inferred blast wave energy. For cases where the blast wave was weaker, such that the shock velocity was not much greater than the cold gas limiting velocity, a correction was applied to the transit time formula following the prescription set forth in Section 3.7. Finally, for argon and hydrogen, a computer code that includes equilibrium chemical effects was utilized to assess possible 'real gas' corrections to the inferred blast wave energy (see Sections 3.3, 3.9 and 3.12). Such corrections were found to be most significant at the lower mass flow rates where the initial energy to mass ratios and, hence, initial temperatures, were highest. The results of applying real gas corrections to the inferred energy conversion efficiencies are presented in Section 4.2.3.2.

Energy conversion results for Ar, H₂, He, and N₂ are presented in Fig. 4.2. To be particularly noted is the observed trend of increasing energy conversion efficiency, E_{BW}/E_{laser} , with increasing mass flow rate. This trend will later be shown to be well correlated with separate observations of the behavior of the laser optical absorptance efficiency vs. mass flow rate. Furthermore, the observed variation of the energy conversion efficiency with gas species appears to suggest decreased conversion efficiencies with increasing ionization potential -- a result which is not surprising if the conversion efficiency is dominated by plasma breakdown and optical absorptance considerations.

Figure 4.3 is a plot that compares the energy conversion efficiency in Ar vs. mass flow rate obtained from both transit time and pressure data. As can be seen there is generally good agreement between the energy conversion efficiencies arrived at by these two different measurements. Finally, Fig. 4.4 illustrates how the energy conversion efficiency varies for different nozzle throat diameters. For the range of throat diameters investigated (0.2 cm to 0.5 cm), at a given mass flow rate a slight improvement in conversion efficiency is obtained at the smaller throat diameters. This result may be due to a higher optical coupling efficiency that results from the higher gas density at focus obtained when using the smaller throat diameter. Such a hypothesis is supported by observations of a similar trend for the optical absorptance efficiency measured for different throat diameters. These latter data will be presented in Section 4.2.3.2.

Specific Impulse Results

In addition to energy conversion efficiency, perhaps an even more important performance parameter of a laser driven rocket is the specific impulse. The specific impulse, I_{sp} , is defined as the exhaust momentum per unit weight of expelled fuel or, more simply, the mass averaged exhaust velocity divided by g , the acceleration of gravity. Thus

$$I_{sp} = \frac{T}{\dot{m}g} = \frac{J}{\Delta mg} = \frac{\Delta m V_e}{\Delta mg} = V_e/g \quad (4.2.5)$$

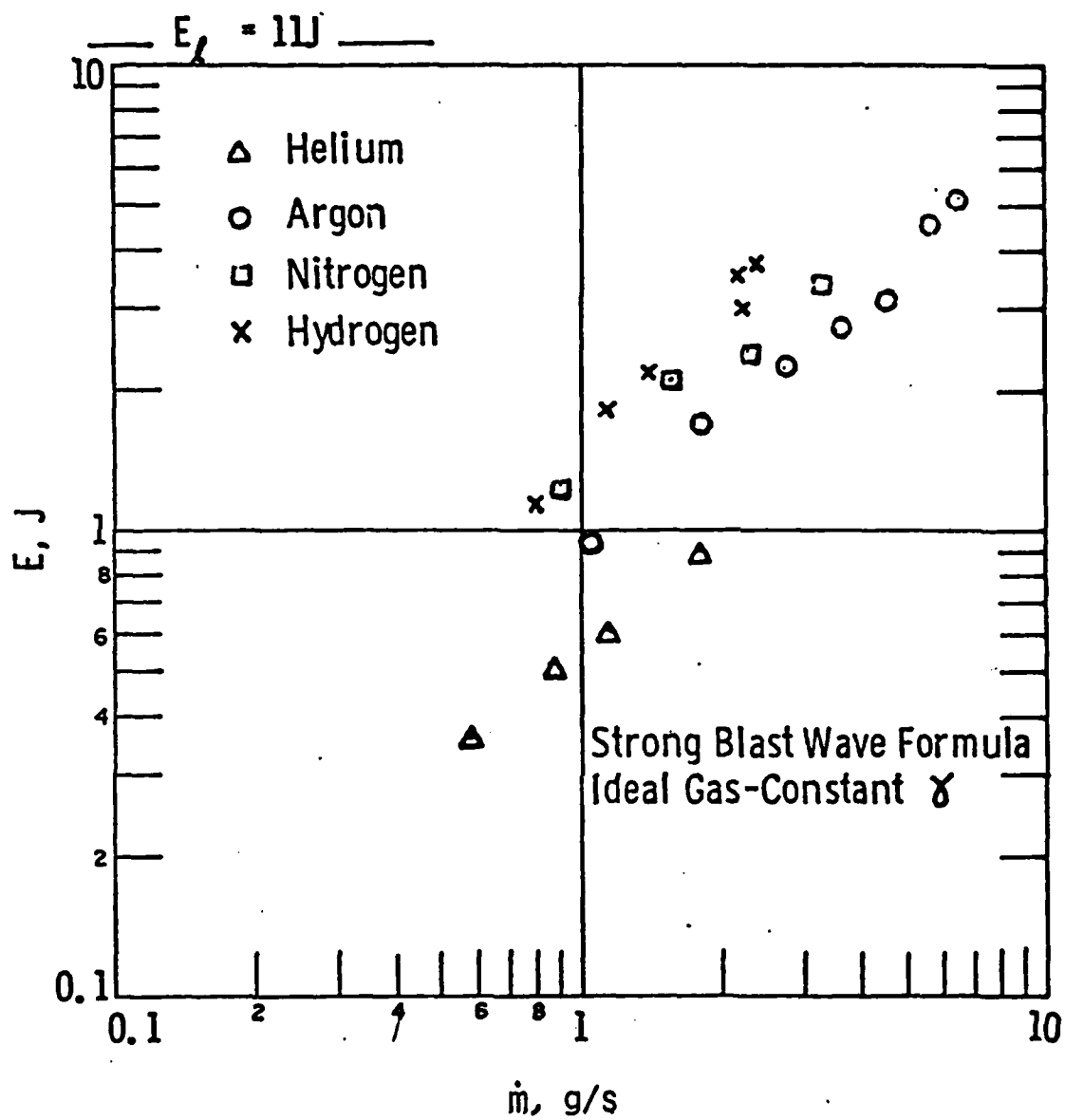


Fig. 4.2 Blast wave energy vs. \dot{m} .

BLAST WAVE ENERGY vs. \dot{m}

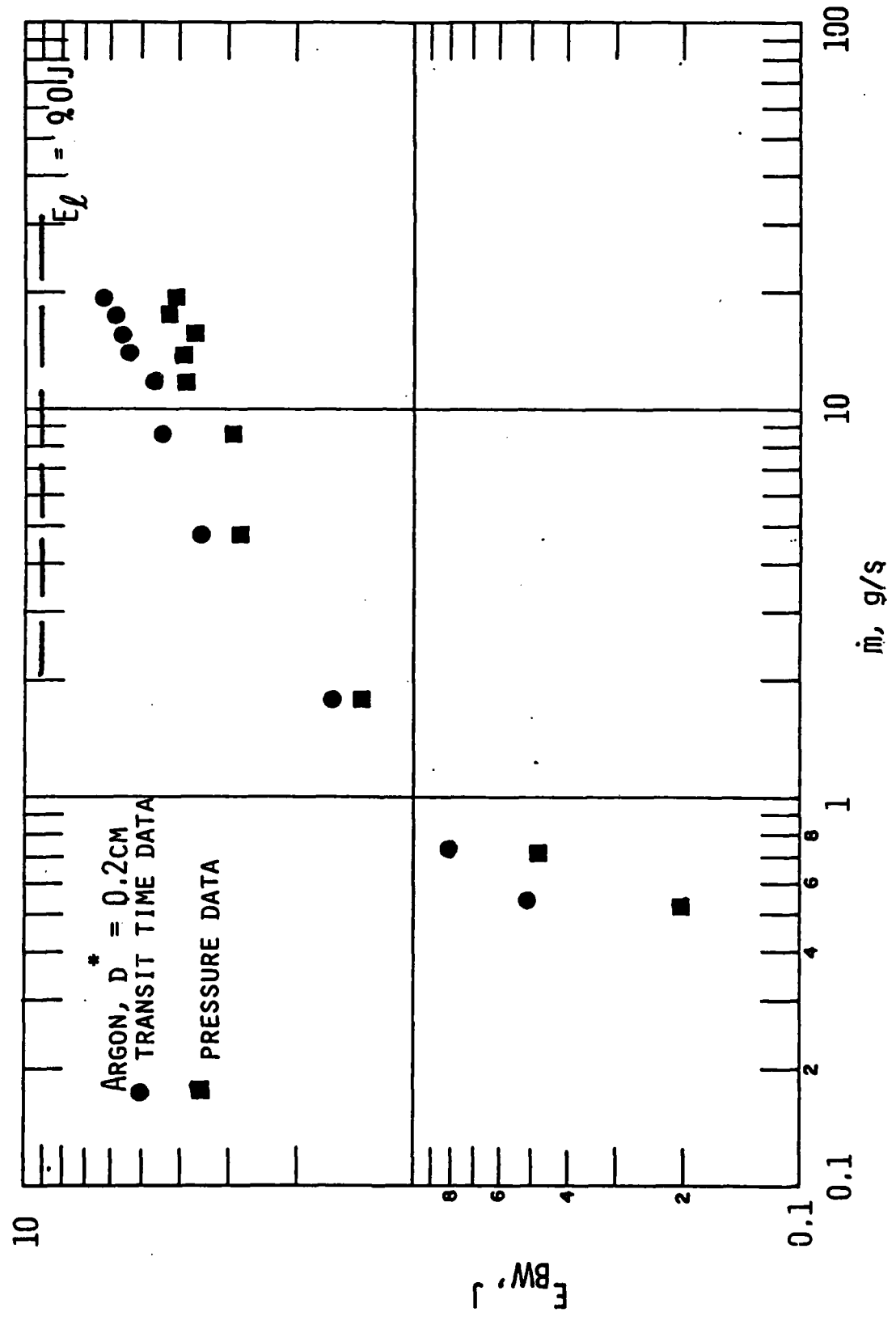


Fig. 4.3 Measured blast wave energy vs. \dot{m} in argon.

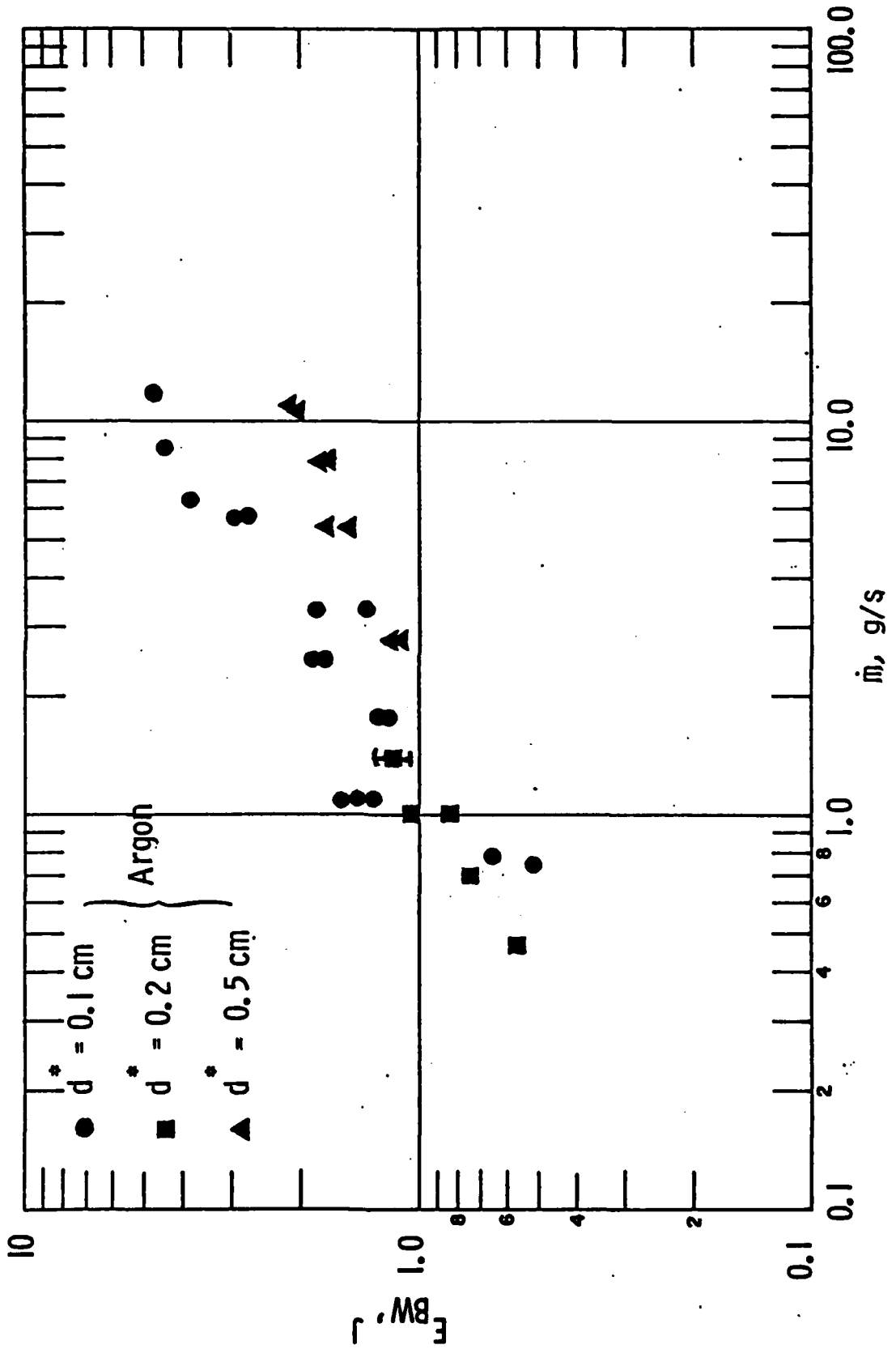


Fig. 4.4 Blast wave energy in argon for different throat sizes.

where T is the average thrust obtained per pulse, \dot{m} is the average mass flow rate between pulses, g is the acceleration of gravity, J is the incremental increase in impulse per laser pulse, V_e is a mass averaged expellant exhaust velocity, and Δm the mass expelled per laser pulse, i.e.,

$$\Delta m = \rho^* u^* A^* \Delta t \quad (4.2.6)$$

where A^* is the nozzle throat area, ρ^* is the initial expellant density at the throat, u^* is the sonic velocity, and Δt the time between laser pulses. Equation (4.2.6) is an upper limit to the expelled mass since it assumes that immediately after the laser fires the propellant efflux recovers to its steady-state value.

From Eq. (4.2.5) it can be seen that a determination of the specific impulse might be made from measurements of the average thrust or impulse imparted per laser pulse (provided the mass flux is known from rocket plenum conditions and the throat area), or, more directly, from a measurement of the exhaust gas velocity. Because of the relative ease of the measurement, most of our specific impulse data have been obtained using pressure transducers mounted at the rocket exhaust to measure the exit velocity of the laser heated mass slug. As a check on the validity of these pressure transducer measurements, a limited number of measurements were also made using a ballistic pendulum to measure impulse.

Specific impulse results obtained for argon and hydrogen are shown in Figs. 4.5 and 4.6. The data presented were obtained from pressure pulse transit time measurements for the second laser pulse. The results are plotted vs. Δm , the mass of the laser heated gas slug, which is simply given by $\dot{m}\Delta t$ where Δt is the laser interpulse time. In contrast to single pulse operation, where the propellant has completely filled the nozzle before the laser is fired, higher specific impulse is expected for a second laser pulse when the propellant is not allowed sufficient time to completely refill the rocket. In the latter case, the laser-driven blast wave overtakes and coalesces with the propellant mass front such that by the exit plane the pressure transducers detect the passage of a laser-heated mass slug rather

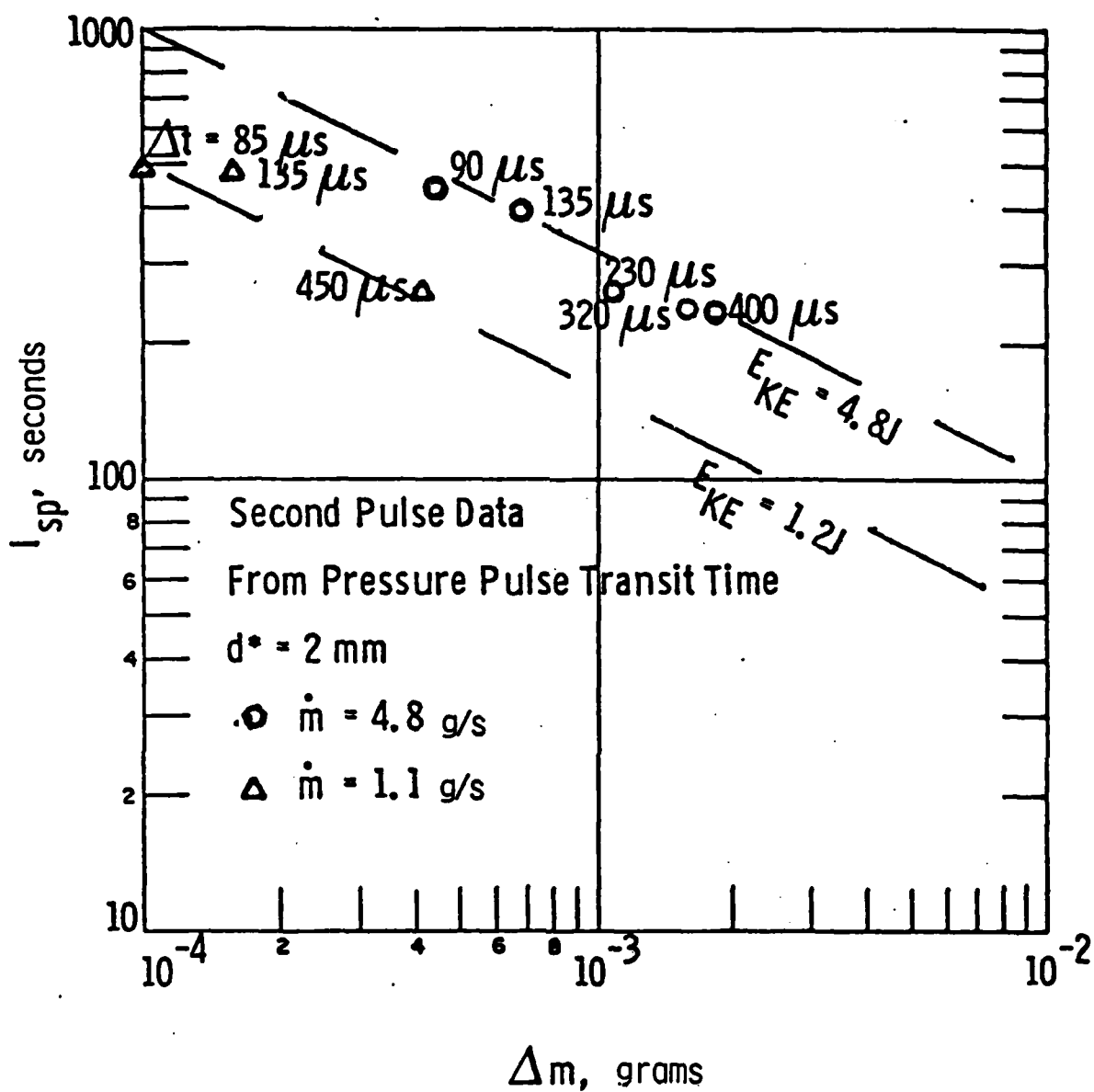


Fig. 4.5 I_{sp} vs Δm for argon; Δt is the delay time between the firing of the first and second laser pulse.

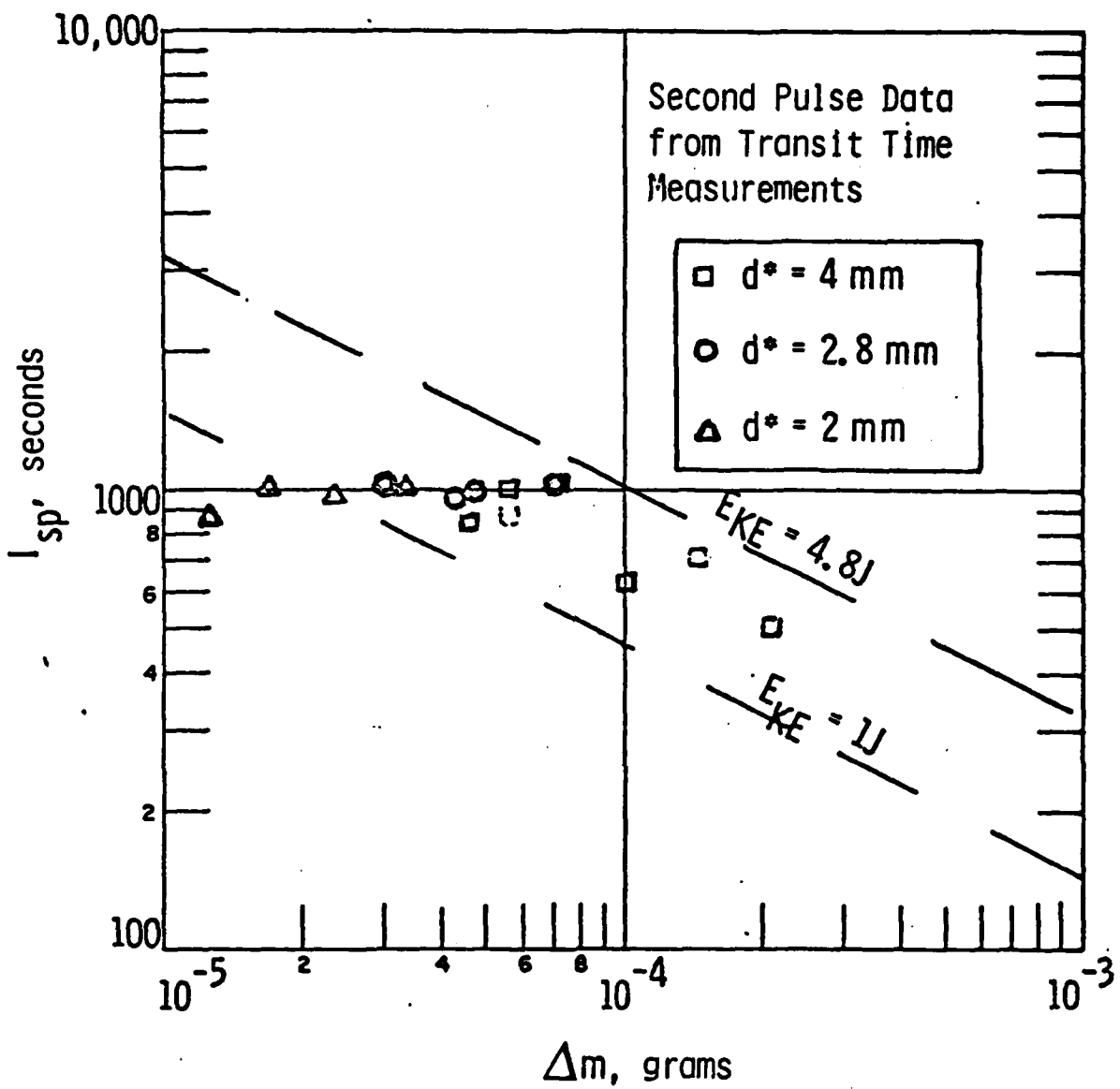


Fig. 4.6 I_{sp} vs. Δm for hydrogen.

than a shock wave moving through an ambient gas background. Higher specific impulse or gas exhaust velocity is expected for this situation because the shocked propellant is able to convert more of its thermal energy into directed kinetic energy as a result of an isentropic volume expansion.

There are a number of important features that should be pointed out regarding the specific impulse results of Figs. 4.5 and 4.6. First, a higher specific impulse, 1000 s, is achieved with hydrogen compared to 500 s with argon. This result is not particularly surprising since considerably higher effective stagnation temperatures would be required in argon compared to hydrogen to yield the same exhaust velocity. A second notable feature of the results is that, for fixed laser energy input, higher specific impulse tends to be achieved at the lower Δm 's. In interpreting this result, however, one must keep in mind that there were two ways in which the amount of expelled mass, Δm , was varied. One way was by changing \dot{m} , the mass flow rate, and the other was by decreasing Δt , the laser interpulse time. From the energy conversion efficiency results shown earlier, decreasing \dot{m} tends to lead to poorer energy conversion and therefore might be expected to adversely affect the achievable specific impulse. On the other hand, by decreasing Δt and keeping \dot{m} constant the same energy conversion might be maintained, and even higher specific impulses achieved due to both higher initial energy to mass ratios and the higher expansion ratios that go with shorter laser interpulse times. The above statements are supported by the data presented in Fig. 4.5. For a given \dot{m} , higher specific impulse is observed for the shorter interpulse times. Very little if any gain in specific impulse is attained, however, by just decreasing \dot{m} -- due presumably to the competing effect of decreased energy conversion efficiency.

In addition to measuring the exhaust velocity of the pressure wave driven by the second laser pulse, specific impulse was determined, for a limited number of measurements, by measuring with a ballistic pendulum the corresponding impulse imparted to the rocket. According to Eq. (4.2.5), the specific impulse can be determined from the laser-induced impulse if the amount of expelled mass is known. For the purpose of the present measurements, the expelled mass was taken to be $\dot{m}\Delta t$; where \dot{m} is the

expellant mass flow rate as determined by the nozzle throat area and plenum delivery pressure, and Δt is the delay time between the firing of the first and second laser pulse. The details of the ballistic pendulum measurement technique were described earlier in Section 4.2.2.

Measurements of laser-induced impulse were performed for argon propellant at a plenum delivery pressure of 1.5 atm and for a nozzle throat diameter of 0.2 cm -- conditions that yield a mass flow rate of 1.4 g/s. The laser-induced impulse measured for the second laser pulse ($\Delta t = 90 \mu s$) was found to be 41 ± 10 dyne-s. Using Eq. (4.2.5), this value of impulse indicates a specific impulse of 325 ± 80 s. Upon inspection of Fig. 4.5, we see that the above value of specific impulse is about 30% less than the corresponding value inferred from the pressure wave transit time measurements. One possible explanation for the result is that the actual expelled mass, Δm , is less than $\dot{m}\Delta t$. Since the specific impulse, I_{sp} , is given by $J/\Delta mg$ (where J is the laser-induced impulse) overestimating Δm will lead to an underestimate of the specific impulse. As was mentioned earlier, $\dot{m}\Delta t$ is an upper limit to the expelled mass since it assumes that immediately after the laser fires the propellant efflux recovers to its steady state value. Of course, in light of the uncertainties inherent in measuring the laser-induced impulse, it is difficult to draw any strong conclusions.

To summarize, the maximum specific impulse obtained for argon and hydrogen propellants was 500 and 1000 seconds, respectively. By optimizing the choice of mass flow rate, laser interpulse time, and nozzle throat diameter such specific impulses can be achieved with energy conversion efficiencies of 40 to 50%.

4.2.3.2 Assessment of Loss Mechanisms

Having obtained experimental measurements for the energy conversion efficiency and specific impulse of a small-scale laser propulsion rocket, it is now useful to assess those loss mechanisms which may be limiting the performance. By identifying and evaluating the dominant loss mechanisms future rockets might be designed with improved performance and efficiency.

In this section we will present results of measurements carried out to evaluate such losses as imperfect laser absorption, losses due to 'real gas' effects (chemistry), and plasma reradiation losses.

Imperfect Laser Absorption

The first possible loss pathway to consider for the laser-driven rocket is that of imperfect laser absorption. Perfect (100%) laser absorption will only occur if the plasma that is formed in the breakdown region is ignited soon enough and is of sufficient size and density to completely absorb the laser radiation. We will present here laser absorption data that were obtained for an operating rocket by measuring the unabsorbed fraction of laser radiation that was reflected back out of the parabolic rocket. These experiments were carried out using calorimeters to determine the time integrated laser absorption, and fast response pyroelectric detectors to determine the time history of the laser absorption. (Optical filters were employed before the detectors to separate out any possible contributions from shorter wavelength reradiation from the hot gas.) All measurements of the return (unabsorbed) laser radiation were referenced and normalized to the return signal that was observed under vacuum conditions (no propellant in rocket). The absorptance in the gaseous propellant was measured as a function of mass flow rate and defined as

$$\alpha_g(t, \dot{m}) = 1 - \left(I_R(t, \dot{m}) / I_R(t, 0) \right) \quad (4.2.7)$$

for the time dependent absorptance and

$$\bar{\alpha}_g = 1 - \left(E_R(\dot{m}) / E_R(0) \right) = \frac{\int \alpha_g I dt}{\int I dt} = \frac{\int [I_R(0) - I_R(\dot{m})] dt}{\int I_R(0) dt} \quad (4.2.8)$$

for the time integrated absorptance. In the above relationships I_R is the return laser intensity and E_R is the return laser energy.

Presented in Figs. 4.7 and 4.8 are the results of calorimetric measurements of the time integrated laser absorptance in argon and hydrogen propellants. The results are plotted vs. the propellant mass flow rate. To be particularly noted is the observed monotonic increase in the absorptance efficiency with increasing mass flow rate. For a fixed nozzle throat size, an increase in mass flow rate corresponds to an increase in the initial propellant density at focus. The observed enhancement in the laser absorptance with increasing propellant density could arise from a decrease in the induction time to breakdown, or an increase in the opacity of the plasma formed at higher initial densities. Time resolved absorptance measurements will be presented below which help to shed light on the mechanisms controlling the achievable absorptance.

Finally, on examining the laser absorptance results for hydrogen, one sees that, for a given \dot{m} , slightly higher absorptances are attained with the 0.2 cm throat than with the 0.4 cm throat. The increase in optical absorptance is probably the result of the increased propellant density that occurs in the vicinity of the throat for the nozzle with the smaller throat area.

It is interesting to compare the above laser absorptance efficiencies to the corresponding measurements presented earlier for the energy conversion efficiencies, i.e., the ratio of the energy observed in the blast wave to the incident laser energy. Figures 4.9 and 4.10 compare these two sets of results.

Turning first to the results for argon, we see that the energy conversion and absorptance efficiencies show qualitatively similar behavior -- both increase monotonically with increasing \dot{m} . The observed energy conversion efficiencies do, however, fall below the measured absorptance efficiencies, suggesting that there are losses in addition to imperfect laser absorption. The reader should be reminded that the blast wave energy efficiencies presented in Fig. 4.9 were calculated from blast wave pressure and transit time measurements assuming a perfect gas. Therefore, for conditions where the energy involved in real gas effects (such as ionization, electronic excitation, etc.) becomes significant, the calculated blast wave energies

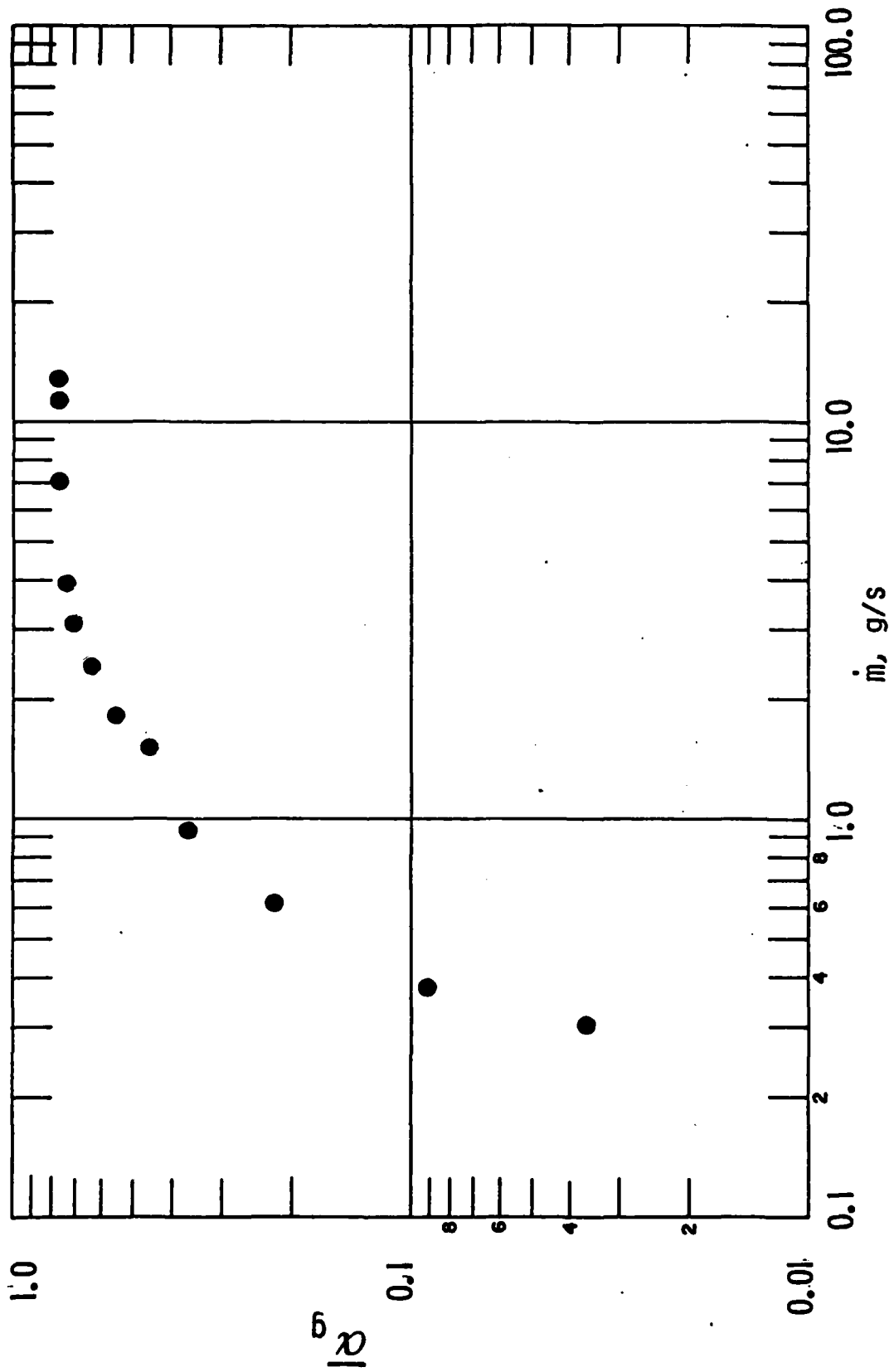
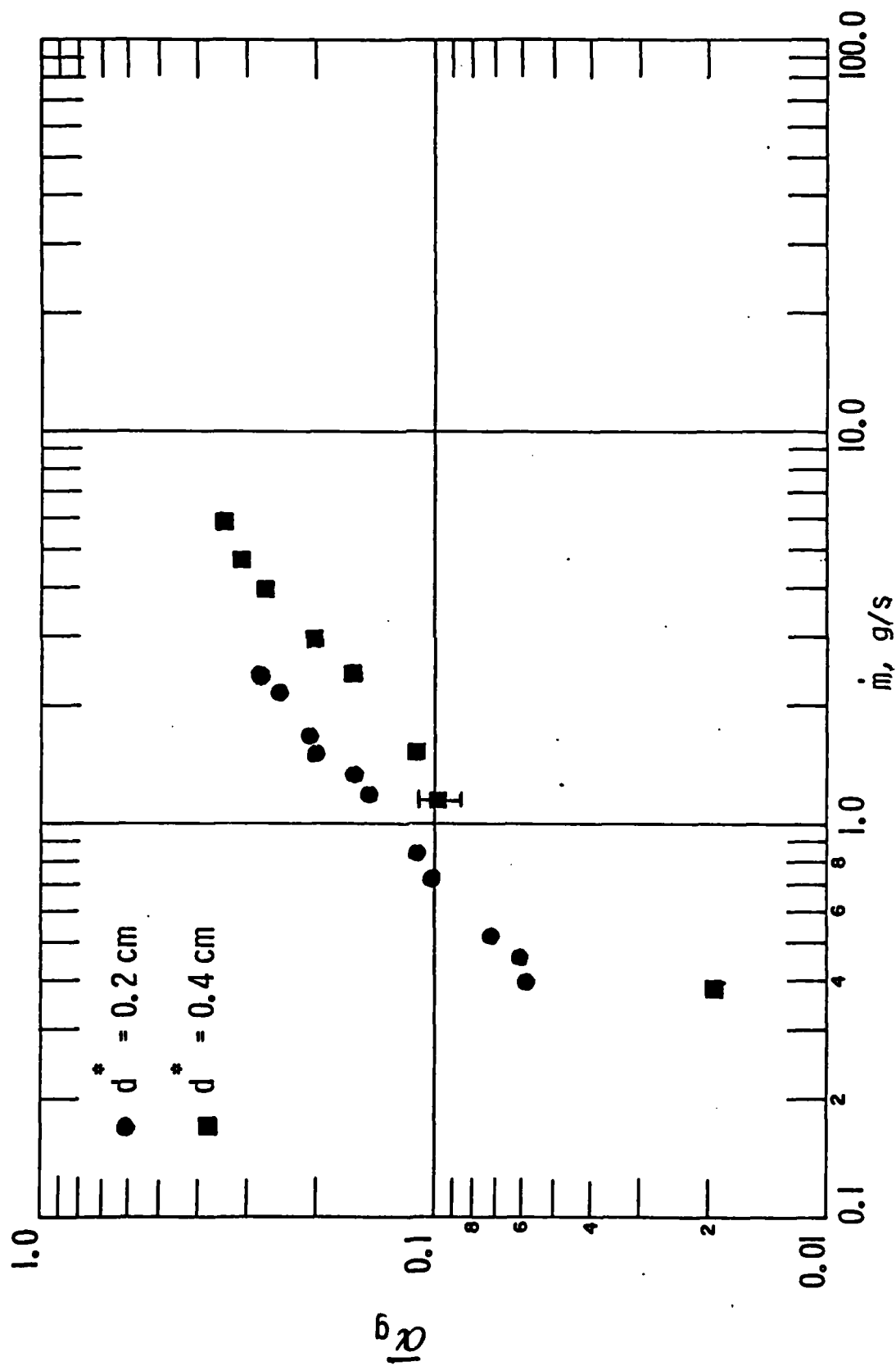


Fig. 4.7 Mean Laser Absorptance in Argon vs. \dot{m} .

Fig. 4.8 Mean laser absorptance in hydrogen vs. \dot{m} .

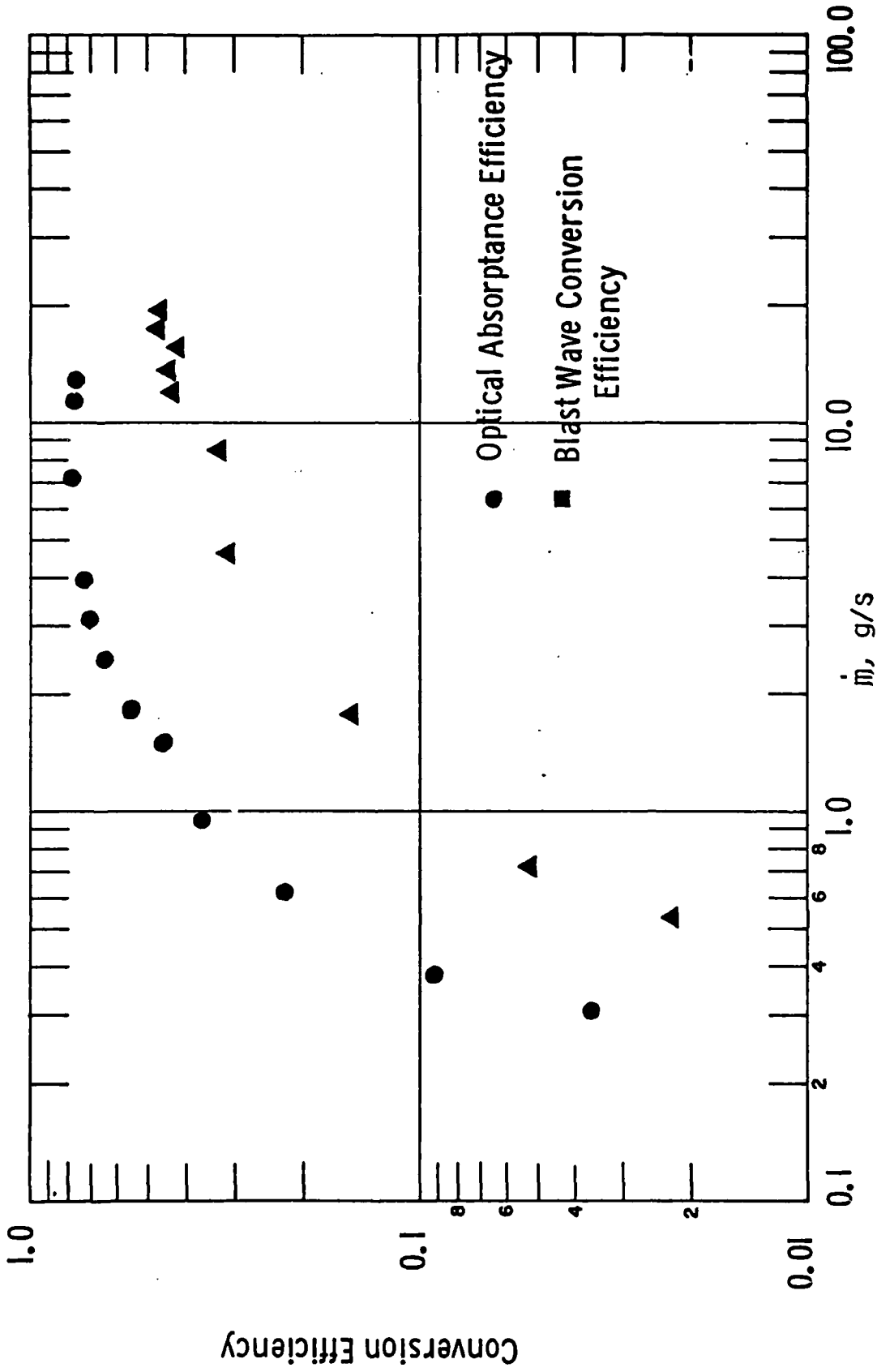


Fig. 4.9 Comparison of optical absorbance and blast wave conversion efficiencies in argon.

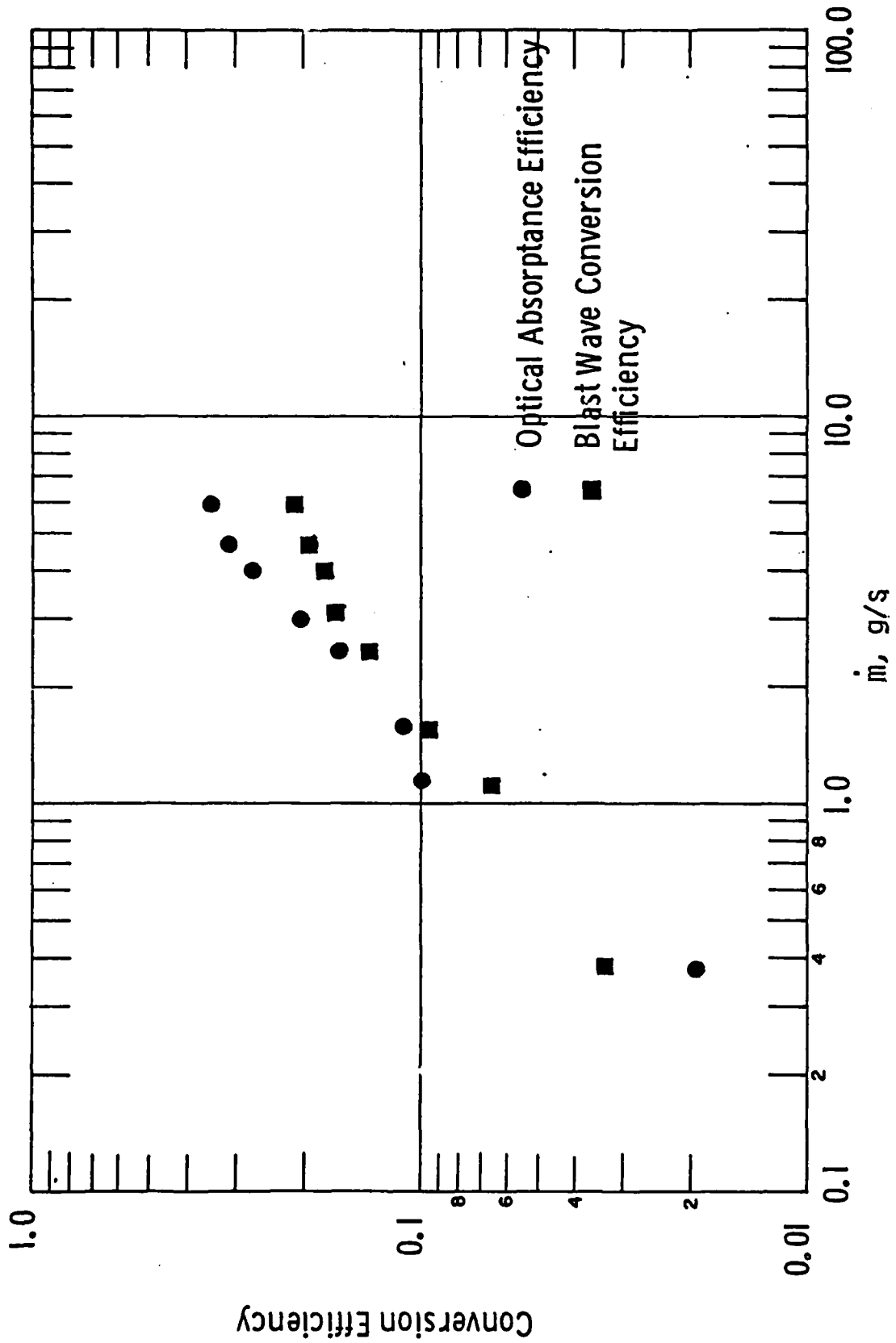


Fig. 4.10 Comparison of optical absorptance and blast wave conversion efficiencies in hydrogen.

are probably underestimates of the actual energy in the laser-heated gas. Sections 3.3, 3.9 and 3.12 of the theoretical modeling section, and a discussion which will follow, present results which deal with real gas effects. Other possible loss channels are plasma reradiation out of the rocket and convective and/or radiative heat loss to the rocket wall. The results of some measurements performed to assess the reradiation losses will be presented later.

A comparison of the energy conversion and absorptance efficiencies obtained for hydrogen is shown in Fig. 4.10. From this plot, one can see an even more striking correlation between the energy conversion and laser absorptance efficiencies measured for hydrogen than was observed for argon. This closer agreement for hydrogen suggests that the losses in hydrogen are more strongly dominated by imperfect laser absorption and less by other losses such as real gas (chemical) effects and radiative losses. Such a result is not surprising since hydrogen has a larger heat capacity per unit mass than argon and, therefore, is not expected to reach as high a temperature for an equal absorbed laser energy. Energy losses to radiation and real gas effects are, of course, larger at higher temperatures.

Time-Resolved Absorptance Measurements

As suggested earlier, imperfect laser absorption can be the result of a finite induction time to plasma initiation and/or a plasma sufficiently tenuous to be non-opaque. In an attempt to obtain more information on the details of the laser absorption process, time-resolved measurements of the fraction of unabsorbed laser radiation were made using a fast response pyroelectric detector.

Shown in Figs. 4.11 and 4.12 are plots of the temporal profiles of the incident and return laser intensity observed for argon propellant rocket runs at two different plenum pressures. The corresponding time dependent absorptances, as defined by Eq. (4.2.7), are plotted for these two cases in Figs. 4.13 and 4.14. From this data and similar measurements for other plenum conditions (other mass flow rates), the following general behavior was observed: (1) for the lower mass flow rates the absorptance rises from zero

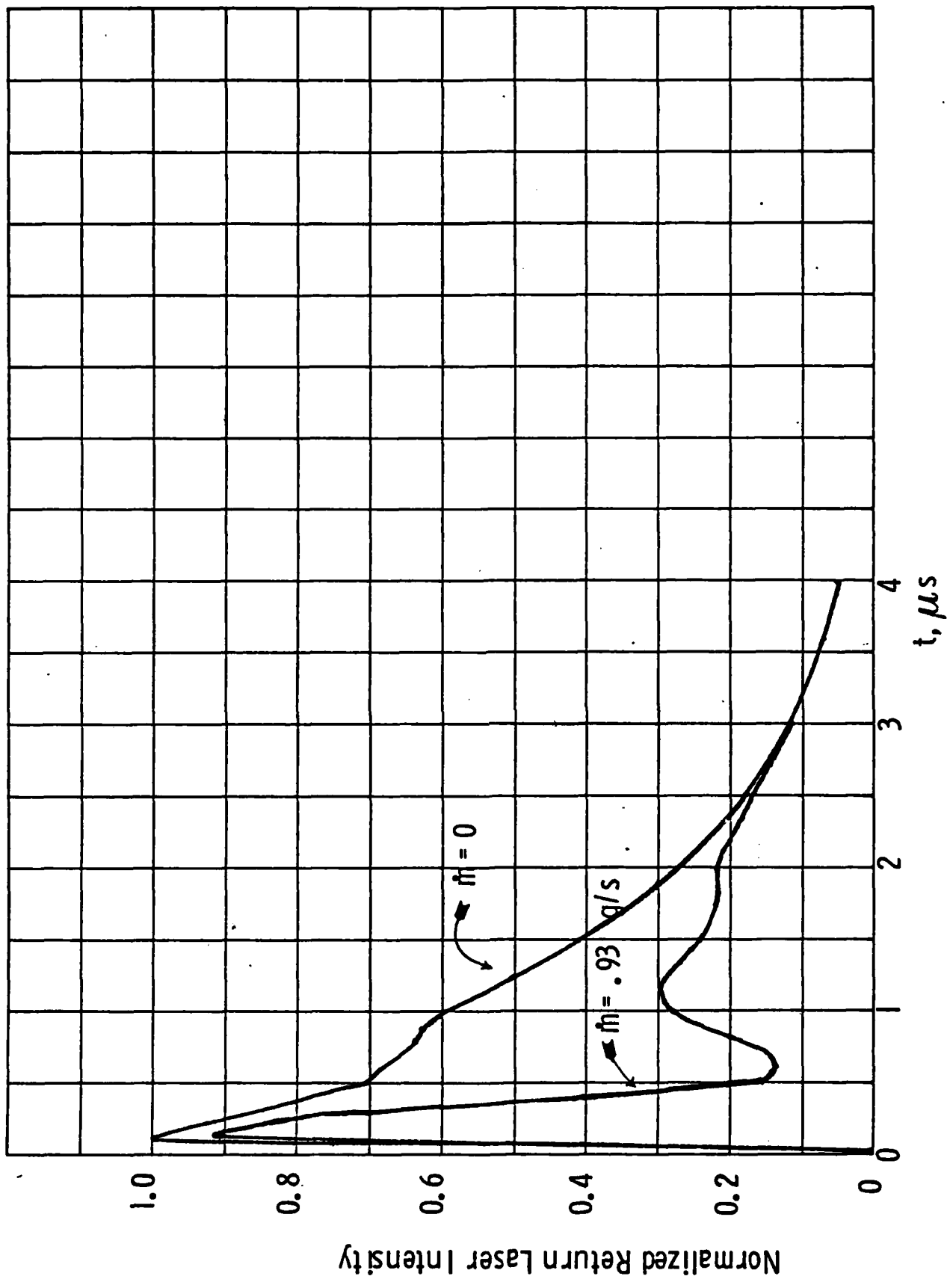


Fig. 4.11 Time history of return (unabsorbed) laser intensity
 $\dot{m} = 0$ vs. $\dot{m} = .93 \text{ g/s}$, argon

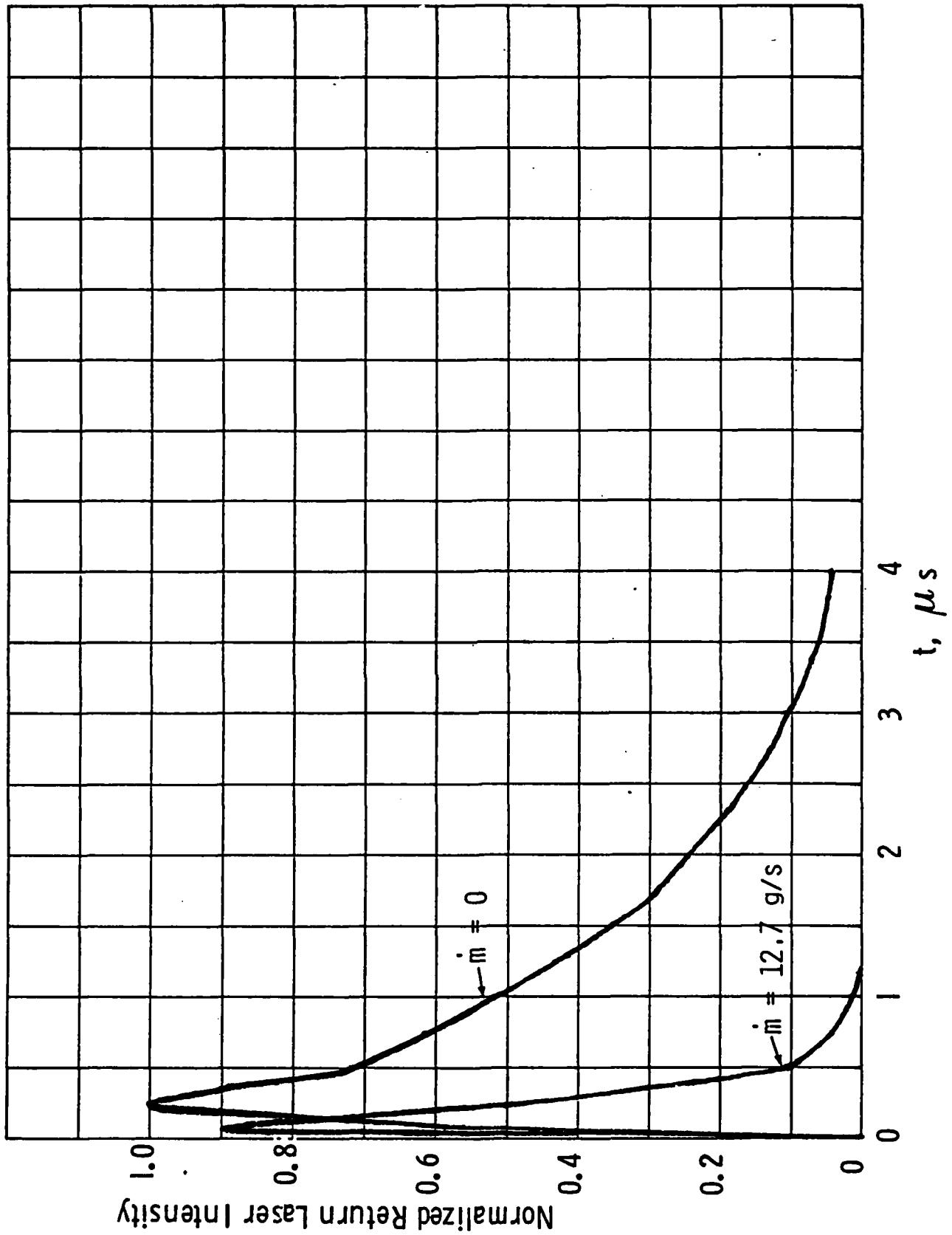


Fig. 4.12 Time history of return (unabsorbed) laser intensity
 $\dot{m} = 0$ vs. $\dot{m} = 12.7 \text{ g/s}$, argon

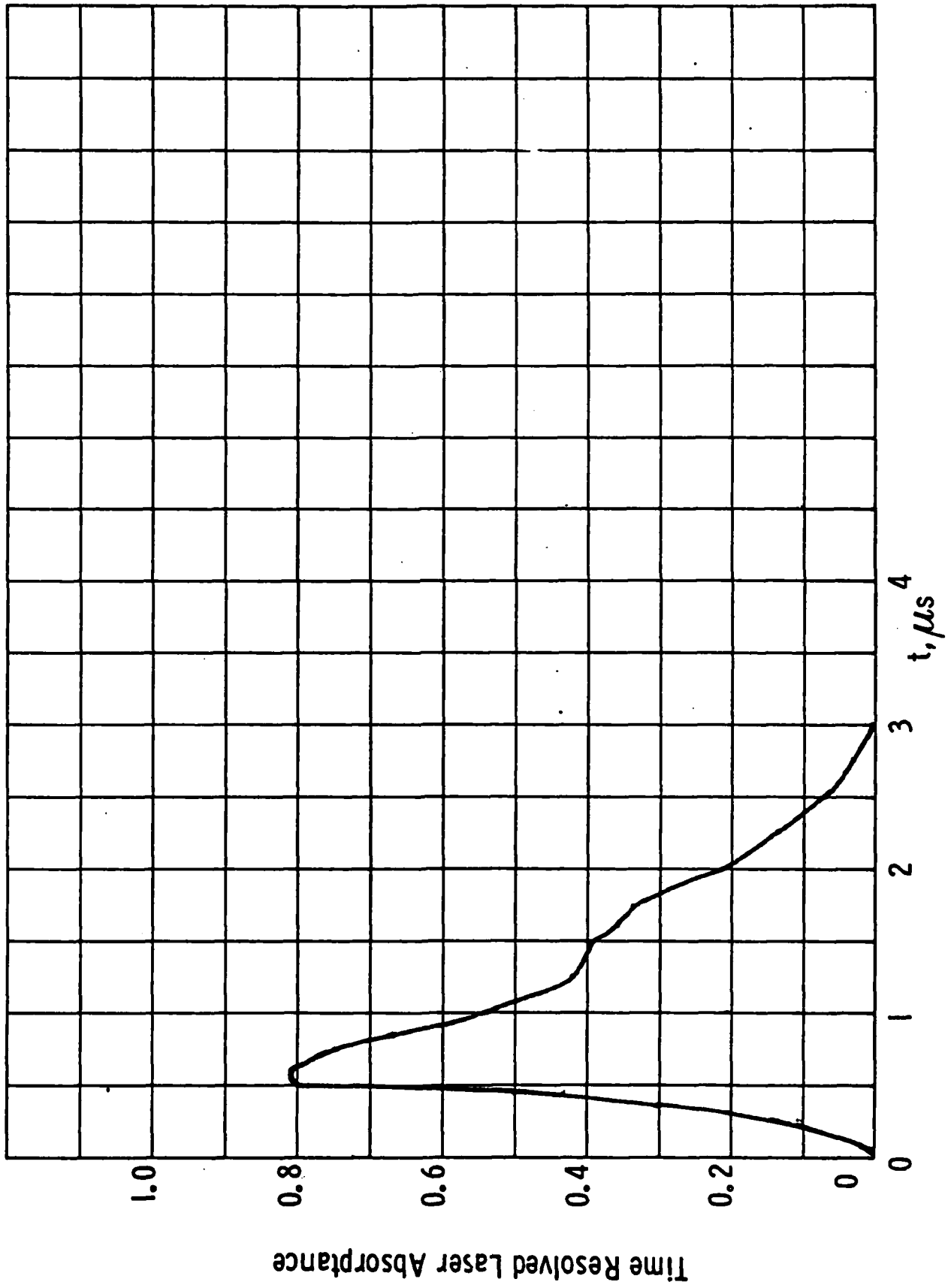


Fig. 4.13 Time history of laser absorbance
 $\lambda = 93 \text{ cm/s. argon}$

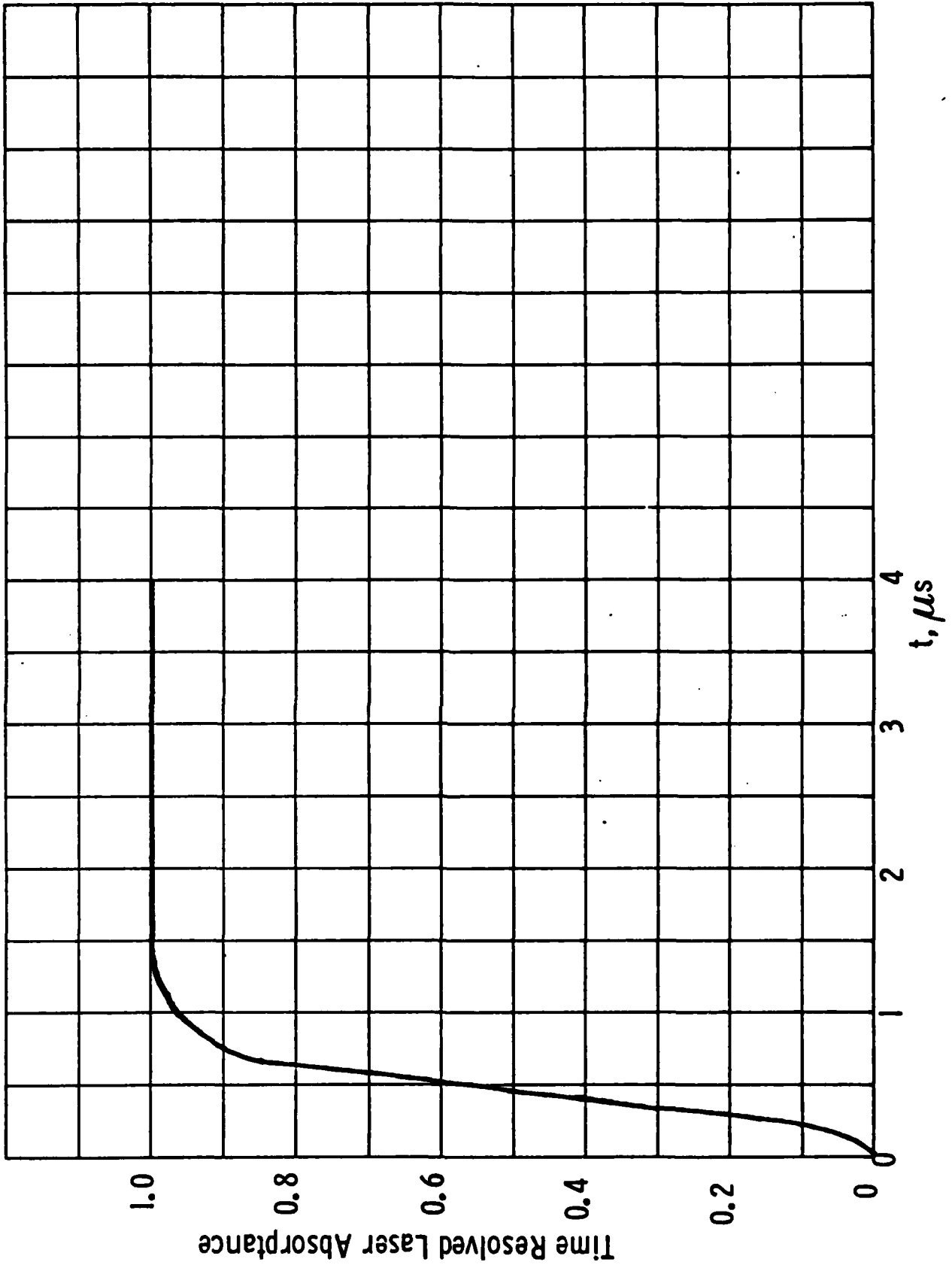


Fig. 4.14 Time history of laser absorbance
 $m = 12.7$ g/s, argon

to some intermediate value shortly after the laser spike and then decreases with time during the remainder of the pulse; (2) for the higher mass flow rates the gas becomes opaque shortly after the initial laser spike and remains so throughout the duration of the laser pulse; and (3) even at the highest mass flow rates studied, a significant fraction of the energy in the initial laser spike is transmitted through the gas unabsorbed.

From the above observations it can be concluded that two mechanisms are responsible for imperfect laser absorption. The first is the induction time to achieve gas breakdown during the initial laser spike, and the second is the non-opacity of the plasma as the LSD wave expands into low density gas. It is this second mechanism that is primarily responsible for absorptance efficiencies below 70% since only about 30% of the laser energy is contained in the initial laser spike and, in general, an absorbing plasma was initiated by the end of this spike.

Time-resolved measurements of the unabsorbed laser radiation may also be integrated according to the far right hand side of Eq. (4.2.8) to yield a mean laser absorptance. This mean laser absorptance can then be compared to the mean absorptance that was measured calorimetrically. Figure 4.15 is a plot that compares these two independent sets of measurements. As can be seen from the plot, there is generally good agreement between the results obtained from the time-resolved and calorimetric absorption measurements.

Chemical Losses

Another factor that can limit the performance efficiency of a laser-driven rocket is chemical losses. The term chemical losses is used here to refer to any energy that is bound up in degrees of freedom of the exit plane gas other than kinetic energy directed out the exhaust. In attempts to assess the importance of such losses in the present experiments, two separate investigations were carried out. The equilibrium code for argon described in Section 3 was run to evaluate the effect of 'real gas' properties on the velocity and pressure of the laser-driven blast wave. This led to a more realistic interpretation of the single-pulse experimental

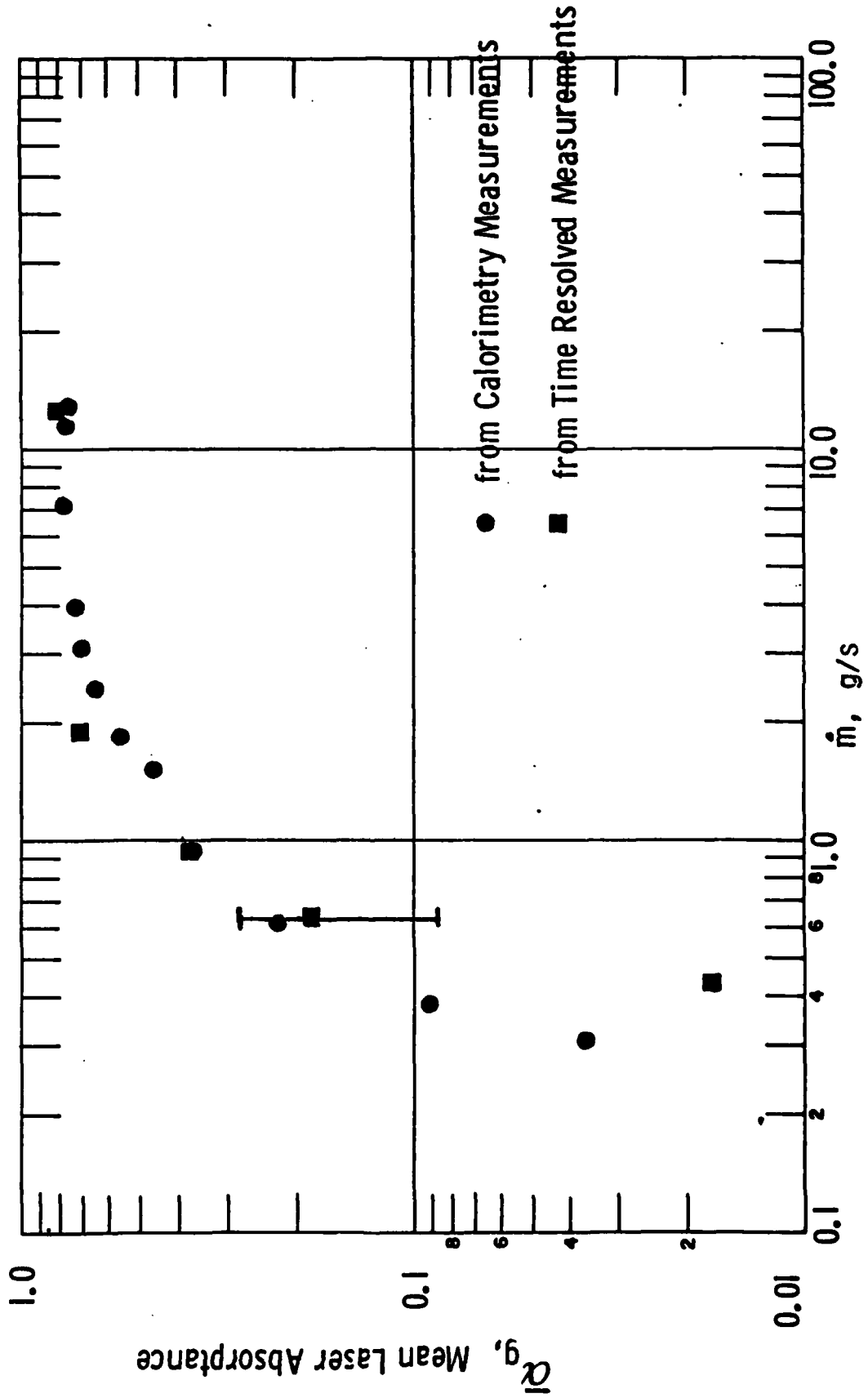


Fig. 4.15 Comparison of mean laser absorptance in argon as determined from calorimetric and time-resolved measurements.

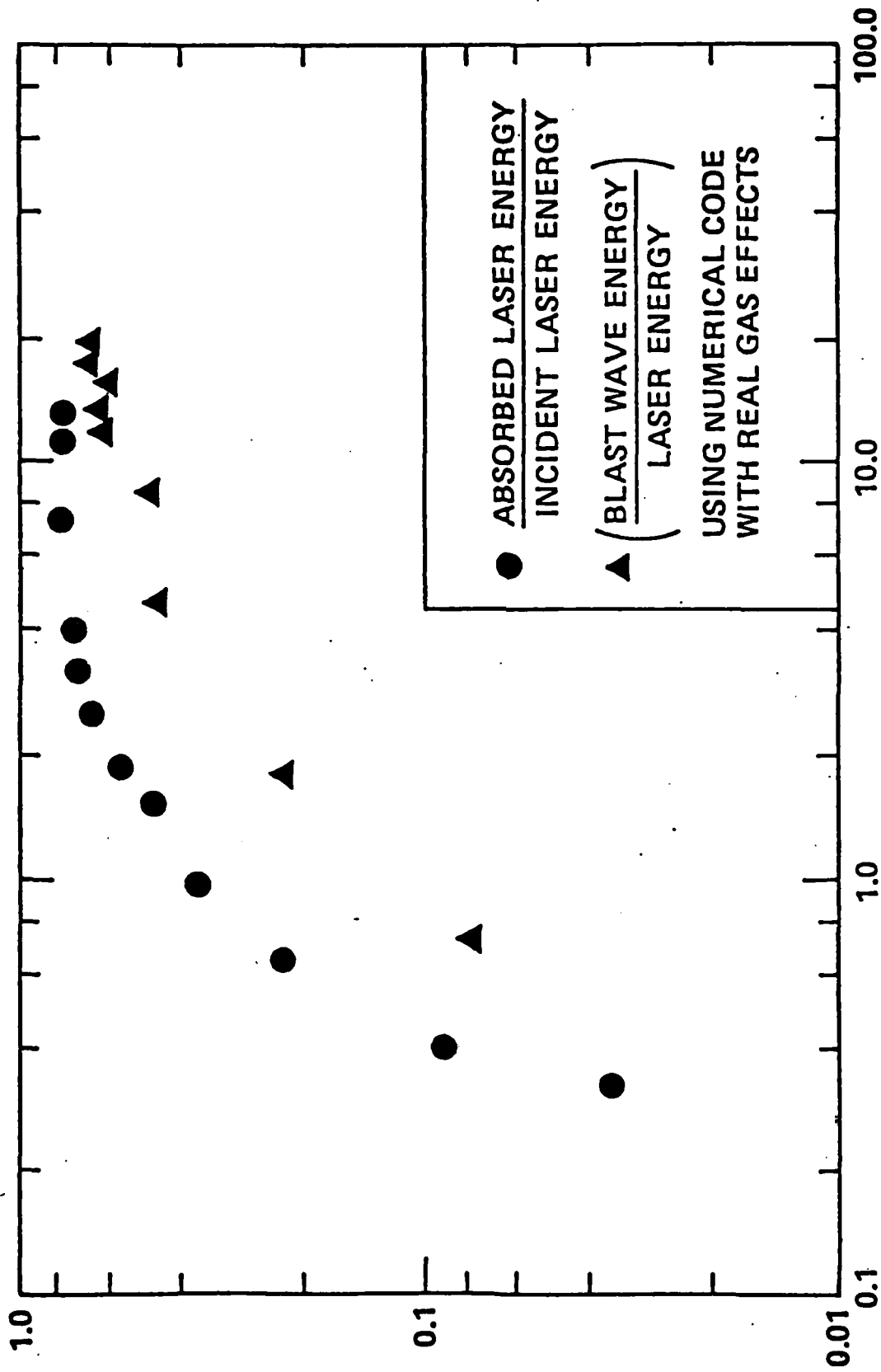
data and resulted in improved estimates of the deposited laser energy. In addition, chemical losses in the single-pulse argon experiments were estimated through radiometric measurements of the temperature of the exhaust gas. A high exhaust temperature of the propellant will tend to lead to increased chemical losses. In an attempt to determine this temperature, radiometric measurements were performed of the argon atomic line emissions. The results of these two studies are described below.

Results of Numerical Code Simulations Including Real Gas Effects

Using the blast wave transit time data described earlier for argon, the blast wave energy evaluated previously assuming perfect argon was re-evaluated using a numerical code that included real argon chemistry (see Section 3.9). Figure 4.16 presents the results of these calculations and compares the inferred laser to blast wave energy conversion efficiencies with the corresponding measured optical absorptance efficiencies. Comparing this plot with that of Fig. 4.9, it is seen that by including real gas effects the energy conversion efficiencies inferred from the shock transit time measurements are from 30% to 60% higher than those calculated assuming perfect argon. In other words, by accounting for the energy partitioning into ionization and electronic excitation, even closer agreement is found between the blast wave energy and the optically deposited energy. Further, it is seen that the agreement is best at the highest mass flow rates. The greater discrepancy at the lower flow rates could be the result of non-equilibrium effects ("frozen" chemistry). At sufficiently low mass flow rates, the gas density in the nozzle could be too low to allow enough collisions (during the nozzle residence time) for the ions and excited argon atoms to relax to the translational temperature. Another possible explanation is that at the lower mass flow rates radiation losses have a larger relative effect.

Radiometric Measurements of the Argon Exhaust Temperature

As mentioned above, it is expected that high nozzle exhaust temperatures will lead to increased chemical losses. This will of course be true if the gas translational temperature is high, but can even be the case when



PROPELLANT MASS FLOW (gms/sec)

Fig. 4.16 Comparison of experimental measurements of the propellant optical absorption efficiency with the measured blast wave conversion efficiency, argon propellant, $\lambda = 10.6 \mu\text{m}$.

the translational temperature is low, if the effective electronic temperature is elevated (non-equilibrium). In order to obtain an experimental determination of the effective electronic temperature of an argon rocket exhaust, radiometric measurements were made of the argon atomic line emissions. Spectroscopic measurements were obtained using a grating spectrometer. All experiments were done for conditions of single CO₂ laser pulses with argon as the propellant. The electronic states of the emitting argon atoms in the exhaust gas were identified. From the intensities of the spectral lines, we were able to deduce the temperature of the exhaust gas making a few reasonable assumptions.

The experimental set-up used is shown in Fig. 4.17. The parabolic nozzle (described in Section 4.2.1) was placed inside a Lucite chamber which was evacuated to a pressure of 180 μ . All experiments were performed at this background pressure and for an argon mass flow rate of 3.5 g/s.

The radiation from the laser-heated exhaust gas was viewed at right angles to the laser optical axis and collected using a 2" diameter, 10 cm focal length quartz lens. The lens was located such that it imaged the entrance slit of a 1/4 meter Jarrell Ash monochromator at a position on the nozzle centerline 16.2 cm downstream of the throat. The monochromator was equipped with a standard grating, 1800 grooves/mm, blazed at 5000 \AA and an efficiency of 60% in the 7000 - 8000 \AA region. The slits used were 250 μ wide and 3 cm high, which corresponds to a resolution of 8.5 \AA . The entire optical system was aligned with the use of a Helium-Neon Laser. Preliminary experiments were performed with an SGD-40 silicon photodiode detector and later measurements were made with an RCA 4840 photomultiplier (PM) tube detector which improved the signal/noise ratio significantly. Since the emission from the exhaust gas was very intense, it was necessary to operate the PM tube at low voltages. Separate experiments showed that the operating voltage of 400 V was in the linear region. The gain of the tube at this voltage was experimentally determined to be 8.6×10^4 . The projected active area of the cathode, considerably larger than the area of the slit,

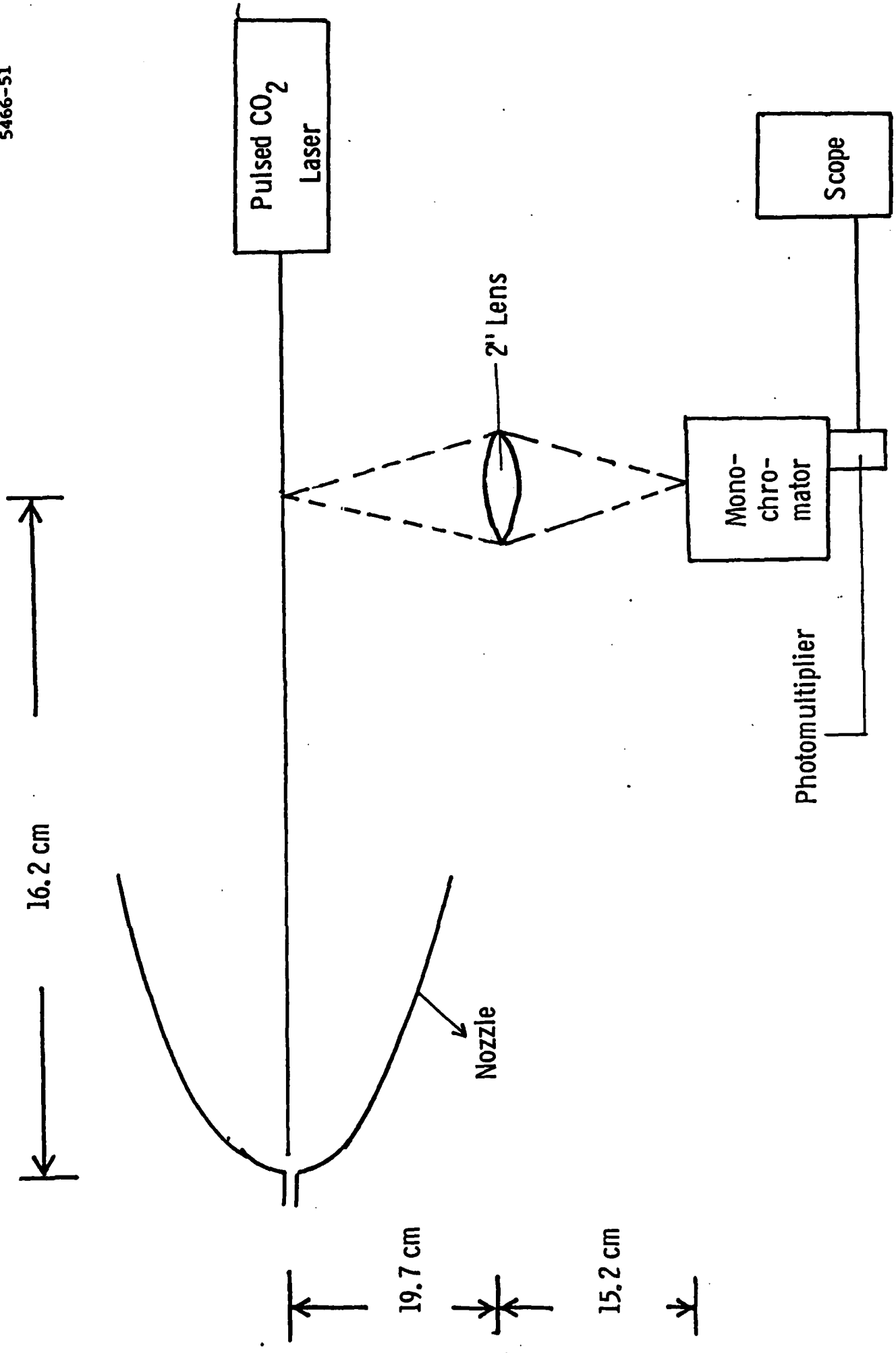


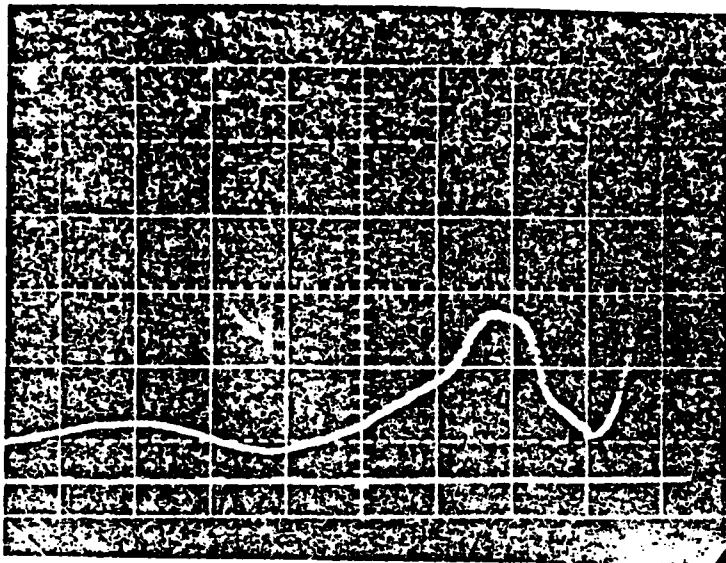
Fig. 4.17 Experimental set-up for radiometric measurements of the nozzle exhaust temperature.

is found to be 7.8 mm x 23.8 mm from the manufacturer's specification. The absolute responsivity of the cathode varies from 5 mA/W at 7000 Å to 0.5 mA/W at 8000 Å. The monochromator wavelength settings were calibrated using the He-Ne laser as well as known Hg lines from a fluorescent lamp. A Corning 2-61 glass filter was introduced at the entrance slit to eliminate any UV radiation reaching the detector in the second order.

In a typical experiment, the monochromator was preset to a wavelength, the propellant argon introduced into the nozzle, the CO₂ laser fired and the output of the PM across a 1000 Ω load resistor (risetime of 140 ns with a cable and scope capacitance of 150 pf) monitored on an oscilloscope. The experiment was repeated several times to ascertain reproducibility, and photographs of the oscilloscope output were taken for various wavelength settings.

Figure 4.18 displays the observed signals in the presence and absence of a Corning 2-61 filter for the monochromator setting of 6965 Å. The emission at this wavelength has been identified (Table 4.1) as originating from the 4s (3/2) ↔ 4p' (1/2). Figure 4.19 displays the results for a monochromator setting of 7465 Å. It is clear that the emission is weak compared to 6965 Å and corresponds to the underlying continuum. Further, the significant drop in intensity with the introduction of the Corning 2-61 filter, shows that a significant portion of this emission arises from the UV region and is detected in the second order. Note should also be made of the distinct temporal profiles of the observed emissions at 6965 and 7465 Å. In general, all the argon emission lines had time histories similar to the 6965 Å, while the continuum was similar to that of 7465 Å. The reason for this difference in behavior is not clear. All the other emission lines were photographed at their peak wavelengths by manually changing the monochromator settings.

The observed emission lines along with their corresponding signal strengths are shown in Table 4.1. By referring to the compilation of atomic transitions of argon made by Wiese, Smith and Miles,^{4.5} these lines were given the assignments indicated in Table 4.1. A representative energy level diagram for argon is shown in Fig. 4.20, where the arrow represents the



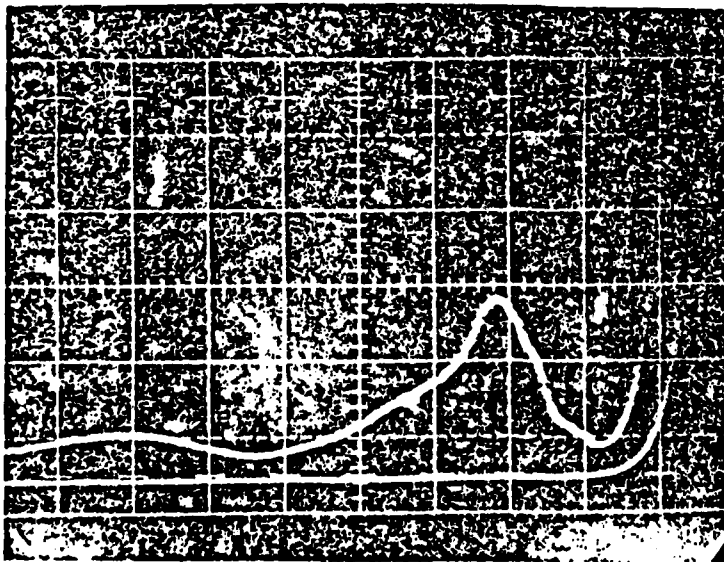
6965Å

0.1 V/cm

20 μs/cm

i
↑

t ←



6965Å

0.1 V/cm

20 μs/cm

Corning 2-61
Filteri
↑

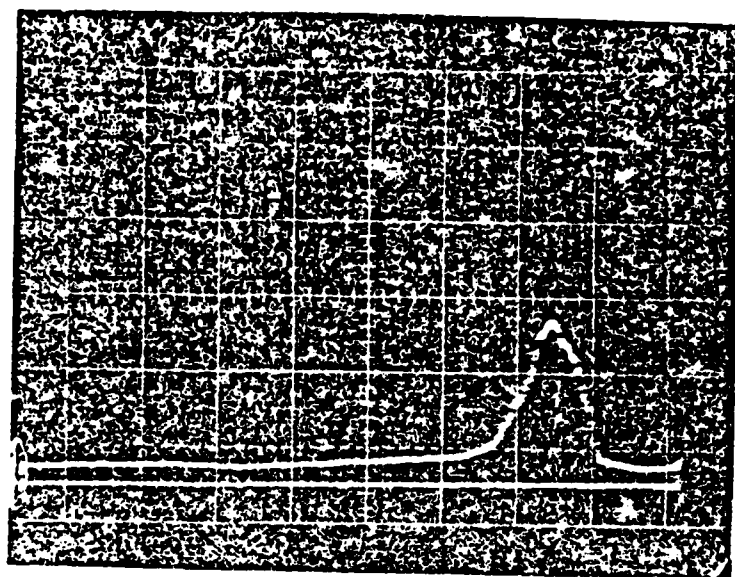
t ←

Fig. 4.18 Observed emission intensity of the argon $4s(3/2) \leftrightarrow 4p'(1/2)$ transition in the laser-heated nozzle exhaust.

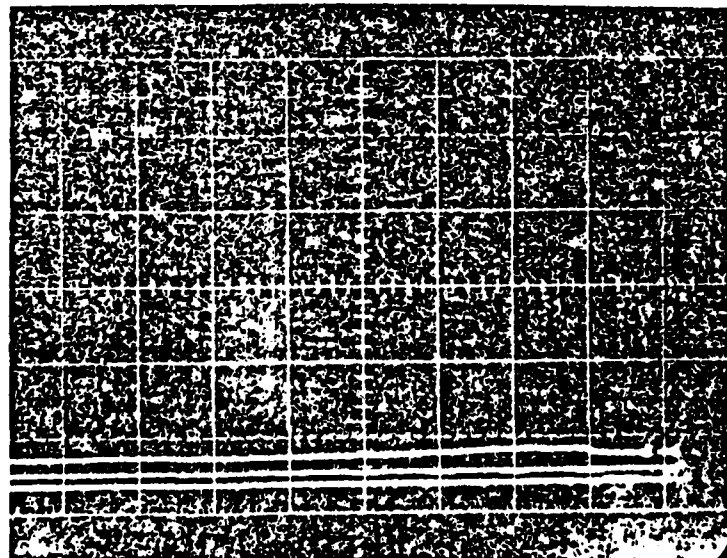
TABLE 4.1

OBSERVED EMISSION LINES FROM THE EXCITED STATES OF ARGON

$\lambda(\text{\AA})$	Assignment	$E_i \text{ cm}^{-1}$	g_i	$E_K \text{ cm}^{-1}$	g_K	Measured Intensity (volts)
6965	$4s(3/2) \leftrightarrow 4p^1(1/2)$	93144	5	107496	3	0.25
7067	$4s(3/2) \leftrightarrow 4p^1(3/2)$	93144	5	107290	5	0.23
7273	$4s(3/2) \leftrightarrow 4p^1(1/2)$	93751	3	107496	3	0.105
7384	$4s(3/2)^0 \leftrightarrow 4p^1(3/2)$	93751	3	107290	5	0.085
7504	$4s^1(1/2)^0 \leftrightarrow 4p^1(1/2)$	95400	3	108723	1	0.185
7514	$4s(3/2)^0 \leftrightarrow 4p(1/2)$	92751	3	107054	1	0.090
7635	$4s(3/2)^0 \leftrightarrow 4p(3/2)$	93144	5	106238	5	0.250
7723	$4s(3/2)^0 \leftrightarrow 4p(3/2)$	93144	5	106087	3	0.180
7948	$4s^1(1/2)^0 \leftrightarrow 4p^1(3/2)$	94554	1	107132	3	0.090



7465 \AA
 0.02 V/cm
 20 $\mu\text{s/cm}$



7465 \AA
 0.02 V/cm
 20 $\mu\text{s/cm}$
 Corning 2-61
 Filter

Fig. 4.19 Observed emission intensity of the continuum of argon in the laser-heated nozzle exhaust, monochromator setting is 7465 \AA .

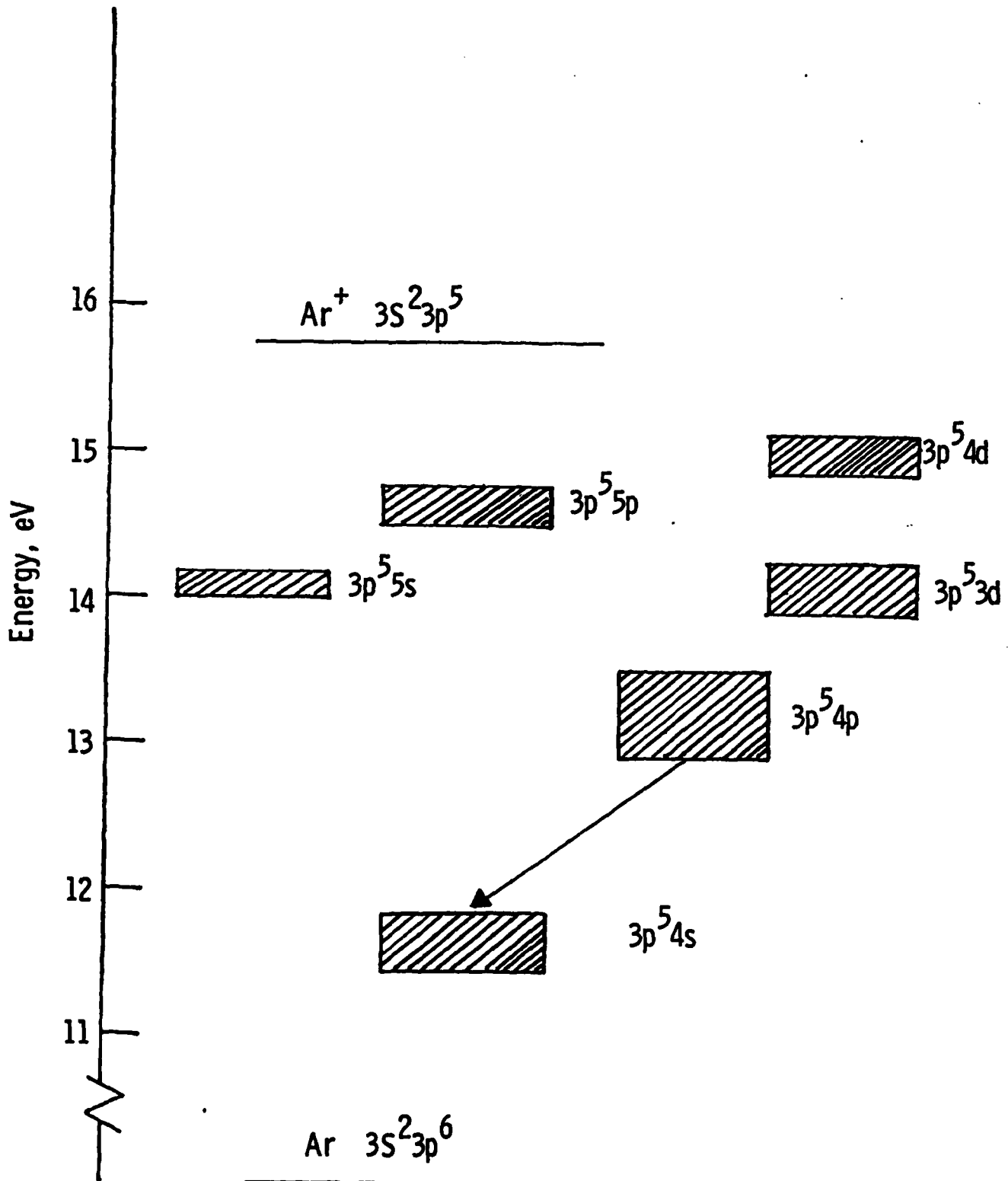


Fig. 4.20 Argon energy level diagram. The observed group of transitions is shown by the arrow.

group of electronic transitions observed here. The measured detector output voltages were converted to watts using the known gain of the PM tube and the absolute responsivity of the cathode. The results are shown as a function of wavelength in Fig. 4,21.

The above measured emission intensities were corrected for grating efficiency (60%). The viewing fluorescence volume and the collection efficiency of the optics was calculated to be 0.7 cm^3 and 0.004, respectively. The transition probabilities for the various transitions were obtained from the tabulation of Wiese et al.^{4,5} It was then a straightforward matter to calculate the populations of the emitting electronic levels. The shock density profile calculations show that the total post shock density of the argon atoms at 16.2 cm from the exit plane of the nozzle is 5.4×10^{16} atoms cm^{-3} . Using this value for the population of the ground state and assuming a Boltzmann distribution, one can calculate the temperature of the exhaust gas at the exit plane. The results are given in Table 4.2. While the mean of these temperatures is 7504 K, the standard deviation is found to be 264 K. Thus, a temperature of 7500 K is indicated for the exhaust gas at the exit plane. The background emission between the lines was measured to be 10×10^{-9} watts per 8.5 \AA .

It remains an open question whether the excited argon atoms are in thermal equilibrium with the ground state argon atoms. The collisional deactivation rate for the density of 5.4×10^{16} molecules cm^{-3} at the exit plane is calculated to be $5.9 \times 10^6 \text{ s}^{-1}$. This value is an order of magnitude slower than the largest radiative decay constant of $4.72 \times 10^7 \text{ s}^{-1}$. Thus, it would appear that the excited atoms may not be in equilibrium with the ground state atoms. We have neglected self-absorption and radiative trapping in our analysis of the experimental data.^{4,6}

Plasma Reradiation Losses

In an attempt to assess the magnitude of the energy that may be lost due to plasma reradiation, measurements were made of the UV/Vis/near IR radiation coming out of the rocket. The experiments were performed using

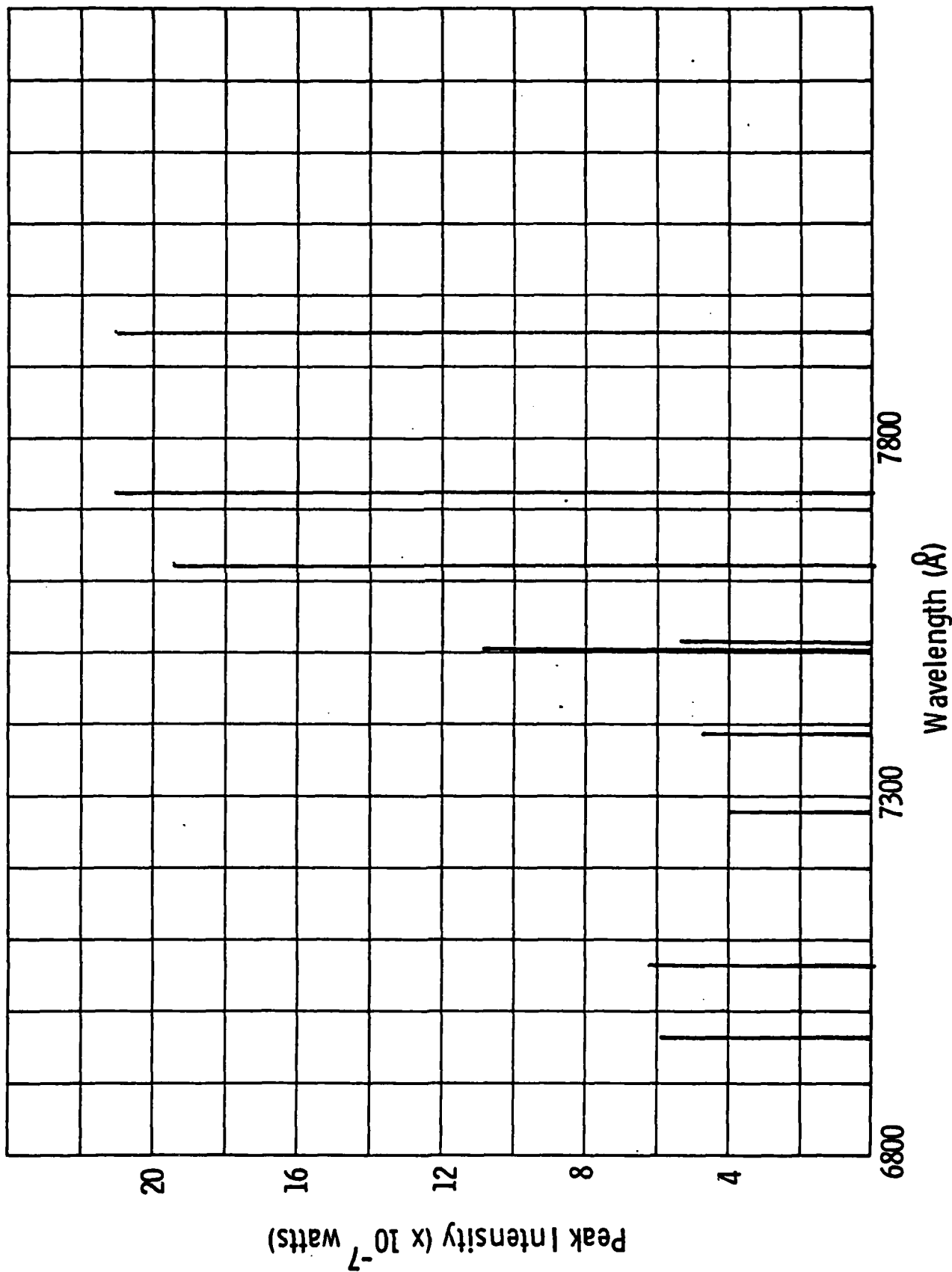


Fig. 4.21 Observed argon emission lines and their relative intensities.

TABLE 4.2
 POPULATION DISTRIBUTIONS OF THE EXCITED ARGON LEVELS AND THE
 CALCULATED TEMPERATURES

$\lambda(\text{\AA})$	$A_{ki} (\times 10^8)$	$E_k (\text{cm}^{-1})$	$\frac{n_k}{g_k}$	$\frac{[Ar^*]}{[Ar]} (\times 10^{-9})$	Temp K
6965	0.067	107496	5.9×10^7	1.1	7514
7067	0.0395	107290	5.5×10^7	1.0	7464
7273	0.020	107496	1.5×10^8	2.8	7859
7384	0.087	107290	2.4×10^7	0.44	7186
7504	0.472	108723	5.0×10^7	0.93	7529
7514	0.430	107054	2.8×10^7	0.52	7206
7635	0.274	106238	3.2×10^7	0.59	7183
7723	0.057	106087	2.8×10^8	5.2	8000
7948	0.196	107132	8.2×10^7	1.5	7600

a Laser Precision energy meter and a quartz filter to reject any 10.6 micron radiation. Estimating the reflection and transmission losses in the optical train and the geometrical sampling fraction of the energy detector, it was found that as much as approximately 1.5 joules, or 15% of the total energy, can be lost out of the rocket in the form of plasma radiation between 2000 Å and 4 microns (the approximate transmission range of the quartz filter).

4.2.4 Summary of Thruster Performance Results at 10.6 μm

Experimental measurements have been made of the performance parameters and efficiency of a small-scale thruster driven by a pulsed CO₂ laser. The thruster model used for these investigations was constructed from a self-focusing parabolic shell of revolution that focused the incoming laser beam to a high intensity spot just downstream of the nozzle throat.

Several expellant gas species were studied including argon, hydrogen, helium and nitrogen. Energy conversion efficiencies upwards of 50% were achieved. Here, energy conversion efficiency is defined as the ratio of the energy observed in the laser-induced blast wave to the incident laser energy. Specific impulse measurements were also carried out for argon and hydrogen demonstrating achievable specific impulses of 500 and 1000 seconds, respectively; with corresponding conversion efficiencies of 40 to 50%. All measurements were made as a function of expellant mass flow rate.

To complement the energy conversion efficiency results, measurements were also made to assess the magnitudes of a number of possible loss mechanisms. These included imperfect laser absorption, real gas effects (chemical losses), and plasma reradiation. For most of the conditions studied, the dominant loss mechanism was found to be imperfect laser absorption - with absorption efficiencies being worst for the lowest nozzle gas densities.

4.3 Absorption Physics Experiments

As was described earlier, the conversion of high power laser energy into blast wave energy using a thruster of the type shown in Fig. 1.1 first involves the laser-induced breakdown process and ignition of a laser-supported detonation (LSD) wave in the propellant. The efficiency of energy conversion will depend upon the time required to ignite an absorbing plasma (breakdown time) and the degree to which the resulting gas can absorb all the laser energy with minimum losses to the surroundings. For efficient absorption of the laser energy by the gas, one would like to operate under conditions where the time to achieve breakdown is short compared to the laser pulse time, and where the product of the effective absorption coefficient at the laser wavelength, k_v , and the plasma scale length is greater than unity. These conditions can be written as

$$\tau_{Br} \ll \tau_p \quad (4.3.1)$$

and

$$\int_0^{\tau_p} k_v v_{LSD} dt > 1 \quad (4.3.2)$$

where τ_{Br} is the time required to achieve breakdown, τ_p is the laser pulse duration, and v_{LSD} is the LSD wave velocity. As is predicted by the theory of Section 2 and will be demonstrated by the experimental data to be presented, the conditions set forth in Eqs. (4.3.1) and (4.3.2) are most readily achieved by using high initial gas densities in the focal region.

In Section 2, theoretical models were presented for laser-induced gas breakdown and laser/plasma absorption at 10.6 μm and 0.35 μm . In order to provide an independent experimental data base as well as to validate the models, absorption physics experiments were carried out to measure the breakdown threshold and subsequent laser absorption of several gases at 10.6 μm and 0.35 μm . The validated laser absorption models are used in the overall thruster performance model described in Section 3.

4.3.1 Experimental Configuration

In order to separate optical and gas breakdown considerations from the issues of the optical quality and flow field of a self-focusing nozzle, the absorption physics experiments were carried out using a static gas chamber and external focusing optics. Figure 4.22 is a schematic diagram of the experimental arrangement used.

The test chamber was constructed of several sections of 30 cm i.d. stainless steel pipe that could be assembled to a length of over 5 meters. The chamber is provided with a pumping stack consisting of an 80 cfm booster blower backed by a 17.7 cfm mechanical oil pump that allows pump-down to an ultimate vacuum of 10^{-4} torr. Chamber fill pressures were monitored with standard Bourdon dial gauges. High purity gases were introduced into the test volume through a gas manifold constructed of copper tubing. The gases could be further purified by passing them through a column of molecular sieve 13X to remove any residual water vapor or hydrocarbons.

The laser beam entered the test chamber through either a fused silica (for 0.35 μm laser) or KCl (for 10.6 μm laser) entrance window. For the purpose of monitoring the incident beam energy and pulse time history, a portion of each laser beam was split off before entering the test chamber. After entering the chamber, the beam was collected by a focusing optic (lens or mirror) and brought to a focus in front of a large Lucite viewing window.

To monitor the gas breakdown and subsequent laser absorption, several diagnostic measurements were employed. First, breakdown was detected by visually observing or photographically recording the formation of a bright spark in the laser focal region. Secondly, measurements were made of the laser radiation transmitted beyond focus. Both time integrated and time resolved measurements were performed using, respectively, a large area calorimeter and a high speed photodetector (pyroelectric detector for 10.6 μm measurements and silicon photodiode for 0.35 μm measurements).

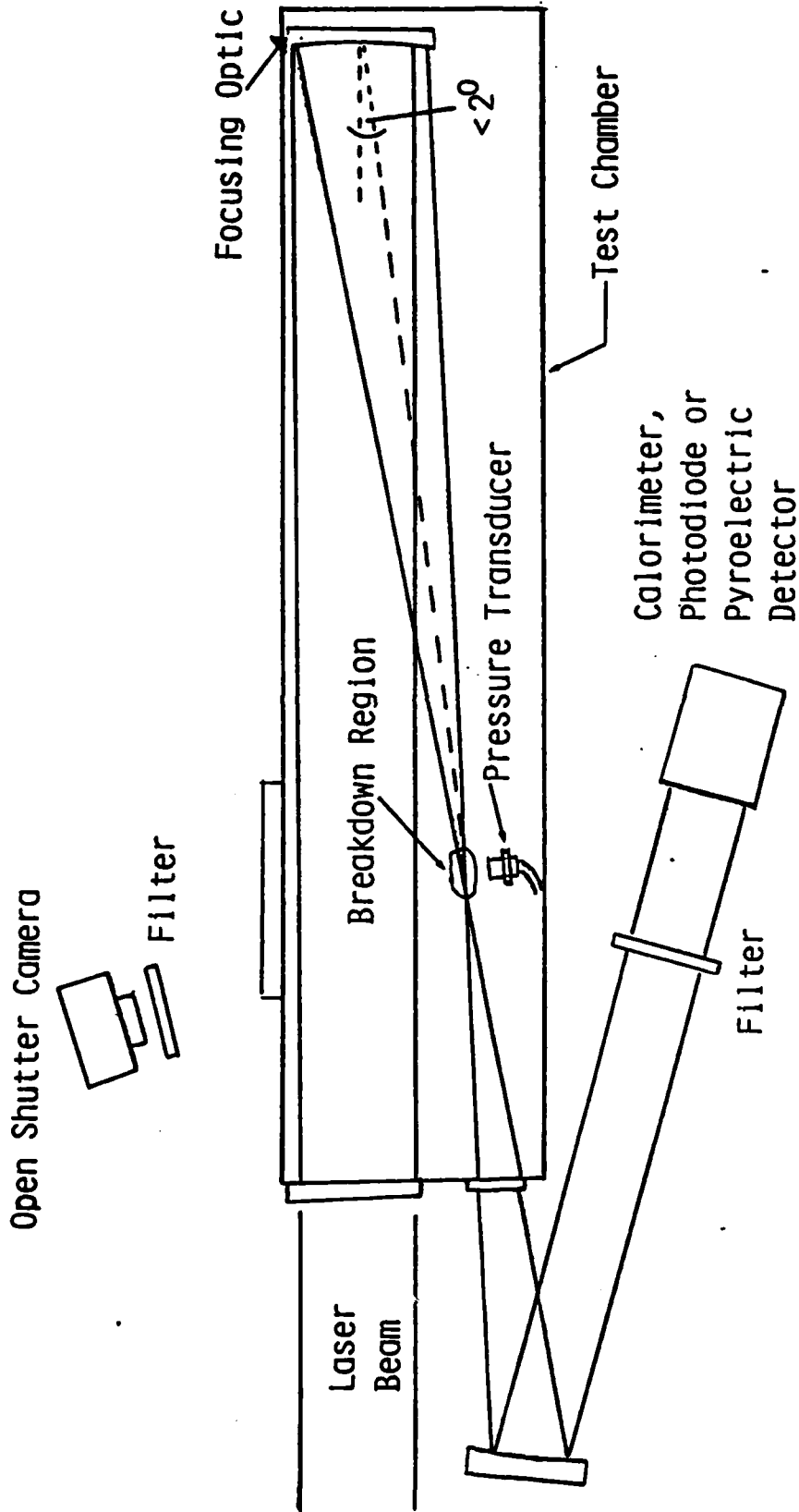


Fig. 4.22 - Schematic diagram of experimental set-up used for absorption physics studies.

The onset of breakdown and plasma formation is indicated by a reduction in the transmitted laser radiation. Finally, a pressure transducer (Kistler 211B4) was mounted in the chamber at a distance of 1 cm from the focus to measure the arrival time and pressure amplitude of the "blast wave" driven by the deposition of laser energy. The pressure transducer measurements were used to infer the fraction of laser energy absorbed by the gas.

In order to determine the power density or intensity at focus, measurements were made of the beam spatial energy distribution, or effective spot area, in the focal plane. For the CO₂ TEA laser pulse, the beam divergence was determined by using long focal length mirrors to take burn patterns of the focal spot in a Lucite block. The use of long focal lengths gave spot diameters and focal depths of sufficient dimensions to facilitate measurements of the minimum spot area. The measured focal spot diameter is related to the effective full angle divergence, θ , by $d_s = f\theta$ where f is the focal length used. Similar techniques were employed to measure the focal beam quality of the UV beam except that, instead of taking burn spot patterns, the beam focal spot was recorded photographically. The results of these measurements showed that the full area UV beam ($\sim 75 \text{ cm}^2$ as it emerges from the laser cavity) could only be focused to an effective spot size that was about five to ten times diffraction limited. It was found, however, that by using an aperture to sample an area that was only about 10% of the full beam, diffraction-limited focusing could be achieved.

4.3.2 Breakdown and Absorption Experiments at 10.6 μm

Using the experimental apparatus and techniques described above, measurements were made of the breakdown thresholds and resulting plasma optical absorptances for several gases at 10.6 μm . The laser used was a Lumonics K-101 TEA laser operated on a single transverse mode (TEM_{00}) with a Gaussian output beam profile. The pulse temporal profile consisted of an 80 ns FWHM gain-switched spike followed by a low intensity tail of about 3 μs duration. Approximately 2/3 of the total pulse energy was contained in the tail. By adjusting the laser gas mixture (principally by removing nitrogen), the low intensity tail could be eliminated. The full pulse energy

in the single transverse mode was 2 J. Breakdown measurements were made using either a 20 cm focal length AR coated germanium meniscus lens or a 76 cm focal length copper mirror, and were performed for f numbers ranging from 9 to 30. Measurements of the laser beam divergence yielded a value that was within 40% of that calculated from diffraction-limited Gaussian optics ($\theta = .6$ mR). Considering the limited precision of the measurements, it was decided to assume diffraction-limited focusing to calculate the intensity at focus. It should therefore be noted that the actual effective focal intensities may have been as much as a factor of two lower than the values that will be presented below.

The principal gases investigated were argon, hydrogen, and to a lesser extent, nitrogen and room air. Except for the air, all gases were of high purity grade and were passed through a column of molecular sieve 13X to remove any possible water or hydrocarbon impurities. Before filling with test gas, the chamber was evacuated to a pressure $\approx 10^{-4}$ torr.

Figures 4.23 and 4.24 present the experimental results obtained for the breakdown thresholds of argon and hydrogen, along with the corresponding PSI theoretical predictions (see Section 2.3). The experimental data include those obtained at PSI as well as the results of Cohn, Hacker, et al.^{4.7} and Hill, et al.^{4.7} Considering the experimental uncertainties in spot size, there is generally reasonable agreement among the various experiments and the PSI theory.

A set of experiments were also carried out to investigate the effect on the observed breakdown thresholds of creating some UV initiated preionization in the laser focal region. The UV preionization was generated by a high voltage spark ignited approximately 2 cm from the laser focus one microsecond prior to the laser firing. It was found that while the spark had little effect on the observed laser breakdown thresholds in hydrogen, it did have a significant effect in the case of argon. Without the spark, the breakdown thresholds in argon were found to be poorly defined. With the help of the spark, presumably by creating some UV preionization, the thresholds in argon were affected in two ways: 1) they were generally found

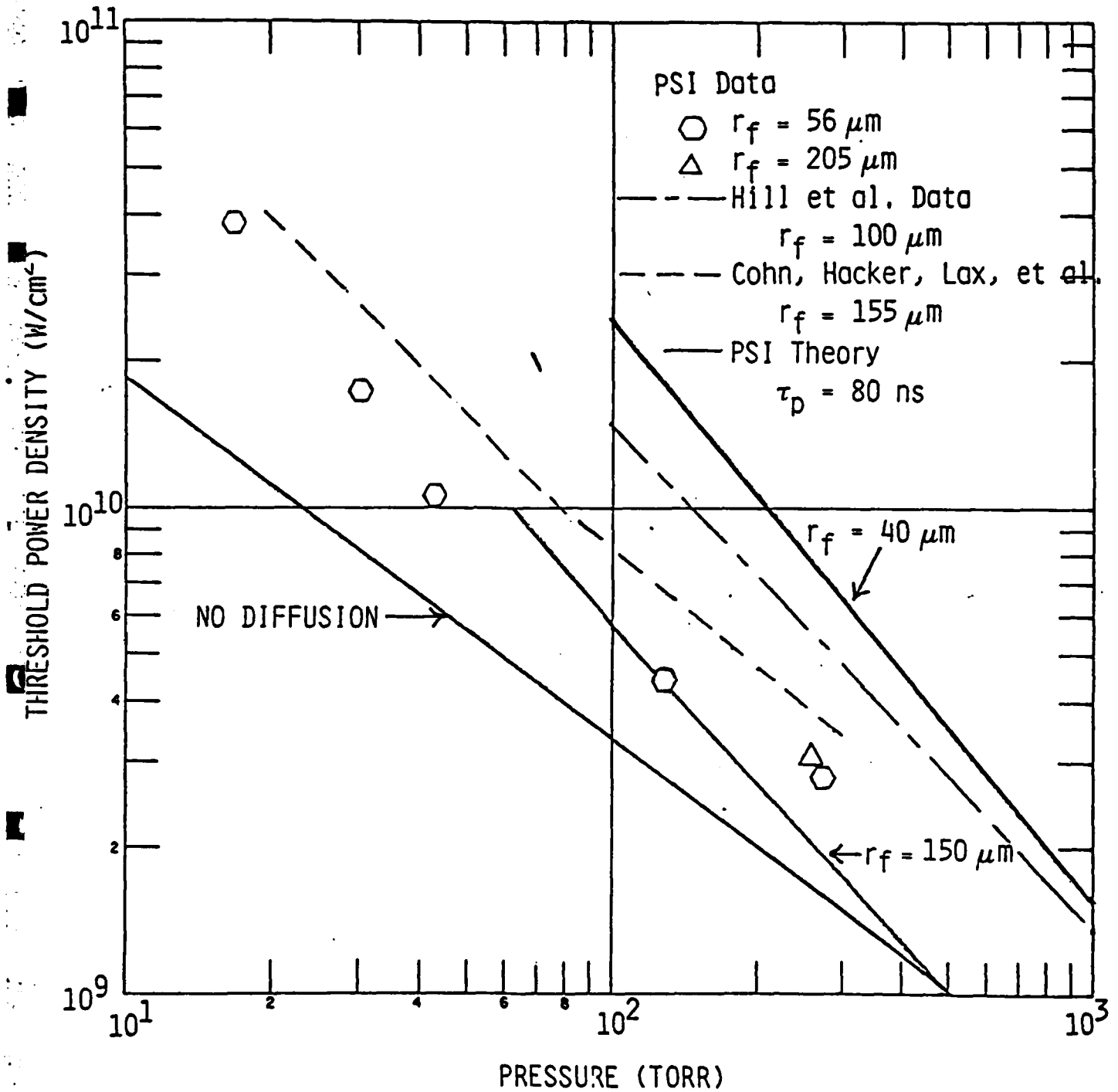


Fig. 4.23 - Comparison of experimentally measured breakdown thresholds in argon with PSI's theory predictions, $\lambda = 10.6 \mu m$, $\tau_p \approx 10^{-7} s$.

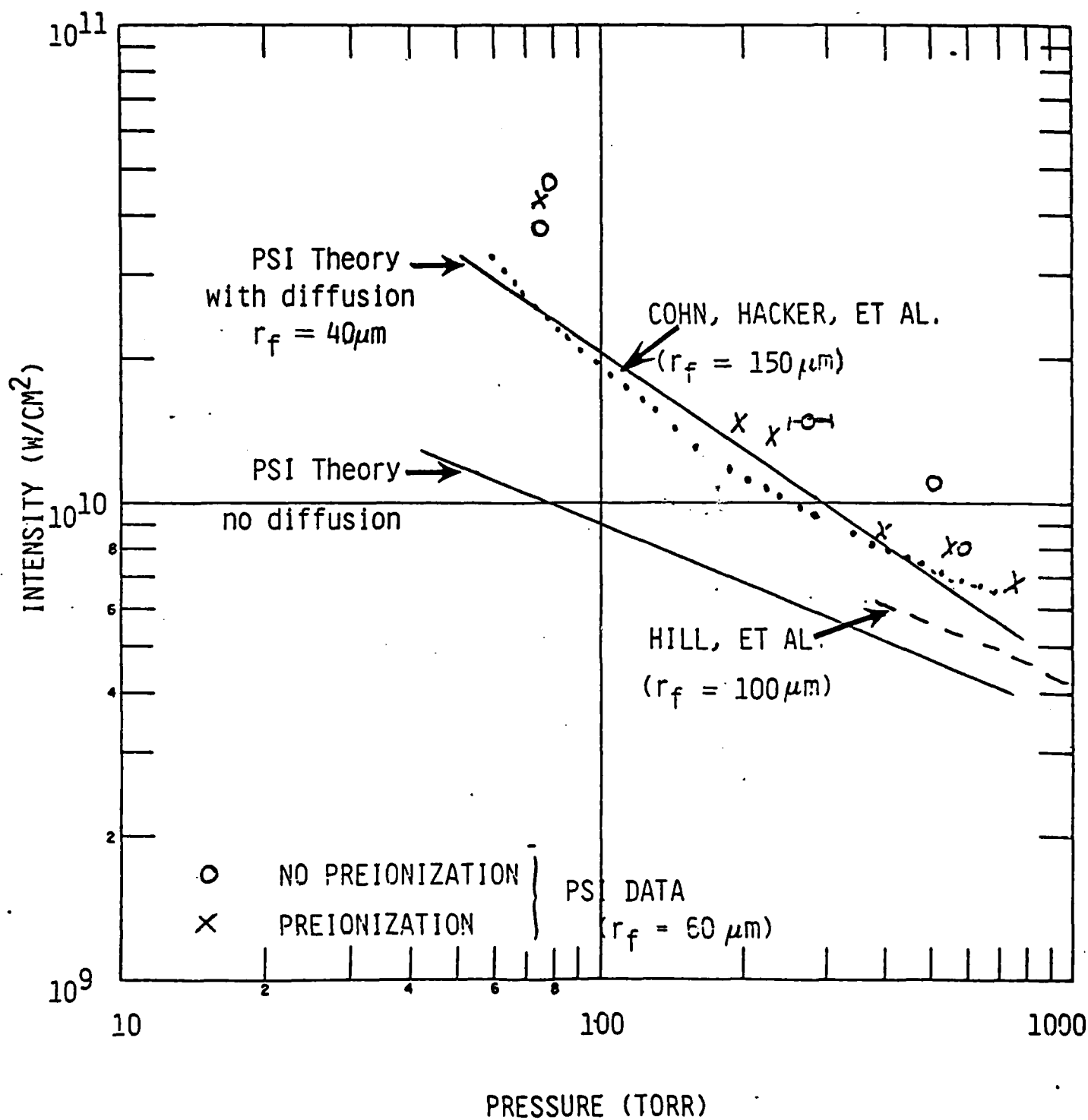


Fig. 4.24 - Comparison of experimentally measured breakdown thresholds in hydrogen with PSI theory predictions, $\lambda = 10.6\mu\text{m}$, $\tau_p = 10^{-7}$ s.

to decrease by a factor of two or more, particularly at the lower pressures, and 2) the thresholds became more reproducible. These observations are consistent with a cascade or avalanche breakdown process resulting from electron impact ionization. To begin such a process requires a few initial electrons in the laser focal region. Considering the small effective focal volumes used in these experiments ($\approx 10^{-5}$ cc) and assuming an ambient electron density of $\approx 10^4$ cc in the room temperature gases,^{4.9} we can see that the probability may only have been 0.1 that an electron was present in the unperturbed focal volume. For this reason, it is not surprising that additional preionization yielded a more reproducible breakdown threshold. The results presented in Fig. 4.23 for argon are those obtained with UV preionization. The reason that a similar effect was not observable in hydrogen is not clear at this time, but may just have been that the spark was less effective at creating UV preionization in hydrogen.

The presence of preionization in the PSI argon experiments may also serve to explain why in Fig. 4.23 the observed breakdown thresholds for $r_f = 56 \mu\text{m}$ are lower than the corresponding theory predictions (corrected for free electron diffusion). As was calculated in Section 2.2 for the present experimental conditions, electron diffusion is expected to become ambipolar for an electron density $> 10^{11} \text{ cm}^{-3}$; with the diffusion coefficient being approximately 250 times less than that for free electron diffusion. Thus, the higher the level of preionization, the sooner in the laser pulse time ambipolar effects will take over, and the smaller will be the losses to diffusion. The above hypothesis is supported by the fact that there is little difference between the threshold measured for a spot radius of $56 \mu\text{m}$ and that found for a spot radius of $205 \mu\text{m}$ ($P \approx 300$ torr). If free electron diffusion were dominant, the threshold for laser breakdown is predicted to be about 4 to 5 times higher for the smaller spot size.

Experimental measurements were also performed to determine the fraction of $10.6 \mu\text{m}$ laser pulse energy that was absorbed following the gas breakdown. As for the breakdown threshold measurements, data were obtained as a function of pressure in constant density backgrounds of argon and hydrogen. Figure 4.25 presents the results found for argon. As can be seen,

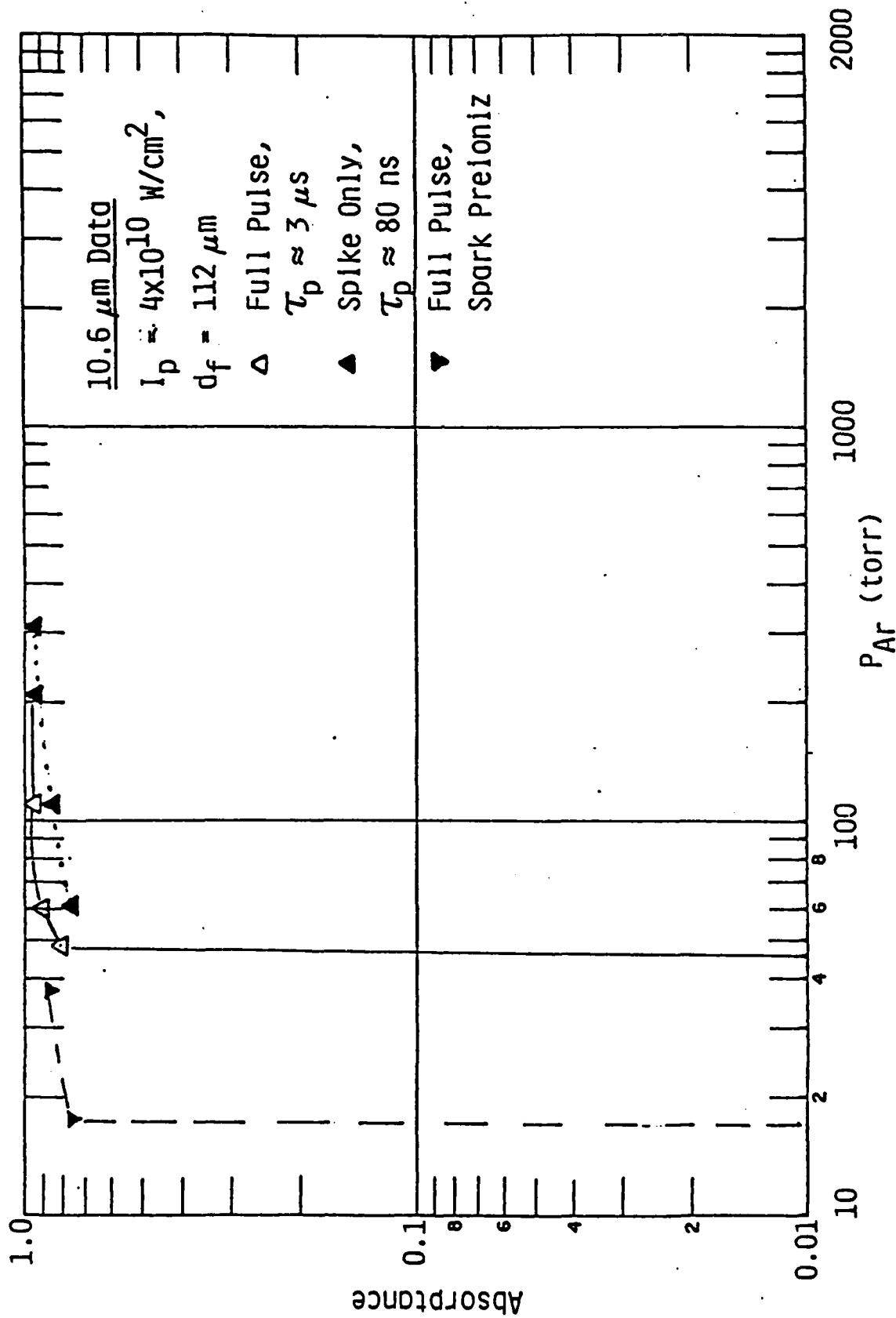


Fig. 4.25 - Fraction of 10.6 μm laser pulse energy absorbed in argon breakdown plasma as a function of the initial gas pressure. The absorbance was determined from optical transmission measurements.

once the threshold for breakdown is exceeded, a substantial fraction ($> 75\%$) of the laser energy can be absorbed. Here, as opposed to measurements performed in the rocket nozzle where the gas density decreased rapidly downstream of the focus (see Section 4.2.3.2), the late time absorption losses are minimal. The primary loss occurs during the induction time to achieve breakdown. Qualitatively similar behavior was also observed for hydrogen. These results suggest that one way to improve the optical absorption efficiency of a thruster might be to tailor the initial nozzle expansion to occur less rapidly. Doing so would result in a uniformly higher gas density in the vicinity of the throat.

The results of the $10.6 \mu\text{m}$ absorption physics studies can be summarized as follows:

- Theory predictions of breakdown thresholds in H_2 , Ar, and air are in reasonably good agreement with present experiments and other available data.
- Of the gases investigated, argon was found to have the lowest threshold for laser breakdown at $10.6 \mu\text{m}$, i.e., $I_T \approx 10^9 \text{ W/cm}^2$ at 1 atm pressure and $\tau_p \approx 10^{-7} \text{ s}$.
- UV preionization of argon leads to a lower and more reproducible threshold for laser breakdown at $10.6 \mu\text{m}$, a result that is consistent with a breakdown process that is initiated by electron-neutral inverse bremsstrahlung heating of electrons.
- High absorption efficiencies ($> .50$) are obtained for CO_2 laser pulses focused into constant density gas backgrounds at relatively low pressures ($P \geq 0.2 \text{ atm}$).

4.3.3 Breakdown and Absorption Experiments at $0.35 \mu\text{m}$

As was stated in Section 1, one of the principal objectives of the present studies was to determine how the absorption physics of pulsed laser propulsion scales from 10.6 microns to visible/UV laser wavelengths. In particular, we sought to ascertain for the XeF laser wavelength ($\lambda = 0.35 \mu\text{m}$) and several potential propellant gases, the degree to which the power density thresholds for laser breakdown, as well as the resulting plasma optical absorptances, depart from that predicted by a simple wavelength scaling

of inverse bremsstrahlung absorption. Qualitatively, we know that for sufficiently large photon energies (short laser wavelength) other laser absorption processes such as multiphoton absorption and direct photoionization of excited states can become important. Supporting this assertion are previous experimental studies^{4.10,4.11} conducted at fundamental and doubled Nd-Yag and ruby laser frequencies and for pulse times of 8 to 20 ns. The results of those investigations indicate that the thresholds for laser/gas breakdown generally increase with decreasing wavelength from the IR to the visible, reach a maximum, and then begin to decrease again toward the UV.

In Section 2.4 a theoretical model was described and calculations presented for the laser-induced breakdown of argon at 0.35 μm . In addition to inverse bremsstrahlung absorption and electron impact ionization, the model included multiphoton ionization and direct photoionization of excited states. In an attempt to validate this model for argon, as well as to provide relevant experimental data for other gases, experiments similar to those described above for 10.6 microns were carried out for 0.35 μm laser radiation. The laser utilized was a commercially supplied e-beam pumped excimer device (Maxwell Laboratories, Inc., MaximerTM 10-1) operated as an XeF laser ($\lambda = 0.353 \text{ m}$). Provided with a positive branch, confocal, unstable resonator optical cavity, the typical output energy of this device is 5 J in a pulse of approximately 0.6 μs duration.

The diagnostics and techniques employed were essentially the same as those described above for the 10.6 μm experiments. The laser energy for each pulse was determined by monitoring with a large area calorimeter a known fraction reflected off-axis from the quartz entrance window to the test chamber. The incident pulse time history was monitored in a similar way using an EG&G UV-040B UV enhanced silicon photodiode. The rise time (10% to 90%) of this photodiode, as it was used in our experiments, was shown to be $\leq 20 \text{ ns}$. The incident pulse energy in the focal plane was varied in two principal ways: 1) the pulse energy was allowed to decay naturally for numerous successive shots on the same laser gas mix, and 2) the energy could be attenuated by factors of 3 by placing sheets of blue-tinted polyester

acetate film in the beam path before the test chamber. The plastic sheets are supplied by Northeast A-V Supplies, Inc. for making transparencies.

For most of the data presented here, the laser beam was focused by a 1.6 meter focal length aluminized mirror. The effective beam irradiance area in the focal plane was determined by attenuating the beam intensity by several orders of magnitude using Wratten neutral density filters and then recording the beam spot on photographic film. When focusing the full output beam (a geometric square 10 cm on a side with the central 5 cm x 5 cm square missing due to eclipsing by the output coupling mirror), it was found that the effective minimum spot size was approximately 5 to 10 times that predicted for diffraction limited focusing.^{4.12} Furthermore, upon close examination, the beam structure at focus was shown to consist of a complex interference pattern having a "feather-like" appearance with several central "hot spots." Unable to determine the source of this "aberration" and to eliminate it, we decided to try to improve spatial coherence by masking the beam so that only a 2.5 cm x 2.5 cm segment was allowed to pass. The resulting focal plane beam profile was found to be well behaved and to possess the characteristic pattern and dimensions of the far field diffraction from a square aperture. For the 1.6 meter focal length mirror, the dimension of the central lobe in the focal plane (containing approximately 80% of the total power) was found to be 5×10^{-3} cm. The power densities at focus that will be quoted below are based upon measurements made with the masked beam.

Experimental measurements of the laser-induced breakdown threshold in argon at $\lambda = 0.35 \mu\text{m}$ are plotted as a function of pressure in Fig. 4.26 along with the corresponding predictions of the PSI theoretical model (see Section 2.4). The data include the PSI measurements made with a nominal 500 ns XeF (353 nm) laser pulse, and the measurements of Alcock et al.^{4.11} performed with a doubled ruby (347 nm) laser pulse of only 8 ns duration. As can be seen, while the data for the 0.5 μs pulse are in reasonably good agreement with the model predictions, the 8 ns threshold data are more than an order of magnitude lower than the corresponding model predictions. Thus, while the model predicts that the threshold power density for breakdown

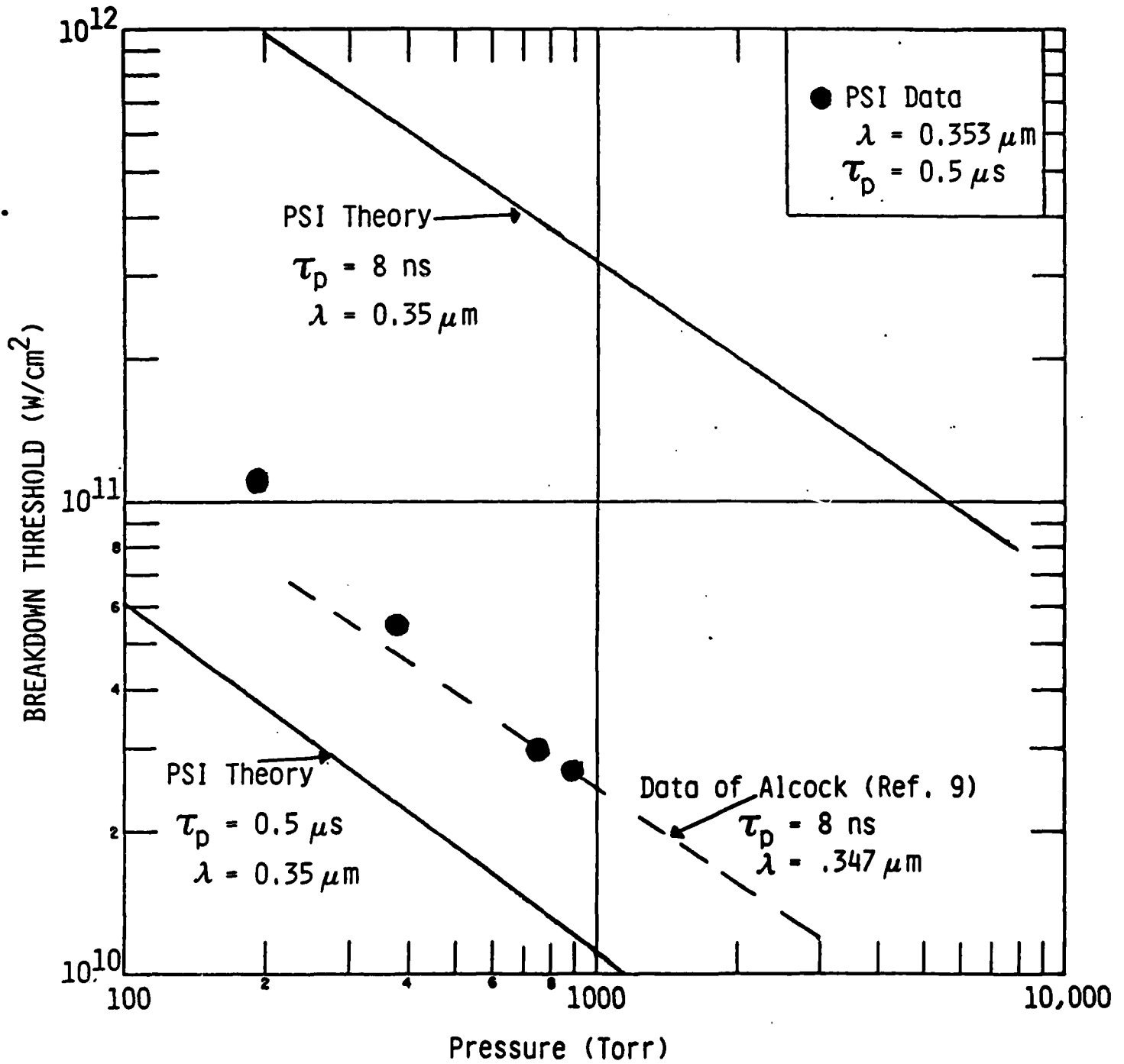


Fig. 4.26 - Argon laser induced breakdown threshold at $0.35 \mu\text{m}$.

should show a strong inverse dependence on pulse duration, e.g., the predicted threshold intensity for an 8 ns pulse is about 25 times higher than that predicted for a 500 ns pulse, the experimental data shown in Fig. 4.26 reveal no such scaling with pulse duration. In fact, the experimental data alone would suggest that there is an intensity threshold for breakdown in argon that is independent of pulse duration. The measured thresholds for both experiments do, however, show a pressure dependence that is in reasonable agreement with the theory and indicative of a breakdown process dependent on collisional mechanisms. As for the relatively "low" thresholds reported in Ref. 4.11, Alcock et al. have suggested^{4.13} that, at least for their experiments, breakdown may have been controlled by effects such as self-focusing and filamentation. Clearly, any future studies devoted to resolving these apparent discrepancies in the argon breakdown threshold at 0.35 μm should carefully address the possible effects of self-focusing.

Quite recently, additional breakdown data have become available as the result of preliminary experiments conducted at the National Laser Users Facility, Laboratory for Laser Energetics, Rochester, N.Y.^{4.14} For those experiments, the frequency tripled output of a glass laser ($\lambda = 0.3513 \mu\text{m}$, $\tau_p = 0.4 \text{ ns}$) was used to determine a laser breakdown threshold in one atmosphere of argon. The measurements, open shutter photographs and optical transmission, indicated a threshold of $6 \pm 4 \times 10^{12} \text{ W/cm}^2$. The large error limits are the result of uncertainties in the beam spatial distribution at focus, as well as difficulties that were encountered in precisely defining the onset of "breakdown." For the result quoted here, the "breakdown" threshold is defined as the lowest power density at which 1) measurable attenuation ($\geq 10\%$) of the transmitted beam was observed, and 2) a "bright" visible glow was seen in the laser focal region. Despite the present inaccuracies, it is clear that this recent data at 0.35 μm indicates a breakdown threshold for a pulse of 0.4 ns duration that is approximately two orders of magnitude higher than the corresponding measurements for pulse lengths $> 8 \text{ ns}$.

Summarized in Fig. 4.27 are all the existing 0.35 μm breakdown threshold data for argon ($P = 1 \text{ atm}$) plotted as a function of pulse duration. Also plotted are the corresponding predictions of the PSI model. The departure of the theoretical curve from a straight line at the highest laser intensities is the result of the increasing dominance of multiphoton ionization. As can be seen, while the threshold data at 0.4 ns and 500 ns are in reasonable agreement with the calculated values, the data obtained with doubled ruby laser pulses ($\lambda = 0.347 \mu\text{m}$, $\tau_p = 8 \text{ ns}$ and 20 ns) fall more than an order of magnitude below the predictions of the model. The source of the latter discrepancy is still not known, but several possibilities must be considered. Dust particles, impurities with low ionization potential, and spatial and temporal beam irregularities could all give rise to an apparently low breakdown threshold.

Despite present uncertainties, the existing data as well as PSI's theoretical model clearly indicate thresholds for argon breakdown at 0.35 μm that are considerably lower than predicted by a simple $1/\lambda^2$ scaling of the corresponding infrared thresholds. This is illustrated in Fig. 4.28 where the data at 0.35 μm are seen to be about a factor of 30 below the $1/\lambda^2$ extrapolation from 10.6 microns ($\tau_p \approx 10^{-7} \text{ s}$). A $1/\lambda^2$ scaling would be expected to hold for a breakdown process dominated by impact ionization due to electrons heated by inverse bremsstrahlung absorption. Apparently, at 0.35 μm additional excitation mechanisms become important such as multiphoton ionization and direct photoionization from excited states of argon.

Breakdown thresholds were also measured for other gases and the results are plotted as a function of pressure in Fig. 4.29. The data points with vertical arrows indicate lower limits for the threshold power densities. The maximum power density attained in this study was approximately $2 \times 10^{11} \text{ W/cm}^2$ and was limited by the Maximer beam quality, total available laser energy, and the available focusing optics. As can be seen from Fig. 4.29, of the gases investigated, argon has the lowest threshold for breakdown at 0.35 μm and hydrogen one of the highest. Unfortunately, because of the complexity of the theoretical analysis of laser breakdown at this wavelength, model predictions were only performed for argon.

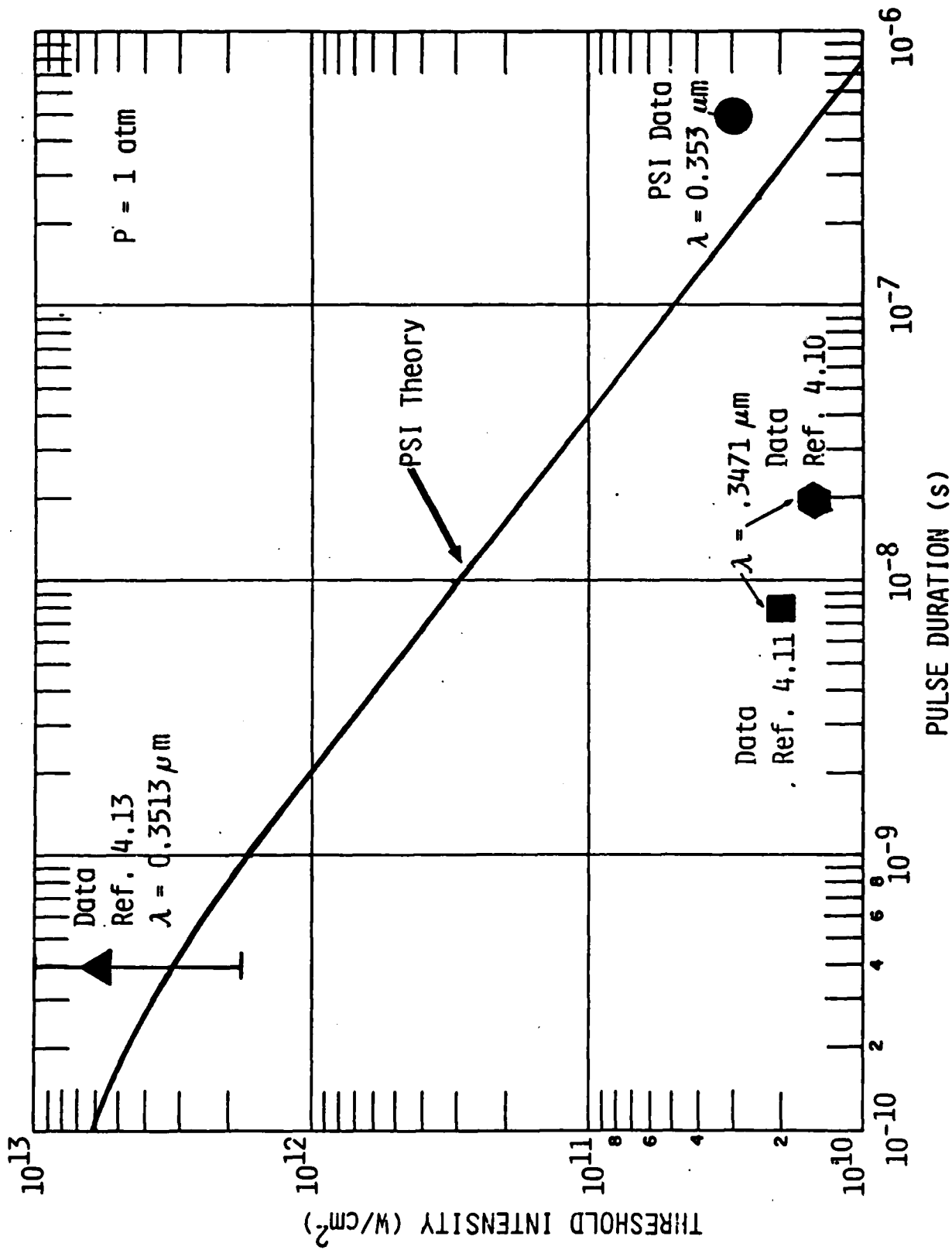


Fig. 4.27 - Laser-induced breakdown threshold for argon, $\lambda = 0.35 \mu\text{m}$,
 $P = 1 \text{ atm}$.

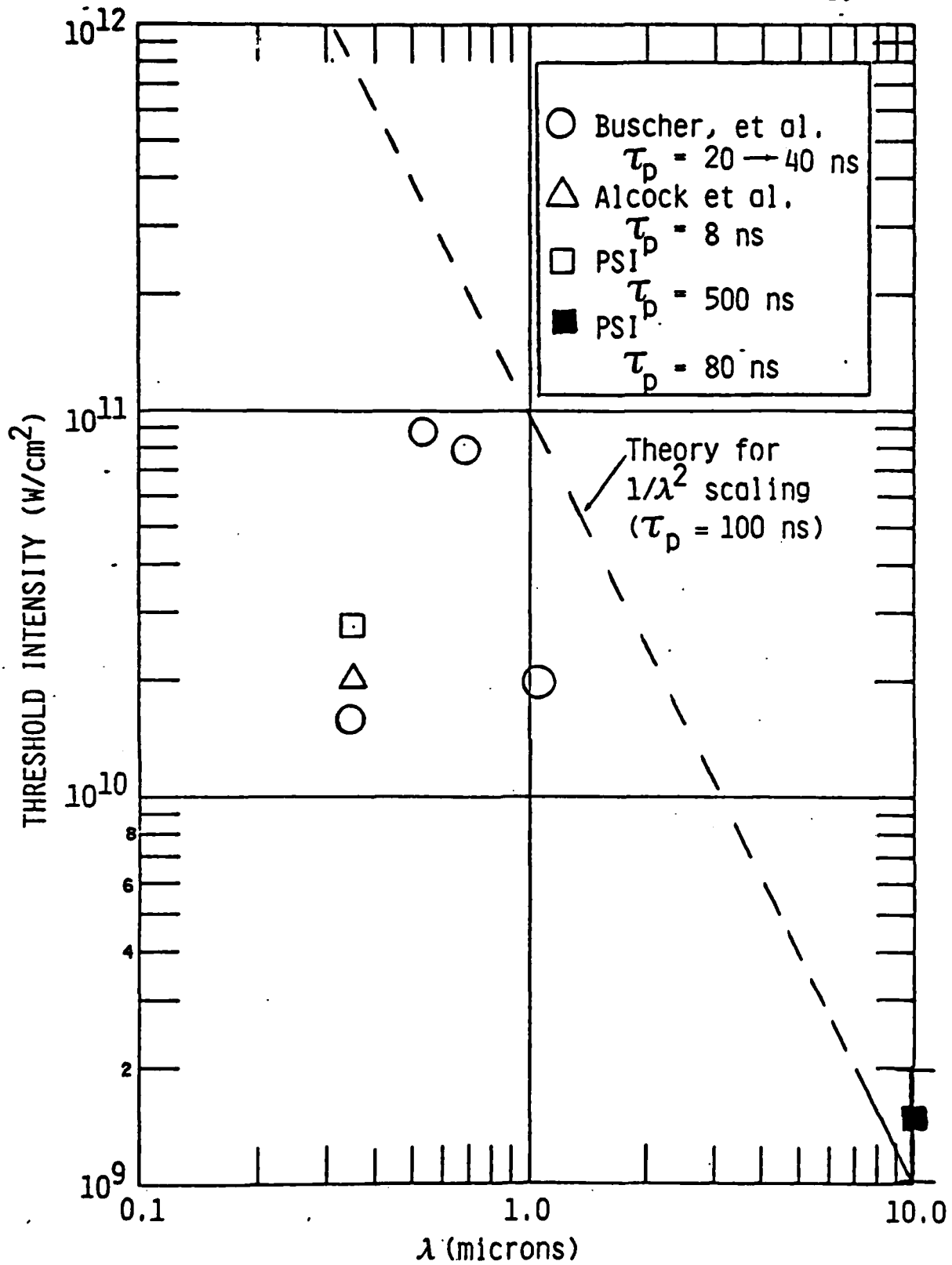


Fig. 4.28 - Laser induced breakdown threshold in argon vs wavelength ($P = 1$ atm).

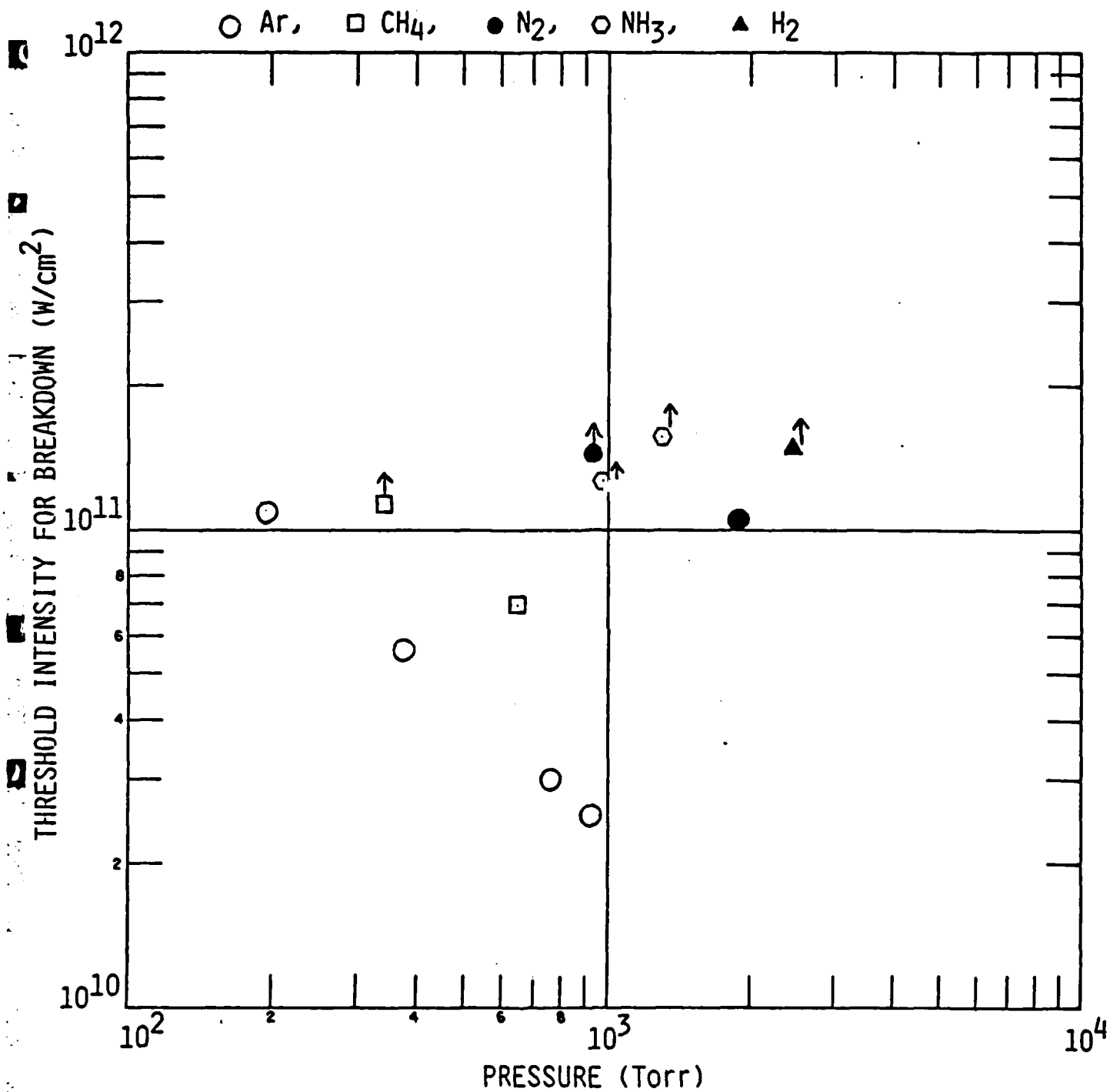


Fig. 4.29 - Experimental laser-induced breakdown thresholds for several gases at $\lambda = 0.35 \mu\text{m}$, $\tau_p = 0.5 \mu\text{s}$.

Finally, as for the absorption physics studies at 10.6 μm , measurements were made to determine the fraction of XeF laser pulse energy that was absorbed in the breakdown plasma. The results obtained from optical transmission measurements in argon are plotted in Fig. 4.30 as a function of the ambient pressure. Also plotted for comparison are the corresponding results observed at 10.6 μm . As can be seen, the data show that respectable absorption efficiencies can be achieved at 0.35 μm , although to do so requires higher gas densities than are needed at 10.6 μm . For example, while greater than 75% of the laser energy can be absorbed at 10.6 microns for argon pressures ≥ 50 torr, to achieve the same degree of absorption at 0.35 μm requires pressures of 1 atm or greater.

The data presented in Fig. 4.30 were obtained from time-integrated optical pulse transmission measurements using a large area calorimeter. A limited number of time-resolved transmission measurements using high speed photodetectors were also performed. The results of the time-resolved measurements showed that subsequent to breakdown the laser-produced plasmas were, in general, only partially absorbing to 0.35 μm radiation (except at the highest ambient argon pressures). This is in contrast to 10.6 microns where the breakdown plasmas were found to be opaque, i.e., transmission losses were associated with the finite time to achieve breakdown.

In order to confirm that the laser beam attenuation observed in the optical transmission experiments was dominated by plasma absorption rather than scattering, a separate determination of the absorbed laser energy was made by measuring the strength of the resulting blast wave. A pressure transducer (Kistler Model 211 B4) mounted 1 cm from the focus and approximately perpendicular to the optical axis was employed to measure the arrival time and amplitude of the laser-driven pressure wave. Applying the theory for a spherical blast wave in a constant density background,^{4.15} the transit times and shock pressures were used to infer the energy in the blast wave. With the incident laser energy known, a blast wave energy conversion efficiency, ϵ_{BW} , was then evaluated as the ratio of blast wave energy to incident laser energy.

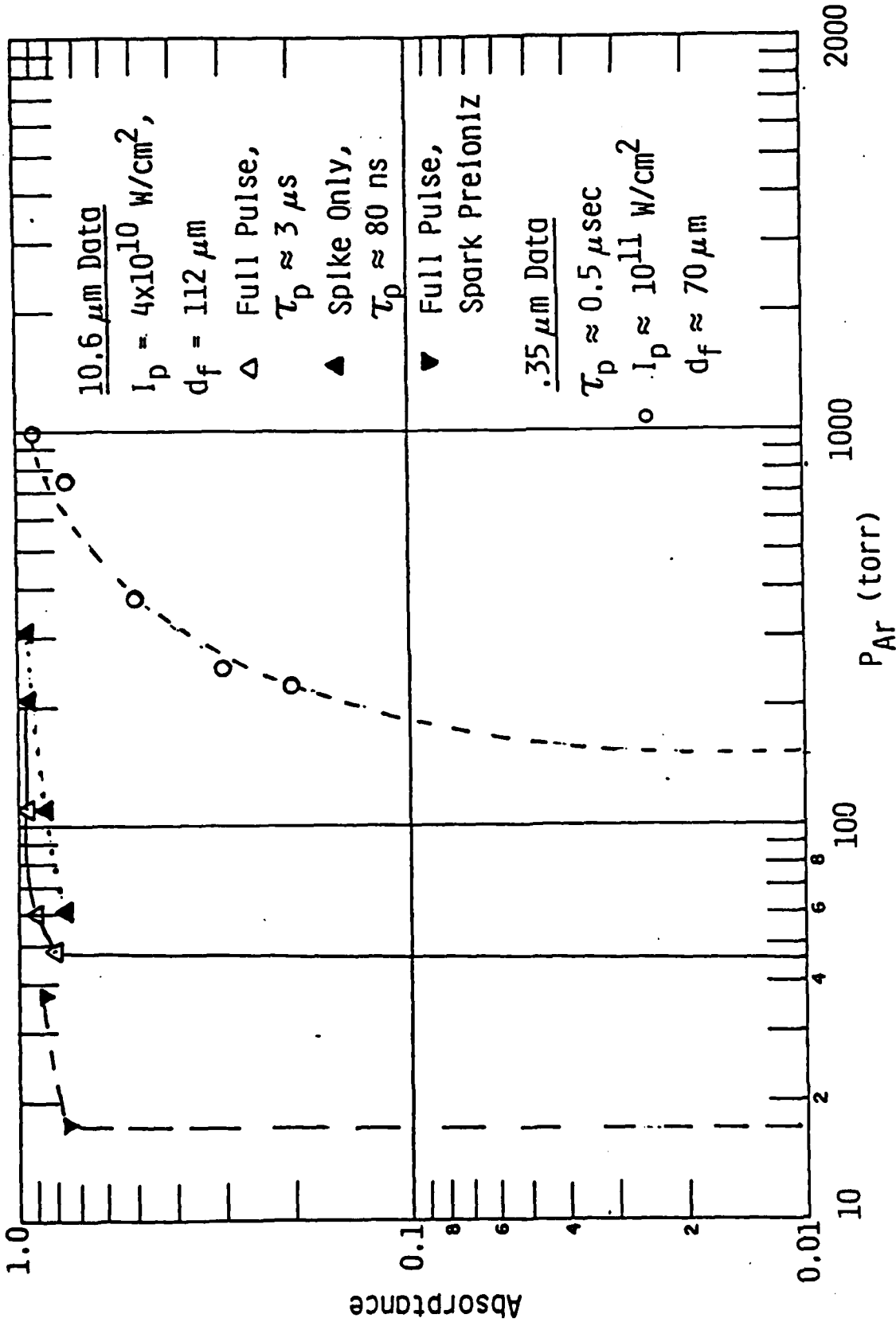


Fig. 4.30 - Fraction of laser pulse energy absorbed in argon breakdown plasma, 0.35 μm vs 10.6 μm .

The resulting conversion efficiencies found for argon, nitrogen and methane at various background pressures are presented in Fig. 4.31. Also shown with the laser to blast wave energy conversion efficiencies are the corresponding "absorptances" determined from the laser transmission measurements. From Fig. 4.31 it can be seen that although the blast wave conversion efficiencies inferred from the pressure transducer measurements appear to correlate reasonably well (in a relative sense) with the measured optical absorptances, the absolute values of the former are generally 1/2 to 2/3 of the latter. There are several possible explanations for this discrepancy: 1) the actual optical absorptance is less than the observed beam attenuation because of significant scattering contributions, 2) the energy observed in the blast wave is less than the optically deposited energy because of energy losses to early time plasma radiation and/or internal excitation, 3) the assumption of a "spherical" wave is poor due to initial preferential growth of the plasma along the laser beam, and 4) the shock wave has become sufficiently weak by the time it reaches the pressure transducer location that our blast wave approximation is inadequate. The effect of scattering should be assessed in future experiments by optical measurements designed to look for laser radiation outside the solid angle defined by the unperturbed beam. The other possible effects mentioned above, (2)-(4), could, in principle, be addressed for the case of argon by applying the numerical code described in Section 3. One modification that would be required, however, is the addition of a sub-routine to calculate argon radiation.

The results of the 0.35 μm absorption physics experiments can be summarized as follows:

- Threshold intensities for gas breakdown by XeF (0.35 μm) laser radiation ($\tau_p \approx 5 \times 10^{-7}$ s) are generally found to be about 20 to 30 times higher than the corresponding thresholds measured at 10.6 μm ($\tau_p \approx 1 \times 10^{-7}$ s). For 1 atm argon, the breakdown threshold at 0.35 μm is 3×10^{10} W/cm². At 10.6 μm , the threshold is 1-2 $\times 10^9$ W/cm².
- The measured breakdown thresholds at 0.35 μm are significantly lower than given by a $1/\lambda^2$ scaling of the corresponding 10.6 μm thresholds. The latter scaling would be expected to hold for a breakdown dominated solely by inverse bremsstrahlung heating.

LASER ENERGY ABSORBED IN BREAKDOWN REGION

- $\lambda = 0.35 \mu\text{m}$, F/16 optics, $\tau_p = 0.4 + 0.6 \mu\text{s}$
 $E_i = 2\text{J}$ $I_f \approx 10^{11} \text{ W/cm}^2$
- $\bar{\alpha}_{\text{opt}}$ determined from optical transmission measurements
- $\epsilon_{\text{b.w.}} = E_{\text{blast wave}}/E_{\text{laser}}$ determined from pressure transducer measurements of blast wave transit time and pressure along with blast wave theory

GAS	P(atm)	$\bar{\alpha}_{\text{opt.}}$	$\epsilon_{\text{b.w.}}$
Ar m = 40 $\gamma = 1.67$.17	--	--
	.27	.09	.05
	.30	.20	.14
	.33	.29	.19
	.33	.31	.23
	.50	.50	--
	1.0	.75	.47
	1.34	>.90	--
N ₂ m = 28 $\gamma = 1.4$	2.36	--	--
	2.70	.81	.41
	3.04	.87	.43
CH ₄ m = 16 $\gamma = 1.2$.47	--	--
	1.0	.21	--
	1.0	--	.27

Fig. 4.31 - Experimental determinations of fraction of XeF laser pulse energy deposited in breakdown gas.

- Of the gases investigated, argon has the lowest breakdown threshold and hydrogen the highest.
- Based on available data and the PSI theory, intensity thresholds for breakdown are seen to decrease with increasing gas pressure. For argon, $I_T \sim p^{-.7}$.
- The PSI theory predictions of the breakdown threshold in argon are in reasonable agreement with data for pulse durations of 5×10^{-7} s and 4×10^{-10} s. Both the model and data indicate an intensity threshold that scales inversely with pulse duration, i.e., $I_T \propto \tau^{-(.72 \pm .05)}$. The model, however, is not able to explain breakdown thresholds obtained with doubled ruby laser pulses ($\lambda = 0.347 \mu\text{m}$, $\tau_p \approx 10^{-8}$ s).^{4.9,4.10} In the latter studies, experimental thresholds are reported that are a factor of 10 to 20 lower than the corresponding predictions of the PSI model. The reason for this apparent discrepancy is still not understood.
- Substantial absorption was achieved in XeF ($0.35 \mu\text{m}$) laser-produced plasmas, particularly for the case of argon. For example, at a pressure of 1 atmosphere, between 50% and 75% laser energy absorption was achieved in argon.
- To achieve high laser energy deposition efficiencies at $0.35 \mu\text{m}$ does require, however, higher gas densities than were needed at $10.6 \mu\text{m}$.
- Assuming similar pulse energies at $0.35 \mu\text{m}$ and $10.6 \mu\text{m}$, the implication of the above results for pulsed laser propulsion is that to achieve efficient performance at $0.35 \mu\text{m}$ with high I_{sp} (high energy per unit mass) will likely require higher gas densities and smaller volume nozzles than are necessary at $10.6 \mu\text{m}$.

Using the results of the above absorption physics studies, an experiment was designed to demonstrate efficient single-pulse energy coupling of XeF laser radiation into a nozzle flow. The experiment utilizes a conical nozzle with external focusing optics. Preliminary results are presented in Section 4.4 for argon and helium propellants.

4.4 Preliminary Single-Pulse Thruster Performance Results at 0.35 μm

To demonstrate efficient energy coupling of pulsed vis/UV laser radiation into a nozzle flow, an experiment was designed that utilizes a conical nozzle and external focusing optics. A schematic diagram of the experiment is shown in Fig. 4.32. Figure 4.33 lists nominal operating conditions for such a rocket to achieve a specific impulse of 1000 s in argon with the available Maximer laser energy. Based upon earlier absorption measurements in constant density backgrounds (see Fig. 4.30), the plenum pressure and nozzle geometry - and hence gas density in the focal region - have been chosen to assure an absorption efficiency $\geq 50\%$.

Preliminary energy conversion efficiency data at 0.35 μm have been obtained with the nozzle configuration shown in Fig. 4.32. Using pressure transducers mounted in the rocket side wall at $R = 4.4$ cm and $R = 9.4$ cm, we have measured blast wave transit times for argon and helium at varying mass flow rates (plenum delivery pressures). The shock transit times were then used to infer the energy in the blast wave by comparing them to the results of either an ideal blast wave similarity solution or a numerical code simulation that models in detail the laser absorption process, multiple ionization, and equilibrium excited state thermodynamics (see Section 3.14). The results of these measurements are presented in Fig. 4.34. As can be seen, the data indicate energy conversion efficiencies at the highest mass flow rates of up to 40% for helium and $\geq 60\%$ for argon. Further, one sees that the conversion efficiencies inferred from the transit time data are even higher if the real gas thermodynamic effects, i.e., ionization and electronic excitation, are accounted for.

The preliminary data presented above for a conical nozzle flow, as well as the data presented in Section 4.30 for constant density backgrounds, clearly suggest that efficient conversion of pulsed XeF (0.35 μm) laser radiation into thruster fluid mechanical energy is possible. Using an argon propellant at moderate delivery pressures, conversion efficiencies $\geq 50\%$ have been demonstrated. The results do indicate, however, that to achieve efficient coupling, higher plenum pressures will probably be necessary for vis/UV operation than are required at 10.6 μm .

SCHEMATIC OF 10J ROCKET EXPERIMENT FOR $\lambda = 0.35 \mu\text{m}$

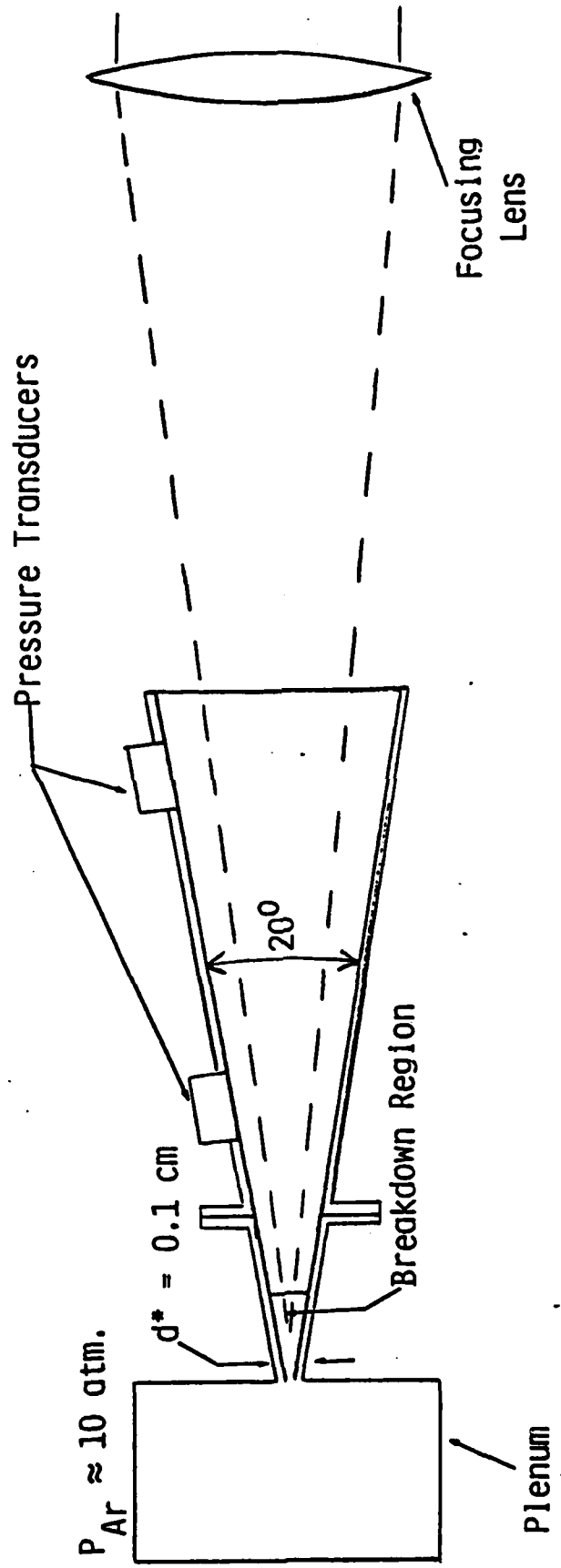


Fig. 4.32 - Schematic of nozzle experiment for 0.35 μm energy conversion efficiency measurements.

- Design Constraints:

Gas: Argon
 I_{sp} : 1000 s
 E_L : 5 to 10 J
 τ_p : $0.5 \mu s$
 $\epsilon_{conv.}$: $\gg 50\%$

- Resulting Nozzle Design:

Plenum Pressure: 10 atm.
 Throat Diameter: 0.1 cm
 Cone Angle: 20°
 Interpulse Time: 1.5 to 3.0×10^{-5} s
 Δm_{pulse} : $.5$ to 1.0×10^{-4} g
 $f\#$: $f/3 \rightarrow f/5$

Fig. 4.33 Design conditions for laboratory experiment to demonstrate $1000 \text{ s } I_{sp}$ in argon, $\lambda = 0.35 \mu m$.

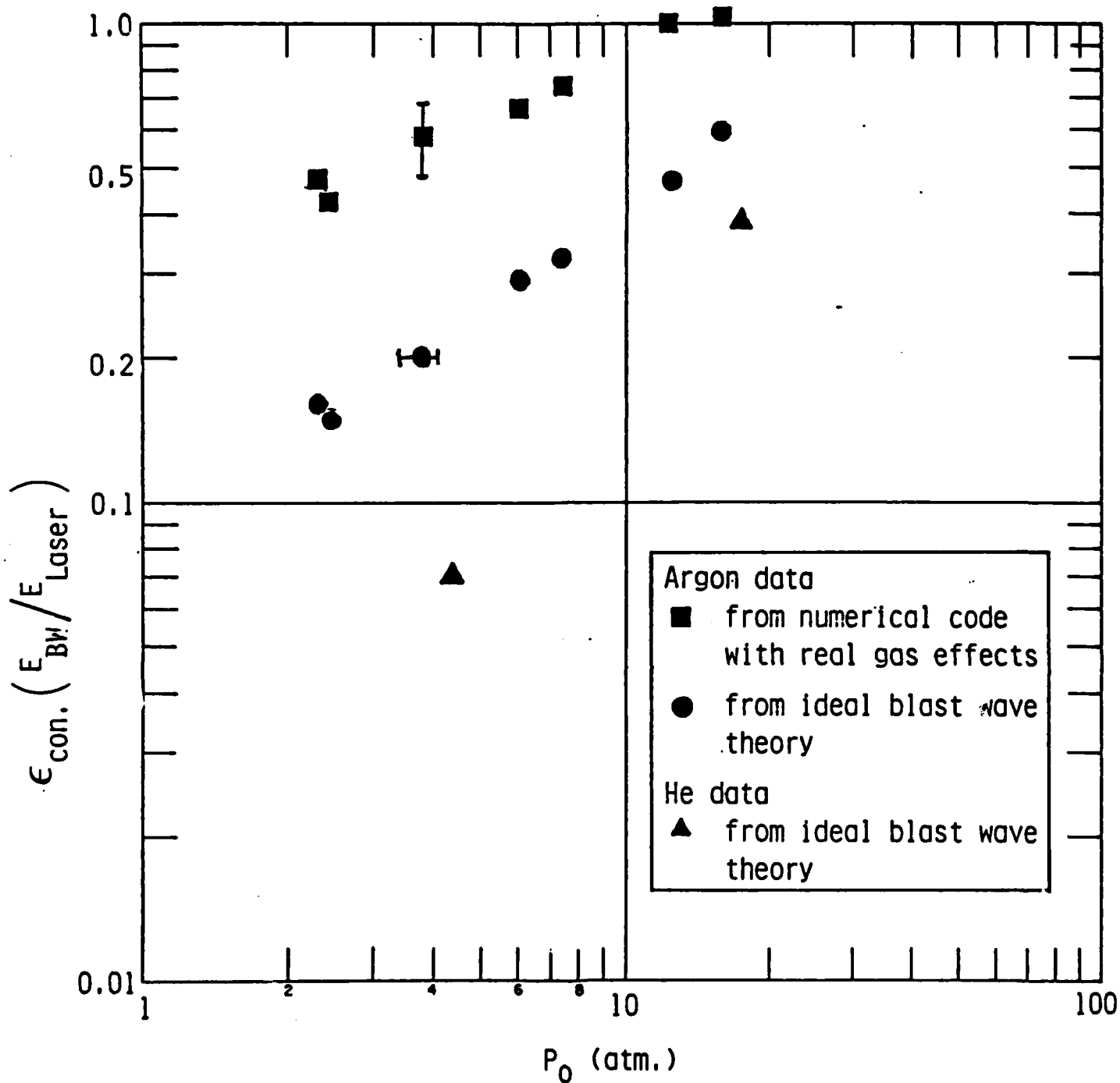


Fig. 4.34 XeF laser to blast wave energy conversion efficiency vs. stagnation pressure. Blast wave energy is inferred from shock transit time measurements in conical nozzle flow. Cone angle is 20° (full angle) and throat diameter is 0.1 cm.

4.5 References

- 4.1 P. E. Nebolsine, A. N. Pirri, J. S. Goela, and G. A. Simons, "Pulsed Laser Propulsion - Final Report," PSI TR-108, Physical Sciences Inc., February 1978.
- 4.2 P. E. Nebolsine, A. N. Pirri, J. S. Goela, and G. A. Simons, "Pulsed Laser Propulsion," AIAA J. 19, 127 (1981).
- 4.3 H. Mirels and J. F. Mullen, "Aerodynamic Blast Simulation in Hypersonic Tunnels," AIAA J. 3, 2103 (1965).
- 4.4 J. H. Jacob, E. R. Pugh, J. D. Daugherty, and D. B. Northam, "An Absolute Method of Measuring Energy Outputs from CO₂ Lasers," Rev. Sci. Instr. 44, 471 (1973).
- 4.5 W. L. Wiese, M. W. Smith, and B. M. Miles, "Atomic Transition Probabilities," Vol. II, Sodium through Calcium, NSRDS-NBS22, p. 187 (1969).
- 4.6 Following the completion of the present work, a relevant analysis of the radiative trapping of electronically excited Ar atoms was brought to our attention; see, B. D. Green, G. E. Caledonia, L. G. Piper and J. S. Goela, "LABCEDE Studies - Final Report," PSI TR-261, Physical Sciences Inc., Sept. 1981. The results of that analysis show that for the argon atom densities of interest in the present study, the optical transitions that were observed were probably radiatively trapped.
- 4.7 H. Cohn, M. Hacker, B. Lax and W. Halverson, J. Appl. Phys. 46, 668 (1974).
- 4.8 G. Hill, D. James and S. Ramsden, J. Phys. D. Appl. Phys. 5, 155 (1972).
- 4.9 C. Grey Morgan, Rep. Progr. Phys. 38, 621 (1975).
- 4.10 H. T. Buscher, R. G. Tomlinson, E. K. Damon, "Frequency Dependence of Optically Induced Gas Breakdown," Phys. Rev. Lett. 15, 847 (1965).
- 4.11 A. J. Alcock, K. Kato, M. C. Richardson, "New Features of Laser-Induced Gas Breakdown in the Ultraviolet," Opt. Comm. 6, 342 (1972).
- 4.12 M. M. Weiner, "Useful Beam Quality Design Curves for Unstable Resonators," Opt. Eng. 13, 87 (1974).
- 4.13 M. C. Richardson and A. J. Alcock, "Interferometric Observation of Plasma Filaments in a Laser-Produced Spark," Appl. Phys. Lett. 18, 357 (1971).
- 4.14 G. M. Weyl, D. I. Rosen, J. Wilson and W. Seka, "Laser-induced Breakdown of Argon at 0.35 μm ," Phys. Rev. A, v. 26, no. 2, p: 1164 (1982).
- 4.15 L. Sedov, "Similarity and Dimensional Methods in Mechanics," Academic Press, 1959.

5. CONCLUSIONS

Thruster Performance Studies

- High specific impulse (I_{sp}) has been demonstrated for a small-scale thruster powered by pulsed CO_2 laser radiation. Using hydrogen and argon propellants, we have achieved I_{sp} 's of 1000 s and 500 s, respectively.
- It has been shown, at least for 10.6 μm performance, that the thruster can take the form of a parabolic (self-focusing) nozzle that requires no external focusing optics.
- The conversion of laser energy into thruster fluid mechanical energy can be accomplished with high efficiency, i.e., $\geq 50\%$. Conversion efficiency is found to be greatest at the highest mass flow rates.
- In the small-scale thruster experiments, imperfect laser absorption (non-opacity of the laser-produced plasma) was found to be an important energy loss mechanism, particularly at the lowest mass flow rates (nozzle gas density).
- Preliminary single-pulse thruster experiments have been performed using XeF (0.35 μm) laser radiation and external focusing optics. The measurements for argon and helium propellants indicate that high laser to blast wave energy conversion efficiency is possible at this wavelength. To achieve high optical deposition efficiency, however, requires that the nozzle gas density in the vicinity of focus be higher than was necessary at 10.6 μm . For fixed laser pulse energy, the latter result leads towards smaller volume nozzles to maintain high I_{sp} .
- We have modeled in detail the fluid mechanics of a single pulse of a thruster heated by a pulsed laser. The model is quasi-one-dimensional and includes laser energy absorption for 10.6 μm and 0.35 μm wavelengths, and equilibrium chemistry of argon or hydrogen propellants. Calculations are made by means of a "shock-capturing" numerical scheme. The results of the calculations have been used to interpret shock wave pressure and transit time measurements to yield estimates of the laser energy deposited in the gas.

Absorption Physics Scaling Studies

- Thresholds measured for laser-induced gas breakdown at 0.35 μm were generally found to be at least 20 to 30 times higher than at

10.6 μm ; e.g., for argon at 1 atmosphere, I_T (10.6 μm , $\tau_p \approx 10^{-7}$ s) = $1-2 \times 10^9$ W/cm² while I_T (0.35 μm , $\tau_p \approx 5 \times 10^{-7}$ s) = 3×10^{10} W/cm².

- For argon at 0.35 μm , the PSI model and limited experimental data suggest a threshold intensity for laser-induced breakdown that scales with pulse duration as $\tau^{-(.72 \pm .05)}$.
- The available data and PSI's model for argon also indicate that the threshold intensity required for breakdown decreases with increasing gas pressure as $p^{-0.7}$.
- The measured breakdown thresholds in argon at 0.35 μm suggest contributions from laser absorption mechanisms in addition to inverse bremsstrahlung absorption. Based on the model, additional mechanisms would appear to be photoionization of excited states of argon and multi-photon ionization.
- To achieve high optical deposition efficiency at 0.35 μm in the laser-produced plasma requires significantly higher initial gas pressure than was necessary for 10.6 microns. For example, while greater than 75% of the 10.6 μm pulse energy was absorbed in argon for $P \geq .02$ atm a similar degree of absorption at 0.35 μm could only be achieved for $P \geq 1$ atm.

Mission Analysis Studies

The conclusions of the analyses performed for defense-related missions of pulsed laser propulsion are included in Vol. II.

DISTRIBUTION LIST FOR
FINAL TECHNICAL REPORT

VOL. I

FOR

Contract #N00014-78-C-0328

Director, Advanced Research Projects Agency 1400 Wilson Boulevard Arlington, Virginia 22209 Attention: Program Management	2
Scientific Officer Director Physics Program Physical Sciences Division Office of Naval Research 800 North Quincy St. Arlington, Virginia 22217 Attn: Dr. W. J. Condell (Code 421)	1
Administrative Contracting Officer DCASMA-GBCA-C6 495 Summer St. Boston, MA 02210	1
Director, Naval Research Laboratory, Att: Code 2627 Washington, D. C. 20375	6
Defense Technical Center Cameron Station Alexandria, VA 22314	12
Office of Naval Research - Boston Dr. Fred W. Quelle Barnes Bldg. 495 Summer St. Boston, MA 02210	2